A study of rolling contact fatigue cracks in lubricated contacts

By

Robbie Balcombe

Thesis submitted to Imperial College London

for the Degree of Doctor of Philosophy

and Diploma of Imperial College (DIC)

April 2012

Tribology Section

Department of Mechanical Engineering

Imperial College London

Abstract

A novel method for coupling fluid pressure and crack deformation for the purpose of analysing rolling contact fatigue (RCF) cracks in lubricated, hydrodynamic and elastohydrodynamic, contacts is presented. The model addresses some of the simplifying assumptions applied to existing models presented in the literature such as: (i) using an imposed fluid pressure gradient inside the crack, (ii) using an imposed fluid pressure at the crack mouth, and (iii) adopting a surface contact pressure, Hertzian or EHL, that does not account for the fluid flow in and out of the crack during loading. The model has been used to model the effect of lubricant/crack interaction in various RCF configurations as the rolling element passes over the pre-formed crack; which has direct application to bearings and rail/wheel contacts. The results of the simulations performed with the fully-coupled fluid/solid solver developed by the author suggest that the cracked component/lubricant interaction contributes significantly to accelerate the rate of surface breaking crack growth in rolling element bearings and wheel/rail type contacts. It is shown through simulations that the lubricant works as a catalyst inside the crack to convert the compressive contact load into a crack opening, tensile fatigue mechanism, through the effect of fluid pressurisation inside the crack. The results obtained using such a model suggest that the opening associated with the fluid action within the crack induces large mode I stress intensity factors. This has been shown to be the principal factor that promotes and influences the rate of rolling contact fatigue crack growth in lubricated contacts.

In addition to the modelling work, an experimental method of analysing RCF cracks in real time has been developed. The technique is based on laser induced fluorescence that allows the penetration of the fluid within the crack to be observed. Though the method would require development to be used to provide results that could be used for quantitative comparisons with crack models, some encouraging preliminary results have been obtained: the technique has been shown to be suitable for measuring, at least qualitatively, the real time evolution of the film thickness in RCF cracks.

Acknowledgements

I would, first of all, like to thank my supervisors Dr Daniele Dini and Dr Andy Olver for their help, encouragement, wisdom and support. I would also like to thank SKF, and in particular Dr Amir Kadiric and Dr Stathis Ioannides, for their interest and financial support (and for sending me to some nice conferences during my PhD). Most of all though I would like to thank Dr Mark Fowell for his invaluable input, guidance, and at times, even moral support, throughout this project.

I would also like to take this opportunity to thank certain members of the Imperial College tribology group who helped to make my time at Imperial College all the more enjoyable, who were always up for going to the pub for a pint after a long week to have some “philosophical” discussions about tribology. In particular I would like to thank; Angelos Zografos, Ales Kratky, Amir Kadiric (for many shots of Sambuca!), Joslyn Hili, Simon Medina, Saverio Reina, Connor Myant, Jessika Nyqvist, Mark Fowell and Mark Ingram. Thanks guys, I couldn’t have done it without you.

Finally I would like to thank my parents Carol and Brian without whom none of this would have been possible.

Table of Contents

Nomenclature 17

Chapter 1 19

Introduction 19

1.1 Introduction 19

1.2 Objectives 20

1.3 Background and basis for innovation 22

Chapter 2 26

Literature Review 26

2.1 Introduction 26

2.2 Fracture Mechanics and RCF 28

2.3 Linear Elastic Fracture Mechanics 29

2.4 Crack Propagation 31

2.5 Mixed Mode Crack Propagation 33

2.6 The Application of LEFM to RCF 36

2.6.1 Boundary Element Methods 37

2.6.2 Greens Function Method 38

2.6.3 Distributed Dislocations 40

2.6.4 Weight Function Method 42

2.6.5 Finite Element Methods 43

2.6.6 Extended Finite Element Method (XFEM) 44

2.7 Lubricated RCF Cracks: a long history, yet an unresolved issue 46

2.7.1 Penetration of Lubricant into RCF Cracks 47

2.7.2 Surface-breaking and sub-surface RCF Cracks 51
2.8 Two Dimensional Models 54
2.8.1 Friction Reduction Mechanism 55
2.8.2 Hydraulic Pressure Mechanism 57
2.8.3 Fluid Entrapment Mechanism 61
2.8.4 Squeeze Fluid Film Model 63
2.8.5 Multiple Cavity Model 68
2.8.6 Three Dimensional Models 70
2.9 Experimental RCF Crack Studies 72
2.10 Duration of Initiation/Propagation 76
2.11 Summary 77
Chapter 3 79
Dry Crack Modelling 79
3.1 Introduction 79
3.2 Modelling Methodology 83
3.3 Formulation 84
3.3.1 Solving Blocks 90
3.4 Validation 106
3.5 Results and Discussion of a dry contact RCF test case 116
3.6 Summary 120
Chapter 4 121
Hydrodynamic Crack Model: Introducing Fluid/Solid Coupling 121
4.1 Introduction 121
4.2 Modelling Strategy and Formulation 125
4.2.1 Fluid Solver 128
4.2.2 Fluid Formulation 130
4.2.4 Fluid Domain Coupling 140
4.2.5 Crack closure 144

4.2.6 Solid Solver 145
4.2.7 Fluid-Solid Coupling 148
4.3 Validation of individual solvers and intermediate steps 151
4.4 Results and Discussion 154
4.5 Summary 169
Chapter 5 170
Elastohydrodynamic (EHL) Crack Model 170
5.1 Introduction 170
5.2 Modelling Strategy and Formulation 173
5.2.1 Fluid Solver 174
5.2.3 Fluid Formulation 177
5.2.4 Solid Solver 179
5.2.5 Coupled EHL Algorithm 186
5.3 Validation & Convergence of the EHL algorithm 193
5.4 Results and Discussion 196
5.4.1 HL vs EHL 196
5.4.2. EHL Isoviscous and Piezo-viscous 204
5.4.3 Higher Pressure Isoviscous EHL models 211
5.5 Summary 232
Chapter 6 234
RCF Crack Propagation in EHL 234
6.1 Introduction 234
6.2 Modelling Strategy and Formulation 237
6.2.1 Solid Solver 239
6.2.2 Crack Growth 241
6.2.3 Crack Propagation Rate 243
6.3 Validation 244
6.4 Results and Discussion 245

6.5 Summary 258
Chapter 7 259
Experimental Development 259
7.1. Introduction 259
7.2. Simulating a Surface-Breaking Crack 260
7.3. Experimental Method for Monitoring the Crack 263
7.3.1 Principles of Laser Induced Fluorescence 264
7.4 Experimental Apparatus 267
7.4.1 Drive and Load System 268
7.4.2 Optical Equipment 270
7.5 Testing and Results 272
7.6. Summary 278
Chapter 8 279
Conclusions and Future Work 279
References 286
Appendices 308
Appendix A 309
Appendix B 310

Table of Figures

Chapter 1:

Figure 1.1. SKF Roller bearing 21

Chapter 2:

Figure 2.1. Schematic illustration of the different regimes of stable crack propagation 32

Figure. 2.2. Relationships between fatigue crack growth modes and relative applied load magnitude 34

Figure. 2.3. Quarter point node, where a single node at a crack tip (shown in red) is split by a number of triangular elements 44

Figure 2.4 Typical 2D XFEM stress field from a crack propagation problem solved using the finite element package Abaqus, (a) σ_x (b) τx_y (c) σ_y 45

Figure 2.5 Schematic of surface cracks on a rail segment used for experimental analysis 48

Figure 2.6 Rail sample following destructive examination, UV light reveals fluid penetration of the surface breaking cracks 49

Figure 2.7 Sequence of interference images showing a micropit passing through a contact, Note the large amount of fluid expelled into the cavitated region in (c) 50

Figure 2.8 Sequence of schematics of surface breaing (a) & (b) and subsurface cracks (c) 52

Figure 2.9 Schematic of the 2D, lubricated, RCF crack model solved in the literature 54

Figure 2.10 Shear mode crack growth accelerated by reduction of friction between the crack faces 56

Figure 2.11 Tensile model crack growth due to hydraulic transmission of contact pressure 57

Figure 2.12 Fluid assisted mechanism of crack growth due to entrapment and fluid pressurisation inside the crack 60

Figure 2.13 Squeeze oil film (SOF) model, with EHL contact pressure 63

Figure 2.14 Squeeze oil film model IV, which takes into account the elasticity of the crack 63

Figure 2.15 Distribution of the pressure along the crack length from SOF model IV 66

Figure 2.16 Multiple cavity model shown in a configuration with two cavities, one full filled one partially filled 68

Figure 2.17 3D Penny shaped crack configuration used by author in the literature 70

Figure 2.18 Cracks in the subsurface of the material shown to stop propagating after a change in the roller direction 73

Figure 2.19 V-shaped indenter used to create pre-cracks 74

Chapter 3:

Figure 3.1.Schematic of the dry crack problem 80

Figure 3.2 Method of separating the full problem into subsets (I) and (II) using Bueckner's principle 84

Figure 3.3 Discretisation of a contact pressure using a series of triangular pressure elements 91

Figure 3.4 (a) Single dislcocation and single stress evaluation point (b) Climb and glide dislocations distributed along the crack length, with multiple points, or nodes where the stress is evaluated to give the solution for the full crack. 96

Figure 3.5.Stress values solved with Muskelishvili's potential compared with the analytical solution 106

Figure 3.6 Subsurface stress plots, normalised by σ/p_{hmax} calculated using Muskelishvili's potential (a) σ_{yy} (b) σ_{xx} (c) τ_{xy} 107

Figure 3.7. Shear stress values solved with Muskelishvili's potential, with friction, compared with the analytical solution 108

Figure 3.8. Relative displacement solved with Muskelishvili's potential compared with the analytical solution 109

Figure 3.9. Stress intensity for a slant crack, of varying angle, under uniform tensile stress 110

Figure 3.10. Schematic of the slot model 112

Figure 3.11 Comparison of the opening displacement for different aspect ratio slots 113

Figure 3.12 Comparison of the shearing displacement for different aspect ratio slots 113

Figure 3.13 Schematic of the Hertzian problem 115

Figure 3.14 Dimensionless SIF histories (a) KI (b) KII 117

Figure 3.14 Comparison of the dimensionless SIF histories for different crack lengths (a) KI (b) KII 118

Chapter 4:

Figure 4.1 – Schematics: (a) the system under investigation and (b) the equivalent wedge geometry. In Figure 1(b) the finite volumes discretisation of the fluid domain is also shown. 121

Figure 4.2 – Overall problem and schematic describing the fluid and solid solvers and their components 126

Figure 4.3 – (a) Fluid ingress on contact approach (b) Fluid pressurisation inside contact 129

Figure 4.4 – Schematic of a column of fluid of volume h dx dy 132

Figure 4.5 – Schematic of the "stepped" discretisation scheme used for the fluid film 135

Figure 4.6 – Diagram of the method of calculating the time-step Δt 148

Figure 4.7. Comparison between FV and analytical solutions for the pressure distribution at the contact interface; the half-Sommerfeld solution is also shown to demonstrate the validity of the wedge approximation for the purpose of development 152

Figure 4.8. Comparison between the normalised volumetric fluxes at the crack mouth computed using the FV solver and the crack volume from the elastic deflection (integrated over the crack length) 152

Figure 4.9. Comparison between the crack deflections computed using the DDT and the FEM package ANSYS for a pressurised crack benchmark problem. 153

Figure 4.10 – (a) Contour plot showing the evolution of the crack opening displacements. (b) "Slices" through the contour plot in Figure 6(a) showing the evolution of the crack opening at three locations within the crack. 156

Figure 4.11 – Crack shape at three instants in time immediately before closure 158

Figure 4.12 Evolution of the crack mouth opening vs. the volumetric flux at the crack mouth 160

Figure 4.13 Evolution of the crack mouth opening vs. the pressure gradient at the crack mouth 160

Figure 4.14. Evolution of the normalised volumetric flux at the crack mouth for the example cases in Table 4.1. 162

Figure 4.15 Evolution of the normalised mode I SIF for the example cases in Table 4.1. 164

Figure 4.16 Evolution of the normalised mode II SIF for the example cases in Table 4.1 164

Figure 4.17 – Comparison of the evolution of the normalised stress intensity factors predicted by the present coupled finite volume (CFV) approach, a Squeeze Oil Film (SOF) model, an uncoupled fluid pressure model (FPM), and an uncoupled tapered pressure model (TPM) from the literature for Case 2 in Table 1: (a) Mode I, and (b) Mode II. 168

Chapter 5:

Figure 5.1.Diagram (a) and schematic (b) of the coupled EHL and RCF crack problem 171

Figure 5.2.Comparison between Doolittle viscosity model and experimental results 176

Figure 5.3 Deformation that is calculated using problem III in the solid solver 181

Figure 5.4 Schematic of the coupling of the segregated fluid/solid solver 187

Figure 5.5 Schematic of the coupling of the segregated fluid/solid solver, where the blue line the solution form the solved used in this model and the red circles is the Dowson et al solution 194

Figure 5.6 Results from different meshes for; (a) Dimensionless pressure (b) Dimensionless film thickness 195

Figure 5.7 Dimensionless pressure ($\underline{p^*} = p.(W_F/a)$) plots (a) Hydrodynamic Pressure (b) EHL Pressure 198

Figure 5.8 Dimensionless film thickness ($h^* = h/a$) plots (a) Hydrodynamic film thickness (b) EHL film thickness 199

Figure 5.9 Schematic of the fluid entrapment mechanism for the EHL case 200

Figure 5.10 Dimensionless normal mod KI SIF plots (a) Hydrodynamic (b) EHL* 201

Figure 5.11 Dimensionless shear mode KII SIF plots (a) Hydrodynamic (b) EHL* 202

Figure 5.12 Dimensionless crack mouth opening plots ($e^* = e/a$) (a) Hydrodynamic (b) EHL 203

Figure 5.13 Comparison of isoviscous and piezoviscous cases (a) EHL film 207

pressure (b) EHL film thickness

Figure 5.14 Piezoviscous results of (a) Viscosity (b) Density 209

Figure 5.15 Comparison of isoviscous case (red) and piezoviscous case (blue) (a) Crack Mouth Opening (b) Differential Pressure 210

Figure 5.16 Comparison of isoviscous case (red) and piezoviscous case (blue) (a) KI (b) KII** 211

Figure 5.17 Isoviscous crack mouth opening including problem (III) (red) and neglecting problem (III) (blue) 218

Figure 5.18 Isoviscous differential pressure, Δp, including problem (III) (red) and neglecting problem (III) (blue) 219

Figure 5.19 Isoviscous volumetric flux, q_c, including problem (III) (red) and neglecting problem (III) (blue) 220

Figure 5.20 Isoviscous case including problem (III) (red) and neglecting problem (III) (blue) (a) KI (b) KII** 222

Figure 5.21 Crack mouth opening for 3 crack lengths; 150μm (black), 100μm (blue), 50 μm (red) (a) including problem (III) (b) and neglecting problem (III) 225

Figure 5.21 SIF's for 3 crack lengths; 150μm (black), 100μm (blue), 50 μm (red) (a) KI (b) KII** 226

Figure 5.22 EHL contact Pressure for low viscosity (blue) and high viscosity case (red) (a) Y = -3E-4 (b) Y = -0.3E-4 229

Figure 5.23 EHL film shape for low viscosity (blue) and high viscosity case (red) (a) Y = -3E-4 (b) Y = -0.3E-4 230

Figure 5.24 SIF's for low viscosity (blue) and high viscosity (red) cases (a) KI (b) KII** 231

Figure 5.25 SIF's from analysis run in the inverse direction 233

Chapter 6:

Figure 6.1 Diagram (a) and schematic (b) of the coupled EHL and RCF crack propagation problem, where the crack length is increased by an incremental step Δa 236

Figure 6.2 Method of rotating the formulation so the axes are in line with the crack 241

Figure 6.3 Schematic of the problem used to validate the curvilinear crack model 245

Figure 6.4 (a – f) Evolution of the crack path due to the propagation steps, Δa 249

Fig. 6.5 Micropit as experimentally observed by Glodež et al. 250

Figure 6.6 Evolution of SIF histories for each load cycle during propagation (a) KI (b) KII 251

Figure 6.7 (a) Crack propagation rate (b) Number of loading cycle required grow the crack by Δa 253

Figure 6.8 The effect of changing the SIF mode used to calculate: (a) Crack propagation rate (b) Number of loading cycle required grow the crack by Δa 255

Chapter 7:

Figure 7.1. Idealised crack created using sapphire inserts. 264

Figure 7.2. Experimental setup with sapphire windows used to simulate a RCF crack. 265

Figure 7.3. Fluorescence principle: a schematic. 268

Figure 7.4 Contact and sample pot 270

Figure 7.5. Polymer roller and lubricant pot. 271

Figure 7.6. Schematic of the optical set up and the tribological contact. 273

Figure 7.7. Red dot illustrates the intended location of the image capture. 275

Figure 7.8. Grey scale image captured by the CCD camera of the fluorescence 277

intensity in the crack (a) with no markings (b) with crack mouth and the meniscus marked on the figure

Fig.7.9 Flourescence intensity along line X-X marked on Fig 7.7(b) 278

Figure 7.10. (a) Fluorescence intensity along line X-X for different loading conditions (b) Average intensity count for different loading conditions 279

Nomenclature

a = crack length (m)	α = dimensionless flow factor
A = area (m^2)	β = dimensionless flow factor ($\alpha/2$)
b = contact width (m)	σ = stress (N/m^2)
b_x, b_y = Burgers vector components	ζ = finite volume co-efficient
B = dimensionless contact width	κ = Kosolov's constant
B_x, B_y = dislocation densities	η = viscosity (kg/ms)
c, d = position of dislocation	ϑ = angle of incline of the crack (°)
C = Paris law coefficient	Γ = bulk modulus (N/m^2)
D = dislocation displacement kernels	μ = shear modulus (N/m^2)
e = displacement (m)	λ = finite volume source term
E = strain energy influence functions	ω = dislocation density weight function
f = friction coefficient	Φ = bounded part of B_x, B_y
F = force (N)	
G = influence function	**Subscripts and superscripts**
h = film thickness (m)	0 = condition at the boundaries
H = Heaviside step function	c = cracked
k = gradient of convergent wedge	C = for the crack film
K = dislocation stress kernels	dd = distributed dlislocation
KI, KII = stress intensity factors ($N/m^{3/2}$)	e = east

m = *Paris Law exponent* *N* = normal traction on crack face (N/m^2) *n* = number of points in quadrature scheme *p* = dimensionless pressure (*pa*/*W*) *q* = volumetric flux (m^3/s) *r* = time step *s* = strain energy density *S* = shear traction on crack face (N/m^2) *t* = time (s) *u* = integration points *U* = lateral velocity (m/s) U_s = rolling velocity (m/s) *v* = collocation points *V* = volume (m^3) *W* = normal load (N/m) *x, y* = global co-ordinate system *Y** = crack offset from the centre of the contact in HL and the centre of the roller in EHL	*F* = for the surface film *in, out* = for flux in or out of the system *ii, jj, ij* = for xx, yy or xy *I, II,* = for the terms of the solid solver (Muskelishvili or the DDT respectively) *m* = finite volume element number *N* = for the normal stress *op* = open *S* = for the shear stress *T* = total *u* = un-cracked *w* = west ^ = for the rotated co-ordinate system * = dimensionless variable

Chapter 1

Introduction

1.1 Introduction

Rolling contact fatigue (RCF) affects the life of gears, rolling-element bearings, industrial rollers in the steel-making process, railway wheels and lines, and a number of other important machine elements. It can occur in both lubricated and dry contacts, where a fluid may be intermittently present (for example moisture on railway wheels and lines). Due to the range of conditions that lead to rolling contact fatigue many investigations into the damage and failure mechanisms have been conducted (e.g. [1-6]). From the existing work in the literature it suggests that cracks can nucleate both at the contact surface and in the subsurface, generally in the presence of grain defects [7]. Also in the latter case, they can grow under repeated contact loading to produce surface-breaking cracks, which have been the focus of much of the existing research. Generally inclined [3, 8] and open toward the surface, exposed to the action of the liquid present in the surrounding environment (water, oil etc.), they have been observed to lead to pitting [4,

6] and catastrophic failure [9]. Experimental and theoretical work suggests that they propagate by a fatigue mechanism generated by cyclic stresses from repeated contact loading through rolling and sliding. However, the exact mechanism that is induced by the repeated contact loading that propagates RCF cracks remains unknown. Although there is anecdotal evidence to suggest what is happening, there is nothing to date which explicitly captures and presents an accurate account of the process.

1.2 Objectives

The objective of this body of work is to research the behaviour of fatigue cracks in the presence of lubricated contacts. The study will focus on the fatigue mechanisms and the crack propagation regimes with particular application to roller bearings, such as the one shown in Fig 1.1. This particular application is chosen because of the industrial partner SKF, but the approaches devised during the research programme are generic and are applicable to the different analysis of a range engineering components where lubricated contacts are present.



Figure 1.1 SKF Roller bearing

The overall aim of the research is to promote the understanding of the interaction between lubricants and fatigue cracks and how this influences crack propagation behaviour, and the degradation of the contact surfaces. The study constitutes a vital step towards the development of the means to predict the failure mechanisms of components undergoing contact fatigue in the presence of lubricating fluids. Existing models have not yet been able to explain the fluid/solid interaction mechanisms governing crack propagation. Furthermore, no experimental methods have been developed which allow us to understand the behaviour of fluids or particles “entrapped” within the crack during a loading cycle. Various researchers have hypothesised different phenomena which may occur during repeated loading cycles but none of these has been experimentally corroborated.

The work documented here will address the modelling limitations highlighted above by presenting a newly developed numerical technique for the analysis of fatigue cracks initiated under lubricated contact regimes and present an experimental technique that, with further development, could be used to corroborate the numerical work. The main objectives are:

1. to present a model that captures the lubricated crack deformation mechanisms;
2. to present a unified approach for the modelling of the solid/fluid interaction during contact cyclic loading;
3. to explore the possibility of investigating experimentally the behaviour of fatigue cracks undergoing loading patterns generated by the solid/fluid interaction.

The work contains a mix of (a) the application of techniques already available to the author and in the research literature, (b) novel developments specific to the fluid/crack interaction, (c) development of existing experimental techniques for monitoring the presence of fluid in an idealised RCF crack during a contact loading cycle.

1.3 Background and basis for innovation

Many complex engineering products such as bearings, gas turbine blades/shafts, gears, railways, bolted flanges, car engines, etc. could not operate without contact and frictional interfaces. Many of these mechanical components are subjected to cyclic contact loading and hence are vulnerable to failure by fatigue and this is of great

concern for both the research and industrial communities [9-44]. Two of the main failure mechanisms encountered in the vast majority of industrial applications, where couplings are of primary importance, are fretting fatigue (FF) [45] and rolling contact fatigue (RCF) [9].

RCF is a phenomenon which can lead to the failure of contacting metallic surfaces due to progressive cracking from the extreme surface or from underneath the contact interface, due to repeated cyclic stresses, and can lead to the detachment of fragments of the affected components; a process known as pitting. RCF can also be found in ceramic on metal contacts where high quality silicon nitride ceramics are used in rolling element bearing applications [40]. Surface initiated cracks are becoming more common in RCF [20] due to the improving steels being used in the manufacture of machine components which is reducing the number of grain defects in the subsurface of the material. These are surface breaking cracks with a mouth that is open upwards with faces exposed to the action of liquid that is present in the surrounding environment (water, oil) liquid that is often required for its lubricating properties. The failure mechanism induced by RCF and the main concern to engineers is pitting, which usually originates from small, surface-breaking or subsurface initiated cracks, which grow under repeated contact loading. At some point, secondary cracks form, and propagate towards the surface. This causes part of the material surface layer to break away creating a void on the surface, where this void is called a pit. Initial micro-pitting is usually an indication of possible progressive macro-pitting. Micro-pitting is characterised

by pits, with a depth usually that does not exceed 30μm. This pitting can cause a range of problems in the rotating system, not least induced vibration, and will ultimately lead to the failure of the rotating mechanism.

The role of fluid, according to experimental observations, experience gathered from engineering practice, and the results of theoretical analyses, is often regarded as the main catalyst for crack growth. This is the reason why such cracks have been of great interest: Keer and Bryant [27], Bower [13], Kaneta and Murakami [26], Murakami et al. [30, 46], Beynon et al. [11], Bogdański et al. [12, 47, 48], Hsia and Xu [49, 50] are some of the researchers who have worked on the topic in the past decade or so. They have considered the effect of lubricating fluid being trapped in the RCF cracks and pressurised by the contact loading, however their work is based on a series of assumptions, assumptions that the work contain herein will address. In this context, it is adequate to couple elastohydrodynamic (EHD) lubrication models and fracture mechanics as a means for quantitatively understanding the problem of crack propagation in lubricated rolling contact fatigue. Although existing models have proved successful in providing a reasonable physical explanation for some of the cracking behaviour observed experimentally and a number of numerical models for the study of this phenomenon have been developed, no attempt has been successful in characterising the coupled behaviour of the fluid solid/interaction in RCF cracks.

Shortcomings of the existing approaches are the lack of coupling between the physics of the fluid and solid in the already implemented methodologies and the lack of

the application of fracture mechanics principles to the assessment of crack propagation during the fatigue process. Furthermore, although some experimental analyses have attempted to demonstrate that the presence of the fluid plays an important role in the crack propagation [51] and have contributed to surface and subsurface examination of cracks and their propagation [44], none of the existing techniques allow direct observation of the fluid/solid interaction within a RCF crack. This body of work, conducted at Imperial College London in partnership with SKF will shed light on these issues.

Chapter 2

Literature Review

2.1 Introduction

The story begins with an experimental hypothesis, proposed by Stewart Way in 1935 [6]: “Pit nucleation on lubricated rolling and sliding surfaces is brought about by the propagation of a tiny surface crack due to hydraulic action caused by fluid penetrated into the crack.” The work, which involved analysing the growth of fatigue cracks in rails under dry and wet test conditions, ignited a new way of thinking and presented the possibility that fluid could be the necessary catalyst for crack propagation in rolling contacts. It has instigated many experimental and numerical studies since. This chapter will form a review of these studies, both numerical and experimental, and will, in particular, review the analytical and numerical techniques that have been developed for analysing cracks and crack propagation.

The analysis of cracks in lubricated contacts has evolved and matured, since Way's pioneering experimental work, with many distinct numerical and experimental techniques being identified and developed to shed light on essentially the same unknown phenomena: the prediction of crack behaviour under contact loading, the liquid/solid interaction between crack and lubricant, the fatigue mechanism governing crack propagation and the direction in which RCF cracks propagate under repeated contact loading. The advance in the complexity and accuracy of numerical crack analysis has been stimulated by the development of computers and computer software with boundary and finite element analysis techniques being the paradigm on which most modern modelling methods converge. Most of the work that has been done in the literature, up to this point, on numerical analysis of RCF cracks is solved in 2D, assuming line, as opposed to point contacts. This work will be the focus of the literature review, where 3D modelling is considered but because of a lack of supporting literature is only covered briefly.

Material science considers crack initiation and propagation in terms of microscopic flaws at grain boundaries, inclusions, micro-structural and compositional in-homogeneities and microscopic stress concentrations [52, 53]. Material scientists consider the nucleation of flaws along persistent slip bands as the initiation of fatigue failure [52]. Chemists on the other hand argue that chemical effects in cracks are a major influencing factor in the initiation of fatigue failure [54]. However, for the purpose of this body of work, fatigue failure is expressed from an engineering standpoint. Considering the effects of crack initiation and propagation in defect free, pure metals

with smooth surfaces where macroscopic stress concentrations and cyclic loading govern crack initiation and propagation [55].

2.2 Fracture Mechanics and RCF

The development of RCF modelling was brought about by the introduction of a new theory, that of linear elastic fracture mechanics (LEFM) [56], and its direct applicability to crack modelling and analysis. The motivation of early work on RCF was to relate elastic stress analysis to observed fatigue behaviour in order to develop load-life equations for machine elements such as roller bearings, an example of which is the work done by Lundberg and Palmgren in 1952 [57].

The increased understanding of RCF was motivated by the growth of the aerospace industry in the 1960's and 1970's with the need for greater performance and reliability [58]. During this early period, the influence of water, lubricants, extreme pressure additives and the effects of residual stresses on RCF and fatigue life were investigated [58-61]: this resulted in a mounting interest in RCF. From continued work, by the mid 1970's, the influence of the material and operating factors on RCF and fatigue life were well understood [62]. However the factors governing RCF crack initiation and RCF crack propagation were still unknown. Failure analysis was based on using S-N plots and Weibull analysis but the contact stresses and the related fatigue mechanisms responsible for crack propagation were still unclear [63].

It was at this point that the use of LEFM was introduced. In the late 1970's, a number of researchers, including Dundurs and Comninou [64] and Hills and Ashelby [65], used fracture mechanics to determine crack stress intensity factors and their effect of crack growth in various contact and plain fatigue scenarios [64-66].

2.3 Linear Elastic Fracture Mechanics

The science of fracture mechanics was developed to understand the causes of failure in structures and machine components. It began with the solution of analytical problems, such as the stress distribution around a hole or a notch of simple geometry [67], and it was then extended to include the solution of more complex problems such as the effects of cracks in an elastic body [68-70]. This presented a problem, because fracture mechanics predicts a singular stress field at a crack tip. It led to the philosophical question of how the material could support an infinite stress directly ahead of the crack front. This situation could only be explained as follows; the material at the crack tip would yield, and be stressed almost asymptotically, but would be constrained by the surrounding material, material stressed below the yield limit. This deduction was the foundation of LEFM [71, 72]. The stress manifests itself as a singularity at the crack tip, while the surrounding region is still behaving within the elastic limit; therefore, a crack can be analysed with a good degree of accuracy using a linear elastic approach as long as a series of conditions are satisfied:

- The diameter of the plastic zone falls below 2% of the crack length.
- The plastic zone does not reach any of the crack components free surfaces.
- The bulk material behaves elastically.

The studies of Irwin [71-73] were a decisive moment in the field of LEFM; they introduced the concept that the magnitude of the stress field ahead of the crack could be expressed in terms of a scalar quantity, the stress intensity factor (*K*), that, for simple crack geometries, incorporated crack length (*a*) and the remote stress (σ_r):

$$K_{mode} = \sigma_r \sqrt{\pi a} \tag{2.1}$$

where, in two-dimensional analyses, the subscript "mode" can be either "*I*" or "*II*" depending on the loading, namely opening and shearing mode respectively; hence the conventional notation of *KI* and *KII* adopted in LEFM.

This quantitative method of analysing the state of stress ahead of the crack tip however, can only generally be applied to large cracks (i.e. > 20μm), because small cracks violate the conditions for the application of LEFM; therefore the use of LEFM is confined to the study of macroscopic crack propagation as opposed to crack initiation or the first stages of (microscopic) crack propagation [74].

2.4 Crack Propagation

The application of LEFM to the analysis of RCF crack propagation due to repeated contact loading and cyclic stresses was first proposed by Paris and Erdogan [75]. They developed a law to relate cyclic crack growth (d*a*/d*N*) to the cyclic range of the stress intensity factor (Δ*K*), combined with two experimentally obtained material constants *C* and *m*, for a fatigue load cycle of constant amplitude, where *m* for steel is typically between 2.5 and 4.

$$\frac{da}{dN} = C(\Delta K)^m \tag{2.2}$$

In practice this classically corresponds to around one lattice spacing per cycle in crack growth, d*a*/d*N* ~ 10^{-10} m/cycle, but values less than this may occur experimentally if crack tips extend at different regions of the crack front, or branching occurs. If Δ*K* becomes larger than an upper bound ΔK_C, crack growth occurs uncontrollably within one cycle and fracture or pitting will occur (in an RCF scenario). For Δ*K* values below a threshold limit, ΔK_{th}, no, or minimal, crack growth will occur [75].

As well as the Paris law another widely accepted crack growth law is the McEvily-Foreman law [76]

$$\frac{da}{dN} = C(\Delta K^2 - \Delta K_{th}^2)\left[1 + \frac{\Delta K}{K_C + K_{\max}}\right] \tag{2.3}$$

where K_{max} is the max K value during a loading cycle. The application of this law is valid over a wider range of crack lengths than Paris's law, incorporating some of the non-linear regions of Fig. 2.1.

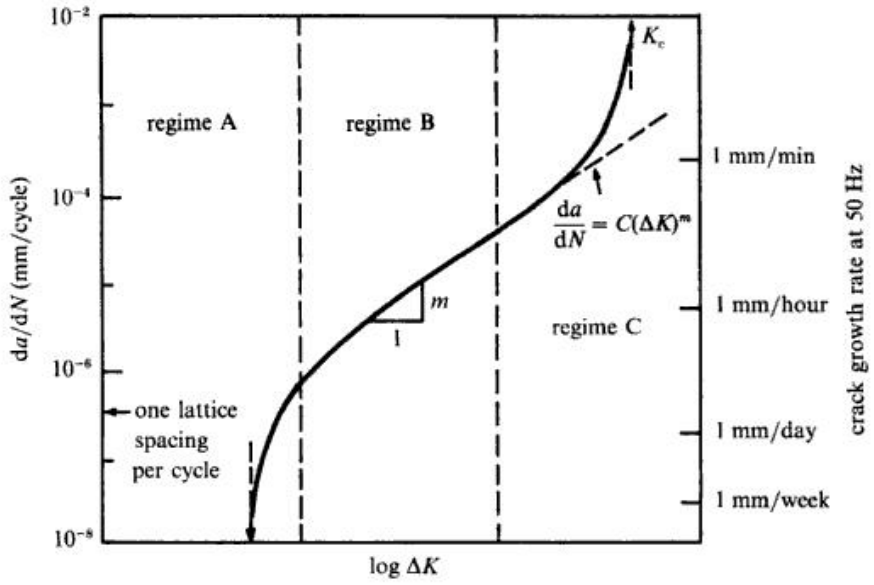


Figure 2.1. Schematic illustration of the different regimes of stable crack propagation [52]

The Paris power law relationship displays a linear relationship between da/dN and log ΔK over the total crack growth resistance curve for a typical alloy, therefore the Paris law is not valid at extreme values of ΔK both high and low. From this plot three distinct regimes can be identified. In regime A, where the average crack growth is less than a lattice spacing, there exists ΔK threshold. Once this threshold has been exceeded crack growth increases non-linearly and rapidly with ΔK. In regime B, a linear variation between da/dN and log ΔK exists, this is the regime over which the Paris law is valid. In

regime *C* however the McEvily-Foreman law can still be applied due to the in incorporation of the variable K_C in the formulation [75].

Other crack growth rate expressions are based on crack tip opening displacement, crack tip shear displacement or the *J* integral approach [77-81]. But for the purpose of this study the classical methods above are deemed sufficient because they are the most widely used by our colleagues in industry and this thesis will focus on the development of methods to study fluid/solid interactions during the crack propagation process rather than the most accurate way to compute stress intensity factors and crack growth rates.

2.5 Mixed Mode Crack Propagation

As mentioned above, for a two-dimensional system there are two types of crack propagation modes, the tensile mode (*KI*) and the shear mode (*KII*). If *KII* is zero then the crack propagation can only be due to the remote tensile load and if *KI* is zero or negative the crack propagation must be in the shear mode. Hua *et al.* [82] developed a way to express crack propagation under biaxial loading where finite *KII*, and positive *KI*, are both present at the crack tip. This corresponds to the so-called “mixed-mode” crack propagation regime, where neither *KI* nor *KII* individually represent the criteria for crack propagation. The diagram below illustrates the derived relationship, which is used to identify the propagation thresholds and the boundaries between different propagation

modes. This allows the dominant mode for a certain case to be obtained, see Fig. 2.2 below.

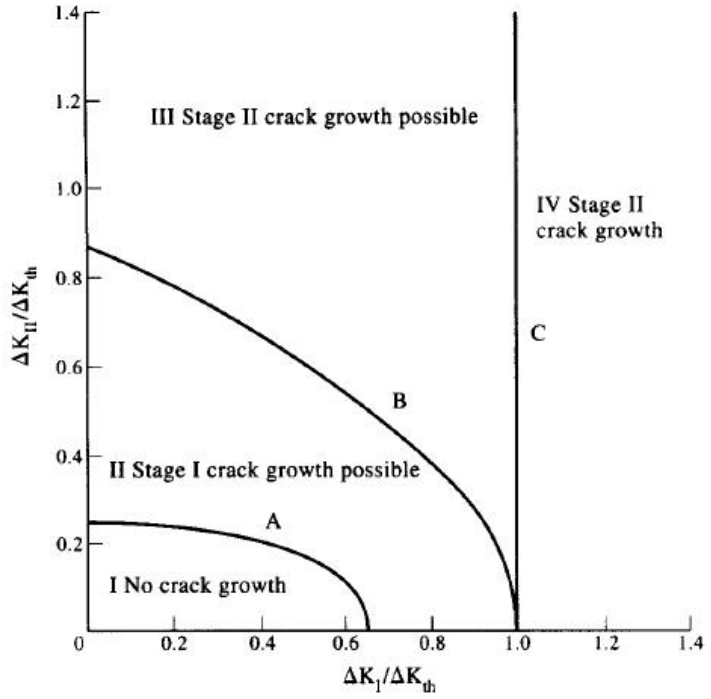


Figure. 2.2. Relationships between fatigue crack growth modes and relative applied load magnitudes [83]

From the figure, it becomes clear that without a significant *KI* the possibility of crack propagation is greatly reduced; this establishes that *KI* is more influential to crack propagation than *KII*. This, of course, is in line with intuition because the opening action corresponding to a mode I loading is expected to cause more growth than the shearing action induced by mode II loading.

Many different methods for evaluating the direction and rate of mixed mode crack propagation have been developed and proposed in the literature; the following section is aimed at providing an overview of the most common and widely applied criteria. For a

thorough review of more recent criteria or for solution tailored to more specific issues, the reader can refer to [83, 84].

The simplest and most widely used theory for evaluating the direction of crack propagation in mixed mode conditions was proposed by Erdogan and Sih [85, 86]. Their criterion states that (i) crack propagation starts from the crack tip in the radial direction, $\theta = \theta_c$, where the tangential stress becomes maximum and (ii) fracture starts when the maximum tangential stress exceeds a critical stress value, equal to the fracture stress in uniaxial tension. Mathematically, when Westergaard expressions are used to describe the stress field near the crack tip for a mixed mode I and II loading case, it can be shown that the above criterion for the crack growth direction θ can be expressed using the following equation [86]:

$$KI\sin^{-} + KII(3\cos^{-} - 1) = 0 \qquad (2.4)$$

This has been supported by many experimental observations, including those by Ravi-Chandar [87], Pook [88] and Chambers et al [89].

The determination of mixed mode crack propagation rates is based on the evaluation of an effective stress intensity factor range, ΔK_{eff}, that comes from an expression incorporating ΔKI and ΔKII; this is then substituted into either the Paris law or the McEvily-Foreman law previously discussed instead of the individual stress

intensity range for a single mode. Tanaka suggested the following expression for determining ΔK_{eff} [74]:

$$\Delta K_{eff} = \left[\Delta KI^4 + 8\Delta KII^4 \right]^{0.25} \tag{2.5}$$

Although other forms of effective stress intensity factors were proposed by Tanaka [74, 90], not reported here, he found the correlation expressed in the equation above to provide the best fit with his experimental data. Another effective stress intensity factor suggested by Yan *et al.* [91] has the following form:

$$\Delta K_{eff} = \frac{1}{2}\cos\frac{\theta_0}{2}\left[\Delta K_I(1+\cos\theta_0)^4 - (3\Delta K_{II}\sin\theta_0)^4 \right]^{0.25} \tag{2.6}$$

where θ_0 is the crack growth direction obtained from the maximum tangential stress criterion outlined above.

2.6 The Application of LEFM to RCF

Linear elastic fracture mechanics has been applied to problems involving RCF, in the literature, to calculate the stress intensity factors (SIF's), K_I and K_{II} at the crack tip for given crack configurations. Therein allowing crack growth rates and crack growth direction to be evaluated using the empirical methods described above with varying

degrees of success, while also allowing the severity of the stresses at the crack tip to be determined quantitatively.

For RCF problems, the main focus has been placed on evaluating surface breaking, near surface and sub-surface cracks within an idealised half-plane or halfspace (semi-infinite body). The methods used to apply LEFM to cracks with particular application to RCF problems can be divided into two main categories: those based on a boundary element approach and those based on a finite element approach.

2.6.1 Boundary Element Methods

Considering first boundary element methods (or boundary integral methods), they pre-date finite element methods and are, for the most part, semi-analytical in nature. This means they are less computationally expensive and therefore more efficient. They are also, at the time of writing, for the purpose of analysing SIF's more accurate because of specific, derived, quadrature schemes that are designed to incorporate singularities into a semi-analytical, integral formulation [55]. Finite element methods, on the other hand, are fully numeric and singularities have traditionally led to ill conditioned matrices and inaccuracies. However, improvements in FEA, and commercial FEA software such as ANSYS and ABAQUS, are beginning to increase the applicability of FEA to crack modelling. The application of boundary element methods in the literature, is generally restricted to two-dimensional problems, due to their semi-analytical nature (and the

limited number of fundamental analytical solutions available for three-dimensional problems) and a lack of supporting commercial software.

Boundary element solution algorithms are derived, in their simplest form, from Bueckner's theorem of the superposition of stresses [55], which is based on linear elastic material behaviour. They are made up of two key fundamental elements; the evaluation of the stresses acting in the body at the crack faces in the absence of the crack, and unknown an quantity that defines the interrelationship between the stresses arising in the un-cracked body and the stresses arising due to the presence of the crack and can be determined using appropriate boundary conditions. The first step requires the direct and shear stresses at the location of the crack to be evaluated as a function of the loading conditions. The second involves analytical or semi-analytical techniques that evaluate the effect of the presence of the crack in an infinite or semi-infinite body on the stress field evaluated in step one [55]. Cracks are generally introduced as unknown strain nuclei or gap functions, whose values can be found by imposing the conditions that the crack faces are either traction free or in contact (when crack closure takes place).

2.6.2 Greens Function Method

Much of the early work on the application of LEFM to crack problems available in the literature, first by Flemming and Suh [92] and then followed by Rosenfield [93], Rubin [94] and Hearle and Johnson [95] for wear and rolling contact fatigue studies uses a

direct Green's function approach. According to such methodologies, the Green's function specifies the SIFs at a crack tip caused by a unit load acting at a given point on a crack face, and therefore the integral of the load acting at all points along the crack face gives the total SIF at the crack tip. The weakness of this method, in the form in the literature, is that it can only be applied to infinite bodies and therefore cannot be used to analyse surface or near surface flaws. The authors have not taken the proximity of the free surface to the crack into account in the formulation; the presence of a free surface will interact with the crack therefore modifying the solution.

The Green's function approach was developed and modified by Hills and Ashelby [65] to include the free surface, through an iterative routine. The routine was based on evaluating the distribution of stress along the surface by enforcing the correct traction distribution for a half-plane starting from a full plane. This was achieved by applying a set of appropriate point forces to cancel out the stress resulting from the full plane solution along the surface, hence satisfying the condition of zero normal and tangential stresses at the free surface. However, the point forces applied then produce a new set of crack face stresses. This process has to be repeated until convergence is achieved. Although this modification to the Green's function approach allows for the presence of the free surface the iterative nature of the algorithm is highly inefficient and a direct method should, if available, be considered as a more viable option.

2.6.3 Distributed Dislocations

The distributed dislocation technique introduced by Dundurs and Cominou [64, 96] and subsequently used, and modified, by Keer and Bryant [97], Hills and Nowell [98] and Kudish [99], is based on using strain nuclei or "dislocation" to define the stress at any point within a half-plane or along the crack face in terms of an integral equation performed over the whole distribution of dislocations along the crack faces, where the boundary value problem is solved. Unlike the Green's function method, the formulation for this method contains the presence of the free surface and can be solved directly without the need for iterations. Therefore, for the purpose of analysing cracks in semi-infinite bodies as opposed to infinite bodies the distributed dislocation technique presents a more elegant and efficient numerical method.

The problem is generally solved by superimposing the solution for an un-cracked half-plane to the contribution of the strain nuclei to the stress and strain field. The unknown magnitudes of the dislocations are computed by satisfying the zero tractions boundary conditions along the crack faces. The approach is defined by a boundary integral equation, that often contains a singularity, that was initially applied to solve for SIF's *KI* and *KII* in 2-D crack problems but has been further developed, by Hills and Nowell *et al.*, and applied to solve for different features such as crack face displacement to evaluate stick/slip condition in closed cracks [55]. In the boundary integral formulation the crack is represented by a continuous distribution of dislocations identified by the Burger's vectors $b_y(c)$ for mode I, or climb dislocations, and $b_x(c)$ for mode II, or glide dislocations, with an unknown density distribution along the crack length. The density of

the dislocations along the crack length is the quantity that defines the interrelationship between the stresses arising in the un-cracked body and the stresses arising due to the presence of the crack.

The unknown dislocation density is then found by discretising the crack boundary and imposing a set of boundary conditions along the crack faces, using a shape function that defines the crack shape and the crack position in the half-plane, then by solving semi-analytically by means of a quadrature scheme that can deal with singular integrals, such as Gauss-Chebyshev. The stress field behaviour at the ends of the crack influences the formulation based on whether the end has a bounded stress (e.g a crack mouth) or a singular stress (a crack tip). The stresses due to the dislocation density can be expressed with the following integral [98]:

$$\pm(x) = \frac{\text{«}}{\text{®}(\text{©}+1)}\int_0^a B(c)\,\mathrm{K}(x,c)\,dc \qquad (2.7)$$

where *a* is the crack length, *K* is a known influence function, *B* is the unknown dislocation density that is derived in [65], *x* is the co-ordinate where the stress is being evaluated (usually along the crack face), *c* is the location of the dislocation that is being evaluated, *μ* is the shear modulus of the material and *κ = (3 – 4ν)* for plane strain, where *ν* is the material Poisson's ratio.

Due to the discrete nature of the solution, the dislocation density is only found at certain points on the crack face therefore a method of extrapolation is required, in this

case, Krenk's [100], to get the values at the crack tip that are then used to calculate the stress intensity factors. The displacement of the crack faces, with respect to the crack tip, is found by the integral of the dislocation density along the crack length starting from the tip.

2.6.4 Weight Function Method

This method like the distributed dislocation method is effectively another take on the Green's function method but with wider applicability, introduced by Watanabe et al [101] and developed by, amongst others, Beghini and Vainshtok et al [102, 103]; however, it is not based on the solution of the stresses. This approach is based on considering the weight function for a cracked geometry as a function of geometry and not the loading condition (where load symmetry restrictions apply). If a prescribed set of conditions are met then it can be applied to obtain *K* values for different types of loading. The method relies on the derivation of a weight function based upon the interrelationship between the strain energy release rate, *G* and the stress intensity factor *K*. For certain geometry with symmetry conditions about the crack line, where the loading is also symmetrical about the line, then the difference between strain energy of the body with the crack and without the crack can be expressed as the following integral:

$$K = \int_0^a h(x,a) * \pm(x) dx \tag{2.8}$$

Where *a* is the crack length, *K* is the stress intensity factor, *σ(x)* is the stress distribution along the crack line in the un-cracked structure and *h(x,a)* is the weight function, that is based on the opening of the crack faces in the direction normal to the crack caused by the load. The weight function *h* is unique for each loading condition and if other loads are applied this function needs to be re-derived. Like the other boundary approaches, this method requires a clear definition of the stress distribution along the crack face, but also requires the corresponding crack displacements to be able to use the strain energy approach. If all of these variables can be prescribed then, generally for simple loading conditions, the *K* values can be calculated. This method although similar to the distributed dislocation technique requires a unique weight function to be derived for each individual case [101, 104]. The distributed dislocation technique in contrast, uses a shape function, or kernel, that once derived can be applied to all problems as the distributed dislocation arrays define the crack geometries.

2.6.5 Finite Element Methods

The use of finite element (FE) techniques to evaluate structural problems is common and during the late 1970's and 80's it was developed and applied to various crack problems [105-108]. The application of this numerical technique to evaluate cracks however presents some problems. Regular finite elements are unable to accurately capture singular behaviour at the tip of a crack in a LEFM type analysis, because the method is numerical and a near singularity leads to ill conditioning. However, authors

have developed ways to get around this problem by using two approaches [106]: the first being the use of a high density of elements around the crack tip coupled with the use of either stresses or displacements at an incremental distance from the crack tip to define the SIF. In this case the displacements proved to be the more accurate of the two.

The second approach involves the use of a ‘quarter point’ node which can introduce a singularity of order 1/*r* on the side of the node at the crack tip. From this, the strain energy release rate and the stress intensity factor can be calculated by extending the crack by a quarter of the length of the crack tip element size. This technique which was first used by Sin and Suh [109], see Fig 2.3., is more accurate than the first method but it requires a good knowledge of dividing a domain into appropriate sub-domains. A well defined sub-division of the geometry is essential to the accuracy of this method.

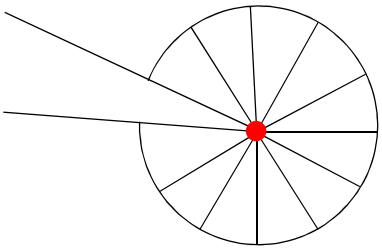
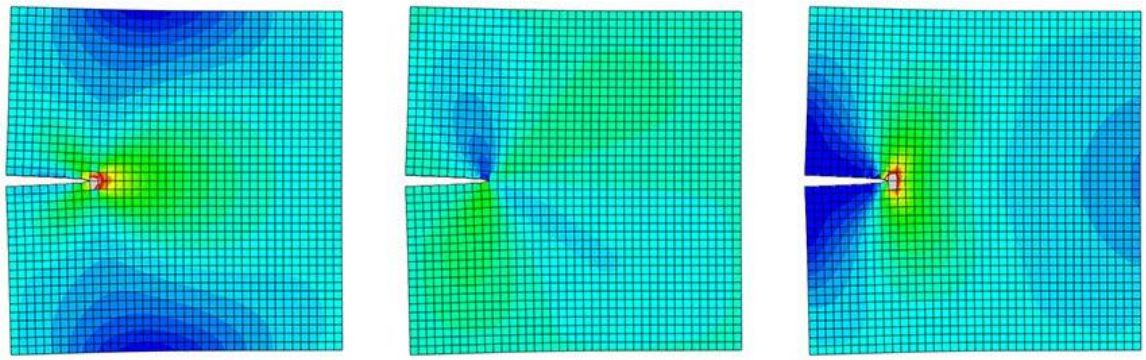


Figure. 2.3. Quarter point node, a single node at a crack tip (red) is split by a number triangular elements

2.6.6 Extended Finite Element Method (XFEM)

This method of crack analysis is in its infancy (it has only been developed in the last decade) but has shown promise to become a very powerful tool for the numerical

investigation of fractured structures, with special applicability to the study of crack propagation [110-112]. The method is based on a modification to the existing FEM. In a standard finite element formulation, a crack must conform to the finite element mesh and re-meshing is required to conduct crack propagation simulations. In contrast, in the X-FEM, a crack is modelled via a displacement approximation: a function that is discontinuous across the crack is added to the displacement approximation to model the presence of a crack via element enrichment. Therefore, the method can treat arbitrary cracks independent of mesh and can capture crack growth without the need for re-meshing. This means that the process of crack propagation can be modelled far more efficiently without very complex and refined meshes in the region of the crack tip, this can be seen in the diagram below (Fig. 2.4a - c) where a uniform mesh is used but the propagation path is accurately captured [113].



(a) (b) (c)

Figure 2.4 Typical 2D XFEM stress field from a crack propagation problem solved using the finite element package Abaqus, (a) σ_x (b) τx_y (c) σ_y [114]

All cracked elements are enriched by a function and the method is able to treat the entire crack with only one type of enrichment function, including the elements containing the crack tip (unless crack closure and friction are to be accounted for). The equilibrium equation and the traction condition are solved by the Newton–Raphson method to obtain the nodal displacements and satisfy the external load simultaneously [115].

This method has been successfully implemented to 3D crack propagation problems [116] with simple loading conditions. It hasn't yet been coupled with a fluid pressure model in 3D, mainly due to computational limitations for fluid/solid coupling. This method is currently not compatible with a fully coupled fluid algorithm, however XFEM, I have no doubt, will be the method used to drive the study of crack propagation in lubricated contacts in the future.

2.7 Lubricated RCF Cracks: a long history, yet an unresolved issue

The possibility that cracks may be propagated by the action of fluid by fluid entrapment or a form of lubricant pressurization was proposed by Way [6]. Way's suggestion was that fluid is forced into the crack by the load as it rolls over the crack mouth, and the faces of the crack are subjected to fluid pressure, this pressure acts to open the crack and generates a large build-up of stress intensity at the crack tip. In support of this hypothesis, a number of experimental studies have shown that lubricant must be present for contact fatigue, such as pitting, to occur in rolling systems [6, 18, 117, 118], and that without a lubricant, rolling contact fatigue is greatly reduced. Therefore, it is

important that this mechanism of interaction be correctly interpreted and incorporated into a fracture mechanics model of rolling contact fatigue.

2.7.1 Penetration of Lubricant into RCF Cracks

Investigations by Godet [119], Jahanmir [120] and, more recently, Kapoor and Fletcher [121] and Olver et al. [5] have produced experimental evidence that there is ingress of fluid into an RCF crack during a contact loading cycle. This is generally the origin of micropitting in gears and bearings,

Godet [119] photographed the side of a disc in a rolling contact and observed edge cracks during rubbing. From these tests he discovered that lubricant penetrated the whole depth of a crack during rolling contact. However, the cracks used in the tests were idealised, spanning the whole width of a disc. Therefore the cracks were likely to provide less resistance to opening than real RCF cracks. This makes them easier to fill, and therefore it is not entirely conclusive whether the results from these tests would translate to real RCF cracks. In the mid 80's Jahanmir [120] used Secondary Ion Mass Spectroscopy (SIMS) to investigate and map the chemical elements, i.e. oil additives, which could be found within sectioned rolling contact fatigue cracks. The tests involved sectioning RCF cracks and analysing the chemical elements found embedded within the cracks using SIMS. The results suggested that the oil additives could penetrate into RCF cracks to depths of at least 150μm. This is a considerable depth, and constitutes one of the best pieces of evidence to date of lubricant penetration.

In a recent study, Kapoor and Fletcher [121] conducted full scale tests on cracked rails with a twelve wheel locomotive, 109 tonnes in weight. Water based UV fluorescent marker was used, giving similar fluid properties to water; the fluid was applied to the surface of the rails using a brush. The testing then took place at low speed (walking pace) with sequential back and forward movement of the locomotive across the test section. After the loading cycles, the rail samples were removed for laboratory examination by breaking them open for internal crack examination (Fig. 2.5).

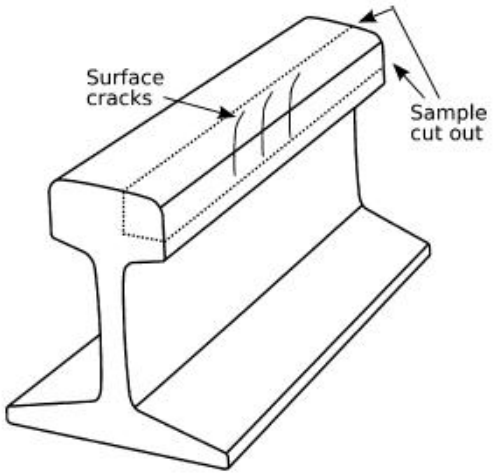


Figure 2.5 Schematic of surface cracks on a rail segment used for experimental analysis [122]

Cracks in all rail sections were broken open to reveal the majority of the crack face of a large rolling contact fatigue crack. Examination of the crack faces under UV light revealed a bright green fluorescent glow on the crack faces (Fig. 2.6).

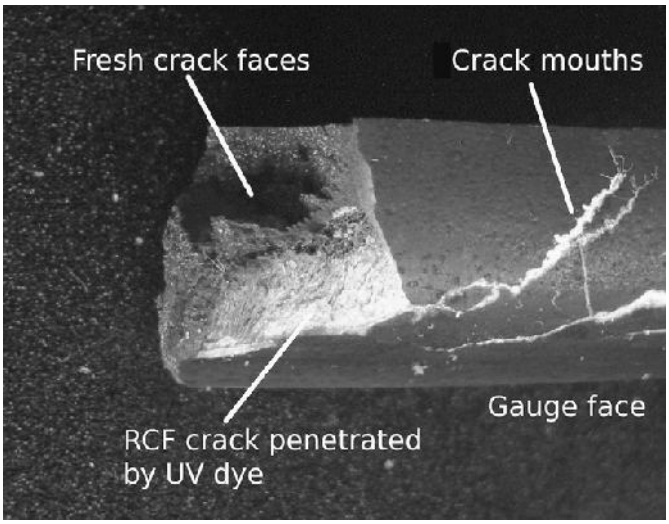
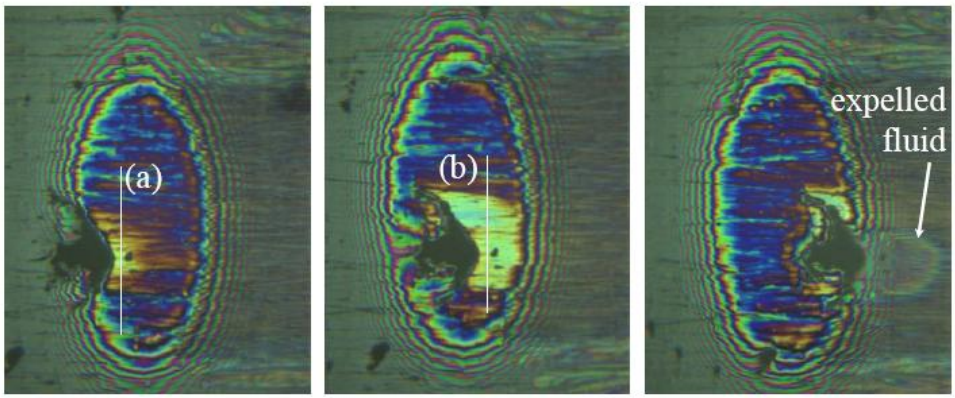


Figure 2.6 Rail sample following destructive examination, UV light reveals fluid penetration of the surface breaking cracks [122]

This green fluorescent glow clearly confirms that the cracks were penetrated by the UV florescent marker fluid during the test. Although the conditions in rails are different to bearings and water is a very different lubricant to oil or grease the same fatigue mechanisms are observed in both, and it can be implied that the factors driving the fatigue mechanisms are also equivalent.

The effect of passing a single micropit, through an elastohydrodynamic contact was investigated by Olver *et al*. [5]. The experiment involved having a loaded roller, with a micropit on the surface, in contact with a sapphire disc in the elastohydrodynamic

lubrication regime. The effect of passing the micropit through the contact was analysed in real time using optical interferometry (see Fig. 2.7).



(a) (b) (c)

Figure 2.7 Sequence of interference images showing a micropit passing through a contact, Note the large amount of fluid expelled into the cavitated region in (c) [5]

The results from the experiment, shown in Fig 2.7, show some interesting features as the micropit travels through the contact. The first image (a) shows that the micropit appears to draw fluid from the surface film as it enters the contact and then as the micropit enters the region of cavitation at the back of the contact, image (c), it expells the fluid into the cavitated zone. This suggests that an exchange of fluid between the surface film and the surface feature, in this case a micropit, does occur.

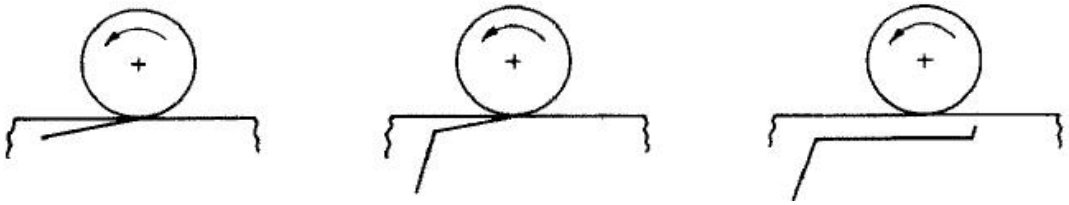
Each of the experimental studies in isolation may not be sufficient to prove beyond doubt that fluid penetration between the surface film and rolling contact fatigue surface features, such as cracks or micropits, does occur, or, more importantly, that it plays an important role in the fatigue life of the components. However, the combination

of the different investigations forms a mounting case and supports further investigation into modelling crack deformation and crack growth using mechanisms based on fluid penetration. Lubricant penetration will only occur in surface breaking and surface initiated fatigue cracks, therefore considering the differences between the behaviour of surface breaking and subsurface cracks may give some insight into the role of the lubricant in the fatigue process and crack growth. From some numerical analysis it has been suggested that the Mode I stress intensity factors for surface cracks can be up to two orders of magnitude higher than those for similar subsurface cracks [99].

2.7.2 Surface-breaking and sub-surface RCF Cracks

Fatigue cracks in general, surface or subsurface, propagate in a way which is related to the relative motion between the surfaces and the variation of the applied load; this is observed to be the case even in pure rolling conditions when the contact stress field, in the Hertzian case, is perfectly symmetrical with respect to the point of contact [123]. Figure 2.8 shows a schematic of surface-breaking and subsurface cracks. Surface-breaking cracks (Fig. 2.8(a)) can either initiate at the surface due to surface features or generate from subsurface cracks growing towards the surface. Subsurface cracks, or ‘pre-pitting cracks’, tend to nucleate at large non-metallic inclusions and grow parallel to the surface of the body for a short period; they then curve at each tip toward or away from the surface. From the direction of motion, the trailing edge (the edge that sees the

load second), grows quicker than the leading edge and turns downward while the leading edge turns up toward the surface, Fig 2.8(c) [123].



(a) (b) (c)

Figure 2.8 Sequence of schematics of surface breaing (a) & (b) and subsurface cracks (c) [123]

This creates a crack which is open to the surface, where the mouth of the crack sees the load before the tip. When the crack is subsurface and parallel to the surface, it is not possible to generate positive tensile stresses acting to open the crack in Mode I; therefore, the mode of fatigue crack growth is Mode II,or shear mode.

Surface breaking RCF cracks have been experimentally shown to propagate when a lubricating fluid is present during the test conditions [6, 18, 117, 118] and in the direction of motion [2, 124], shown in Fig 2.8(a). It has been hypothesised by different authors in the literature that, like sub-surface cracks, surface breaking cracks also propagate in the mode II shear fatigue mechanism [2, 95, 125]. Several theoretical models, such as Keer & Cheng [126] Kaneta et al [127], Bower [2] and more recently Bogdanski et al [125], have been developed to calculate Mode II SIF's at the tip of an RCF crack as the rolling element traverses the surface; this is based on evaluating the shearing of the crack faces during a rolling contact cycle. The results from all of the

models produce similar predictions of Mode II SIF; the predicted values are in a SIF range which is large enough to promote crack growth. However, they cannot explain why the direction of motion is important to crack growth because models based simply on the shearing effects of the crack faces predict the same cycle of stress intensity at the crack tip irrespective of the direction of motion.

A significant discovery made by Laird and Smith [128] was that despite promising results from theoretical and numerical investigations, it has proven very difficult to propagate surface cracks in Mode II in laboratory experiments. From an extensive series of tests carried out to investigate the behaviour of cracks under shear loading, the results of the tests show that if a compressive stress is applied acting perpendicular to the crack, in dry conditions, it causes the crack to lock up and prevents it from propagating. However, if the compressive stress acting perpendicular to crack face is reduced, the crack faces begin to slip and the cracks may propagate, but under these conditions the cracks tend to branch and then propagate as Mode I.

Otsuka et al [129] were able to propagate cracks in Mode II by applying a small tensile stress acting perpendicular to the crack, so that the faces of the crack are pulled apart, and then subjecting the crack to cyclic shear stress, where the SIF range exceeded the threshold value for propagation. Under these conditions, Mode II propagation can be seen in coarse grained steels. When the Mode II stress intensities are increased however, the crack once again, as in Smith's case, branched and began to propagate in Mode I, perpendicular to the principal tensile stress.

The experimental studies suggest that Mode II alone is not sufficient to propagate surface breaking cracks. The experimental tests demonstrate that a modification of the friction coefficient (i.e. a lubricant film) or a tensile stress, acting perpendicular to the crack face, is required to achieve crack growth under laboratory test conditions. The next section will address the possible mechanisms that have been hypothesised and modelled in the literature to try and capture how the lubricant may interact with a surface breaking RCF crack to modify the friction co-efficient between the faces or generate tensile stress acting on the crack faces.

2.8 Two Dimensional Models

Firstly, in this section, we will consider the two dimensional models from the literature which are approximated by a roller in contact with a cracked, lubricated plane. Schematically, this is expressed as a line contact acting on an idealised, cracked elastic half plane while invoking the plane strain condition, see Fig. 2.9.

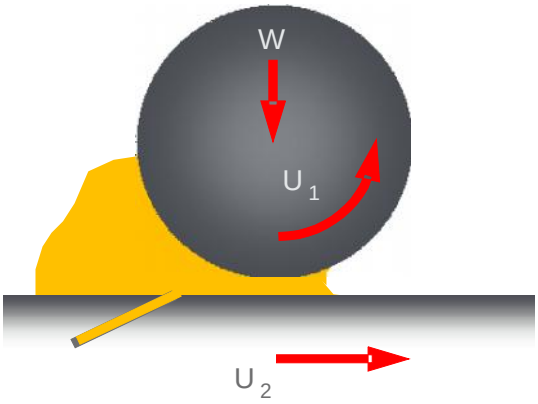


Figure 2.9 Schematic of the 2D, lubricated, RCF crack model solved in the literature

The characteristics of a line contact are such that the pressure in the z-plane remains almost constant, except at the edges of the roller, therefore it can be analysed with a reasonable degree of accuracy in 2D with the plane strain approximation. The degree of approximation worsens if the 2D crack is adopted to represent the central slice of 3D rolling contact problem in the presence of cracks; the model will then only describe the central slice of a penny shaped crack. Care needs to be taken in such cases to describe the fluid flow and assumptions need to be made about the crack configuration and its shape with respect to the contact area. The models have been built using LEFM with a mixture of the boundary element and finite element techniques previously discussed.

2.8.1 Friction Reduction Mechanism

When it enters an RCF crack, the lubricant may coat the surfaces and form a lubricant film reducing the friction coefficient between the cracks faces; this can in turn increase

the slip, or shearing displacement, of the crack faces and the shearing at the crack tip which is shown by a number of authors to significantly increase the *KII* SIF [125-127, 130]. The lubricant penetrates the crack (under a mixture or surface tension and capillary forces), covers both crack faces with a film reducing the interfacial friction (typically from around 0.6 to 0.1) [8], and allows the faces to slip under the contact load, inducing a large shear deformation. To model this effect, the faces of the crack are taken to be in contact, apart from the thin lubricant film formed between the two faces, the crack is considered to be closed. This scenario usually corresponds to negligible or compressive normal stresses and no opening of the crack faces (see Fig 2.10). Based on this model the crack has no induced KI and is assumed to propagate entirely in mode II.

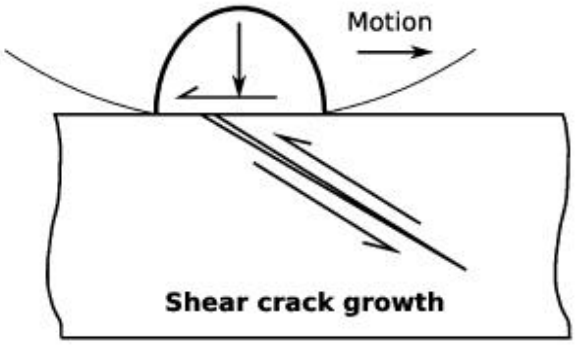


Fig 2.10 Shear mode crack growth accelerated by reduction of friction between the crack faces [2, 122]

Different values of friction coefficient have been applied in the literature, and the effect of varying the friction coefficient has been investigated [131], however no real attempt has been made to measure the actual friction coefficient inside a lubricated crack. This

mechanism has never been experimentally corroborated but authors have argued for its relevance by suggesting that the lubricant film that enters the crack is too thin to accumulate and support pressure transferred from the surface film [2].

The friction reduction model provides a simple way to model the lubricant in the crack but offers little towards a better understanding of the way that the crack deforms and propagates under the coupled effect of the lubricant penetration and contact loading.

2.8.2 Hydraulic Pressure Mechanism

From Way's original hypothesis of a hydraulic pressure build-up inside the crack, a model for the effects of the hydraulic pressure mechanism was developed by Keer and Bryant [97] and by Murakami and Kaneta [3]; it has also been used more recently by Flasker and co-authors [132, 133]. The model is based on the assumption that the lubricant penetration is sufficient to fill the crack as the load approaches and then as the load rolls over the crack mouth the fluid inside the crack is pressurized by the contact load, shown in Fig 2.11. These features are common to all the models, however there is a difference of opinion on what profile the pressure inside the crack will take and some are based on a Hertzian contact pressure at the interface [3, 97] and more recently author's have used an EHL contact pressure [132]. There is no attempt in any of these models to actually investigate the pressure profile acting on the crack faces, or any transient fluid effects, the pressures are assumed and imposed. Foord *et al* [134] were

the first to point out that as fluid flows into the crack; the pressure is likely to vary along the length of the crack, the variation being a function of the load, the velocity, the rate of change of the crack film thickness (the rate of crack opening/closing) and the viscosity of the fluid.

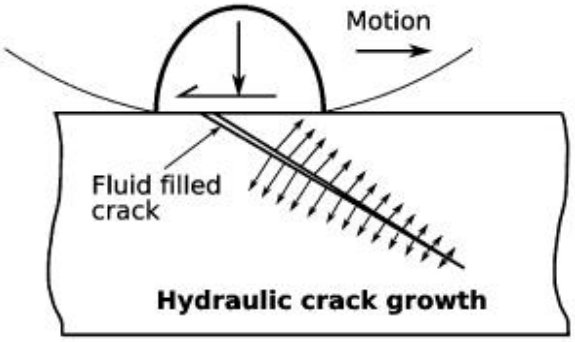


Fig 2.11 Tensile model crack growth due to hydraulic transmission of contact pressure [2, 122]

Kaneta *et al* [3] and Keer *et al* [97], both assume a linear tapered pressure gradient from crack mouth to crack tip. The pressure is equal to the Hertzian, or surface film pressure, at the mouth and zero pressure at the tip. A significant gradient; it would create a large instantaneous pressure driven flow between the surface film and the crack tip. During the period of a load cycle when the crack is undergoing rapid opening this pressure gradient would be a reasonable approximation because you would expect a large ingress of fluid. However when the crack is closing, when the internal fluid pressure is lower than the compressive pressure due to the contact load, and the fluid is

being squeezed out of the crack this gradient would appear to be unphysical and therefore unrealistic, however it was deemed a reasonable first iteration.

Flasker *et al* [132, 133] have assumed a constant pressure within the crack, equal to the Hertzian or surface film pressure at the crack mouth. Again, it can be considered valid at a certain stage of the load cycle, when the rate of change of the crack film thickness (or crack opening/closing) tends to zero, it is not valid when the crack is opening or closing. This is why; when the crack is opening, fluid enters the crack at the mouth which suggests that the pressure at the tip of the crack must be lower than the mouth, when the crack is closing the fluid is being expelled at the mouth which suggests that the pressure at the tip must be higher than at the mouth otherwise the fluid would not flow. When the crack shape is changing a pressure gradient will exist in the crack film, the intensity of this gradient is something that needs to be calculated.

These two predicted and prescribed pressure profiles, Flasker *et al* [132, 133] and Keer *et al* [97], represent an upper bound (constant pressure) and lower bound (tapered pressure) solution for the unknown fluid pressure inside the crack. However, due to the transient nature of the crack shape and crack film thickness, the flow of the fluid as well as the transient surface film pressure, the pressure inside the crack should be solved as a variable. A variable that changes during a load cycle because the loading on the crack changes during a loading cycle. At an instant in time where the crack is analysed using the hydraulic pressure model the real hydraulic fluid pressure will lie somewhere between the upper and lower bounds prescribed by Flasker *et al* [132, 133] and Keer *et al* [97].

Somewhat surprisingly, Kaneta *et al* [3] and Keer *et al* [97] predict very different stress intensity values and ranges for a single load pass while using the same prescribed pressure gradient, with Keer *et al* [97] predicting values a factor of tens times larger than Kaneta *et al* [3]. As a result, Keer *et al* [97] conclude that because of the huge growth rates predicted from their model that this is unlikely to be the cause of RCF crack growth. Kanteta *et al* [3] however take the opposite view stating that this is the most likely mechanism of RCF crack growth. In the literature it is suggested by Bower that this mechanism is unlikely [8] because when the load between the contacting bodies are high enough to cause RCF a very thin layer of lubricant exists that separates them and therefore it is hard to believe that a significant amount of fluid could be forced into the crack under loading. However, it is actually now believed that most of the fluid enters the crack as the load is approaching the crack and not while the load is acting directly on the crack [1, 99]. Bower also argues that this model doesn't capture the unidirectional nature of the relationship between the direction of the contact load pass and crack growth. However Kaneta *et al* [3] propose that this inaccuracy may be overcome by modelling and accounting for the process by which the fluid enters and exits the crack more accurately, but until now a rigorous analysis of this process has not been attempted.

2.8.3 Fluid Entrapment Mechanism

As the contact load reaches the crack, the crack is pulled open by a traction force (a negative shear force induced by over-rolling). Fluid then flows into the crack by capillary action and as the load moves farther, the mouth of the crack is closed and the fluid becomes sealed inside the crack unable to escape (See Fig 2.12) [3, 8]. The entrapped fluid is assumed to be incompressible and at constant pressure so the solution is based on finding the unknown pressure to maintain the entrapped volume within the crack. The trapped fluid has two effects, firstly the fluid pressure can generate Mode I stress intensities as the fluid is forced towards the crack tip; secondly the fluid keeps part of the crack open and therefore reduces the resistance of the crack to shearing therefore also increasing the Mode II stress intensities. The cycle of Mode I and Mode II stress intensities are evaluated as the load traverses the crack.

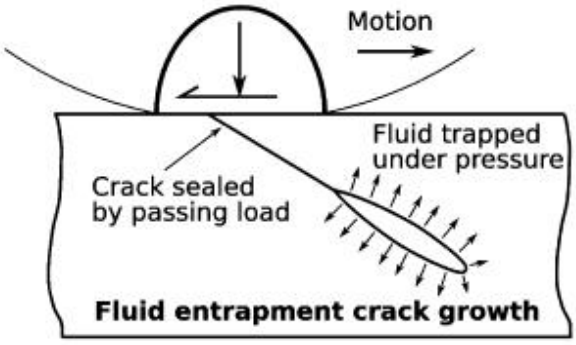


Figure 2.12 Fluid assisted mechanism of crack growth due to entrapment and fluid pressurisation inside the crack [2, 122]

This model successfully captures the effect of the direction of motion on two counts. Firstly the fluid can only be trapped in the crack if the mouth passes under the contact before the tip; otherwise the fluid is pushed out of the crack by the traversing load. Secondly, the stress intensities are affected by frictional locking between the faces of the crack when the fluid is pushed out.

The volume of fluid that is trapped inside the crack is the main parameter of the method which influences the solution. This is sensitive to the direction of motion of the load but is also sensitive to the surface traction, where a driving traction pulls the crack open further therefore more fluid is entrapped and a breaking traction has the opposite effect. As a result, the stress intensities are sensitive to the direction of the surface traction and the stress intensities are greater under a driving traction (over rolling).

The entrapment method however doesn't actually analyse the behaviour of the fluid and investigate whether the crack will actually close as it enters the contact it merely imposes this condition as an assumption. The method of analysing the crack once the lubricant has been entrapped is based on sound physics but the main limitation to this model is that it is only valid when the crack is closed at the mouth. It assumes that the crack mouth remains closed throughout the loading cycle. This simplifies the problem of evaluating the fluid pressure in the crack, to one of a conservation of volume/mass, and also removes the possibility of an interaction between surface film and the crack film.

For the crack to close as soon as it enters the contact, the crack would have to be only partially filled, which for long cracks could very well be the case. But, for shorter

cracks that could be fully filled as they enter the contact some analysis of the mechanism of interaction between the fluid and solid is required to check whether the crack does in fact close or whether the fluid becomes pressurized and causes it to open. Therefore this method requires some development to analyse what happens as the crack enters the contact rather than assuming and imposing this condition.

2.8.4 Squeeze Fluid Film Model

S. Bogdànski [1] recently developed a new model to evaluate RCF cracks, based on evaluating the coupled action of a squeeze film built up inside the RCF crack and the external pressure acting at the contact interface in a line contact in the EHL regime (see Fig 2.13). The model is based on evaluating the effect of the periodic squeezing in the crack, due to the compressive contact load, where the crack film acts like a 'squeeze film' from lubrication theory [1]. The surface pressure in the contact interface is found using a numerical solution to the EHL contact problem and the pressure in the crack is evaluated separately using a wedge shaped squeeze film model, using Reynold's equation and a set of imposed boundary conditions at either end of the crack film.

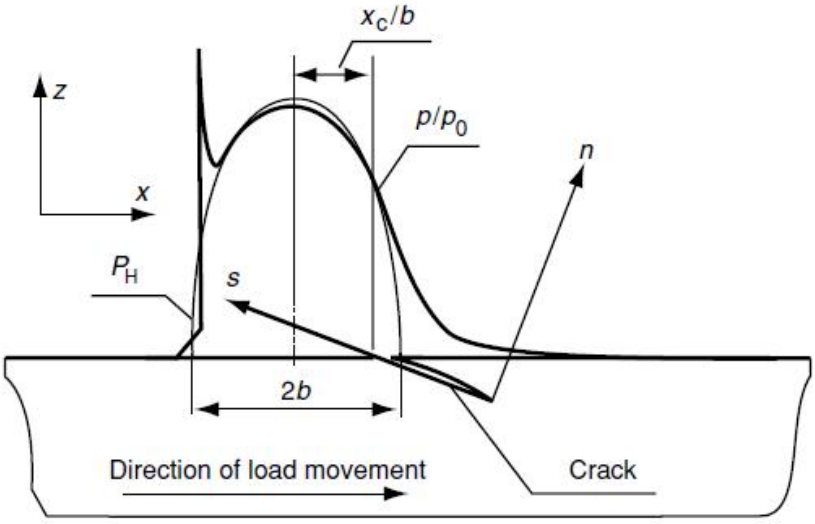


Figure 2.13 Squeeze oil film (SOF) model, with EHL contact presure [1]

Four simplified models were presented however this section will consider just the most highly developed model, shown in Fig 2.14:

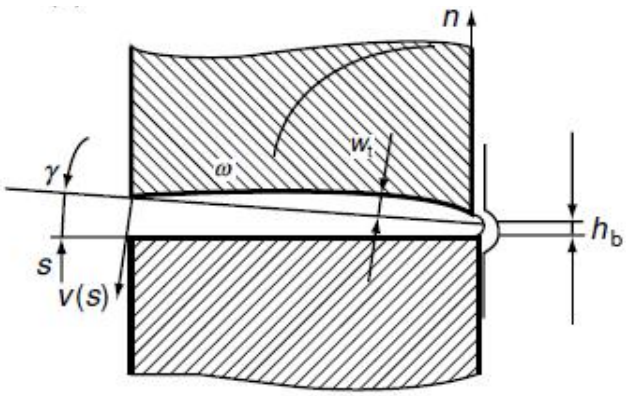


Figure 2.14 Squeeze oil film model IV, which takes into account the elasticity of the crack [1]

The 1D EHL model was applied with a modification to the surface film shape due to the presence of the crack, creating a step in the surface film, therefore modifying the

surface pressure. The surface 'oil film shape equation' was modified from the original to include the effects of the change in stiffness of the surface of the plane due to the presence of the crack and also the effect of the fluid pressure inside the crack altering the surface film shape.

The squeeze film pressure is then derived analytically from Reynold's equation, where the viscosity varies with Barus' [1] and the density is constant, where there is an imposed pressure at the point at which the crack meets the surface film (mouth pressure) and a zero pressure gradient at the crack tip ($dp/dx = 0$) , to satisfy the boundary conditions for Reynold's equation. The solution is based on the crack face rotating by a constant rotational speed, where the tangential velocity is linearly varying along the crack length by $v = \omega.s$. This is then modified to take into account the effect of the deformation of the crack face (W_t), where the total displacement at a given point on the crack face is subtracted from the distance travelled by the rotation of the crack face as a rigid wall. The deflection of the crack faces is found using influence functions derived from an FE analysis. Also an imposed minimum thickness is applied at the crack tip so that $v \neq 0$ and $h \neq 0$ at any point. Throughout the load pass, the mouth pressure is maintained constant at an imposed value of 100MPa, and the crack face is assumed to always be closing as a rigid wall with an imposed velocity.

This model represents the first attempt, in the literature, to model the interaction between a surface breaking RCF crack and the lubricant that considers transient fluid effects and the liquid/solid interaction. The modification of the crack shape due to the fluid pressure and the re-evaluation of this effect on the fluid pressure is an important

feedback loop that is required to accurately model this problem, and is something that previous authors have failed to address. This deflection has a significant effect on the pressure gradient that is built up inside the RCF crack. However there has not been any attempt to capture the important fluid/fluid interaction that occurs at the interface between the crack film and the surface film. This interaction, that can only be captured by coupling the two films together and solving the entire fluid problem as one domain, also has a major effect on the solution.

The fundamental simplifying assumptions that have been applied to this model make it somewhat unphysical. The imposed boundary condition applied at the crack mouth, which is maintained constant throughout the load pass, straightaway introduces an error by imposing a discontinuity, or a pressure step, in the fluid domain. As the crack enters the contact interface, the pressure at the mouth of the crack is maintained at the Reynold's boundary condition of the imposed mouth pressure. Directly above this, in the surface film, the fluid is at the EHL film pressure which is much lower. This pressure step would induce a large and instantaneous pressure driven volumetric flux creating a large ingress of fluid into the RCF crack. If this fluid were to flow into the crack then in reality the crack would not be closing it would be opening and therefore a negative squeeze, and perhaps cavitation would be the result.

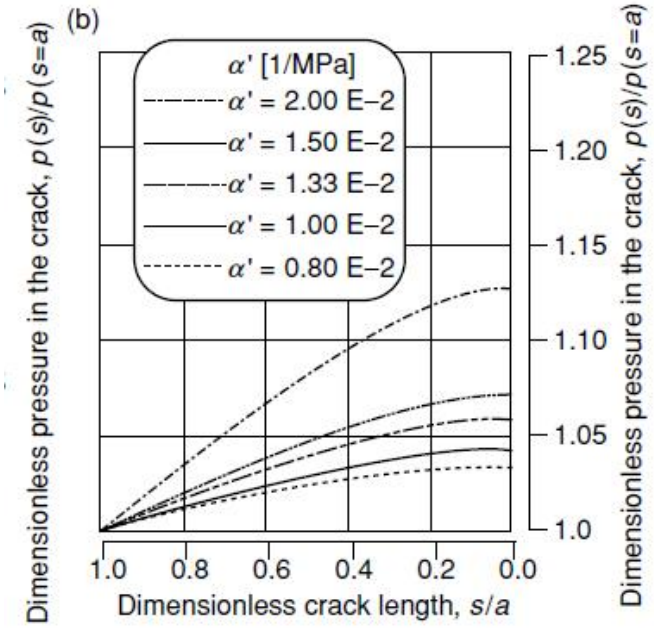


Figure 2.15 Distribution of the pressure along the crack length from SOF model IV [1]

In actual fact, the predicted pressure profile by Bogdànski, shown in Fig 2.15, for different Barus exponents α shows a positive gradient inside the crack where the pressure at the crack tip (at 0) is higher that the crack mouth (at 1). Although valid for a crack that is closing where the fluid is being squeezed out of the crack, this profile would be wrong if the crack was opening. This highlights the importance of coupling the two films together to preserve continuity.

To assume that the crack is always closing again introduces error to the solution. An accurate model should evaluate the shape of the crack at each time step and based on a comparison with the shape at the previous time step, evaluate whether it is in fact opening or closing. To assume that dh/dt is always negative is inherently wrong. It, as

you would expect, always gives a positive pressure gradient. In actual fact to calculate accurately what is happening in the crack, the method of solution requires a coupled iterative routine to find both the pressures in the whole fluid domain and the film thicknesses. From the calculated film thicknesses at each time step d*h*/d*t* can be found rather than assumed.

2.8.5 Multiple Cavity Model

Developed by Kudish and Burris [99] the multiple cavity model is presented as a; "new mathematical model for lubricated elastic solids weakened by cracks" where the interaction of the lubricant with the elastic solid within cavities of surface breaking cracks is the focus. The model considers a crack in an elastic half-plane loaded by a moving normal and tangential contact stress transmitted through an incompressible lubrication film, where the half plane is pre-stressed by a compressive residual stress acting to close the RCF crack. The solution is based on solving a system of integro-differential equations with boundary conditions formed of alternating equations and inequalities. It has been used to consider a series of different scenarios based on different boundary conditions such as the development of several cavities some of which are completely filled and others which are partially filled, where the fully filled cavities experience pressurisation, shown in Fig 2.16.

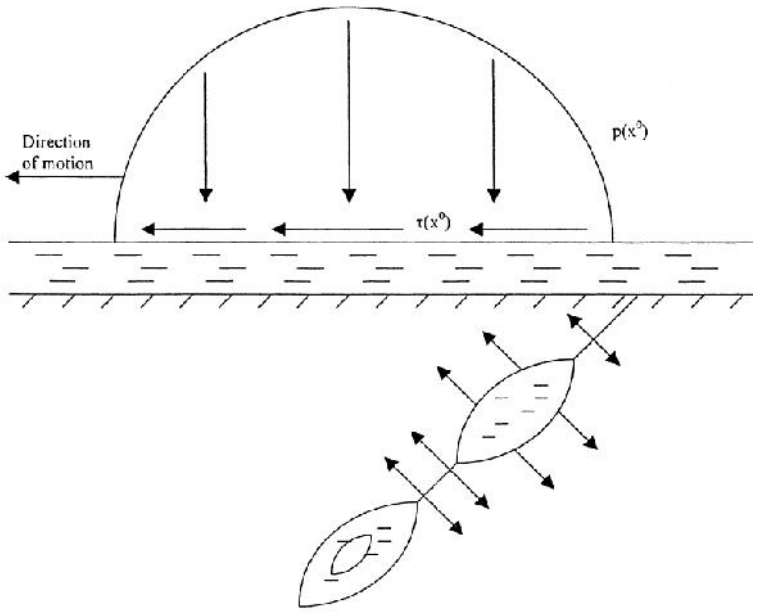


Figure 2.16 Multiple cavity model shown in a configuration with two cavities, one full filled one partially filled [99]

A somewhat abstract approach, the process of how the cavities may be formed has been overlooked and the model looks at evaluating the possible behaviour of the RCF crack should the situation arise. One of the analysed cavity configurations is used here as an example, shown in the diagram, to demonstrate the model and discuss the feasibility. In this configuration the mouth of the crack is closed and locked where the subsequent crack path is also locked until it reaches a cavity which is fully filled and pressurised. Then as you continue along the crack path there is another region of locking and then finally a cavity that is only partially filled and therefore not pressurised.

This configuration seems plausible when considering something at an asperity level, where it could be argued that the pockets, or cavities, of entrapped fluid were

being trapped between asperity contacts and therefore some may be partially filled and some may be fully filled, But at a macroscopic level, when analysing cracks of the order of 100μm and assuming the crack face is smooth, it seems unlikely that this configuration within the crack could arise. Under compressive loading a partially filled cavity would be compressed until the fluid inside the cavity was providing a tensile load to balance the compression, and therefore the cavities would always be pressurized under compressive loading. Further to this, the fluid trapped in the crack would tend to be pushed towards the crack tip and form one large filled cavity rather than a series of separated ones.

2.8.6 Three Dimensional Models

Three dimensional models, by their very nature, are more computationally expensive than two dimensional models. Therefore the simulated interaction between the fluid and solid that has been analysed in 3D is limited to a couple of simple models. In 3D the cracks are idealised using a semi elliptical, 'penny shaped', shown in Fig 2.17, shaped geometry and like the 2D models solved with LEFM using boundary element and finite element methods, where the applied load can either be a point contact or a line contact.

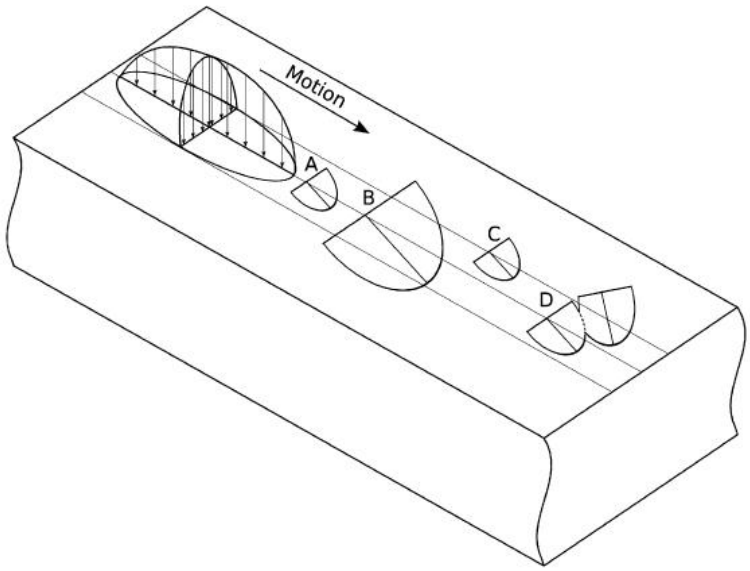


Figure 2.17 3D Penny shaped crack configuration used by author in the literature [135]

In the three dimensional analyses the effect of the third SIF Mode III, out of plane shear, can also be evaluated and presented. Murakami and Kaneta were the first to propose a three dimensional model [136] based on the hydraulic pressure mechanism which has already been discussed and won't be revisited here. More recently Kapoor [135] and Bogdànski [137, 138] also presented three dimensional models. Kapoor has also used the hydraulic pressure mechanism and Bogdànski has presented different models that use both the hydraulic pressure mechanism and the fluid entrapment mechanism previously discussed.

The future of the field of research lies in accurate three dimensional analyses; however up to this point in time no model has been successful in fully capturing the interaction between the lubricant and the RCF crack in two dimensions. It is therefore

important to first, develop the understanding of this effect using two dimensional analyses and then extend it to the more complex three dimensional analyses.

2.9 Experimental RCF Crack Studies

There is a lack of experimental work in the literature that deals directly with the mechanism of interaction between the lubricant and the RCF crack. There is however, anecdotal evidence that has been used to infer the possible mechanism. Starting from the very first experimental study that conceived the whole research field, conducted in 1935, Way's experimental study was based on investigating the effect of water on the propagation of cracked rails [6], . From his paper "Pitting in rolling contacts", the results determined that fluid effects in RCF contacts where cracks were present on one or both of the contact surfaces, increased the propensity for RCF cracks to grow. In certain test cases, when the lubricant, water, was not present in the test conditions no pitting occurred whatsoever This result was attributed to hydrostatic pressure build up in the fluid which penetrated the crack however the mechanism was not actually investigated or verified, it was simply deemed the most reasonable explanation.

Fujita and Yoshida [124] demonstrated that RCF crack initiation and propagation are influenced by the direction of motion. The study compared the fatigue lives of rollers that were run for a number of cycles under an initial load (in this example 120kg/mm^2) where the load was then changed (in this example to 100kg/mm^2) and the roller was run

until failure[1]. The rollers were initially run for a number of cycles under the same initial load however; under the second load in certain cases the direction of rolling was changed.

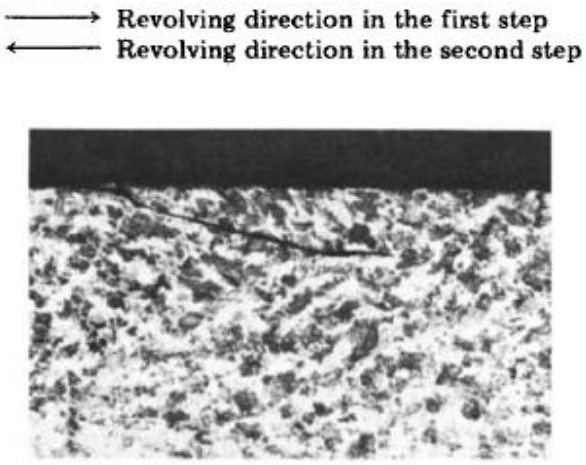


Figure 2.18 Cracks in the subsurface of the material shown to stop propagating after a change in the roller direction [124]

Fig.2.18 shows the transverse section of a roller, with a clear surface breaking crack, From this experimental work the idea of crack propagation being sensitive to the direction that the contact load traverses, was first presented however no real investigation into the reason for this was undertaken. The reason for the directional phenomena again is attributed to potential lubricant effects, where if the crack was suddenly to be loaded at the tip before the mouth, any residual lubricant inside would be

[1] which was defined as a condition where the pitted area accounted for 3% of the roller surface

squeezed out as the contact load traverses from crack tip to crack mouth, nullifying and removing any lubricant effect.

Bogdànski [139] more recently conducted tests similar to those of Way [139], and in his experimental tests he saw similar trends. However in contrast to Way, Bogdanski used oil as well and water as the lubricating fluid and he attempted to address how the amount of fluid that ingresses into the crack during a loading cycle is dependent on certain operating conditions such as the lubricant viscosity and loading frequency. The tests were carried out using the fatigue machine the Instron 8500, this machine continuously supplies oil to the contact during the test where a fluctuating load, 1500Kg in this case, is applied with a specified frequency, 5Hz in this case, and the crack growth is monitored using ultrasound, using an ultrasonic detector INCO DI-8T.

The surface breaking cracks were created using a pre-cracking method, rather being allowed to develop naturally, where the surface was initially indented to give a V shaped notch 0.3mm wide and 0.2mm deep, using the indenter shown in Fig 2.19. From the stress concentration induced by the notch surface breaking cracks developed however these cracks were not the type of cracks seen in RCF because they grew perpendicular to the surface to give vertical, rather than inclined cracks. This is because the repetitive loading that was used was not a cyclic contact loading but instead a remote cyclic tensile and compressive loading. This simplification was deemed sufficiently accurate for this study, as the objective was to investigate whether fluid does ingress the crack and whether it affects the crack growth rate.

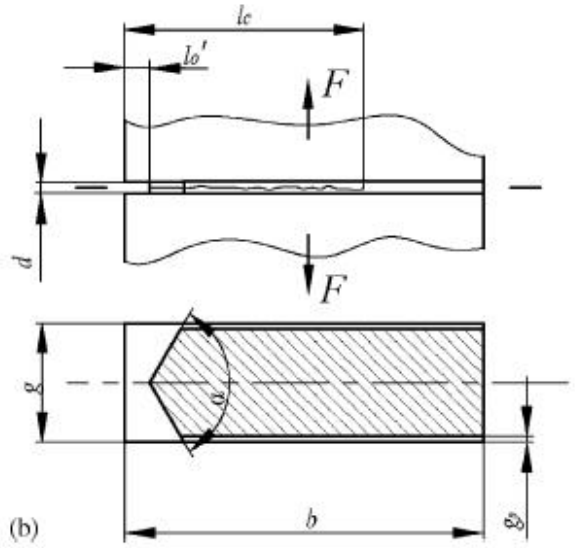


Figure 2.19 V-shaped indenter used to create pre-cracks [118]

The experimental tests showed that when the lubricant was present in the experimental conditions the crack growth rate was accelerated, by up to 20%. The tests were split into sections where different loading frequencies were used and it was found that the amount that the crack growth rate was accelerated by the presence of the lubricant was dependent on the loading frequency, where higher loading frequencies appeared to reduce the influence of the lubricant on the crack growth rate. This was attributed to the fact that at higher frequencies the crack has less time to fill with lubricant, and if the crack does not have sufficient time to be fully filled then lubricant pressurisation will not occur. It was also shown that viscosity will influence the ingress of fluid, where higher viscosity lubricants require more time to fill the crack. These results, though interesting, are not truly representative of a repeated rolling contact or a RCF crack. That the cracks

are vertical and are being loaded in tension and compression means that an already considerable mode I, or *KI*, will be induced from the loading condition that will lead to rapid crack propagation and dominate over any lubricant effects inside the crack. Therefore, in actual fact, an up to 20% increase in the crack propagation rate due to the presence of the lubricant in reality could represent a conservative estimate.

These studies have raised some questions, and identified some currently unexplained aspects of the phenomena of RCF crack growth and pitting, however they have not been able to clarify the exact causes. Lubrication effects have been implied as the route cause but no physical evidence yet exists to render this beyond doubt. The reason that no physical evidence exist is because to witness the effect of fluid pressurisation opening an RCF crack, in situ, under real operating conditions is something that is very challenging and as yet is beyond the capabilities of current experimental methods.

2.10 Duration of Initiation/Propagation

The importance of understanding how surface breaking cracks behave and how they propagate is inherently linked to the duration of the fatigue life that surface cracks and surface crack propagation occupies. The formation of an RCF crack involves two distinct processes, crack initiation and subsequent crack propagation. Initiation concerns the formation of a crack to the threshold of delectability and propagation is its subsequent growth to failure. In the literature authors suggest that propagation occupies

between 20% and 80% (on average around 50%) of total RCF lifetime, based on experimental data, a considerable amount.

With ever improving steels that contain fewer inclusions a shift from sub-surface initiated RCF to surface initiated RCF is being witnessed. Previously, RCF was generally nucleated in the subsurface at material inclusions and then propagated to the surface. However in recent years there has been a shift toward surface initiated RCF where stress concentrations at surface flaws trigger the nucleation of surface cracks, cracks that propagate down into the substrate material. With this, the interest in surface breaking cracks is growing, and therefore the relevance of studying surface breaking cracks is also mounting, and becoming more in line with industrial applications.

2.11 Summary

The modelling and experimental work that is discussed in this review has identified two key points that have not yet been presented in the literature. The first of which is a model that captures the fluid/solid interaction between a lubricant and an RCF crack in a loaded contact, while solving the pressure and flow in the lubricant film rather than imposing assumed values, a model that takes into account the full coupling between the displacement of the crack, and the fluid pressurisation in the lubricant film. Then a model that will use this method of analysis to evaluate a contact loading cycle and based on the results of a sequence of cycle's, model the fatigue process including the crack propagation and pitting. Furthermore, there is not yet an experimental study that

has been able to explicitly show the fluid/solid interaction inside an RCF crack during a loading cycle. This body of work is aimed at addressing these two key areas, to improve the general knowledge of the behaviour of RCF cracks in lubricated contacts, and the mechanism that leads to pitting and RCF component failure.

Chapter 3

Dry Crack Modelling

3.1 Introduction

This chapter introduces the foundation of the crack modelling methodology that will be used throughout this thesis. While each chapter will introduce a new layer of complexity, this chapter provides the fundamental formulation and the first building block of the coupled fluid/solid formulation developed in chapters 4 and 5. It also provides a basis for comparison with benchmark cases, as it deals with simple model, whose solutions is readily available in the existing literature.

The aim of this study is to conduct a complete analysis of the interaction between lubricants and deforming contacting bodies, which obviously involves the development a fluid and solid solver and while also solving for their interaction. This is indeed a very

comprehensive task; therefore in order to build the formulation gradually, the starting point of this study is the modelling of cracks without the added complexity of calculating the lubricant fluid pressure, thereby neglecting the fluid/solid interactions. Furthermore, if the solution to a dry crack analysis proves to be similar to that from a complex iterative, fluid/solid coupled solver then, although the complex solution may be more accurate, the added computational expense cannot be justified. Dry crack modelling involves evaluating an RCF crack while neglecting the effect of the lubricating fluid, and any induced effects like lubricant pressurisation. The contact pressure on the surface of the cracked body is the only loading condition, where the contact is of a Hertzian nature, and the solution contains no time-dependant or history dependant variables. Furthermore, to a first approximation, the contact pressure and the crack displacement are only coupled in one direction, whereby the contact pressure affects the crack displacement but the crack displacement does not affect the contact pressure. Therefore the equations used to describe the model and the method of solution can be posed simply without the need for coupling or an iterative solver. The lack of any history-dependant or time-dependent variables also means that the model can accurately capture the physics of the problem under investigation using a quasi-static analysis; this means that the problem can be modelled as a series of linear, static analyses solved in sequence, where the order of the sequence does not affect the outcome of the simulation. Here, a static solution will be obtained for different positions of the crack in the contact patch until the full contact has been traversed. A schematic of the problem is depicted in Fig 1(a).

The model to be considered in this chapter is a roller in contact with a cracked half-plane, which gives rise to the well known Hertzian line contact pressure distribution [123, 140], shown in Fig 3.1;

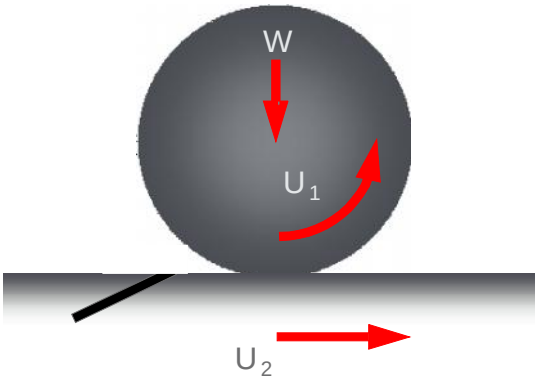


Figure 3.1.Schematic of the dry crack problem

This is the standard configuration used when modelling crack problems for roller bearings [2, 97, 125]. The crack is surface-breaking and inclined (usually at about between 15° to 20° to the horizontal plane) and loaded by a moving Hertzian line contact where the effects of the lubricant on the surface and in the crack are ignored. The crack has a stress singularity at the tip and its shape is taken to be infinitesimally thin when un-loaded, so it is considered as a line of zero thickness when un-deformed. If the crack faces are closed (in contact) frictional effects act as they shear against each other; usually this is captured using a conventional Coulomb frictional law with a pre-determined friction coefficient. The same treatment is also applied to the surface of the half-plane, where a shearing traction is induced by the frictional interactions between the rolling element and the cracked surface.

The following assumptions are made in formulating the problem:

1. The model obeys linear elasticity;
2. The crack surface and outer surfaces are perfectly smooth;
3. The problem can be modelled in 2D using the plane strain assumptions;
4. The crack has a stress singularity at the tip (no blunting is explicitly introduced)

Assumption (1) is justified in the case of most engineering applications such as wheel rail contacts and bearings, in which the stress field remains elastic except for a small zone of plasticity at the crack tip that encompasses less than 2% of the crack length. Assumption (2) is imposed to simplify the analysis, but is justified because stresses induced by surface roughness are concentrated at the surface and do effect the stress field deep into the subsurface. Assumption (3) is based on the fact that the contact is a line contact and therefore the contact pressure doesn't vary a large amount in the out-of-plane direction. Assumption (4) is a consequence of the fact that the crack tip can be indeed treated as sharp for the level of resolution used here. The macroscopic analysis is based on the small scale yielding assumption not being violated and, therefore a detailed characterisation of potential crack tip blunting is unnecessary

3.2 Modelling Methodology

To model this system using a half-plane contact approximation, two distinct effects need to be considered and combined; they are shown in Fig. 3.2: (i), the effect of the Hertzian contact pressure on the loaded half-plane; (ii) the behaviour of the crack as the half-plane is loaded. If we think in terms of stresses, then the two effects that will be evaluated are the stress in the half-plane due to the Hertzian contact pressure and the stress induced by the crack as it is loaded and it displaces. The analyses to be performed look predominantly at the stress field because the aim is to investigate the propensity of the RCF crack to grow and cause component failure. This effect can be quantified by two numerical parameters, the two stress intensity factors SIFs, KI and KII, and therefore to obtain these parameters the stress field of the system must be evaluated.

The system, will encounter a very small concentrated region of plasticity at the tip of the crack. However this small region, less than 2% of the crack length, will be considered not to interfere with the linear elastic stress field, an assumption that has been widely accepted for this type of crack analysis [55], and is known as small scale yielding. Therefore the effect of the different loading conditions on the half-plane, the Hertzian contact pressure and the RCF crack displacement, can be isolated, solved separately and then combined using Bueckner's principle of superposition of stresses [55].

3.3 Formulation

The formulation is developed to evaluate the effect of the moving contact pressure from the loaded roller acting on the cracked body. Within the linear elastic theory framework, the cracked body is treated as a two-dimensional half-plane in plane strain [123]. The methodology is derived from Bueckner's principle (Bueckner 1958) which is based on the superposition of stresses [55]; Bueckner states that if you are within the elastic limit, individual loads and the associated stresses generated by their application can be considered in isolation and then their contribution combined in any sequence to give the same result as solving for all the loads concurrently. The influence of plasticity at the crack tip on the solution is assumed to be negligible so the problem is solved using the linear elastic theory [141] and linear elastic fracture mechanics principles can be applied to study the crack.

From Bueckner's principle the solution is divided into two separate problems (see Fig. 3.2): The first problem to be solved is the one dealing with the determination of the state of stress in an un-cracked body subject to external pressure (problem I in Fig. 3.2). In the context of this model, this is the stress in the half-plane resulting from the Hertzian contact pressure. The second problem is the state of stress induced by dislocations, of unknown density deployed along the crack path (problem II in Fig. 3.2).

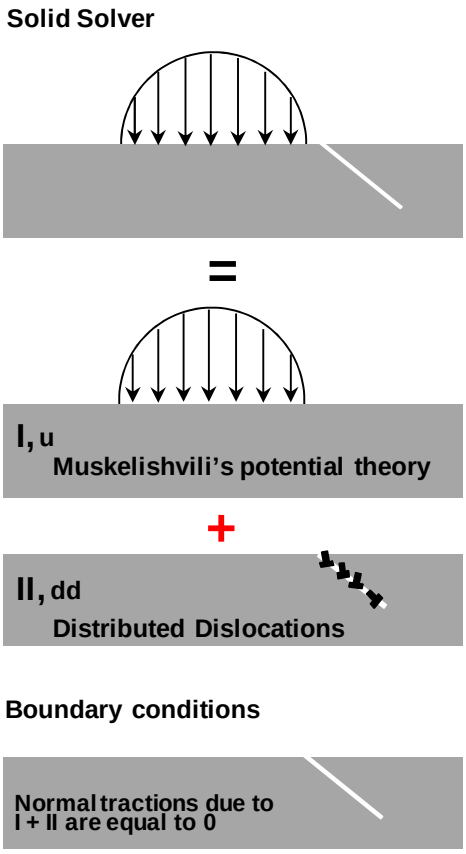


Figure 3.2 Method of separating the full problem into subsets (I) and (II) using Bueckner's principle

The dislocations are defined as climb in the axis perpendicular to the crack path (normal) and glide in the axis parallel to the crack path (shear). These climb and glide dislocations are a mathematical tool used to evaluate the crack, and therefore are merely a theoretical construct not a physical representation of the crack. The density of the dislocations at any point along the crack length can be thought of as a quantification of the amount that the crack is opening and the amount the crack is slipping or

shearing. The climb dislocation density quantifies the amount the crack opens, or displaces in the normal direction, and the glide dislocation density quantifies the amount the crack slips, or displaces in the tangential (shear) direction. Further to this, the climb dislocation density can be used to evaluate *KI*, the normal stress intensity factor, and the glide dislocation density can be used to evaluate *KII*, the shear stress intensity factor. Therefore, the mathematical formulation is based on finding the value of these two unknown quantities, the climb and glide dislocation density; this method of crack analysis is known as the distributed dislocation technique (DDT).

Considering the two stress problems separately, and applying the superposition principle, the resultant state of stress in the loaded and cracked body can be found as the sum of the contributions from the two problem sub-sets. This can be expressed mathematically as:

$$\pm_{ij}^{T}(x,y) = \pm_{ij}^{u}(x,y) + \pm_{ij}^{dd}(x,y) \qquad (3.1)$$

where the superscripts *T*, *u,* and *dd* refer to the total half-plane stresses, the un-cracked half-plane stresses, and dislocations induced stresses respectively.

This is true, provided that the boundary conditions at the crack faces and at the remote boundaries (at “infinity”) are satisfied. These boundary conditions are imposed to ensure that the mathematical problem is well defined and has a unique solution. They are imposed at the crack faces based on the characteristics of the surfaces of the crack, i.e. they specify whether the crack faces are open or in contact (closed). The boundary

conditions on the crack faces can also change along the crack length, should the crack be partially open and partially in contact; in these cases, the transition from open to closed is captured using a Heaviside step function.

For a surface breaking slant crack, considering a rotated coordinate system ($\hat{x},\hat{y}$) and denoting the normal and shear stresses along the crack faces $N(\hat{x})$ and $S(\hat{x})$ respectively [55], the boundary conditions can be written for an open crack as:

$$\begin{aligned} N(\hat{x}) &= \pm {}^{u}_{\hat{x}\hat{x}}(\hat{x},0) + \pm {}^{dd}_{\hat{x}\hat{x}}(\hat{x},0) = 0 \\ S(\hat{x}) &= \pm {}^{u}_{\hat{x}\hat{y}}(\hat{x},0) + \pm {}^{dd}_{\hat{x}\hat{y}}(\hat{x},0) = 0 \end{aligned} \qquad 0 < \hat{x} < a \qquad (3.2a)$$

or for a partially, or fully closed, crack as:

$$\begin{aligned} N(\hat{x}) &= \pm {}^{u}_{\hat{x}\hat{x}}(\hat{x},0) + \pm {}^{dd}_{\hat{x}\hat{x}}(\hat{x},0) < 0 \rightarrow \quad g(\hat{x}) = 0 \\ S(\hat{x}) &= \pm {}^{u}_{\hat{x}\hat{y}}(\hat{x},0) + \pm {}^{dd}_{\hat{x}\hat{y}}(\hat{x},0) = -fH(\hat{x} - a_{op})N(\hat{x}) \end{aligned} \qquad 0 < \hat{x} < a \qquad (3.2b)$$

where $\hat{x} = x\cos^{-}$, $\hat{y} = x\sin^{-}$, a is the crack length, a_{op} is the open portion of the crack, $g(\hat{x})$ is the surface gap function (hence equal to zero when the crack is closed), f is the Coulomb friction coefficient and H is the Heaviside step function, $H(\hat{x} - a_{op}) = 1$ when $\hat{x} < a_{op}$ and zero when $\hat{x} > a_{op}$. The Heaviside step function is used to trigger a change in the boundary conditions when the crack transitions from open to closed.

The boundary conditions used are physically representative, if there is no fluid pressure acting inside the crack the crack faces are stress free; these are the boundary conditions expressed in Eq. (3.2a). This implies that the stress induced by the dislocations distributed along the crack, must be equal and opposite the stress induced by the contact pressure.

When the crack faces are closed there is zero relative normal displacement of the crack but there is still a non-zero shear displacement. Since the material continuity is re-established and the crack virtually disappears, in any region where the crack is closed the contribution of the climb dislocations can be removed from the formulation because their density is equal to zero. The boundary condition for the shear stress at the crack face is obtained by applying Coulomb friction [142] and checking for slip and stick regions by checking frictional law violations within the closed paths. In a first approximation, and for lubricated cracks (low friction coefficient), sliding of the closed paths will be hypothesised. The step function is used to switch the boundary conditions between parts of the crack that are open and parts of the crack that are in contact, these are the boundary conditions expressed in Eq. (3.2b). When the crack is partially closed, the length of the open part of the crack can be evaluated iteratively, this process will be discussed in more detail later in this chapter.

By using these boundary conditions, the unknown values of the climb and glide dislocation densities along the length of the crack can be found. From these, the stress intensity factors can be calculated and the stress anywhere in the half-plane can also be found from the Airy stress function.

Due to the relatively low values of friction coefficient applied to the crack faces, the assumption is made that when the crack is partially, or fully closed, stick does not occur at any point at the crack interface. This means that no residual stress can be locked into the half-plane during the analyses; therefore the evaluation of the stress in the half-plane has no history dependence. The presence of a stick and slip transition along the crack could however be easily captured following a more general scheme which accounts for stick-slip transitions at the contact interface [55]. To couple the boundary conditions so that a unique set of boundary conditions can be applied to the full crack length whether it is fully or partially open, Eqs. (3.2a & b) are combined to give:

$$\begin{aligned} &N(\hat{x}) = 0 && a_{op} < \hat{x} < a \\ &S(\hat{x}) + fH(\hat{x} - a_{op})N(\hat{x}) = 0 && 0 < \hat{x} < a \end{aligned} \tag{3.3}$$

The combined boundary conditions above require that when $a_{op} > 0$, the two stress fields, normal and shear, be evaluated over different intervals. In the closed section of the crack the normal stress field is not altered by the presence of the crack and no discontinuity in the stress field is observed, while the shear is still evaluated over the full crack length.

Once the problem has been formulated, the aim is to find the unknown distribution of dislocations from σ^{dd} which satisfy the boundary conditions given by Eq. (3.3).

3.3.1 Solving Blocks

The semi-analytical formulations used to derive the stress and displacement fields within the half-plane for problems I and II will be individually described. The stress and displacement fields from the loading at the half-plane surface (I), or contact interface, are evaluated using Muskelishvili's potential theorem and the stress and displacement fields created by the crack (II) are computed using the distributed dislocation technique, described in full in [55, 98, 143]. The boundary conditions that are used to solve the distributed dislocation technique, require the stress in the uncracked half-plane due to the contact load to be known, therefore although Bueckner's theorem will be used, the modelling methodology needs to follow a sequence, where problem (I) is solved first, and the solution of problem (I) is used to solve problem (II). In light of this, the description of the formulation will also follow this sequence.

3.3.2 Evaluating the Stress Field without the Crack

The stress and displacements fields created by the loaded roller in contact with the half-plane are found using Muskelishvili's potential theorem [144]. At this stage in the solver

sequence the crack is not yet introduced and the half-plane is considered in absence of the crack. For this model, the loaded roller is represented by a Hertzian contact pressure [140] applied to the surface of the half-plane, where the pressure distribution along the contact length is found from the Hertzian expression:

$$p(r) = p_0 \left(1 - \frac{r^2}{B^2}\right)^{1/2} \tag{3.4}$$

where p is the pressure, r is the location of a point in the contact, B is the contact semi-width and p_0 is maximum pressure.

The potential theorem is a Green's function method for analysing sub-surface stresses resulting from different types of contacts. For this case, the Hertzian contact pressure profile is discretised using a linear piecewise discretisation of triangular elements [145], as shown in Fig. 3.3.

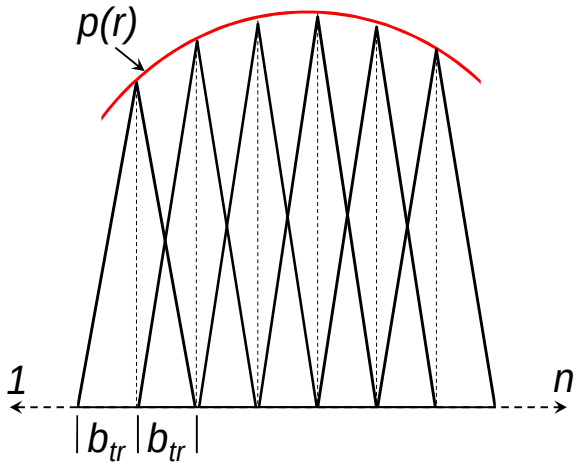


Figure 3.3 Discretisation of a contact pressure using a series of triangular pressure elements

The formulation for a triangular distribution of pressure on a half-plane is used as a pressure element to discretise the desired contact pressure at the surface of the half-plane using a linear piece-wise approximation (shown in Fig. 3,3), by superimposing the effect of each individual triangular pressure element on the half-plane. Again in this solution sub set, the formulation is making use of the assumption of linear elasticity and the principle of superposition.

The stress components are expressed in terms of a complex potential $\ddot{}(z)$ and its derivatives. The formulation, which is based on the solution to the bi-harmonic equation, demonstrates that the equations of 2D elasticity possess a general solution in terms of two arbitrary harmonic functions and allow the problem to be reduced to a Riemann-Hilbert problem from complex variable theory. The coordinate system is expressed in the complex form:

$$z = y - i.x \tag{3.5}$$

where $i = \sqrt{-1}$.

As the input for the variable *z*, the coordinates of the node points of the mesh of the crack and the nodes at the centres of triangular pressure elements are taken, expressed in complex form. Therefore, z is the distance in vector form from the node

points of the mesh of the crack to the node points at the centre of the triangular pressure elements. A linear interpolation is assumed to characterise the stress values between those that are evaluated at the node points. This can be used to extract stress values along a line using a 1D mesh (e.g. ahead of the crack tip, where the highest stress gradients are expected), or can be used to plot the contour stresses in a whole half-plane subsurface using a 2D mesh.

The relationship between the potential $\ddot{}(z)$ and the stress components, σ_{xx}, σ_{yy} and τ_{xy}, is expressed as:

$$\pm^{tr}_{xx} + \pm^{tr}_{yy} = 2[\ddot{}_{tr}(z) + \overline{\ddot{}_{tr}(z)}] \qquad (3.6a)$$

$$2\pm^{tr}_{xx} + 2\pm^{tr}_{yy} - 2.i\pm^{tr}_{xy} = 2[(\bar{z} - z)\ddot{}'_{tr}(z) - \overline{\ddot{}_{tr}}(z) - \ddot{}_{tr}(z)] \qquad (3.6b)$$

where $\ddot{}'(z)$, $\overline{\ddot{}(z)}$, and $\overline{\ddot{}}(z)$ are the first derivative, the conjugate function and the conjugate function in the conjugate variable of $\ddot{}(z)$ respectively. The potential function for a triangular load element of magnitude *F(y),* where *F(y)* = $p_H(y)$ + *i.f.*$p_H(y)$, and centred at (*x=0*, *y=0*) can then be introduced here:

$$\ddot{}_{tr}(z) = \frac{F(y)}{2®.i}\left(1 - \frac{z}{b_{tr}}\right)\ln\left(\frac{z - b_{tr}}{b_{tr}}\right) - \left(1 + \frac{z}{b_{tr}}\right)\ln\left(\frac{z + b_{tr}}{z}\right) \qquad (3.7)$$

where b_{tr} is the width of each individual triangular element. The magnitude of p_H represents the maximum pressure of the triangular pressure element, i.e. the contact pressure at that location, and f is the surface friction coefficient. From the two expressions, Eqs. (3.6a 3.6b), the unknown stress values can be found; where the two unknowns, σ_{xx}, σ_{yy}, are found using the simultaneous equations obtained using the real part of the expressions and τ_{xy}, which can be evaluated directly from the imaginary part of Eqs. (3.6a & 3.6b).

In the same way as the stress, the displacement field (e_x, e_y) induced by a triangular element can also be found using the Muskelishvili's potential theorem method:

$$2\mu\left(e_x^{tr} + ie_y^{tr}\right) = \kappa\phi_{tr}(z) - z\overline{\phi_{tr}'(z)} - \overline{\psi_{tr}(z)}, \tag{3.8}$$

where $\phi_{tr}'(z) = \omega_{tr}(z)$ and $\psi_{tr}'(z) = -z\omega_{tr}'(z) - \overline{\omega_{tr}}(z) - \omega_{tr}(z)$

This will give the displacement anywhere in the half-plane, resulting from the contact pressure. This time there is only one expression, because there are only two displacement components; the real part will be used to determine e_x, and the imaginary part to find e_y. Using this formulation only gives the displacement derivatives, because it is formulated on integrating the stress functions, based on Hooke's law. When performing the integral the constant of integration is unknown. The absolute displacements are therefore computed as relative displacements with respect to a

datum point very remote from the surface, where the displacement is zero or negligible. Thus, the relative displacements can be taken to be the same as the total displacements.

The formulation above evaluates the effects of one triangular pressure element loading the half-plane. The full stress and the displacement fields in the half-plane are calculated by superimposing the contributions of each individual triangle summing their effect, where *n* is the number of triangular elements used to discretise the contact pressure, i.e.:

$$\pm_{ij}^{u}(\hat{x},\hat{y}) = \sum_{k=1}^{n} \pm_{ij,k}^{tr}(\hat{x},\hat{y}) \tag{3.9a}$$

$$e_{ij}^{u}(\hat{x},\hat{y}) = \sum_{k=1}^{n} e_{ij,k}^{tr}(\hat{x},\hat{y}) \tag{3.9b}$$

where *i* and *j* can be *x* or *y*

It should also be noted that, for convenience when representing the state of stress ahead of the crack tip and to calculate the SIFs, the Mohr's circle transformation has been applied to the stresses to give the stress field relative to the rotated crack co-ordinate system ($\hat{x},\hat{y}$) along the crack line. In a similar manner the displacements can be multiplied by the rotation matrix, to express them in the rotated crack co-ordinate system ($\hat{x},\hat{y}$).

For the model in this chapter, this method is used to study the effect that a moving Hertzian pressure profile has on the cracked half-plane. However, using the linear triangular discretisation method it is possible to discretise and describe any arbitrary contact pressure relatively accurately; therefore, this method for analysing the stress and displacement fields due to contact pressure will also be used in later chapters when more complex fluid film pressures will be calculated.

3.3.3 Introducing the Crack

For the second problem sub set in the solver sequence the effect of the presence of the crack is now considered. The solution from problem (I) will be used as an input into the formulation of problem (II).

Characterised by a line of discontinuity in the stress field of the half-plane, the presence of the crack is simulated using distributed dislocations, or strain nuclei, of unknown densities along the crack length, shown in Figs.3.4a & b. This method has been well documented in the literature [55, 98], and used to solve for a multitude of different crack problems. In this thesis, however, only a description of the formulation of this method for the specific application of solving a surface-breaking, slant crack is presented.

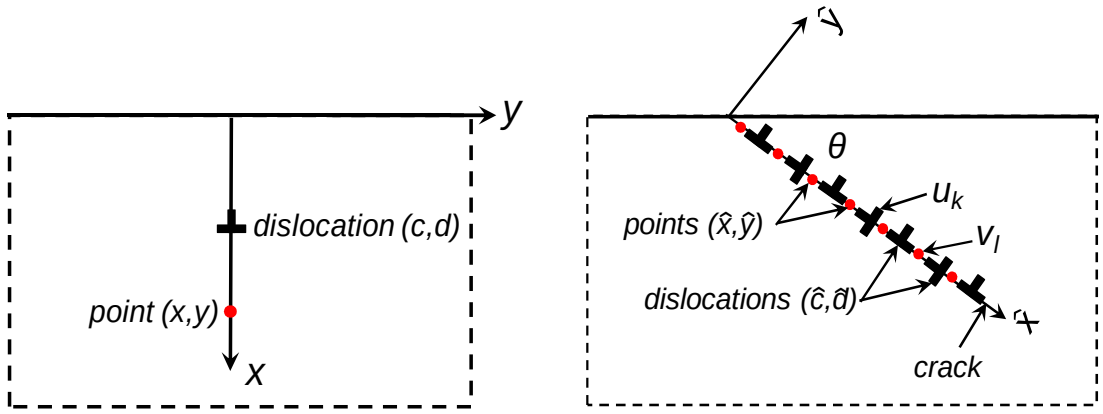


Figure 3.4 (a) Single dislcocation and single stress evaluation point (b) Climb and glide dislocations distributed along the crack length, with multiple points, or nodes where the stress is evaluated to give the solution for the full crack.

The stresses induced at a point (*x, y*) due to a single dislocation positioned at (*c, d*) can be found from the Airy stress function, which like the Muskelishivili potential is also a solution to the bi-harmonic equation, as [144]:

$$\pm_{ij}^{dd}(x,y) = \frac{2\mu}{\kappa(\kappa+1)}\left(b_x K_{xij}(x,y,c,d) + b_y K_{yij}(x,y,c,d)\right) \qquad (3.10)$$

where μ is the shear modulus of the material, κ is Kosolov's constant, b_x and b_y are the 'glide' and 'climb' components of the Burgers vector representing the distributed dislocations, and K_{xij} and K_{yij} are known influence functions that have been derived

elsewhere and are reported in Ref. [55], with two of them containing a simple Cauchy kernel and the other two being bounded.

In order to simplify the mathematical formulation of the problem, it is customary to solve with respect to a local coordinate system that is rotated to the angle of incline of the crack (θ). The Burgers vector components can be expressed in the rotated coordinate system by multiplying using the rotation matrix:

$$\begin{pmatrix} b_x \\ b_y \end{pmatrix} = \begin{pmatrix} \cos^{-} & \sin^{-} \\ -\sin^{-} & \cos^{-} \end{pmatrix} \begin{pmatrix} b_{\hat{x}} \\ b_{\hat{y}} \end{pmatrix} \tag{3.11}$$

By substituting Eq. (3.11) back into Eq. (3.10) and by applying the Mohr's circle transformation to the influence functions (K_{xij} and K_{yij}), the normal and shear components of the stress tensor due to one dislocation can be written in the rotated coordinate system in terms of the rotated Burgers vector and rotated influence functions as:

$$\pm_{\hat{y}\hat{y}}^{dd}(\hat{x},\hat{y}) = \frac{2«}{®(© + 1)}\left(b_{\hat{x}} K_{\hat{x}}^{N}\left(\hat{x},\hat{y},\hat{c},\hat{d}\right) + b_{\hat{y}} K_{\hat{y}}^{N}\left(\hat{x},\hat{y},\hat{c},\hat{d}\right)\right) \tag{3.12a}$$

$$\pm_{\hat{x}\hat{y}}^{dd}(\hat{x},\hat{y}) = \frac{2«}{®(© + 1)}\left(b_{\hat{x}} K_{\hat{x}}^{S}\left(\hat{x},\hat{y},\hat{c},\hat{d}\right) + b_{\hat{y}} K_{\hat{y}}^{S}\left(\hat{x},\hat{y},\hat{c},\hat{d}\right)\right), \tag{3.12b}$$

where $\hat{x} = \cos^{-}(x)$, $\hat{y} = \sin^{-}(x)$, $\hat{c} = \cos^{-}(c)$, and $\hat{d} = \sin^{-}(c)$, and $K_{\hat{x}}^{N}$, $K_{\hat{y}}^{N}$, $K_{\hat{x}}^{S}$, $K_{\hat{y}}^{S}$ are the transformed influence functions, that will we now refer to as kernels. If we now consider the effect of a continuous distribution of infinitesimal burgers vectors along the crack line that have densities that can be expressed as:

$$B_{\hat{x}}(\hat{c}) = \frac{db_{\hat{x}}(\hat{c})}{d\hat{c}}, \; B_{\hat{y}}(\hat{c}) = \frac{db_{\hat{y}}(\hat{c})}{d\hat{c}} \tag{3.13}$$

The stresses along the crack faces in the rotated coordinate system are given in generalised form by:

$$\begin{aligned} N(\hat{x}) &= \pm \sigma_{\hat{y}\hat{y}}^{u}(\hat{x}) + \frac{2\mu}{\kappa+1}\left(\int_0^a B_{\hat{x}}(\hat{c}) K_{\hat{x}}^{N}(\hat{x},\hat{c}) d\hat{c} + \int_0^a B_{\hat{y}}(\hat{c}) K_{\hat{y}}^{N}(\hat{x},\hat{c}) d\hat{c} \right) = 0 \quad 0 < \hat{x} < a \\ S(\hat{x}) &= \pm \sigma_{\hat{x}\hat{y}}^{u}(\hat{x}) + \frac{2\mu}{\kappa+1}\left(\int_0^a B_{\hat{x}}(\hat{c}) K_{\hat{x}}^{S}(\hat{x},\hat{c}) d\hat{c} + \int_0^a B_{\hat{y}}(\hat{c}) K_{\hat{y}}^{S}(\hat{x},\hat{c}) d\hat{c} \right) = 0 \quad 0 < \hat{x} < a \end{aligned} \tag{3.14}$$

It should be noted here that Eq. (3.14) is a generalised case that's valid when the crack is fully open and both sets of dislocations are distributed along the entire length of the crack, using the boundary conditions expressed in Eq. (3.2a). This means that the integration lengths for both $N(\hat{x})$ and $S(\hat{x})$ are the same, however when the crack becomes partially closed $N(\hat{x})$ and $S(\hat{x})$ will be evaluated over different lengths, where

$N(\hat{x})$ is only evaluated over the open portion of the crack, $a_{op} < \hat{x} < a$, and the boundary conditions in Eq. (3.2b) are applied. When the open part of the crack then tends to zero, $a_{op} = 0$, then $N(\hat{x}) = 0$.

Another important characteristic of this formulation is that the crack opening displacement, $e_{\hat{y}}^{dd}(\hat{x})$, and the crack slip displacement, or tangential displacement, $e_{\hat{x}}^{dd}(\hat{x})$, at any location within the opened and closed (for the slip displacement) portion of the crack can be directly obtained by integrating the climb or glide dislocation density respectively between the crack tip and the location of interest along the crack, $\hat{x}$, where:

$$B_{\hat{y}}(\hat{c}) = -\frac{de_{\hat{y}}^{dd}(\hat{c})}{d\hat{c}} \Rightarrow e_{\hat{y}}^{dd}(\hat{x}) = -\int_{a}^{\hat{x}} B_{\hat{y}}(\hat{c})\, d\hat{c}$$
$$B_{\hat{x}}(\hat{c}) = -\frac{de_{\hat{x}}^{dd}(\hat{c})}{d\hat{c}} \Rightarrow e_{\hat{x}}^{dd}(\hat{x}) = -\int_{a}^{\hat{x}} B_{\hat{x}}(\hat{c})\, d\hat{c}. \quad (3.15)$$

When the crack is partially closed, the open length of the crack, the parameter a_{op} and the exact point at which the crack closes is an unknown. The value of parameter is found iteratively using the following condition:

$$-\int_{a_{op}}^{a} B_{\hat{y}}(\hat{c})\, d\hat{c} = 0 \quad (3.16)$$

This integral condition ensures that the normal displacement is zero at the lower limit of integration a_{op} (or the end of the open part of the crack), and to satisfy this condition an imposed value of the open length of the crack a_{op} is iterated upon until the condition in Eq. (3.16) is satisfied. A second convergence condition is also checked, that the displacement at all points before the end of the open length of the crack, a_{op}, are positive. This iterative process is applied to this model using the iterative routine known as the bisection method [146].

3.3.4 Combining the Crack and Stress Field to Solve the Distributed Dislocations

The expressions for the stress field of the crack (problem (II)) and the stresses caused by the contact load (problem (I)) have been derived. They will now be combined and formulated so that the distributed dislocation technique is used to evaluate the unknown dislocation densities which satisfy equilibrium and compatibility of displacements everywhere within the cracked domain in the presence of the applied contact loading. The boundary conditions for crack opening and closing are first of all imposed by substituting Eq. (3.14) into Eq. (3.3), which gives:

$$N(\hat{x}) = \pm^{u}_{\hat{y}\hat{y}}(\hat{x},0) + \frac{2\alpha}{\beta(\gamma+1)}\left(\int_0^a B_{\hat{x}}(\hat{c})K^N_{\hat{x}}(\hat{x},\hat{c})d\hat{c} + \int_{a_{op}}^a B_{\hat{y}}(\hat{c})K^N_{\hat{y}}(\hat{x},\hat{c})d\hat{c}\right) = 0 \qquad a_{op} < \hat{x} < a$$

$$S(\hat{x}) = \left(\pm^{u}_{\hat{x}\hat{y}}(\hat{x},0) + fH(\hat{x}-a_{op})\pm^{u}_{\hat{y}\hat{y}}(\hat{x},0)\right) +$$
$$\frac{2\alpha}{\beta(\gamma+1)}\left(\int_0^a B_{\hat{x}}(\hat{c})\left(K^S_{\hat{x}} + fH(\hat{x}-a_{op})(\hat{x},\hat{c})K^N_{\hat{x}}\right)d\hat{c} + \int_{a_{op}}^a B_{\hat{y}}(\hat{c})\left(K^S_{\hat{y}}(\hat{x},\hat{c}) + fH(\hat{x}-a_{op})(\hat{x},\hat{c})K^N_{\hat{y}}\right)d\hat{c}\right) = 0 \quad 0 < \hat{x} < a \tag{3.17}$$

The presence of Cauchy kernels, which become singular as $\hat{x}$ tends to $\hat{c}$, means that Eq. (3.17) cannot be solved in closed form. Therefore, a robust numerical quadrature scheme is required to obtain an accurate but approximate solution. The interval of integration is normalised, where two different normalisation expressions are used because the shear stress $S(\hat{x})$ will always be evaluated over the full crack length (0 < *x* > *a*), therefore they are normalised by:

$$v = \frac{2\hat{x}}{a} - 1, \qquad 0 < \hat{x} < a$$

$$u = \frac{2\hat{c}}{a} - 1, \qquad 0 < \hat{c} < a \tag{3.18}$$

The normal stress effects $N(\hat{x})$ will be evaluated over the length (a_{op} < *x* > *a*), therefore they are normalised by;

$$\bar{v} = \frac{2\left(\hat{x} - a_{op}\right)}{a - a_{op}} - 1, \qquad a_{op} < \hat{x} < a$$

$$\bar{u} = \frac{2\left(\hat{c} - a_{op}\right)}{a - a_{op}} - 1, \qquad a_{op} < \hat{c} < a \tag{3.19}$$

When $a_{op} = 0$, Eq. (3.18) is the same as Eq. (3.19)

This gives the integral equations in normalised form as:

$$\pm^{u}_{\hat{y}\hat{y}}(\bar{v}) = \frac{2\text{«}}{\text{®}(\text{©}+1)}\left(\int_{-1}^{1} B_{\hat{x}}(u) K^{N}_{\hat{x}}(\bar{v},u)\,du + \int_{-1}^{1} B_{\hat{y}}(\bar{u}) K^{N}_{\hat{y}}(\bar{v},\bar{u})\,d\bar{u}\right) \qquad -1 < \bar{v} < 1$$

$$\pm^{u}_{\hat{x}\hat{y}}(v) + fH\left(v - \frac{a_{op}}{a}\right)\pm^{u}_{\hat{y}\hat{y}}(v) = \frac{2\text{«}}{\text{®}(\text{©}+1)}.$$

$$\left(\int_{-1}^{1} B_{\hat{x}}(u)\left((K^{S}_{\hat{x}}(v,u) + fH\left(v - \frac{a_{op}}{a}\right)K^{N}_{\hat{x}}(v,u)\right)du + \int_{-1}^{1} B_{\hat{y}}(\bar{u})\left(K^{S}_{\hat{y}}(v,\bar{u}) + fH\left(v - \frac{a_{op}}{a}\right)K^{N}_{\hat{y}}(v,\bar{u})\right)d\bar{u}\right) = 0 \quad -1 < v < 1 \tag{3.20}$$

To evaluate the singular integrals it is necessary to express the dislocation densities as the product of the bounded functions, $\text{¤}_{\hat{x}}(u), \text{¤}_{\hat{y}}(\bar{u})$, and a weight function, $\mu(u), \mu(\bar{u})$ [147], such that:

$$B_{\hat{x}}(u) = \text{¤}_{\hat{x}}(u)\mu(u); \;\; B_{\hat{y}}(\bar{u}) = \text{¤}_{\hat{y}}(\bar{u})\mu(\bar{u}) \tag{3.21}$$

where $\text{¤}_{\hat{x}}$ and $\text{¤}_{\hat{y}}$ are two unknown bounded functions and, $\mu(u)$ and $\mu(\bar{u})$ are the regular fundamental functions; by assuming a bounded (at the crack mouth and at the

opening length for glide and climb dislocations respectively) and singular (at the crack tip) solution for both glide and climb dislocations, the regular functions can be written as $\mu(u)=(1-u)^{-1/2}(1+u)^{1/2}$ and $\mu(\bar{u})=(1-\bar{u})^{-1/2}(1+\bar{u})^{1/2}$. A Gauss-Jacobi type quadrature is applied to the discrete form of the Eqs. (3.17): a series of integration (u_k) and collocation (v_i) points are used to discretise the crack length, a, and the open length, $a_{op}<\hat{x}<a$ into a series of nodes using quadrature formulae for bounded and singular Cauchy kernels [55] which produce a set of $2n$ simultaneous equations with $2n$ unknowns. Two sets of offset nodes are used to evaluate the crack because the stresses are evaluated on one set of nodes, the collocation points, and the dislocation densities are evaluated on the other set of nodes, the integration points. This is because the influence functions that are used, (K_{xij} and K_{yij}) become singular if the dislocation densities and the stresses are evaluated at the same nodal points, i.e. if $\hat{x}-\hat{c}=0$.

In particular, by discretising the normalised coordinate sets using the following distribution of nodes along the crack length:

$$u_k,\bar{u}_k=\cos\left(\frac{2k-1}{2n+1}®\right);\qquad k=1,...,n$$
$$v_i,\bar{v}_i=\cos\left(\frac{2i}{2n+1}®\right);\qquad i=1,...,n \tag{3.22}$$

and combining the integrals with the appropriate weight functions, we obtain:

$$\frac{2\alpha}{\beta(\gamma+1)}\sum_{k=1}^{n}\left[\begin{array}{l}\dfrac{2\beta(1+u_k)}{2n+1}\varphi_{\hat{x}}(u_k)K_{\hat{x}}^{N}(\bar{v}_i,u_k)+\\ \dfrac{2\beta(1+\bar{u}_k)}{2n+1}\dfrac{a_{op}}{a}\varphi_{\hat{y}}(\bar{u}_k)K_{\hat{y}}^{N}(\bar{v}_i,\bar{u}_k)\end{array}\right]=\pm_{\hat{y}\hat{y}}^{u}(\bar{v}_i) \qquad i=1,\ldots,n \qquad (3.23a)$$

$$\frac{2\alpha}{\beta(\gamma+1)}\sum_{k=1}^{n}\left[\begin{array}{l}\dfrac{2\beta(1+u_k)}{2n+1}\varphi_{\hat{x}}(u_k)\left\{\begin{array}{l}K_{\hat{x}}^{S}(v_i,u_k)+\\ f H\left(v_i-\dfrac{a_{op}}{a}\right)K_{\hat{x}}^{N}(v_i,u_k)\end{array}\right\}\\ +\dfrac{2\beta(1+\bar{u}_k)}{2n+1}\dfrac{a_{op}}{a}\varphi_{\hat{y}}(\bar{u}_k)\left\{\begin{array}{l}K_{\hat{y}}^{S}(v_i,\bar{u}_k)+\\ f H\left(v_i-\dfrac{a_{op}}{a}\right)K_{\hat{y}}^{N}(v_i,\bar{u}_k)\end{array}\right\}\end{array}\right]=\left[\begin{array}{l}\pm_{\hat{x}\hat{y}}^{u}(v_i)+\\ f H\left(v_i-\dfrac{a_{op}}{a}\right)\pm_{\hat{y}\hat{y}}^{u}(v_i)\end{array}\right] i=1,\ldots,n$$

(3.23b)

Eqs. (3,23a & b) can be easily solved using a standard computer library routine, such as LU decomposition, to find the unknown distributions $\varphi_{\hat{x}}(u),\varphi_{\hat{y}}(\bar{u})$. This allows the unknown dislocation densities to be computed and stress and displacement fields induced by the surface loading to be evaluated everywhere within the solid. Mode I and Mode II stress intensity factors can also be directly evaluated using Krenk's interpolation formulae [148] where;

$$\varphi_i(1)=\frac{2}{2n+1}\sum_{i=1}^{n}\left[\cot\left(\frac{2i-1}{2n+1}\frac{\beta}{2}\right)\times\sin\left(\frac{n}{2n+1}(2i-1)\beta\right)\varphi_i(u_i)\right] \qquad (3.24)$$

The stress intensity factor can then be found, where *i = I, II* denotes the mode, normal or shear:

$$K_i = 2\sqrt{2}\sqrt{®a}\,\frac{«}{© + 1}¤_i(1) \tag{3.24}$$

3.4 Validation

The two elements of solution formulated in the previous section will be first individually compared with, and validated against, analytical and existing solutions from the literature. First we consider the classical two-dimensional frictionless Hertzian contact problem and the Muskelishvili piece-wise linear triangular discretisation of the Hertzian contact pressure. The results obtained computing the stress field using the discretised form of the pressure distribution can be compared with the known surface and sub-surface stress distributions and the surface displacement values obtained from the analytical solution and available in the literature [140, 149]. Let us consider first the three stress components at the surface (*xx, yy and xy*), shown on Figs. 3.5 & 3.6; the abscissa is normalised by the contact semi-width, *b*/2, and the stresses by the maximum Hertzian pressure (p_{Hmax}). The stress values have also been inverted so that rather than being equal and opposite to the applied pressure at the surface they can directly be compared to the applied pressure. From the figure it can be seen that the values obtained from the semi-analytical Muslelishvili potential formulation are in perfect agreement with the analytical solution. The stresses in the *x* and direction are equal to

the applied Hertzian pressure and, because the contact is frictionless, the shear stress at the surface is zero.

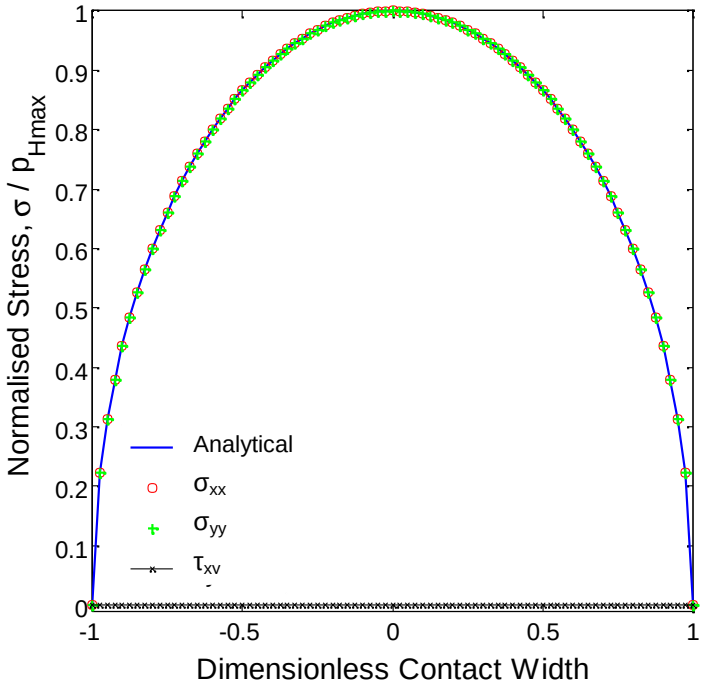
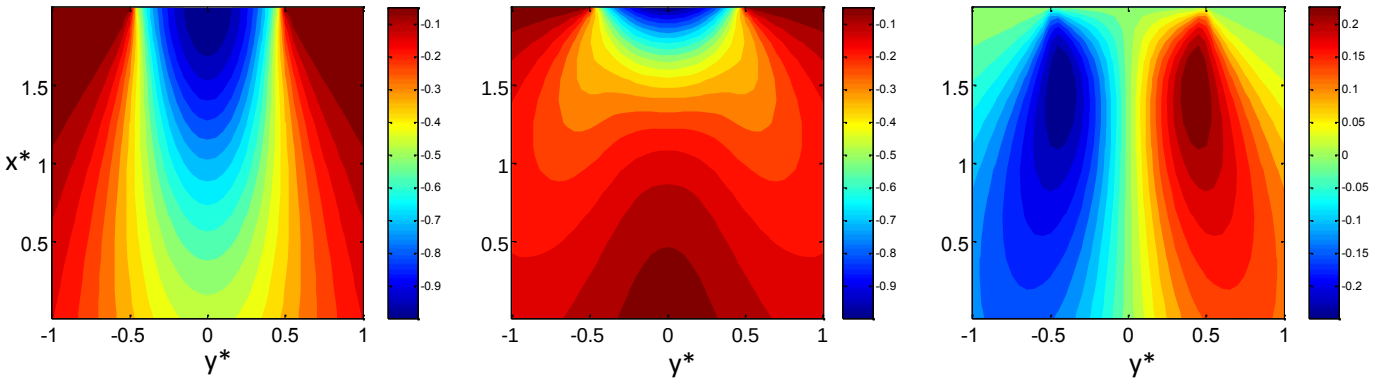


Figure 3.5.Stress values solved with Muskelishvili's potential compared with the analytical solution

Considering now the subsurface stress plots, the distributions of the stresses shown in Fig. 3.6a - c agree very well with the solutions from the literature, [144].



(a) (b) (c)

Figure 3.6 Subsurface stress plots, normalised by σ/p_{hmax} calculated using Muskelishvili's potential (a) σ_{yy} (b) σ_{xx} (c) τ_{xy}

To show the capabilities of the numerical code to deal with shear tractions as well as normal pressures, a frictional sliding problem is now considered; for a value of the friction coefficient at the surface of 0.25, a non-zero shear stress at the surface is retrieved. It is expected that the shear stress at the surface is equal to the normal stress multiplied by the friction coefficient, from Coulomb's law [142]; the plot in Fig. 3.6 demonstrates again that the Muselishvili potential theorem applied to a piece-wise distribution of surface tractions provides a very good agreement with the analytical solution (as long as the number of triangles is greater than about 25 - here 60 elements are used).

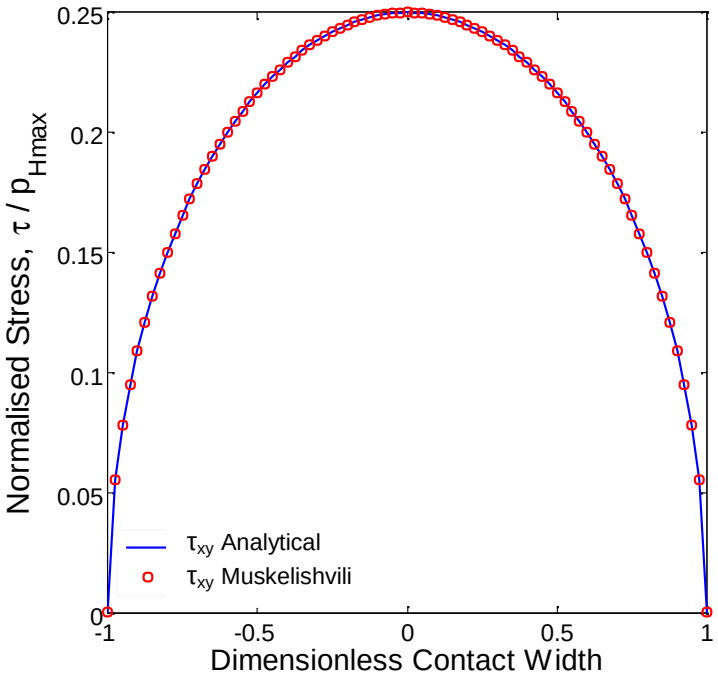


Figure 3.7. Shear stress values solved with Muskelishvili's potential, with friction, compared with the analytical solution

Although the displacement due to the Hertzian contact is not used for the analysis of the crack presented in this chapter, in order to have a complete validation of all aspects of the method a comparison between the surface displacement obtained from the application of the Muskelishvili potential theorem to the problem discretised using the piecewise linear triangular distribution of tractions, and the analytical solution is presented. The displacement components are plotted relative to the displacement at the centre of the contact in Fig. 3.8.

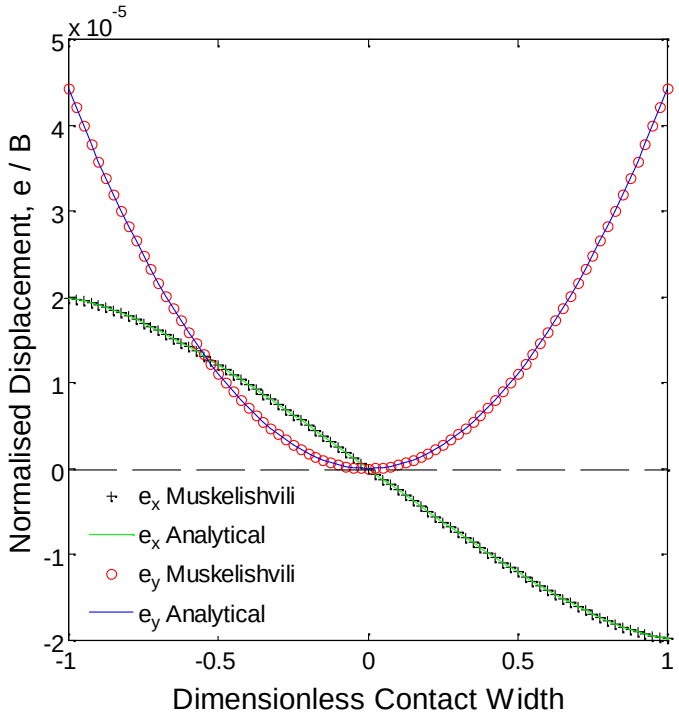


Figure 3.8. Relative displacement solved with Muskelishvili's potential compared with the analytical solution

As with the stress values, the displacement values obtained from the Muskelishvili potential theorem show a very good agreement with the analytical values.

To validate the results obtained using the distributed dislocation technique applied to the slant crack, the solution has been compared with the solution presented by Hills and Nowell [98] for the case of an applied remote tension to the cracked half-plane. The comparison between the results obtained in [98] and those computed by the author is shown in Fig.3.9 The angle of inclination of the crack θ is incremented between 0° (vertical crack) to 90° and the stress intensity factors KI and KII are

computed and compared. The close match of the results shows that the implementation of the technique has been carried out satisfactorily and that the predicted K_I and K_{II} values computed using the dislocation densities are reliable.

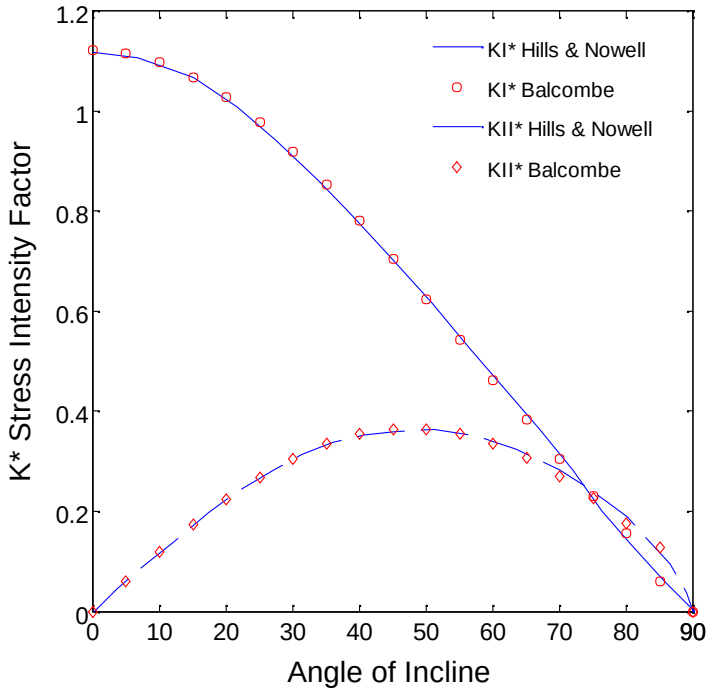


Figure 3.9. Stress intensity for a slant crack, of varying angle, under uniform tensile stress

It should be noted that after about *75*° inclination angle, and, more in general, when θ becomes very large, some precaution need to be used to ensure accuracy due to the fact that the interaction between the surface tractions and the dislocations deployed along the crack renders the solution to the problem slightly less stable.

The validity of the assumption that is used in this thesis, i.e. that the crack can be expressed using a line of zero thickness is put to the test by now considering a crack

with a non-zero thickness, namely a high aspect ratio slot configuration fully described in two-dimensions. The formulation of the slot is derived using the DDT method described in this chapter; however the derivation is more complex. The derivation will not be described here, as it is convoluted but the principles have already been described in [150] in detail. To summarise, the dislocations are distributed not along a 1D line as in the case of a crack but they are distributed along the curvilinear path of the outline of a slot, shown in red on the Fig 3,10. The same boundary conditions are used for the surface of the slot to, in effect; “punch out” this material from the half plane by creating a free surface and the corresponding zero tractions. The same general methodology is employed, however the quadrature scheme used to evaluate the integral equations is different, because when evaluating the slot there is no longer a singularity in the stress field because the crack tip is replaced by a blunted radius. This blunted radius is something that is seen in real cracks and known as crack tip plasticity, the radius can be calculated from the stresses induced by a load cycle. However the 2D model is more complex to solve and requires far more node points to converge, 300 instead of 30. This is because of the very high aspect ratio that is needed, a considerable number of nodes have to be distributed before a single node is located on the end radius, because of the discretisation scheme, where the end radius needs more than a single point to be accurately resolved.

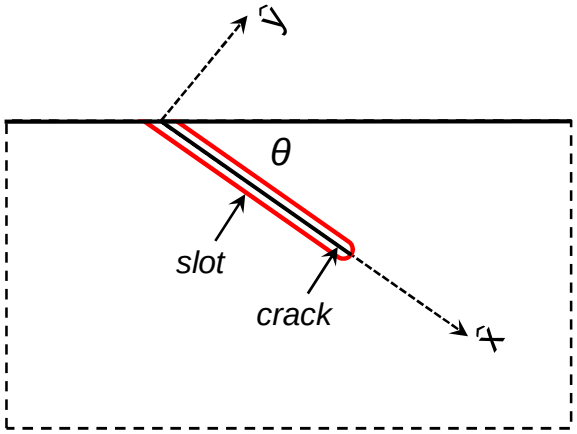


Figure 3.10. Schematic of the slot model

The thickness of the slot is varied to investigate the sensitivity of the results to this parameter and a comparison is drawn. The quantity that is chosen for comparison is the dimensionless displacement (displacement/crack length) of the crack faces in the normal and shear directions, where the loading condition that is used is a tensile, remote stress that is acting to open the crack with a uniform intensity in the horizontal direction. The crack is inclined from the horizontal plane by an angle of 25° to reflect the angle of inclination used in the analysis, and the model is solved using 250 node points, this high number of nodes is needed to resolve the small radius required at the tip of the slot model.

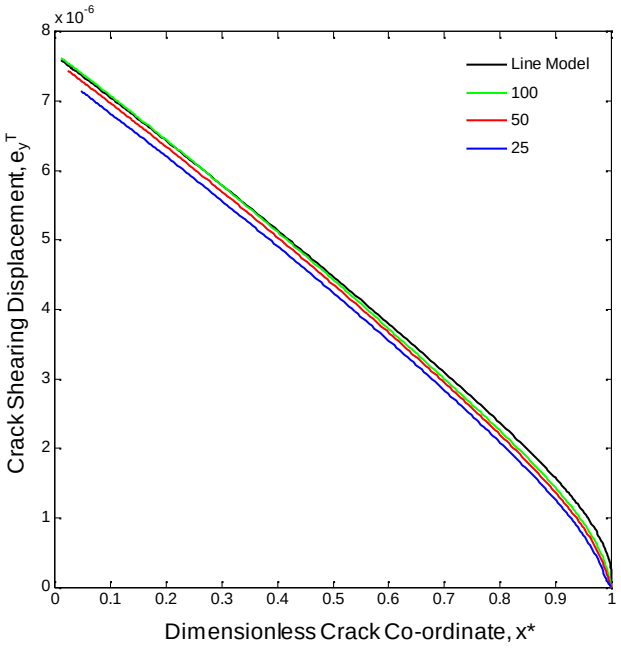


Figure 3.11 Comparison of the opening displacement for different aspect ratio slots

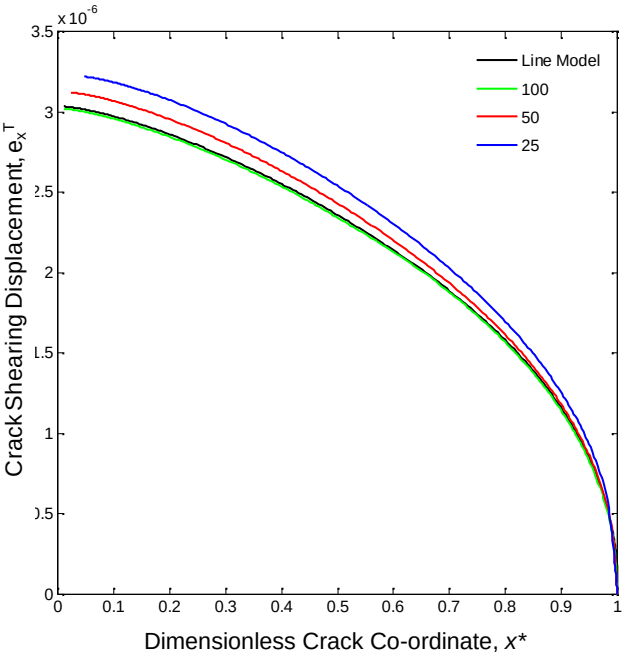


Figure 3.12 Comparison of the shearing displacement for different aspect ratio slots

The results expressed in the Figs 3.11 & 3.12, demonstrate the effect of changing the aspect ratio of the crack, where the aspect ratio is defined as the crack length/crack width. The same problem has also been solved using the 1D crack model, and this is also plotted on the graph. The comparison between the different aspect ratio analyses shows that as the crack becomes thin, when the aspect ratio is >100, the 2D crack model behaves the same as if it's modelled using the 1D line model. This result can be taken to be true because the displacement is calculated directly from the variable that is being evaluated in the semi-analytical method, the dislocation density. Therefore if the calculated displacement is the same for both the 2D and 1D crack it follows that everything else, such as the stress field and the stress intensity factors will be the same because they are also calculated as a function of the dislocation density.

The implications of using the slot model are considerable; the slot model for this simple analysis, with this very small crack tip radius requires around 300 nodes to converge, because the curved radius at the tip needs to have a considerable number of points to accurately resolve its shape. The 1D model however converges with 30 nodes, which means that the solution time is vastly reduced for the model using the 1D case. In addition, when the 2D crack is used the crack no longer has a singularity at the tip, so the well-known method from the literature for quantifying the propensity of a crack to grow using the stress intensity factors is no longer valid and an alternative method would need to be derived. With these points in mind, the 1D model will be used for all the crack analyses in this study.

3.5 Results and Discussion of a dry contact RCF test case

The analysis presented in the results section of this chapter describes the simulation of a Hertzian line contact passing over a dry, cracked, half-plane. The half-plane material properties are given by $E = 210\ GPa$, and $\nu = 0.3$. The friction coefficient applied to the surface of the half-plane and the crack faces is $f = 0.25$, inducing a shearing effect in both the crack and contact interfaces. at the surface. The ratio between contact width b and the crack length a is $b/a = 2$.

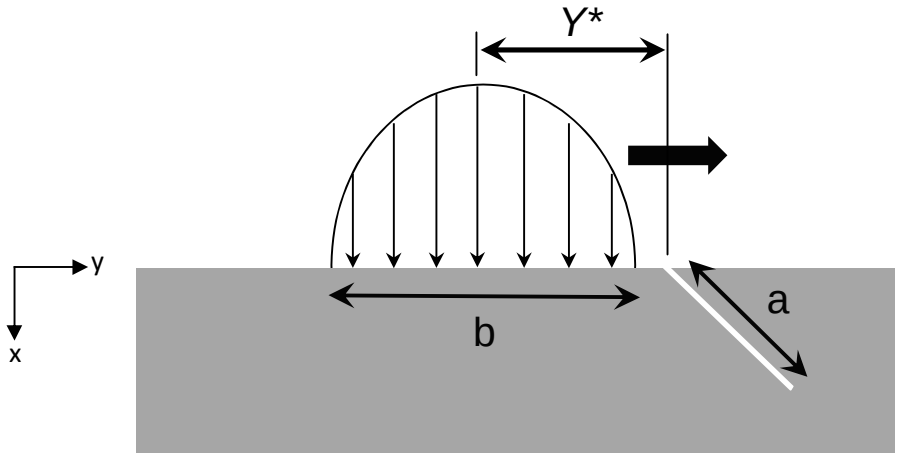
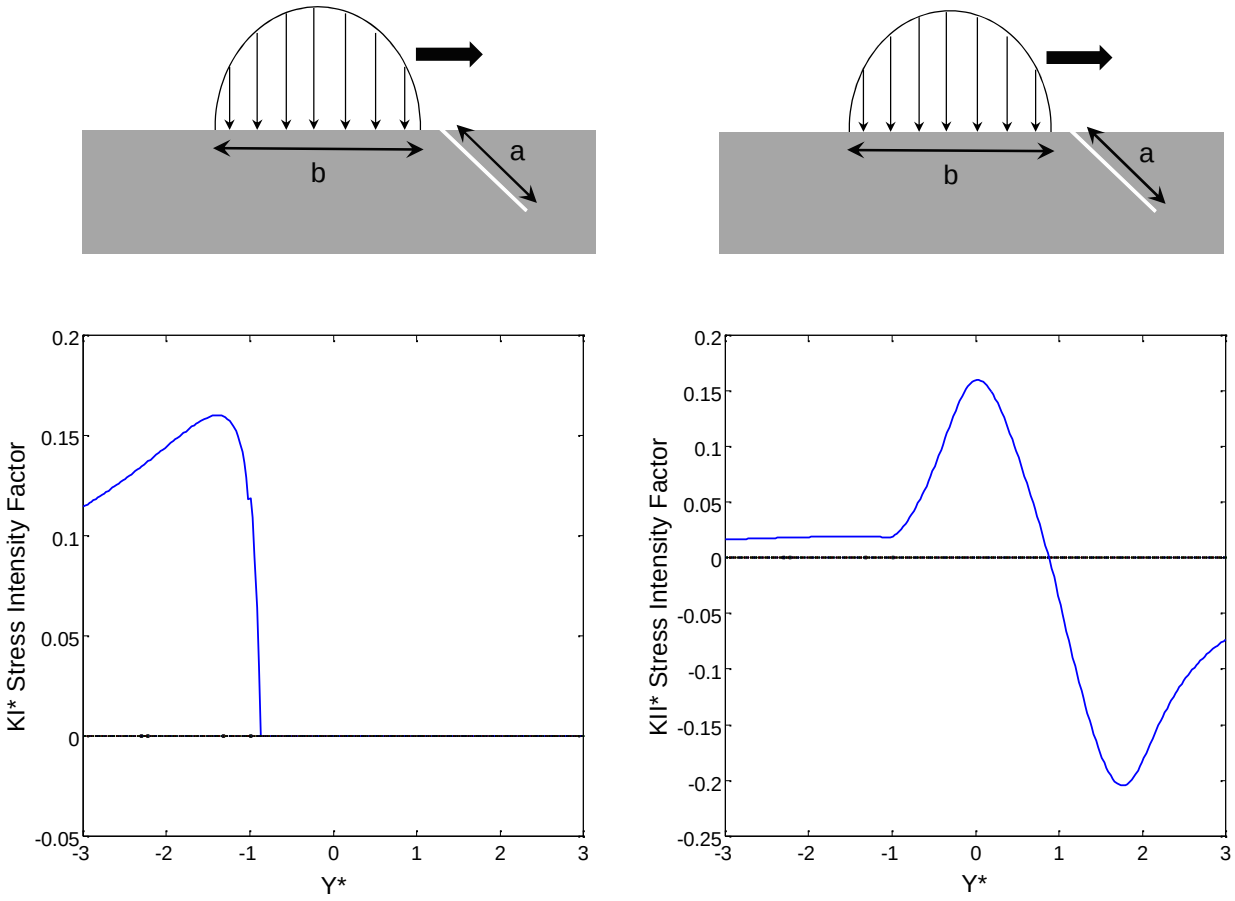


Figure 3.13 Schematic of the Hertzian problem

The evolution of the stress intensity factors, *KI* and *KII*, obtained when the line contact traverses the crack is shown in Figs. 3.14a and 3,14b, where the quantity on the x-axis *Y** is the dimensionless, ($Y^* = y/a$) offset between the crack mouth and the centre of the contact. Considering *KI* first, shown in Fig. 3.14a, as the load approaches the crack, i.e. $-3 < Y^* < -1.5$, the shearing effect at the surface produces crack opening, inducing a positive *KI* SIF. This is a direct consequence of considering the presence of friction and

shearing tractions acting at the surface. However, once the crack enters the contact patch, $Y^* > -1$, the compressive loading and the shearing effect immediately close the crack and therefore *KI* tends to zero (note that when the crack is closed, *KI* is set to zero as negative values of *KI* are not considered as possible source of crack propagation and are therefore neglected). For the second part of the loading cycle, $Y^* > 0$, the crack remains closed and no tensile SIF is induced because the crack is effectively contained within a fully compressive stress field.

Considering now K_{II}, during the approaching phase, i.e. $-3 < Y^* < -1.5$, the shear stress is positive this effect in KII like the effect in KI is brought about by the shearing effect at the surface combined with the compressive load pressing down one side of the crack, and therefore one crack face, generating a net shearing effect at the crack tip. Once the crack enters the contact this shearing effect continues and rises rapidly until the majority of the load is transferred to the other side of the crack. This triggers a change in the trend, and as the load is being applied across the crack the shearing direction begins to change and then switches from positive to negative. Once the crack has passed through the contact, $Y^* > 1$, the effect of the application of the surface load gradually fades away and the stress intensity factor tends slowly to zero (this can easily be demonstrated by enlarging the domain of analysis).



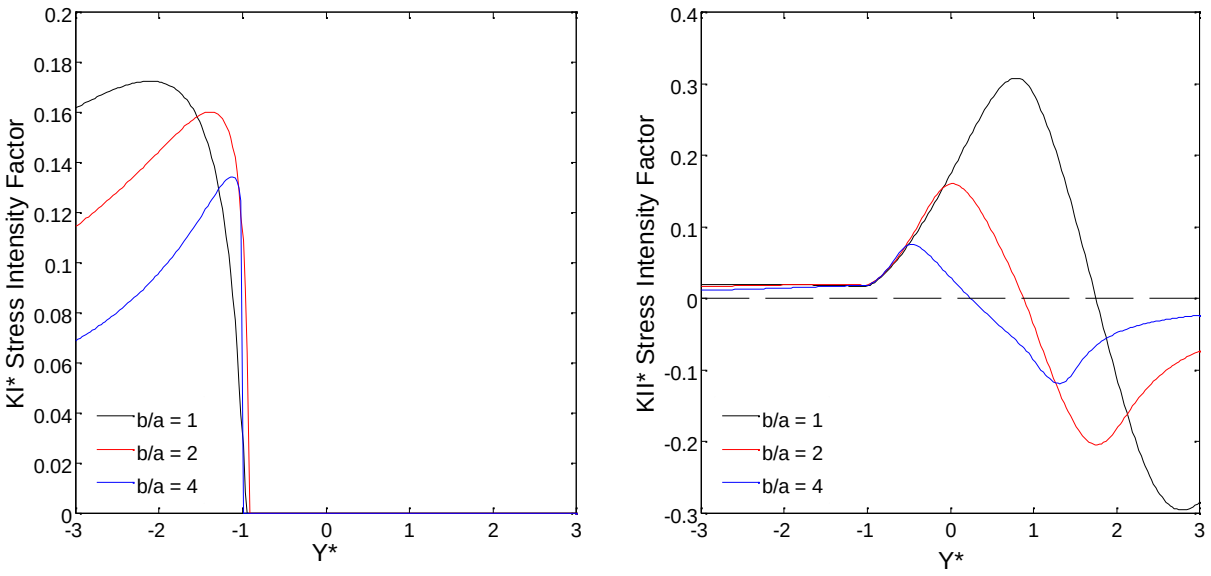
(a) (b)

Figure 3.14 Dimensionless SIF histories (a) *KI* (b) *KII*

The important point and the emphasis of this analysis is that without the presence of fluid inside the RCF crack, closure happens immediately after the crack enters the contact patch. Therefore, the tensile SIF becomes zero, and K_{II} becomes the dominant SIF. The K_I values are non-zero when the load approaches the crack, but the magnitude of the SIF is strongly influenced by the friction coefficient applied to the surface. The

analyses carried out using the present loading conditions the geometry suggest that the RCF crack, if it were to be propagated, it would propagate under Mode II.

Let us now consider the effect of increasing the crack length on both mode I and mode II SIFs. The results presented in Fig.3.15a and 3.15b show that the effect of increasing the crack length is to increase the magnitude of the maximum values obtained for both K_I and K_{II}; this in turn causes an increase in the severity induced by the presence of the crack, at least for the limited range of crack lengths, *a*, considered here.



(a) (b)

Figure 3.14 Comparison of the dimensionless SIF histories for different crack lengths (a) *KI* (b) *KII*

Furthermore, in the case of *KII* the trend is also affected by the crack length; the transition point for the SIF from positive to negative is strongly influenced by the crack

length: the shorter the crack length the earlier the transition occurs. This can be attributed to the fact that, since the crack is inclined at 25° from the vertical axis,, as the crack length increases it takes longer for the majority of the load to be transferred across to the opposite side of the crack; therefore, this delays the reversing the shearing direction.

3.6 Summary

A dry RCF model has been formulated and presented; the formulation has been validated and some example problems have been discussed. The lack of any tensile loading on the crack faces means that the dominant fatigue mechanism for this case is shear; this is shown by the larger range in *KII*, mode II stress intensity factor. Without a tensile loading mechanism, opening is only induced by the remote surface loading during its approach towards the crack and its magnitude is important only if a relatively high friction coefficient is used to characterise the contact interactions between the rolling element and the half-plane.

Chapter 4

Hydrodynamic Crack Model: Introducing Fluid/Solid Coupling

4.1 Introduction

The previous chapter introduced the application of modelling methods based on fracture mechanics to that of solving an RCF crack problem. This chapter develops the model outlined in chapter three and introduces the concept of combining the already developed solid solver based on fracture mechanics with a fluid solver based on formulating the fluid flow in the crack and between the contacting bodies using the Reynold's equation. This will enable the model to accurately account for the presence of a lubricant in the RCF problem. This chapter describes a section of work published by the author, where sections of text and the results have been used directly, the published article is available here [151].

In this chapter a novel approach for modelling the crack passing through a hydrodynamically lubricated (HL) contact is presented. The model captures the interaction between the fluid pressure and the solid deflection along the crack faces using a coupled finite volume and distributed dislocation solver. The model addresses some of the assumptions made by researchers who have tackled this problem in the past to shed light on the mechanisms which govern crack propagation in a lubricated contact. It shows that by linking the fluid behaviour (flow and pressure) and the elastic deflections it is possible to overcome one of the main limitations of more classical uncoupled models [3, 4], which rely on having to assume and then prescribe the fluid pressure at the crack mouth and/or the fluid pressure gradient in the crack during the contact loading cycle.

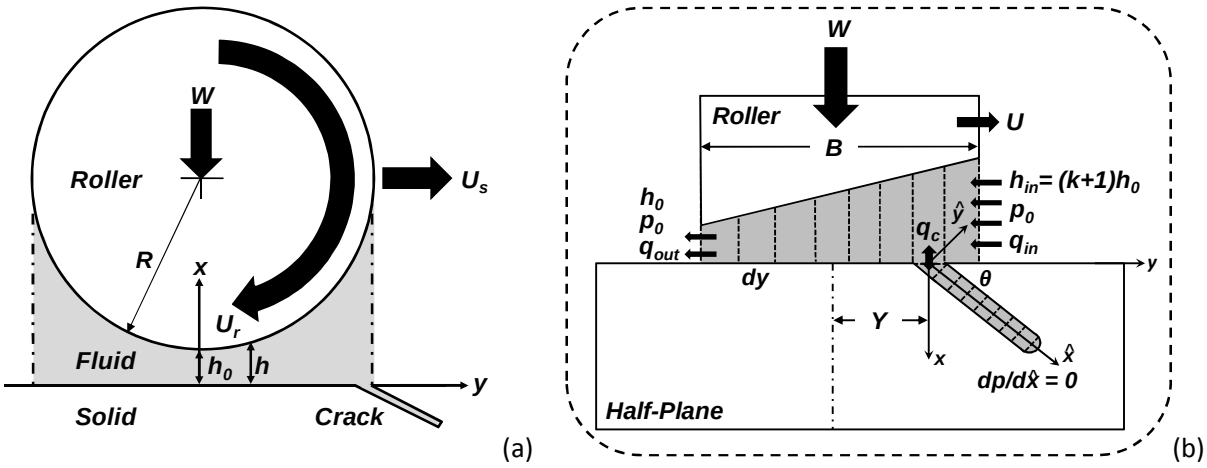


Figure 4.1 – Schematics: (a) the system under investigation and (b) the equivalent wedge geometry. In Figure 1(b) the finite volumes discretisation of the fluid domain is also shown.

A schematic of the 2D problem to be considered in this chapter is shown in Fig. 4.1(a). The model is a simplified roller bearing in contact with a cracked lubricated body, where the components are of similar materials. It has been approximated by considering a cracked semi-infinite, elastic body loaded by a cylindrical roller where the roller and the cracked body are separated by a pressurised lubricant film.

The roller is further simplified using a flat convergent surface (see Fig. 4.1(b)) to reduce the complexity of the shape of the fluid film at the contact interface, to that of a hydrodynamic wedge. Although the surface film in this case is simplified, it allows the author to investigate the fluid/solid interaction within the crack by removing the need to assume the fluid pressure or the fluid pressure gradient in the crack film. As a first approximation, this could be considered analogous to neglecting the divergent section of the roller, where the fluid would experience cavitation, as demonstrated by the Sommerfeld solution [152]. Throughout this chapter, the length of the hydrodynamic wedge B, the convergence gradient, K, and the load, W, are imposed but the minimum film thickness, h_{in}, and the fluid pressure, p, are calculated from hydrodynamic lubrication theory. The pitch of the wedge is chosen to generate a pressure profile similar to that of the half-Sommerfeld solution for a roller on a wetted plane characterised by a radius, R. Equivalence between the hydrodynamic wedge and the half-Sommerfeld solution is drawn by matching the load support from the fluid film pressure, W (see Section 3).

The following simplifying assumptions are made when formulating the problem, they include the assumptions applied in Chapter three and additional assumptions applied to the fluid solution:

1. The solid model obeys linear elasticity;
2. The crack surface and outer surfaces are perfectly smooth;
3. The problem can be modelled in 2D;
4. The deformation of the surface of the cracked body does not affect the hydrodynamic solution at the roller/half-plane interface;
5. The fluid domain is always fully flooded;
6. The lubricant is isoviscous and Newtonian.

Assumptions (1-3) have already been justified in chapter three; therefore, assumptions (4-6) will be addressed here. Assumption (4) is valid only in the case of a lightly loaded contact; this limitation will be addressed in the subsequent chapters. Assumption (5) combines two sub-assumptions: (a) that the contact at the surface is working in the fully flooded regime (which is likely to be true in rolling element bearings but unlikely in wet wheel rail contacts) (b) that the crack is totally filled with fluid prior to entering the contact. There is some experimental evidence for this latter assumption in wheel rail contacts [153] although there is no data available for oil lubricated rolling element bearings. Assumption (6) is not true for bearings lubricated with mineral oils; however it

is valid for wheel rail contacts where the “lubricant” is water. This assumption will be addressed in the subsequent chapters.

4.2 Modelling Strategy and Formulation

The model is composed of an inclined crack (inclined at 20° from the horizontal plane), loaded by a convergent hydrodynamic wedge, that is fully flooded in the HL regime. The crack is expressed using LEFM and is assumed to have a singularity at the tip; this also means it is assumed to be infinitesimally thin when unloaded. The transient response of the elastic solid induced during the loading is ignored because of the difference in the time scale required to capture the elastodynamics (<*1E-8* s) and the hydrodynamics (<*1E-2* s). Therefore only the transient fluid effects are considered. At each time-step; that is characterised by a unique position of the crack in the contact, the solution is based on finding the equilibrium state between the fluid pressure and the crack opening. This equilibrium is found through an iterative algorithm, where the shape of the crack and the fluid pressure are updated until the rate of change, or the derivative, of both tend to zero. The transient nature of the fluid pressure is captured by incorporating the time derivative of the film shape into the solution, d*h*/d*t*. This time-dependant, history dependant variable introduces a non-linearity to the solver, which means that the solution at each time step depends on the solution at the previous time step and the overall solver configuration is no longer quasi-static or explicit.

The modelling strategy is first to divide the contact loading cycle into a series of discrete time steps, where each time step is defined by the position of the crack in the contact; then at each time step, the lubricant pressure and the crack shape are evaluated. At each of the incremental time-steps, t, two independent algorithms; a fluid solver based on a finite volume representation of the Reynolds' equation [154] and an elastic solid solver based on the distributed dislocation technique [55] are coupled at the liquid/solid interface. The coupling strategy is shown in Fig. 4.2 and a flow chart of the step-by-step implementation of the coupling of the algorithms is reported in Appendix A. This type of solver coupling is known as an extrusion coupling, where the two solvers are segregated and coupled through the transfer of coupling variables, fluid pressure and solid displacement in this case. The values of these variables are transferred between the different solvers, fluid and solid, at the interface where the two solvers interact. Each solver has a unique mesh; therefore an interpolation function must be used to adapt the meshes. The interaction between the two algorithms is defined using an iterative scheme that; within each time step, imposes the extrusion coupling and transfers information between the solvers, where both are updated until the error converges below a pre-defined, relative tolerance.

The error is quantified by the sum of the change of the lubricant pressure inside the crack, $dp(a)/dL$ at all the nodes, and the sum of the change of the film shape inside the crack, $dh(a)/dL$ at all the nodes, in each iteration, where L is the iteration number. It is important to note here that the solution contains time steps, t, where the crack position is updated against time which gives time derivatives, for example dh/dt. But it

also contains iteration steps within each time-step, denoted *L*, where the film thickness and the fluid pressures are updated. Convergence of each time-step is found by using the iterations, *L*.

This means that the model has partial differentials variable in time, *t*, and partial differentials variable in iteration, *L*. To summarise, there are time-steps which dictate the position of the crack in the contact, but within these time-steps there are iterations that are used to evaluate the correct film thickness (*h*) and film pressure (*p*).

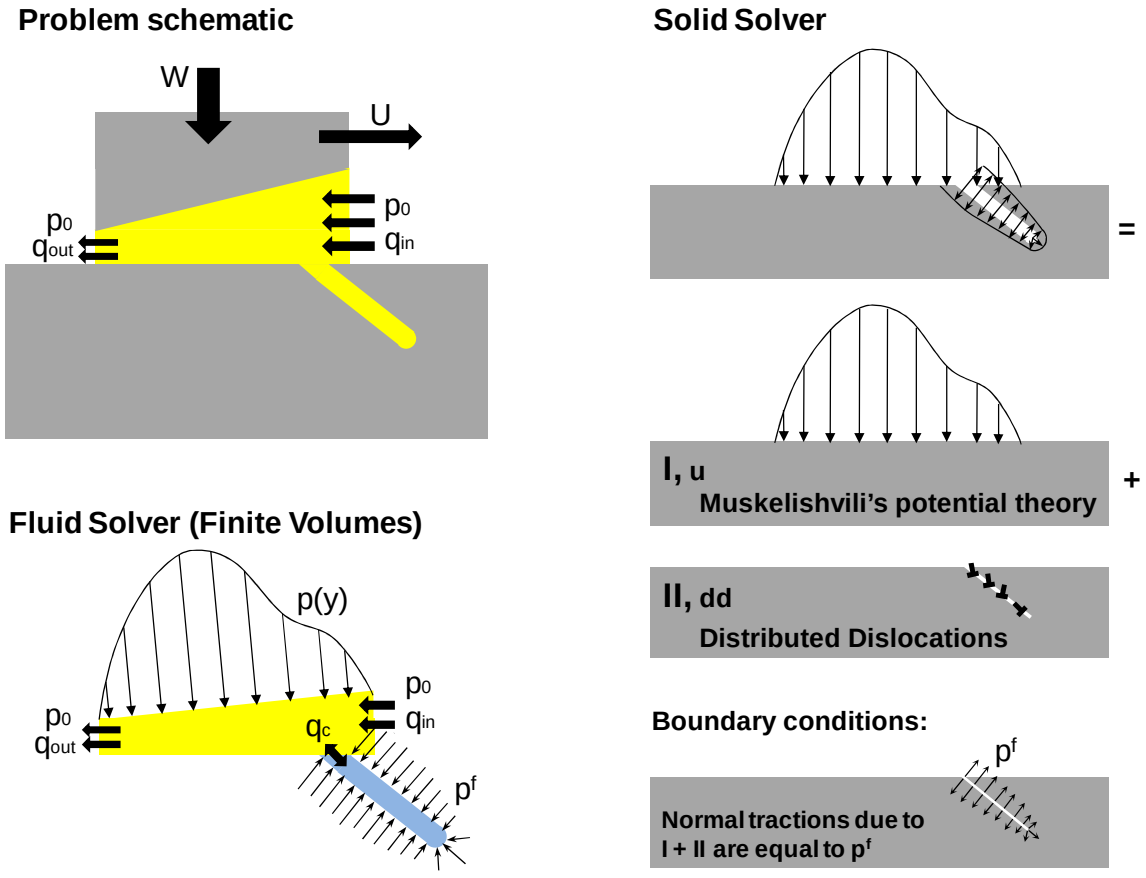


Figure 4.2 – Overall problem and schematic describing the fluid and solid solvers and their components

4.2.1 Fluid Solver

The fluid solver is designed to simulate the effect of fluid pressurisation in the hydrodynamically lubricated (HL) rolling contact, where a RCF crack is present on one of the contact surfaces. To model the fluid domain a solution that contains two separate fluid films, one in the crack and one on the surface, that considers the lubricant film separating the two solid bodies, is proposed. Both of the films have unique behaviour, but they can be coupled at the boundary at which they join, where both must behave consistently in order to preserve continuity of flux. The fluid solver allows for a flow of fluid between the two films, where the overall solution is based on the conservation of mass in the fluid domain. The mass flow rate at the inlet to the fluid domain is equal to the mass flow rate at the crack mouth combined with the mass flow rate at the outlet and therefore mass is conserved.

The physical effects that the fluid solver is designed to capture are that of fluid flow into the crack and fluid pressurisation, both of which are concisely explained here, with the aid of Figs 4.3a & b, for a more complete description refer to [1, 3]. As the contact load approaches the RCF crack, the contact pressure, and in certain cases a shearing effect at the surface, open the crack allowing the lubricating fluid, or base oil in the case of bearings, to fill the crack through surface tension and capillary forces. The assumption used during this analysis, that the crack is fully filled as it enters the contact, relies on the time required to fill the crack, known as the characteristic penetration time [155], being shorter than the loading frequency. Otherwise the crack will not have time to be fully filled on the approach of the contact pressure.

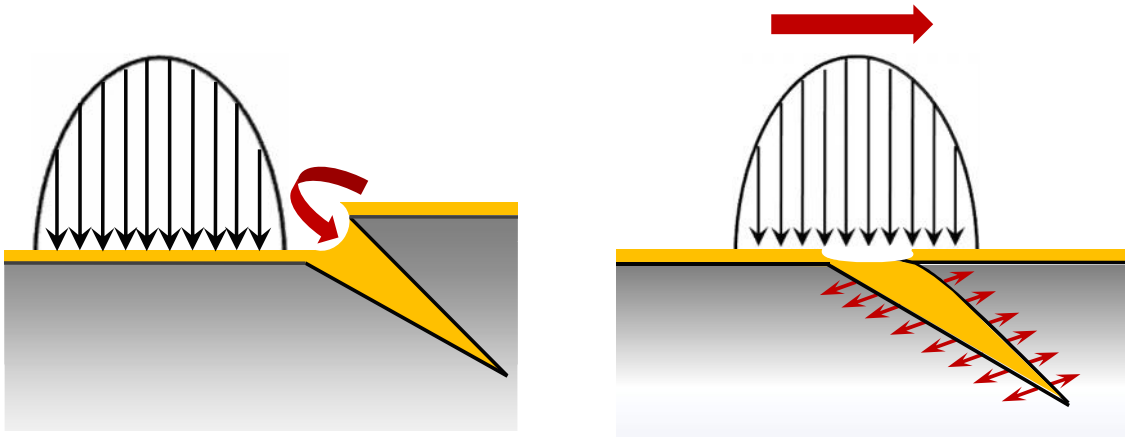


Figure 4.3 – (a) Fluid ingress on contact approach (b) Fluid pressurisation inside contact

Within the contact patch the lubricating fluid becomes pressurised as it is compressed by the contact load, where the fluid pressure provides load support and maintains a clearance between the solid bodies. When the crack enters the contact, assuming that the crack is fully filled, the volume of lubricant contained in the crack is also compressed and pressurised by the contact load. Furthermore, inside the crack the fluid is pressurised by the surface film pressure at the crack mouth; where the pressure is transmitted from the surface film through to the lubricant film in the crack. The pressurised fluid inside the crack applies a load to the crack faces which then translates into crack opening. This crack opening creates a ‘suction’ type flow into the crack from the surface film.

4.2.2 Fluid Formulation

The formulation of the fluid solver in this chapter is essentially an extension of the squeeze film model proposed by Bogdánski [1] to include the surface film. By including the surface film it removes the need to have any approximated boundary conditions because the true and physical boundary conditions of zero pressure at the inlet and outlet of the fluid domain, either side of the contact patch, and that of a zero pressure gradient at the crack tip can be applied. In Bogdánski's case he had to estimate the pressure at the crack mouth because the fluid film that he solved only considered the crack, and without considering the surface film, the fluid pressure at the crack mouth cannot be calculated it must be imposed.

The fluid formulation is mass conserving which imposes that the flow of the lubricant into the system is equal to the flow of lubricant out of the system combined with the flow between the surface film and the crack film ($q_{in} = q_{out} + q_c$). The crack can draw lubricant from the surface film (positive flux) as it opens and squeeze lubricant into the surface film as it closes (negative flux). This interaction between the films gives a coupled effect with each fluid film affecting the fluid flow and the pressure distribution in the other.

To solve an analytical solution of the first order differential Reynold's equation is not trivial and a numerical method is used to tackle the problem. A finite volume method (FV), similar to that of Arghir [154], is used here whereby the fluid domain is divided into a series of control volumes or cells.

4.2.2.1 Reynolds Equation

Osborne Reynold's defined the equation that describes pressure in a thin, converging film, the Reynold's equation [156]. The equation is a simplification of the full Navier-Stokes equations based on the following simplifying assumptions;

1. Body forces, such as gravity are negligible
2. Pressure is constant through the thickness of the film
3. No slip occurs at the boundaries, *i.e.* the velocity of the fluid is the same as the wall velocity
4. The lubricant is Newtonian, *i.e.* the stress in the fluid is linearly proportional to the shear rate
5. The flow in laminar
6. Inertia effects are negligible
7. Viscosity is constant through the thickness of the film

Based on these assumptions the derivation of the flow for an element, or column, of fluid, Fig. 4.4, in the *x* and *y* directions can by expressed by first considering the flow per unit length in the *x* and *y* directions respectively;

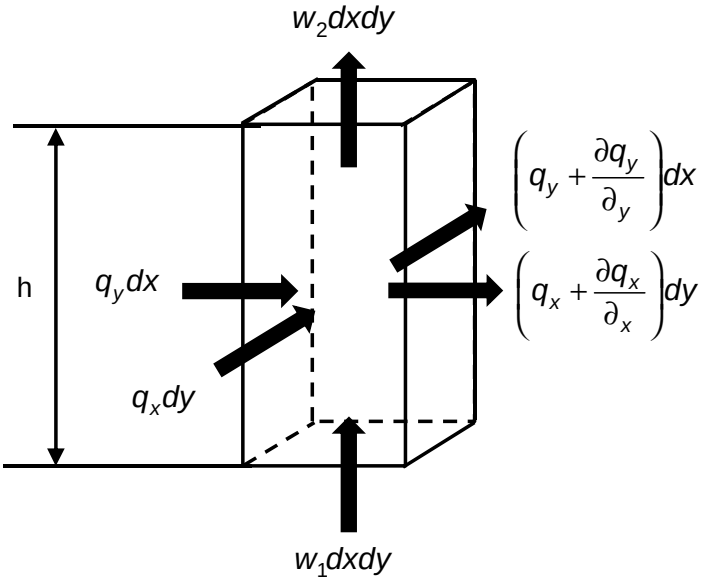


Figure 4.4– Schematic of a column of fluid of volume *h* d*x* d*y* [156]

$$q_x = \int_0^h u dz = \tag{4.1}$$

$$q_y = \int_0^h v dz \tag{4.2}$$

Then integrating gives

$$q_x = \left[\frac{\partial p}{2 « \partial x} \left(\frac{z^3}{3} - \frac{h z^2}{2} \right) + (U_2 - U_1) \frac{z^2}{2h} + z U_1 \right]_0^h \tag{4.3}$$

$$q_y = \left[\frac{\partial p}{2\eta\partial y}\left(\frac{z^3}{3} - \frac{hz^2}{2} \right) + (U_2 - U_1)\frac{z^2}{2h} + zU_1 \right]_0^h \tag{4.4}$$

when evaluated this gives, for both *x* and *y* directions;

$$q_x = -\frac{\rho h^3}{12\eta}\frac{\partial p}{\partial x} + (u_2 + u_1)\frac{\rho h}{2} \tag{4.5}$$

$$q_y = -\frac{\rho h^3}{12\eta}\frac{\partial p}{\partial y} + (v_2 + v_1)\frac{\rho h}{2} \tag{4.6}$$

Considering all the elements in the fluid domain except the one at the crack film/surface film interface, assuming steady state conservation of flow gives the sum of the fluxes in and out of each control volume;

$$\frac{\partial q_x}{\partial x} + \frac{\partial q_y}{\partial y} = 2\rho(w_1 - w_2) \tag{4.7}$$

These equations can be combined to give the Reynolds equation in two dimensions as;

$$\frac{\partial}{\partial x}\left(\frac{\rho h^3}{\eta}\frac{\partial p}{\partial x}\right)+\frac{\partial}{\partial y}\left(\frac{\rho h^3}{\eta}\frac{\partial p}{\partial y}\right)=6\left[\frac{\partial}{\partial x}\left(\rho h\left(u_1+u_2\right)\right)+\frac{\partial}{\partial y}\left(\rho h\left(v_1+v_2\right)\right)\right]+2\rho\frac{dh}{dt} \quad (4.8)$$

where, x and y are the coordinates in the flow plane, along and transverse to the flow direction respectively. h is the lubricant film thickness, u_1, u_2, v_1, v_2, are the sliding velocities of the bearing surfaces in the x and y direction respectively. The bearing is lubricated with a lubricant of viscosity η, and density, where the pressure in the lubricant film is p. For the evaluation of the fluid film in this model however we are only considering a one dimensional case therefore the equation can be simplified and re-written neglecting the spatial derivative in y and considering only the derivative in x, as;

$$\frac{\partial}{\partial x}\left(\frac{\rho h^3}{\eta}\frac{\partial p}{\partial x}\right)=6\left[\frac{\partial}{\partial x}\left(\rho h\left(u_1+u_2\right)\right)\right]+2\rho\frac{dh}{dt} \quad (4.9)$$

This is the one dimensional form of the Reynold's equation used for this study.

4.2.3 Finite Volume Formulation

To solve the Reynold's equation within the framework of this model, a discretised set of equations based on the one dimensional Reynold's equation are derived. The formulation uses a piecewise discretisation of the solution domain and a numerical method of evaluating the Reynold's equation. The method allows for an approximate

solution to be found, where the accuracy of the solution is dependent on the number of discrete (or mesh) elements used.

To demonstrate the discretisation scheme we consider the convergent wedge, previously discussed where the linear wedge is divided into *n* steps of height *h,* shown in Fig. For each of these step elements of uniform height it is possible to derive, using the Finite Volume (FV) method, a discretized form of the one dimensional Reynold's equation. The first order Reynold's equation relies on the film heights, *h*, and the pressure being stored on a staggered mesh. This is shown in Fig 4.5, the values of pressure are stored at nodes, $i = 1 \rightarrow n+1$, and film heights at nodes, $j = 1 \rightarrow n+1$. This introduces an error to the solution, this error is directly proportional to the mesh element size, and therefore as the mesh elements become small the error becomes negligible. Therefore when using this method a mesh convergence study is required.

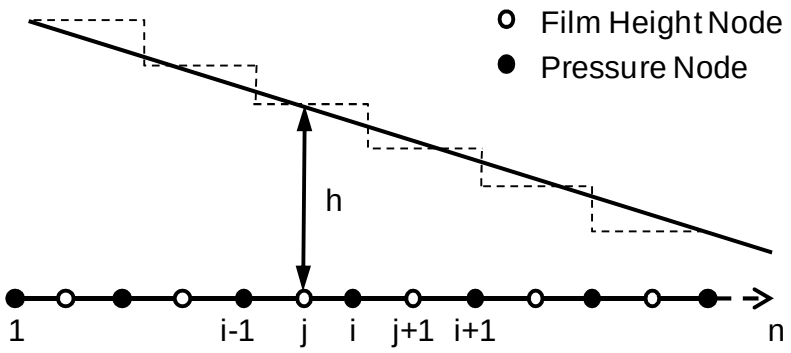


Figure 4.5 – Schematic of the "stepped" discretisation scheme used for the fluid film

The one dimensional version of the Reynold's equation Eq. (4.9) can be written, assuming incompressibility, as;

$$\left(-\frac{h^3}{12«}\frac{\partial p}{\partial x} + \frac{Uh}{2} \right) = 0 \tag{4.10}$$

where;

$$U = \frac{u_1 + u_2}{2} \tag{4.11}$$

From this the starting point for obtaining the finite volume discretised form of the partial differential equation is the conservation of flux q at each discretisation cell boundary. Considering a continuous film thickness this results in

$$q_{j+1} - q_j = 0 \tag{4.12}$$

$$q_{j+1} = -\left(\frac{h^3}{12«} \right)_j \frac{p_{i+1} - p_i}{x_{i+1} - x_i} + \frac{Uh_{j+1}}{2} \tag{4.13}$$

$$q_j = -\left(\frac{h^3}{12«} \right)_j \frac{p_i - p_{i-1}}{x_i - x_{i-1}} + \frac{Uh_j}{2} \tag{4.14}$$

The consistency rule then leads to the following discretised equation:

$$T_i p_i = T_{i-1} p_{i-1} + T_{i+1} p_{i+1} + S_i \tag{4.15}$$

$$Y_i = \frac{\left(h^3/12\mu\right)_{j+1}}{x_{i+1}-x_i} + \frac{\left(h^3/12\mu\right)_j}{x_i - x_{i-1}},\ T_{i-1} = \frac{\left(h^3/12\mu\right)_j}{x_i - x_{i-1}},\ T_{i+1} = \frac{\left(h^3/12\mu\right)_{j+1}}{x_{i+1}-x_i} \tag{4.16a – c}$$

$$S_i = -U(h_{j+1} - h_j)/2 \tag{4.17}$$

The coefficients of the discretised equation are always positive, $T_i, T_{\pm 1} > 0$, and (with the exception of the domain boundaries) the main diagonal coefficient is always the sum of the neighbouring coefficients, $T_i = T_{i+1} + T_{i-1}$.

In this approach the, pressures are defined at nodes and the film thickness is defined at the centre of the cells, therefore the meshes are offset, or staggered. For the one dimensional example, pressure and film thickness are characterized by $(p, p^w, p^e)_i$ and by $(h, h^w, h^e)_i$ respectively. If we consider first the formulation for the cells that don't contain the crack mouth, integrating the Reynold's equation on the discretization cell *i* gives;

$$q_i^e - q_i^w = 0 \tag{4.18}$$

$$q_i^e = -\left(\frac{h^3}{12«}\right)_i^e \frac{p_i^e - p_i}{x_{j+1} - x_i} + \frac{Uh_i^e}{2} \tag{4.19}$$

$$q_i^w = -\left(\frac{h^3}{12«}\right)_i^w \frac{p_i - p_i^w}{x_i - x_j} + \frac{Uh_i^w}{2} \tag{4.20}$$

To obtain a discretised relationship similar to Eq. (4.20), pressure values on cell boundaries p_i^e and p_i^w must be expressed as a function of the pressure values in the surrounding nodes, p_{i+1} and p_{i-1}. The procedure for the cell boundary $x_{i+1/2}$ is expressed here. Firstly, in agreement with the finite volume approach, the flux continuity will be enforced at the cell boundary;

$$q_i^e = q_{i+1}^w \tag{4.21}$$

$$q_i^e = -\left(\frac{h^3}{12«}\right)_i^e \frac{p_i^e - p_i}{x_{j+1} - x_i} + \frac{Uh_i^e}{2},\ q_{i+1}^w = -\left(\frac{h^3}{12«}\right)_{i+1}^w \frac{p_{i+1} - p_{i+1}^w}{x_{i+1} - x_{j+1}} + \frac{Uh_{i+1}^w}{2} \tag{4.22a - b}$$

Substituting Eq. (4.22a & b) back into Eq. (4.21) gives;

$$-\left(\frac{h^3}{12«}\right)_i^e \frac{p_i^e - p_i}{x_{i+1/2} - x_i} + \frac{Uh_i^e}{2} = -\left(\frac{h^3}{12«}\right)_{i+1}^w \frac{p_{i+1} - p_{i+1}^w}{x_{i+1} - x_{i+1/2}} + \frac{Uh_{i+1}^w}{2} \tag{4.23}$$

The above relationship can be re-arranged as;

$$b_i^e P_i^e + b_{i+1}^w p_{i+1}^w = b_i^e p_i + b_{i+1}^w p_{i+1} + \frac{U(h_i^e + h_{i+1}^w)}{2} \tag{4.24}$$

$$b_i^e = -\frac{(h^3 / 12«)_i^e}{x_{j+1} - x_i} \tag{4.25}$$

$$b_{i+1}^w = -\frac{(h^3 / 12«)_{i+1}^w}{x_{i+1} - x_{j+1}} \tag{4.26}$$

where for the case of the crack film, $U = 0$;

$$b_i^e p_i^e + b_{i+1}^w p_{i+1}^w = b_i^e p_i + b_{i+1}^w p_{i+1} \tag{4.27}$$

This can be written in the generalised form for P_i as;

$$P_i = \frac{1}{b_i^e}\left(b_i^e P_i^e + b_{i+1}^w P_{i+1}^w - b_{i+1}^w P_{i+1} - \frac{U(h_i^e + h_{i+1}^w)}{2}\right) \tag{4.28}$$

This gives rise to a sparse tri-diagonal matrix of size n x n, and it is possible to solve when $b_1 p_1 = 0$ and $b_n p_n = 0$. These two expressions arise from the boundary conditions imposed on the problem, that the pressure is zero at each end of the fluid film. These Dirichlet type boundary conditions mean that p_1 and p_n are both known and the rest of the values in the domain can then be computed. The solution is iterated until the rate of change of the sum of the squares of the finite volume element residuals of pressure drops below 10^{-5}, that is to say that the rate of change of the total pressure residual has dropped below 0.001%.

4.2.4 Fluid Domain Coupling

To adapt the discretised form of the Reynold's equation to this problem, a special case has to be made to capture the coupling of the two fluid films, because the fluid domain is divided into two parts, namely the surface film and the crack film (see Fig. 4.1b). In this solution, q_c, is the term which is used to couple the two fluid films at the crack mouth. The boundary conditions to be considered for the surface film are zero pressure (p_0) at both the inlet and outlet boundaries where the film thickness is imposed at all points and takes the form of a convergent surface defined by the gradient of the convergence wedge, k. The minimum surface film thickness at the thin end of the wedge, h_0, is calculated from hydrodynamic lubrication theory as:

$$h_0 = \sqrt{\frac{-6U_s \mu B^2 k^*}{W}} \tag{4.29}$$

where;

$$k^* = \frac{1}{k^2}\left(-log[k+1] + \frac{2k}{k+2}\right) \tag{4.30}$$

The crack film boundary conditions are a zero pressure gradient at the crack tip (*i.e.* no flux) and a flux in and out of the crack through the boundary at the crack mouth, q_c, driven by the pressure gradient at the crack mouth.

The film thickness within the crack is the combination of the calculated plastic radius at the crack tip, h_{c0}, which remains constant and the crack face displacement, $e_{\hat{y}}^T(\hat{x})$, which is driven by the fluid pressure. The initial crack face displacement at each time step is defined using the converged crack face displacement from the previous time step. Where the first time step is initialized using a crack face displacement solution when the crack is a fraction outside of the contact, where outside the contact the crack is not acted upon by the effects of the crack film pressurisation.

While in the solid solver the crack is considered to have zero thickness while unloaded, in the fluid solver this is not possible. Therefore it is argued that the crack faces, in the absence of any load are separated by a distance which corresponds to a

residual plastic deformation of the crack tip, the plastic radius. The magnitude of this radius is such that the aspect ratio of the crack is still large therefore the representation of the crack in the solid model as 1D when unloaded is still valid. The plastic radius can be calculated using a linear elastic fracture mechanics (LEFM) model (e.g. Dugdale-type model [157]). Example calculations for the geometry, lubricants and loading conditions explored in this paper (see Table 1) show that the plastic crack tip opening displacement obtained from the evolution of the mode I stress intensity factor during the loading cycle from the Dugdale model [157] correspond to values of h_{c0} in the 100 to 200 nm range. Therefore the value of h_{c0} used in the analyses is chosen to lie within this range and is, at least in first approximation, deemed as representative of the operating conditions studied here. A more accurate analysis would require a more detailed calculation of the evolution of the plastic field ahead of the crack tip but this is outside the scope of the analysis.

Although the FVM formulation used is the same for the entire fluid domain, the fluid domain is split into two separate parts, one that evaluates the film formed between the convergent wedge and the half-plane surface and one which evaluates the fluid film inside the crack. The two films are coupled using the term that characterises the flow exchange between them. The corresponding volumetric flux term is characterised by the pressure gradient and the film thickness at the crack mouth and is given by the non-dimensional expression;

$$q_c^* = -h_{mouth}^{*\,3} \frac{dp_{mouth}^*}{d\hat{x}^*} \tag{4.31}$$

One limitation of this coupling is that the crack mouth must be contained within one finite volume element. This term, q_c^*, constitutes a boundary condition for the solution of the crack film because it provides the link between the pressure gradient and the flux at the point where the crack film meets the surface film. If we now consider Eq 4.21, with the additional volumetric flux from the crack and again enforcing the flux continuity gives the following;

$$q_i^e = q_{i+1}^w + q_c \tag{4.32}$$

This therefore gives the following;

$$-\left(\frac{h^3}{12\mu}\right)_i^e \frac{P_i^e - P_i}{x_{i+1/2} - x_i} + \frac{Uh_i^e}{2} = -\left(\frac{h^3}{12\mu}\right)_{i+1}^w \frac{P_{i+1} - P_{i+1}^w}{x_{i+1} - x_{i+1/2}} + \frac{Uh_{i+1}^w}{2} + q_c \tag{4.33}$$

This can be written in the generalised form for P_i

$$P_i = \frac{1}{b_i^e}\left(b_i^e P_i^e + b_{i+1}^w P_{i+1}^w - b_{i+1}^w P_{i+1} - \frac{U(h_i^e + h_{i+1}^w)}{2} + q_c\right) \tag{4.34}$$

where U can be zero in the case of the crack film and q_c can be zero for all elements except the one that contains the crack mouth, in the surface film and the crack. So by adding the volumetric flux in the form of a source term the coupling between the films can be captured.

4.2.5 Crack closure

If the crack closes and the fluid becomes entrapped within the crack, the fluid pressure solution is no longer coupled with the crack and surface film. The flux between the two films (q_c^*) tends to zero. Surface pressure can then simply be solved using the analytical solution for the convergent wedge from hydrodynamic theory [158] and the pressure of the entrapped fluid can be evaluated by applying an amount of compressibility to the fluid by imposing a constant value of bulk modulus (Γ) where:

$$\Gamma^* = -V^* \frac{\partial p^*}{\partial V^*} \tag{4.35}$$

The imposed value of compressibility is larger than the real value, this effectively relaxes the solution because numerical stability is difficult to be achieved by imposing incompressibility because this produces instabilities due to the large changes in pressure with respect to volume. This form of relaxation is necessary in order to obtain a converged solution, and is deemed to be a sufficient first approximation.

4.2.6 Solid Solver

The solid solver from the coupled algorithm is required to evaluate the effect of the fluid pressure acting on the cracked body. Stresses from the loading condition and the crack along with the deformed crack shape are all evaluated, where the deformed crack shape is later fed into the fluid solver. The superposition principle is once again applied and the framework for the solid solution in this chapter is the same as that of the dry model presented in Chapter three. However for the HL model described here the loading condition consists of fluid pressure acting at the crack faces and at the contact interface as opposed to a Hertzian contact. Because the fluid pressure acts directly on the faces of the open part of the crack, the boundary conditions for the problem can be written as;

$$\begin{aligned} &N(\hat{x}) = p_f && a_{op} < \hat{x} < a \\ &S(\hat{x}) + fH(\hat{x} - a_{op})N(\hat{x}) = 0 && 0 < \hat{x} < a \end{aligned} \qquad (4.36)$$

where p_f is the fluid pressure at the crack face. There is no shearing effect on the crack face from the fluid pressure because the fluid pressure acts perpendicular to the surface, inducing no shearing component.

The stresses, $\pm\frac{u}{\tilde{ij}}$, arising from the hydrodynamic pressure on the half-plane surface are evaluated using the triangular piecewise linear discretisation of the fluid

pressure together with the Musliishivili's potential theorem as outlined in Chapter three. For this case, however, the friction coefficient has been removed because the surfaces are separated by the pressurised fluid film as opposed to the Hertzian contact and the fluid is assumed to produce no shearing effect.

4.2.6.1 Solid Formulation

The solving blocks of Problems (I) and (II) from Chapter three are again applied here where substituting the boundary conditions from Eq. (4.36) into Eq. (3.14) gives the following

$$N(\hat{x}) = \pm^{u}_{\hat{y}\hat{y}}(\hat{x},0) + \frac{2«}{®(© +1)}\left(\int_{0}^{a} B_{\hat{x}}(\hat{c}) K^{N}_{\hat{x}}(\hat{x},\hat{c})\, d\hat{c} + \int_{a_{op}}^{a} B_{\hat{y}}(\hat{c}) K^{N}_{\hat{y}}(\hat{x},\hat{c})\, d\hat{c} \right) = p_f \qquad a_{op} < \hat{x} < a$$

$$S(\hat{x}) = \left(\pm^{u}_{\hat{x}\hat{y}}(\hat{x},0) + fH(\hat{x} - a_{op}) \pm^{u}_{\hat{y}\hat{y}}(\hat{x},0) \right) +$$

$$\frac{2«}{®(© +1)}\left(\int_{0}^{a} B_{\hat{x}}(\hat{c}) \left(K^{S}_{\hat{x}} + fH(\hat{x} - a_{op}) \right)(\hat{x},\hat{c}) K^{N}_{\hat{x}} \right) d\hat{c} + \int_{a_{op}}^{a} B_{\hat{y}}(\hat{c}) \left(K^{S}_{\hat{y}}(\hat{x},\hat{c}) + fH(\hat{x} - a_{op}) \right)(\hat{x},\hat{c}) K^{N}_{\hat{y}} \right) d\hat{c} \Bigg) = 0 \quad 0 < \hat{x} < a$$

(4.37)

Using the same discretisation and quadrature schemes from Eqs (3.21 & 3.22) gives the following;

$$\frac{2\pi}{\eta(\Gamma+1)}\sum_{k=1}^{n}\left[\begin{array}{l}\frac{2\eta(1+u_k)}{2n+1}\Delta_{\hat{x}}(u_k)K_{\hat{x}}^{N}(\bar{v}_i,u_k)+\\ \frac{2\eta(1+\bar{u}_k)}{2n+1}\frac{a_{op}}{a}\Delta_{\hat{y}}(\bar{u}_k)K_{\hat{y}}^{N}(\bar{v}_i,\bar{u}_k)\end{array}\right]=\pm_{\hat{y}\hat{y}}^{u}(\bar{v}_i)+p_f \qquad i=1,\ldots,n$$

$$\frac{2\pi}{\eta(\Gamma+1)}\sum_{k=1}^{n}\left[\begin{array}{l}\frac{2\eta(1+u_k)}{2n+1}\Delta_{\hat{x}}(u_k)\left\{\begin{array}{l}K_{\hat{x}}^{S}(v_i,u_k)+\\ fH\left(v_i-\frac{a_{op}}{a}\right)K_{\hat{x}}^{N}(v_i,u_k)\end{array}\right\}\\ +\frac{2\eta(1+\bar{u}_k)}{2n+1}\frac{a_{op}}{a}\Delta_{\hat{y}}(\bar{u}_k)\left\{\begin{array}{l}K_{\hat{y}}^{S}(v_i,\bar{u}_k)+\\ fH\left(v_i-\frac{a_{op}}{a}\right)K_{\hat{y}}^{N}(v_i,\bar{u}_k)\end{array}\right\}\end{array}\right]=\left[\begin{array}{l}\pm_{\hat{x}\hat{y}}^{u}(v_i)+\\ fH\left(v_i-\frac{a_{op}}{a}\right)\pm_{\hat{y}\hat{y}}^{u}(v_i)\end{array}\right]. \qquad i=1,\ldots,n$$

(4.38)

The solution for the deformed crack shape requires the displacement of the crack faces due to the fluid pressure in both of the fluid films, crack and surface, to be evaluated. The displacement of the crack faces arising from the distributed dislocations, $e_{\hat{i}}^{Cdd}(\hat{x},0)$, is found from Eq. (3.15), The displacement of the crack faces due to the hydrodynamic pressure on the surface of the half-plane, $e_{\hat{i}}^{Ctr}(\hat{x},0)$, is found by Eqs. (3.8 – 3.9b) which is described and validated in Chapter three; where *i* can be $\hat{x}$ or $\hat{y}$. These two contributions are combined to give the following in terms of $\hat{x}$ and $\hat{y}$;

$$e_{\hat{x}}^{CT}(\hat{x},0)=e_{\hat{x}}^{Cdd}(\hat{x},0)+e_{\hat{x}}^{Ctr}(\hat{x},0) \qquad (4.39a)$$

$$e_{\hat{y}}^{CT}(\hat{x},0) = e_{\hat{y}}^{Cdd}(\hat{x},0) + e_{\hat{y}}^{Ctr}(\hat{x},0) \tag{4.39b}$$

where superscript *C* denotes crack. The two contributing factors to the crack face displacement can be superimposed to give the total crack face displacement, however because only the crack opening due to the dislocations is required to update the crack film thickness, Eqs. (4.39a & b), are simplified to give;

$$e_{\hat{x}}^{CT}(\hat{x},0) = e_{\hat{x}}^{Cdd}(\hat{x},0) \tag{4.39c}$$

$$e_{\hat{y}}^{CT}(\hat{x},0) = e_{\hat{y}}^{Cdd}(\hat{x},0) \tag{4.39d}$$

This means only the contribution to the displacement due by the dislocations is solved at the crack faces.

4.2.7 Fluid-Solid Coupling

To capture the transient behaviour of the system, namely the fluid, a time dependent and history dependant algorithm is required. The time step, Δt^*, can be evaluated as a function of the distance the contact moves, dy^*, divided by the lateral speed, U_2, hence (shown in Fig. 4.6):

$$\Delta t^* = \frac{dy^*}{U_2} \tag{4.40}$$

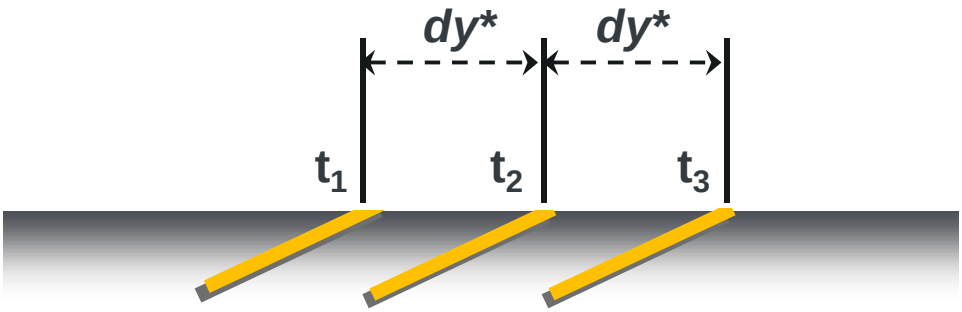


Figure 4.6 – Diagram of the method of calculating the time-step *Δt*

At each time step, coupling between the solid and the fluid gives the instantaneous film thickness everywhere in the fluid domain. The coupling is captured using an iterative routine that imposes the interaction at the solid/fluid interface inside the crack; the surface film thickness is imposed by the shape of the convergent wedge. The fluid pressures, both at the surface and within the crack, are first calculated using the finite volume method formulation together with the new boundary condition at the crack mouth derived from the moving load and finally the rate of change of the film thickness, which is initialised by d*h*/d*t* = 0, but can then be calculated from;

$$\frac{dh(\hat{x},0)}{dt} = \frac{e_{\hat{y}}^{CT}(\hat{x},0)^{t_2} - e_{\hat{y}}^{CT}(\hat{x},0)^{t_1}}{t_2 - t_1} \quad a_{op} < \hat{x} < a \tag{4.41}$$

The pressure values are then interpolated from the fluid mesh and applied at the nodes of the solid domain as triangles of traction (at the half-plane surface), and the nodes of the boundary element, distributed dislocation technique, (in the crack). The deformation of the crack in is then evaluated and is added to the initial crack film thickness, $h_{c,0}$, which, as mentioned above, can be directly computed considering crack tip plasticity within the LEFM framework. At a specific iteration step, L, within a time step, t, the fluid film thickness within the crack is given, in dimensionless form, by;

$$h_C^*(\hat{x},0) = h_{C,0}(\hat{x},0) + e^{CT}_{\hat{y}}(\hat{x},0) \tag{4.42}$$

Every time the film thickness in the crack is changed, the fluid solver is called and the pressures in the FVM solution updated using the modified crack profile. The iterative process is repeated until the fluid pressure outside and inside the crack combined with the film thickness inside the crack have converged, see appendix A, *i.e.* when:

$$\frac{dh_C^*(\hat{x},L)}{dL} \to 0. \tag{4.43}$$

Once the solution has converged the next time-step is considered ($t \rightarrow t+\Delta t$) and the position ($Y^*=Y^*+dy^*$) of the crack relative to the contact centre is updated. The process is repeated until the crack has traversed the loaded area. At each instant, t, the

converged solution at the previous time step, *t-1*, is used to initialise the solvers, with the exception of the first step. The first step is initialised using the solution for a dry crack solved outside the contact.

4.3 Validation of individual solvers and intermediate steps

While it is difficult to find benchmark solutions to validate the fully coupled problem as this is the first instance when a coupled fluid/solid solver is used for RCF cracks in the presence of lubrication, it is important to consider some of the intermediate steps and perform validation of the individual solvers, which correspond to the individual solving blocks of the overall algorithm presented in Appendix A. To this end, the hydrodynamic solution for the linear convergent wedge, the volumetric flux used for the fluid coupling of the two films at the crack mouth and the crack opening due to the fluid pressure acting at the crack faces were considered as the quantities to independently check to verify the validity of the fluid solver, the coupling methodology and the solid solver respectively. Benchmark solutions obtained using either analytical or numerical techniques are used to assess the accuracy of the proposed algorithms and the suitability of the proposed approach for coupling the fluid and the solid solvers.

In Fig. 4.7 the analytical pressure distribution produced by a linear wedge in the absence of the crack is compared to that produced by the equivalent “half-Sommerfeld” [152] solution for a cylinder on a lubricated plane. Of course, the two solutions do not show perfect agreement as they correspond to different physical problems; however,

the similarity between the pressure distributions obtained under the effect of the same normal load confirms that using a linear wedge to approximate the physical problem under investigation (see Fig.4.1) is appropriate for development purposes. The comparison between the finite volume solution obtained by the fluid solver implemented by the author and the analytical solution for a linear convergent bearing is also shown. The two methods compare well, confirming the correctness and the accuracy of the numerical formulation.

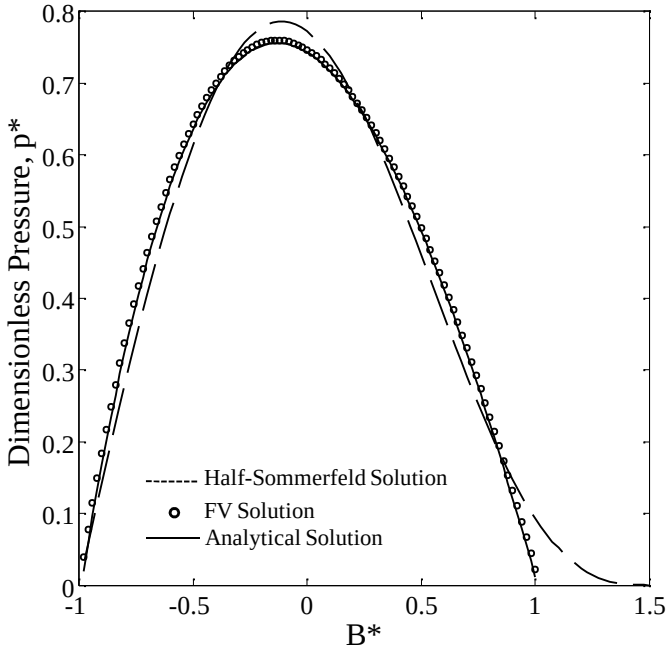


Figure 4.7. Comparison between FV and analytical solutions for the pressure distribution in the contact

As previously stated the coupling between the surface film and the film within the crack is achieved through the use of the flux term evaluated in a cell connecting the interface between the crack and the surface film.

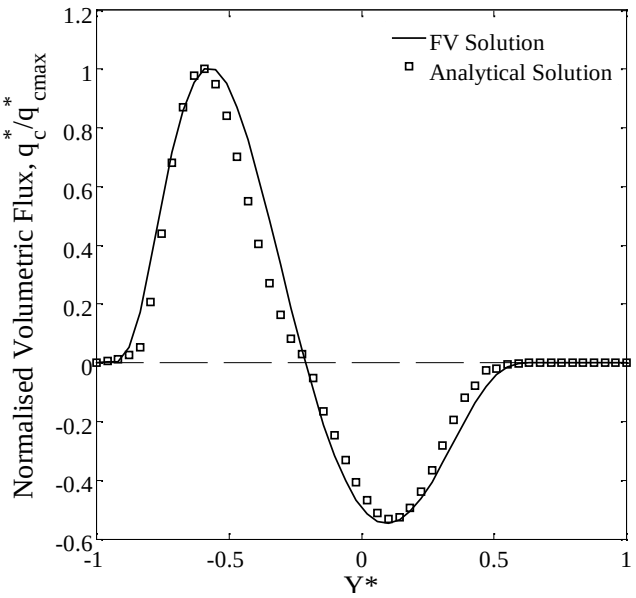


Figure 4.8. Comparison between the normalised volumetric fluxes at the crack mouth computed using the FV solver and the crack volume from the elastic deflection (integrated over the crack length)

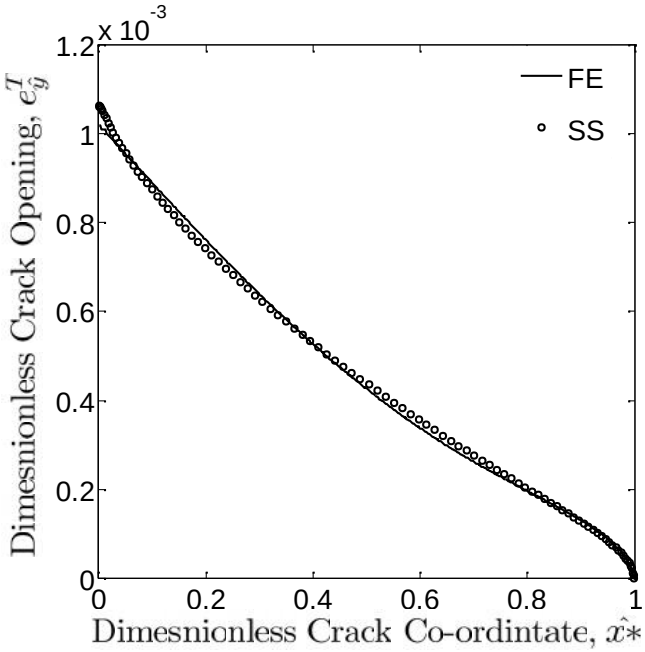


Figure 4.9. Comparison between the crack deflections computed using the DDT and the FEM package ANSYS for a pressurised crack benchmark problem.

As previously stated the coupling between the surface film and the film within the crack is achieved through the use of the flux term evaluated in a cell connects the interface between the crack and the surface film. The suitability of this term in representing the flux from the crack to the film or from the film to the crack can be assessed by comparison of this term with the integral change in the crack deflections (*i.e.* the change in the volume of fluid filling the crack). Fig. 4.8 shows this comparison; good agreement between the magnitudes of the two measures of flux between the films is demonstrated. It should be noted that positive flux indicates flow into the crack and negative flux corresponds to fluid drawn from the crack. This supports the use of this simple coupling method for application in this problem.

Finally, a measure of the applicability of the current distributed dislocation technique in accurately modelling the presence of pressurised fluid in a cracked solids can be obtained through comparison with converged finite element (FE) solutions (here the FE package ANSYS 11.0 was used). Fig. 4.9 shows the results obtained using the two numerical methods for an edge crack in a half-plane with a constant pressure applied along its faces: the deflections at the crack faces, identified here by the crack opening, are again in good agreement with small discrepancies occurring at the crack mouth, mainly due to the difference in the discretisation used for the two techniques.

4.4 Results and Discussion

In this section the case of a rolling contact fatigue crack in a half-plane, inclined at 25° to the surface, traversed by a loaded convergent hydrodynamic bearing is presented as

a test case. It serves to outline the method and the framework developed by the author for analysing lubricated cracks. Three different geometries are considered and compared (see Table 1).

Case	**Liquid**	**a**	**B**	**h_0**	**U_S**	**W_F**	**E**	**σ_Y**	**η**	**θ**	**k**
		μm	μm	nm	m/s	N/m	GN/m^2	MN/m^2	Pa/s	°	
1	Base Oil	200	200	152	0.2	5000	210	800	0.137	25	0.325
2	Base Oil	100	200	152	0.2	5000	210	800	0.137	25	0.325
3	Base Oil	50	200	152	0.2	5000	210	800	0.137	25	0.325

Table 4.1 – Example problems parameters

Considering case 2, the variation in crack shape and pressure with respect to time, *i.e.* as *Y** varies from *-1* to *1*, is shown in Fig. 4.10. In particular, the contours plotted in Fig. 4.8(a) provide the full history of the crack opening and closure, while Figs. 4.8(b) are "slices" through the contours identified by the letters A to C and provide the deflections experienced at three locations within the crack during the loading cycle. The initial crack opening corresponds to a rapid fluid pressurisation inside the crack and the development of a large positive pressure gradient from crack mouth to crack tip. As a result, the crack begins to draw lubricant from the surface film allowing it to fill. This process continues until the opening reaches a maximum (*i.e.* when the action of the external load balances the effect of the fluid pressurisation), at which point the pressure gradient along the crack length tends to zero. There now exists, although only instantaneously, a constant pressure distribution similar to that hypothesised when using a hydraulic pressure model [159].

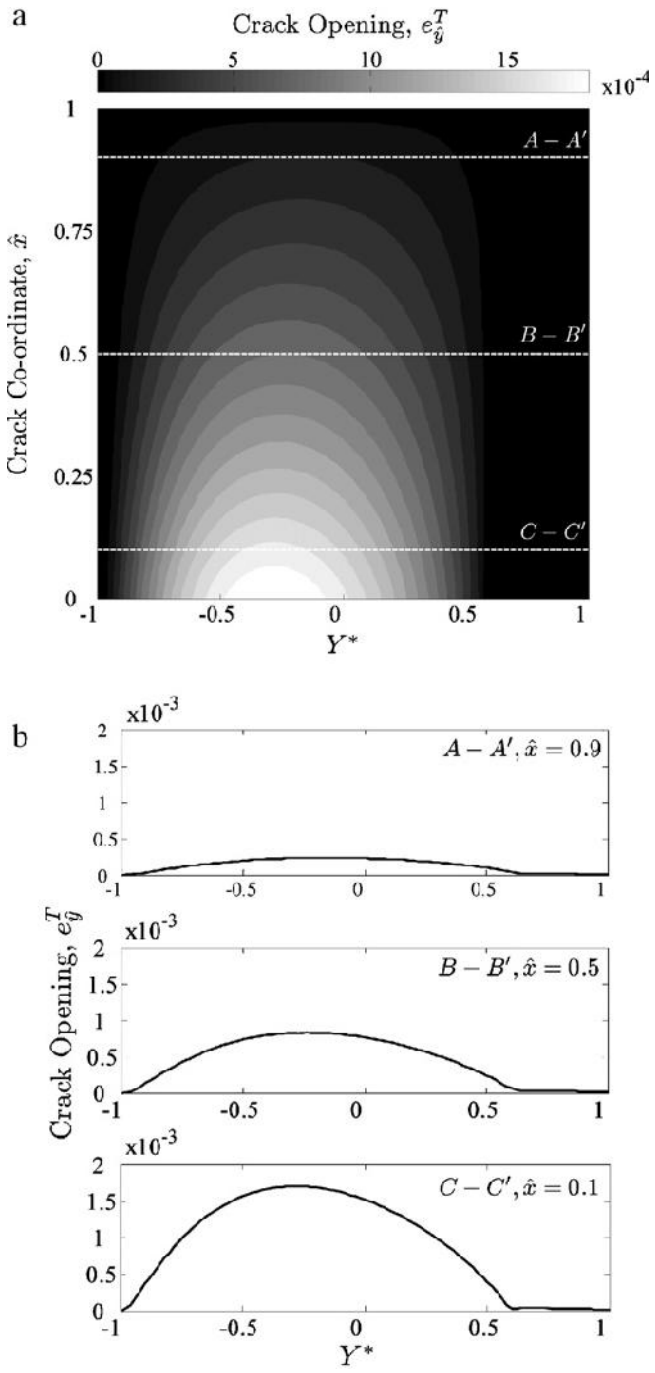


Figure 4.10 – (a) Contour plot showing the evolution of the crack opening displacements. (b) "Slices" through the contour plot in Figure 4.10(a) showing the evolution of the crack opening at three locations within the crack.

Once the crack passes the point of maximum surface pressure, $Y^* > -0.25$, it starts to close and continues to close as Y^* tends to 1. During this phase of the loading cycle, lubricant is squeezed out of the crack and a negative pressure gradient exists from crack tip to crack mouth. As the fluid is squeezed into the surface film, the surface pressure rises; this acts to restrict the flow of lubricant out of the crack. In this way the surface film controls the rate at which the crack closes.

Some comments about the implications that a fully coupled calculation has on the fluid pressure distribution within the crack are appropriate. Unlike other existing models, the proposed methodology captures the transient evolution of the squeeze term ($\mathrm{d}h(\hat{x})/\mathrm{d}t$). The presence of the crack mouth flux term determines the influence of the local surface film pressure on the crack film. This overcomes one of the main limitations of uncoupled models, where hypotheses have to be made about the fluid pressure at the crack mouth and the pressure gradient within the crack in order to establish the behaviour of the cracked body under loading [1, 4, 121, 160]; imposing such restrictions corresponds intrinsically to modifying the exchange of flux between the surface film and the crack in an uncontrolled fashion, with the possibility for an instantaneously infinite flux to occur in order to maintain the enforced boundary condition. In the proposed coupled model this is not the case; the fluid film on the outer surface and the solid deflections act to regulate the flow at the crack mouth, much like a valve.

If we focus on the evolution of the pressurised crack shape, Fig. 4.11 shows the crack deflections, and therefore the crack film shape, at three instants in time immediately before closure. The crack surfaces begin to “arch” towards closure near the crack mouth

as the load continues to traverse across the crack, *Y* > 0.6*. This behaviour is driven primarily by the negative pressure gradient within the crack film. The surface loading at the mouth starts to dominate, prevailing over the internal fluid pressure and as *Y** increases the faces at the crack mouth touch. Then as *Y** continues to increase the section of the crack nearest to the mouth comes into contact.

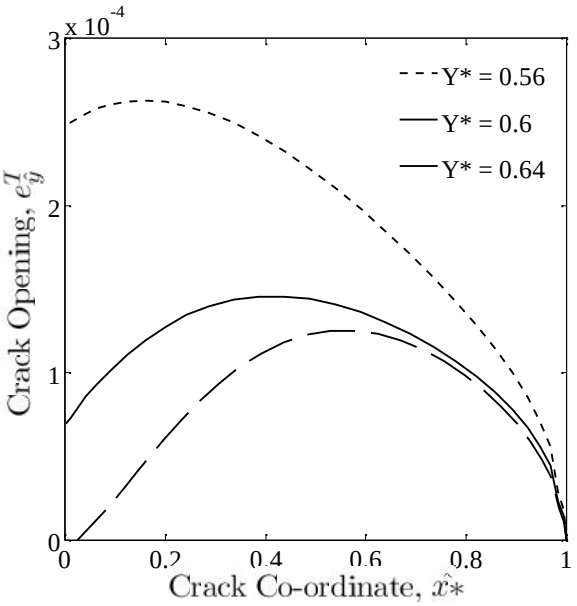


Figure 4.11 – Crack shape at three instants in time immediately before closure

The closure stops the flow of lubricant between the surface film and the crack film (q_c once again tends to zero) uncoupling the problem and providing a fixed volume of entrapped lubricant. At this point the behaviour of the solution changes and the coupled film FV solution is replaced by an analytical solution for the surface pressure. This is combined with a constant fluid pressure inside the crack resulting directly from the compressibility or bulk modulus of the lubricant. As the load continues to traverse, *i.e.* as *Y** tends from *0.75* towards *1*, the entrapped fluid becomes compressed and

increasingly pressurised. This pressurized, entrapped fluid maintains a degree of opening at the tip of the crack, restricting the crack from completely closing.

The coupling between the crack film and the surface film can be illustrated and quantified by considering the relationship between the crack mouth displacement, $e_{\hat{y}}^{T}(0)$, the volumetric flux (Fig. 4.12) and the normalised pressure gradient, Δp^*, in the crack (Fig. 4.11), where:

$$\Delta p^* = \frac{p_{ctip} - p_{cmouth}}{p_{cmouth}}. \qquad (4.44)$$

From Figs. 4.12 & 13, which show one load cycle as Y^* varies from *-1* to *1*, the strong relationship between the fluid pressure and the flow of lubricant between surface film and crack film is evident. In the portion of the loading cycle corresponding to positive pressure gradients, *i.e.* when the crack is opening, the lubricant flows into the crack. The magnitude of the flux can be directly correlated to the intensity of the positive pressure gradient. The converse is true when the pressure gradient is negative. Furthermore the point at which the solution returns a zero pressure gradient which is also the point of maximum opening, is directly related to the point of zero flux. This coupling between the crack shape, the pressure and the resulting flow illustrates the strong connection between the solution and the inherent physics of the problem.

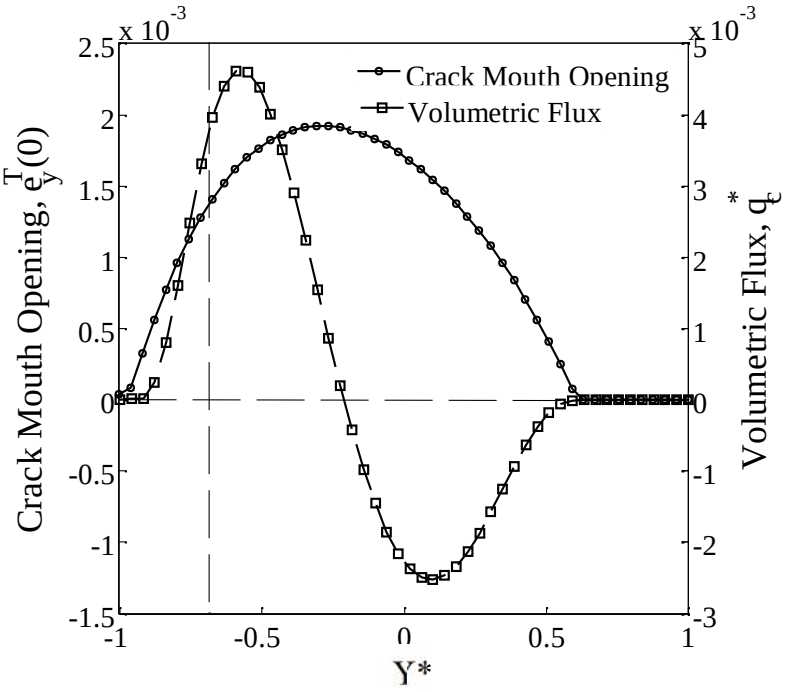


Figure 4.12 Evolution of the crack mouth opening vs. the volumetric flux at the crack mouth

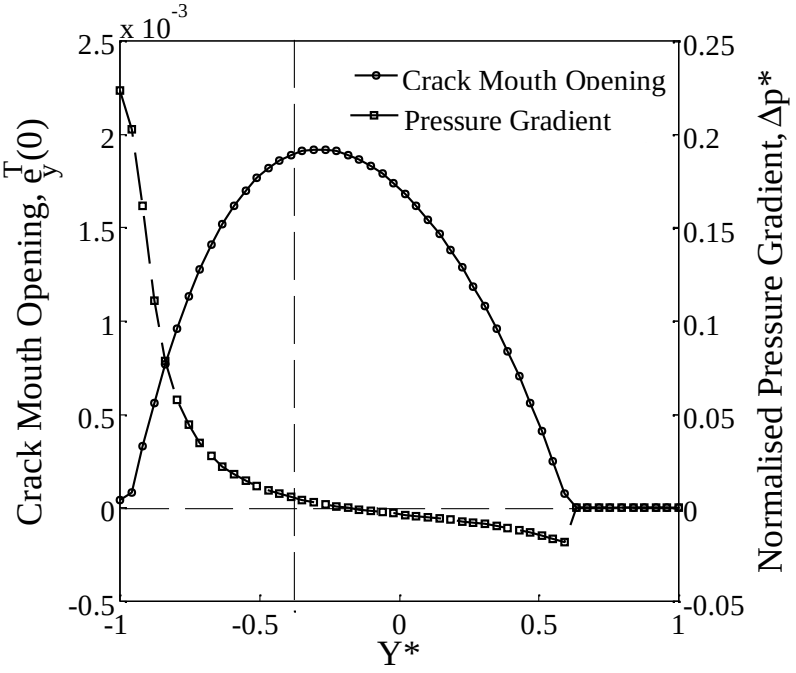


Figure 4.13 Evolution of the crack mouth opening vs. the pressure gradient at the crack mouth

Let us now look at the normalised coupling flux term, whose evolution is shown for cases 1 - 3 in Fig. 4.14. The results demonstrate that the crack length affects the flow between the surface and the crack film. While the bearing traverses the cracked region, there is a first a positive flux of lubricant, which corresponds to fluid being “pumped” into the crack; this reaches a maximum, when the action of the pressurised liquid is still capable of counteracting the external load, and then starts to decrease until it becomes negative. At this stage fluid starts draining from the crack until closure takes place (or until the load moves away from the cracked portion of the half-pane is closure does not take place): this corresponds to the negative flux peak and to the subsequent reduction of the flux term to zero. For a short crack, $b = 4a$ (see Fig 3.13), the transition from positive to negative is reached quickly ($Y^* \approx -0.4$) whilst for the longer crack, $b = a$, the transition comes later ($Y^* \approx 0$). The flow patterns illustrate the effect of the crack length on the cycle of the crack opening and closing. This is because the longer crack has a longer period of opening, which, in turn, leads to the longer crack having a greater period of positive flux because the positive pressure gradient within the crack takes longer to reduce to zero. This intuitively corresponds to the physical behaviour of the system, whereby longer cracks are expected to draw more lubricant from the surface film. Furthermore, the integral of the positive flux is also noticeably larger than the integral of the negative flux which can be attributed to the entrapment of some fluid in the crack when q_c tends to zero at closure.

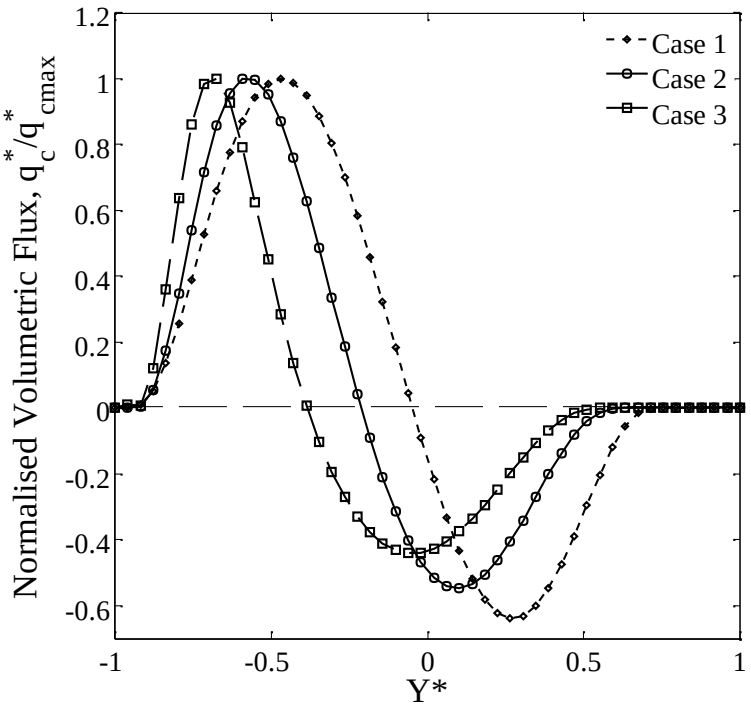


Figure 4.14. Evolution of the normalised volumetric flux at the crack mouth for the example cases in Table 4.1.

The Stress intensity factors (SIF) which govern crack propagation are important measures of the criticality of a crack, and its propensity to grow. The relative deviation (ΔK) and the load ratio (R) can be used in a wide range of models for prediction of crack growth rates, da/dN. These include the models first postulated by Paris *et al.* [161] but also a number of more advanced damage accumulation type models [84, 117, 162, 163].

Figs. 4.15 & 4.16 shows the normal mode (or mode I) SIF, *KI*, and the shear mode SIF, *KII*, for cases 1-3. Both quantities are normalised using the maximum surface film pressure and the crack length, i.e.

$$K_I^* = \frac{K_I}{p_{\max}\sqrt{®a}} \tag{4.45}$$

where $p_{\max}$ is the maximum pressure at the surface. By comparison of the traces of SIF with those for fluid pressure and opening displacement it is clear that a high degree of coupling exists within the problem. The mode I stress intensity factor with respect to time can, as expected, be directly related to the severity of the crack opening displacement. Hence the more the crack opens the greater the likelihood of crack growth, KI_{min} being negligible when the contact is far from the crack. Because the pressurized fluid is the factor driving the crack opening, it can be argued that the fluid pressure is directly linked to the severity of crack propagation in the normal mode (*KI*). When the crack experiences partial closure it maintains a degree of opening, therefore *KI* remains greater than zero, but the severity of the damage in this part of the loading cycle strongly depends on the characteristics of the entrapped fluid and can be considered as generally mild.

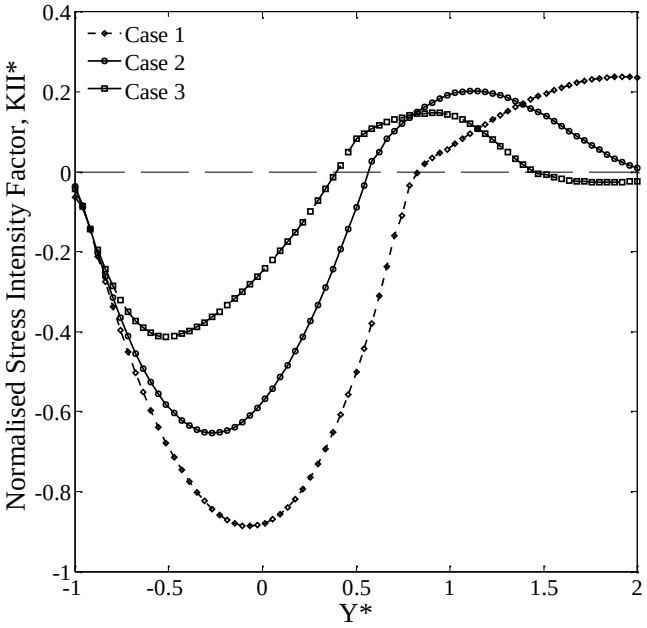


Figure 4.15 Evolution of the normalised mode I SIF for the example cases in Table 4.1

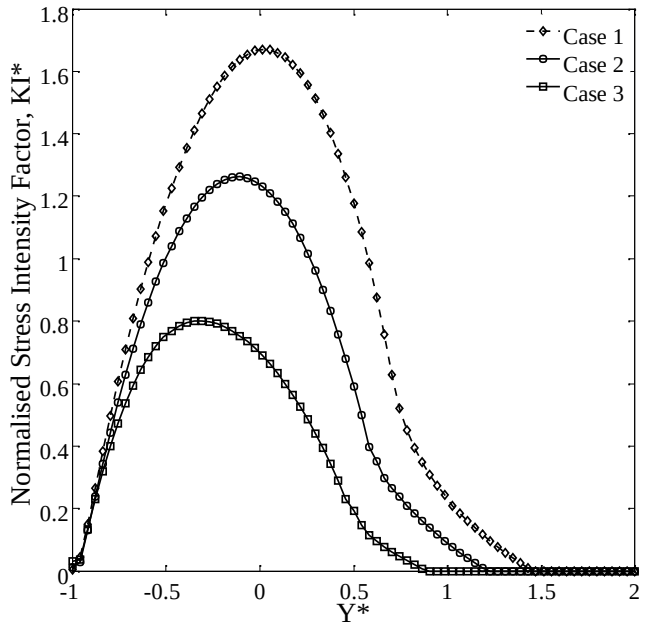


Figure 4.16 Evolution of the normalised mode II SIF for the example cases in Table 1

Focussing now on the mode II stress intensity factor, Fig. 4.16 shows the evolution of *KII* during the loading cycle. The fluid pressure on the surface dominates the solution; this can be seen from the correlation in shape between *KII* and the fluid pressure. Although less severe than *KI* in absolute value, it can still contribute to crack propagation and in particular kinking. The combined effect of the external loading and of crack opening generates shearing at the crack tip and corresponding relatively large *KII* values. This is strongly affected by the angle of inclination.

From Figs. 4.13 & 4.14 it is also clear that the magnitude of the SIF is directly related to the length of the RCF crack. Longer cracks yield higher SIF and, therefore acceleration in crack growth rate, d*a*/d*N*, is coupled with an increase in crack length. This is an intuitive correlation, because as the crack grows its capacity to open under the action of the internal pressurised fluid increases. The load on the crack faces, i.e. the integral of the pressure along the crack faces, is proportional to crack length. Therefore, as the crack length increases, so does the load applied to the crack faces. This causes an increased tendency of the crack faces to open, which in turn produces a rise in the SIFs and facilitates RCF crack propagation. The amount by which the RCF crack opens during a loading cycle is proportional to the rate at which it will propagate. However, it should be kept in mind that the analyses discussed in this thesis are under the hypothesis of the crack being fully flooded at the start of the simulation. Obviously, while for short cracks this hypothesis is realistic, for longer cracks it may not be valid as penetration of the fluid within the crack will be a complex function of crack length,

bearing speed and viscous properties of the fluid (capillary effects might also play a role [47]). The investigation of crack filling is however outside the scope of the present contribution.

Figures 4.15a & b show a comparison between the stress intensity factors obtained using the current coupled finite volume (CFV) model, a Squeeze Oil Film (SOF) model [1], an uncoupled fluid pressure model (FPM), characterised by a constant pressure applied along the crack faces [4, 121, 159], and an uncoupled tapered pressure model (TPM) [4, 160], characterised by a pressure varying linearly along the crack faces. It should be noted that all the models from the literature assume that the behaviour of the fluid within the crack is not directly coupled to the solution of the problem at the contact interface, and therefore the pressure at the crack mouth is arbitrarily defined.

It is immediately clear that the coupled model proposed by the author gives considerably different results to those produced by any of the models already available in the literature. These differences are twofold. Firstly, the current coupled model captures the physics of the problem and allows following the evolution of the fluid/solid interactions without introducing approximations and/or hypothesis on the evolution of the fluid pressure within the crack. This is achieved by directly computing the effect of the changing crack film shape on the fluid pressure and of the fluid pressure on the fluid flow both inside and outside the crack. This is not possible using other existing models. The uncoupled methodologies in the literature tend to provide an imprecise prediction of the crack displacement history and, as a consequence, of the evolution of the stress

intensity factors within the loading cycle [121]. This may lead to significant differences in the predicted crack propagation rates when using a Paris-type crack propagation law [117, 121, 161, 162].

Secondly, from Figs. 4.17a & b it is clear that the range of stress intensity factors (defined as $K_{max} - K_{min}$ for both mode I and mode II) at the crack tip of RCF cracks is strongly affected by the assumptions made at the crack mouth. In the example considered by the author, the coupled approach produces a reduced range of SIFs as a result of the feedback mechanism created by the interaction between the fluid film in the crack and the fluid film on the surface. Any closure or opening of the crack is driven by the surface pressure. However, when the surface pressure causes a variation in the crack shape; lubricant must be drawn from the surface film or pushed into the surface film; this causes a necessary fluctuation in the surface pressure and reduction in the flux. In this way, a physical feedback loop serves to "damp" the flux between the two sections of the lubricant film and the deflections of the crack face. This limits both the maximum rate of opening and the maximum rate of closure at the crack mouth. As a direct result this gives a reduction in the range of the SIFs; implying a lowering of the predicted mode I and mode II driven crack propagation rates with respect to models which do not employ a fully coupled approach.

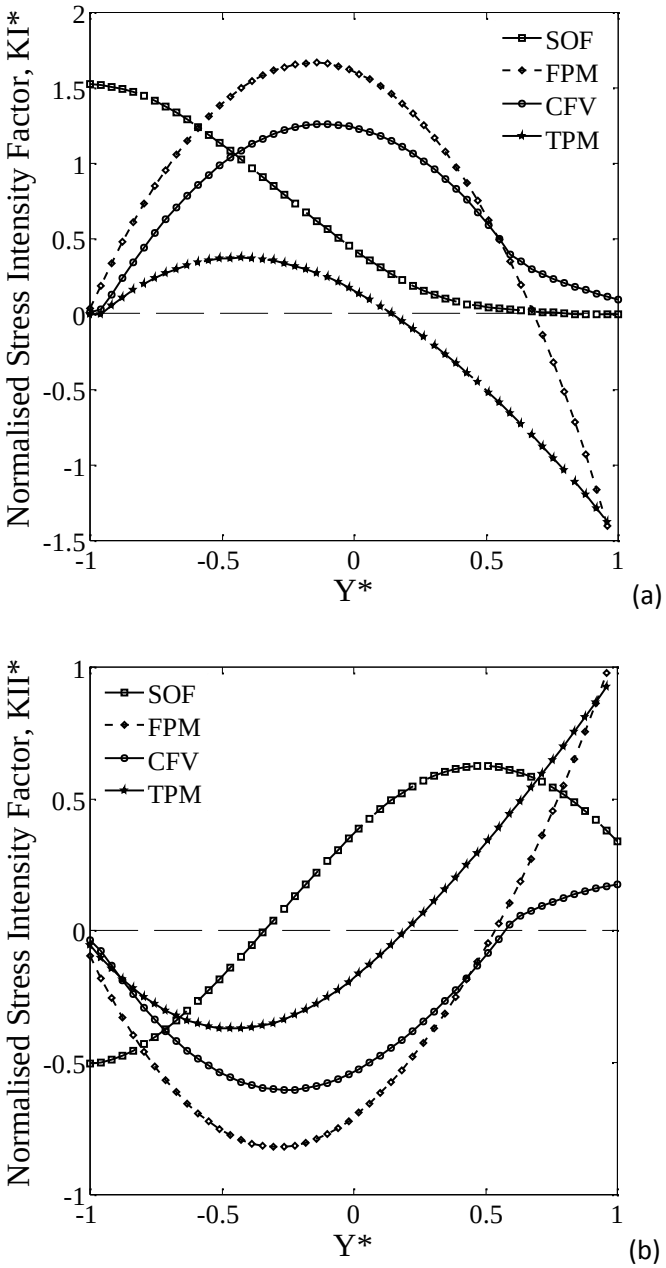


Figure 4.17 – Comparison of the evolution of the normalised stress intensity factors predicted by the present coupled finite volume (CFV) approach, a Squeeze Oil Film (SOF) model [1], an uncoupled fluid pressure model (FPM) , and an uncoupled tapered pressure model (TPM) from the literature for Case 2 in Table 1: (a) Mode I, and (b) Mode II.

4.5 Summary

In summary, the author has presented a novel solution to a problem in which a single inclined crack passes through a lubricated rolling line contact. To achieve this, a coupled fluid–solid solver has been developed that uses Linear Elastic Fracture Mechanics (LEFM) to model the solid body and a Finite Volume (FV) formulation of the Reynolds equation to model the lubricant film. This approach predicts differences in both the evolution and the range of the stress intensity factors computed at the crack tip of a typical RCF crack when compared to 'fluid pressure' models available in the literature. These differences result primarily from the coupling between the fluid within the crack and the fluid film on the surface, through quantifying the flux at the crack mouth, and serve to demonstrate the importance of considering the surface film. Given similar material characteristics, the results presented in Figs. 4.17a & b obtained using the coupled approach developed by the author suggest a reduced crack propagation rate compared to the literature when a LEFM-based approach, such as Paris' Law is applied [117, 121, 161, 162]. This leads to an increase in predicted component lives, which gives a more realistic outcome with respect to the estimates produced by existing models available in the literature. The existing model are known to over-predict crack propagation rates [121] and therefore only provide a lower bound on components fatigue life.

Chapter 5

Elastohydrodynamic (EHL) Crack Model

5.1 Introduction

Elastohydrodynamic lubrication is defined as “the mechanism that describes the separation by a lubricant film of two elastic machine elements loaded against each other and in relative motion. In this context, machine elements means two contiguous bodies whose surface geometries would put them in point or line, light touching contact. Furthermore they are not necessarily purpose-built to be supported by a lubricant film” *Gohar* [164].

The transition from a HL to an EHL solution means introducing the elastic deformation of the surfaces of the rolling bodies that are separated by the lubricant film. The roller and the cracked plane, shown in Fig. 5.1, are therefore allowed to deform and are combined with the solution of the deformable crack described in the HL method outlined in Chapter four. This chapter develops this model further; it applies the same general coupling methodology for the fluid pressure and the solid deflection to solve for the coupled RCF crack deflection and EHL. Furthermore, to render the formulation more

realistic, the simulations are now performed with load control by maintaining constant load throughout the loading cycle and calculating the surface lubricant film shape, which is no longer imposed as in the previous chapter. Pressure effects such as piezoviscosity and compressibility will also be considered in this chapter and implemented in the solver. The EHL solution is, like the HL solution, based on a fluid/solid interaction algorithm that captures the interaction between the fluid pressure and the solid deflection by means of a coupled finite volume and the distributed dislocation solver.

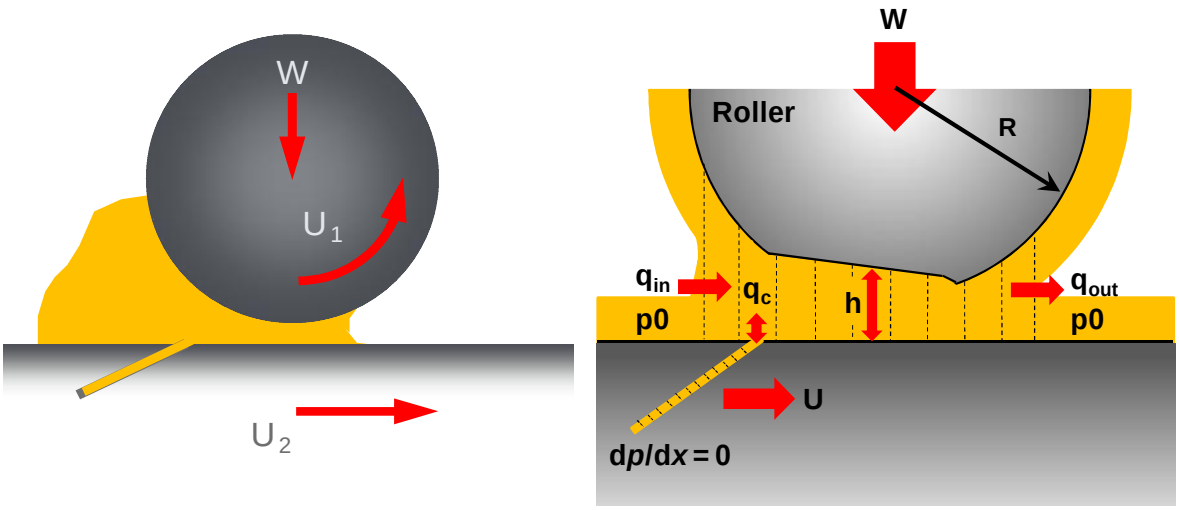


Figure 5.1.Diagram (a) and schematic (b) of the coupled EHL and RCF crack problem

A schematic of the physical problem to be considered in this chapter is shown in Fig. 5.1b. A roller is loaded against a cracked half-plane and the two bodies are separated by a thin fluid film. The solution is defined by the contact load, W, the lateral speed, $0.5*(U_1 + U_2)$, the radius of the roller, R, the viscosity, μ, and the density of the lubricant,

ρ. All other variables are calculated with the iterative algorithm. The surface film shape, the crack film shape, the contact width and the film pressures are found by imposing, and maintaining, the contact load and solving for the elastic deflections. The fluid solution used in this chapter is therefore a fully coupled EHL algorithm.

The following simplifying assumptions are made when formulating the problem; they include the assumptions applied in Chapter 3 and 4 and an additional assumption needed to define the piezoviscosity and the compressibility of the fluid:

1. The solid model obeys linear elasticity;
2. The crack surface and outer surfaces are perfectly smooth;
3. The problem can be modelled in 2D using the plane strain assumption;
4. The radius of curvature of the roller is much larger than the contact region;
5. The fluid domain is always fully flooded;
6. The conditions are isothermal;
7. The lubricant is Newtonian;
8. The Doolittle pressure viscosity [165] and Dowson pressure density model [166] are taken to be accurate and correct.

The assumptions have been addressed and justified in the previous chapters. Assumption (8) has been justified experimentally [165], though not by the author, and the pressure-density relationship has been chosen for its simplicity, as the aim here is to

test the effect of compressibility on the system response, and because of this is the most widely applied in the literature [164, 166].

5.2 Modelling Strategy and Formulation

The crack problem is once again solved using LEFM ignoring the elasto-dynamic effects for the solid while resolving the transient fluid flow outside and inside the crack. The two bodies are elastic and deform to create a smooth conformal line contact, where the surface roughness, or asperity height, is considered to be small enough compared to the length of the contact width so as to not affect the elastic solution or the film hydrodynamics [164].

The first step of the modelling strategy is once again to divide the contact loading cycle into a series of discrete, sequential, time steps where each time step is defined by a different crack position in the contact. At each time step, *t*, the full EHL solver, that calculates the fluid pressure and film thickness on the surface, is coupled with the solver for the crack film thickness and crack film pressure, already presented in Chapter four. The algorithm used to evaluate the EHL solution is the forward iterative scheme originally presented by Gohar [164]. The method involves using a series of embedded iterative loops and is explained in detail later in this chapter. The coupling between the fluid and the solid solver, the finite volume fluid solver and the distributed dislocation (or BEM) solid solver, is then imposed using the same method of fluid/solid coupling discussed in Chapter four.

5.2.1 Fluid Solver

The fluid solver captures the effect of fluid pressurisation in an EHL contact, where a RCF crack is present on one of the contacting surfaces. The framework of the solution is the same as that used in Chapter four, where the fluid domain is split into two separate fluid films that are coupled at the crack mouth, where flow into or out of the crack may occur, and again the fluid solution is formulated based on mass conservation. The effect of pressure dependant viscosity and density are introduced, this means the viscosity and density are no longer constant and requires the Reynold's equation to be re-formulated where the constant density and viscosity terms are replaced with pressure dependant functions.

5.2.1.1 Viscosity

Lubricant properties are pressure dependant and two significant properties affected by high pressures are viscosity and density [166]. If we consider viscosity first, from a tribological perspective, it is one of the most important properties of a lubricant because it is a determining factor of the film thickness and pressure in the fluid film. The viscosity of the fluid can be defined as the resistance to flow that arises from molecular forces and internal friction from the relative movement of molecules. Numerous studies have investigated the rheological behaviour of lubricants in EHL and one of the most accurate available in the literature is the free volume model, first introduced by Doolittle [165] in

1951. It is based on the principle that the resistance to flow of a liquid increases relative to the volume of molecules present, per unit volume. The volume variation with pressure is described by an equation presented by Tait [167]. It considers the occupied volume of the closest packed liquid molecules and the free volume available in the liquid for molecular transitions. This model was originally developed by Eyring et al in 1940 [168], but Doolittle [165] proposed the first free-volume model based on a physically-grounded concept:

$$\eta = \eta_0 \exp\left[B \frac{V_{occ}}{V_0} \left[\frac{1}{\frac{V}{V_0} - \frac{V_{occ}}{V_0}} - \frac{1}{1 - \frac{V_{occ}}{V_0}} \right] \right] \tag{5.1}$$

where the volume variation is described by the Tait equation of state [167]:

$$\frac{V}{V_0} = 1 - \frac{1}{K_0' + 1} \ln\left[1 + \frac{p}{K_0} (1 + K_0') \right] \tag{5.2}$$

B, K_0, K'_0, V_{occ} and V_0 are the Doolittle parameters: bulk modulus at $p = 0$, pressure rate of change of the bulk modulus at $p = 0$, dimensionless coefficients for poiseuille flow, reference temperature, occupied volume and volume at ambient pressure respectively.

Comparing the predicted viscosity as a function of pressure computed using the Doolittle model with some experimental results at room temperature obtained by SKF, a good agreement is found for the tested pressure range, shown in Fig.5.2.

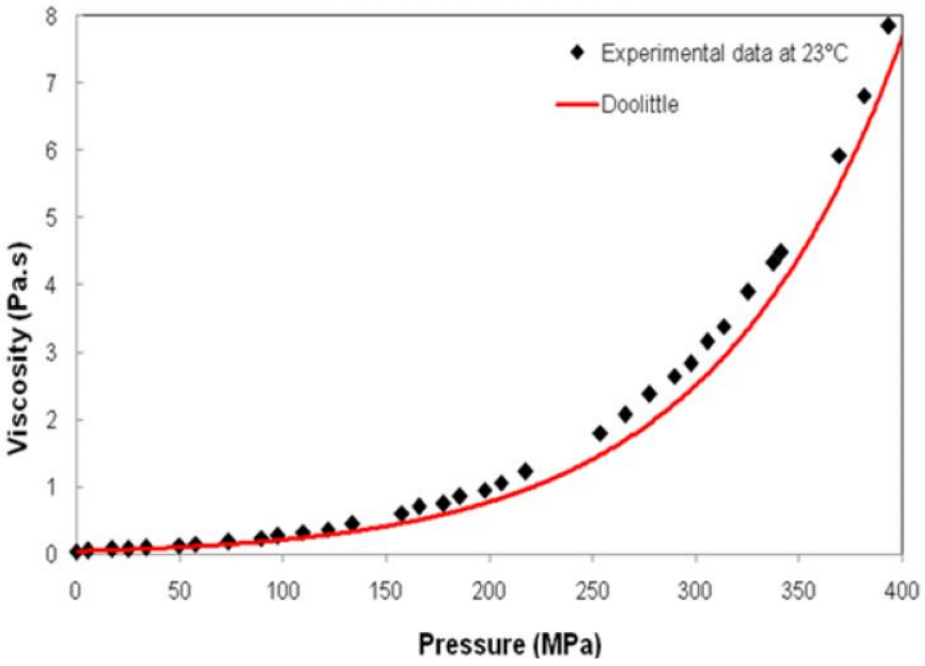


Figure 5.2.Comparison between Doolittle viscosity model and experimental results

5.2.1.2 Compressibility

The second pressure dependant lubricant property to be considered is the density. The rate of variation of density with pressure is roughly linear at low pressure but decays at high pressure, where the limit of compression of mineral oil is around 25 % [166], giving a maximum density increase of around 33%. The compressibility formula used in this

model, Eq. (5.3), is based on figures supplied by the Thornton Research Centre, where the relationship has been experimentally extrapolated.

$$\rho = \rho_0 \left(1 + \frac{0.009p}{1 + 0.026p} \right) \tag{5.3}$$

Where ρ is the calculated density, ρ_0 is the initial density and p is the pressure. It should be noted that this formula for compressibility is strictly only valid for mineral oil being compressed by steel rollers [166].

5.2.3 Fluid Formulation

The fluid formulation in this chapter is essentially an extension of the model proposed in Chapter 4, to include the elastic deformation of the contacting bodies. This is achieved by removing the imposed surface film thickness and replacing it with the calculated film thickness resulting from the applied load. The solution has a series of convergence criteria based upon the rate of change of the film pressure, rate of change of flux, and the integral of the pressure being equal to the applied load, all of which must fall within an imposed convergence tolerance. The fluid model is posed for a pressure dependant fluid where the effect of pressure on viscosity and density are introduced; however, thermal effects are ignored.

The Reynolds equation Eq. (4.9) is modified to include the non-linear viscosity and density pressure dependences introduced in the previous sub-sections. The viscosity and density are evaluated using values from the previous iteration step as a starting point; however, because the variation in pressure becomes very small as the solution converges, the error in the density and the viscosity becomes negligible, the method for evaluating the viscosity and the density is therefore explicit.

The friction effect on the surfaces of the cracked body is also evaluated by considering the shear stress at the walls. The shear stress in a lubricant film can be expressed as:

$$\tau(x) = \left(y - \frac{h(x)}{2} \right) - \frac{\partial p(x)}{\partial x} \frac{h(x)}{\eta} U \tag{5.4}$$

Therefore the wall stress, *i.e.* the shear stress acting on the surface at $y = 0$, is:

$$\tau(x) = \left(- \frac{h(x)}{2} \right) - \frac{\partial p(x)}{\partial x} \frac{h(x)}{\eta} U \tag{5.5}$$

The shear stress induced by the shearing resistance of the lubricant will therefore replace the friction coefficient between the sliding surfaces introduced in the dry crack analysis, in Chapter 3.

5.2.4 Solid Solver

The solid solver evaluates the effect of fluid pressure acting on the cracked body. The superposition principle is once again employed and the framework for the solid solution in this chapter is similar to that of Chapter 4. However, the EHL problem contains the added element of evaluating the displacement of the surface of the half-plane and the roller because the lubrication regime is now elastic; this displacement will be denoted as problem (III). Therefore to evaluate the stress and deformation fields in the solid bodies from the effect of the EHL loading condition the solution to three sub-problems is needed: problems (I) and (II) have been already discussed in detail in Chapters 3 and 4 and problem (III) is discussed in this chapter. The stress solution is once again formulated based on the following boundary conditions, also expressed in Eq. (3.3):

$$\begin{aligned} &N(\hat{x}) = p_f && a_{op} < \hat{x} < a \\ &S(\hat{x}) + fH(\hat{x} - a_{op})N(\hat{x}) = 0 && 0 < \hat{x} < a_{op}. \end{aligned} \tag{5.6}$$

using Eqs (3.1 - 3.24) the unknown stress intensity factors and the crack shape can be found.

Problem (III) evaluates the effect of the pressure generated inside the EHL contact on the deformations of the roller and the cracked half-plane, shown using the red lines in Fig 5.3. This element of the mathematical model is needed to solve the EHL film

thickness for the fluid solver. Problem (III) is also broken down into two problem subsets, one which evaluates the effect of the EHL contact pressure on the half-plane and the roller, in absence of the crack, and the other which evaluates the deformation induced by the presence of the crack on the surface of the half-plane. The first of the problem (III) subsets is solved using the Muskelishvili theorem applied to displacements, Eq. 3.8, from chapter three. The second requires a numerical integration scheme, based on a series of influence functions that are combined with the dislocation density found in problem (II), to give the displacement anywhere in the half-plane (x,y) due to a dislocation located at a point (c,d).

The surface deflections are needed to be able to capture the coupling between the surface fluid pressure and the change in the surface film shape induced by the elastic deformations; these in turn affects the film thickness in the EHL model and the fluid solver needs to be updated after the surface deformations have been computed. To complete the formulation, the effect of the crack mouth opening on the surface film should also be included, since the opening creates a step in the film thickness across the crack mouth.

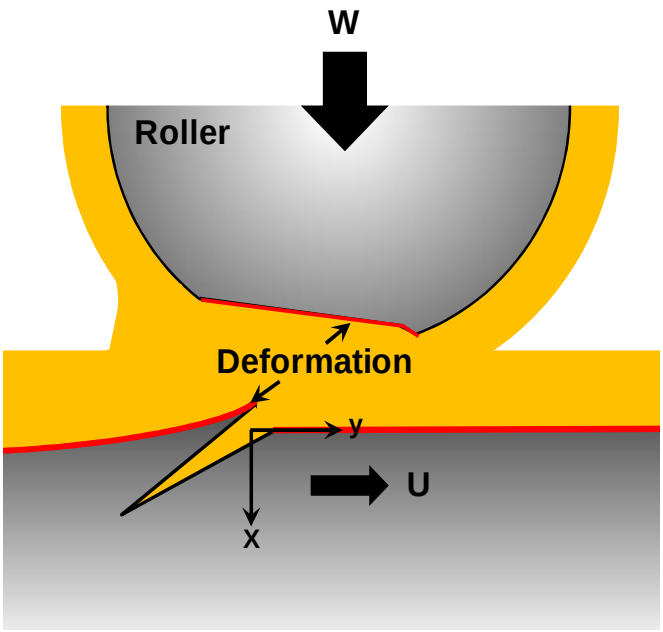


Figure 5.3 Deformation that is calculated using problem III in the solid solver

The starting point for problem (III) is the formulation used for the evaluation of the displacement induced by a dislocation near the interface between two bonded half-planes (effectively giving a full plane, or infinite body made of two half-planes). This is expressed using the notation of Dundurs and Mura [169] which gives the displacement at a point (*x,y*) due to a dislocation (*c,d*) near a straight interface in the body where the dislocation is present:

$$e_x^{dd}(x,y) = \frac{1}{2®(© + 1)}\left(b_x D_{xx}(x,y,c,d) + b_y D_{yx}(x,y,c,d)\right) \qquad (5.7a)$$

$$e_y^{dd}(x,y) = \frac{1}{2®(© + 1)}\left(b_x D_{xy}(x,y,c,d) + b_y D_{yy}(x,y,c,d)\right) \tag{5.7b}$$

where D_{ij} are displacement influence functions reported in [55] and b_x and b_y are the burgers vector components and κ is the Kosolo'vs constant for the body with non-zero rigidity [55]. The formulation is then modified, to account for the fact that the dislocation is near the surface of a single half-plane. This is done by setting the rigidity of the second body (i.e. the Young's modulus) to zero and then re-deriving the influence functions, also reported in [55]. This makes the second bonded half-plane infinitely more deformable than the first, which creates the equivalent of a free surface at the interface between the two bonded half-planes. The burgers vector values are solved with respect to the local coordinate system rotated to the angle of incline of the crack (θ). The Burgers vector components are expressed in the rotated coordinate system by multiplying by the rotation matrix, Eq. 3.11

By substituting Eq. 3.11 back into Eqs. (5.7a & b) and by applying the transformation matrix, the influence functions for the formulation of the displacement are transformed to be solved into the rotated coordinate system in terms of the rotated Burgers vector as:

$$e_x^{dd}(\hat{x},\hat{y}) = \frac{1}{2®(© + 1)}\left(b_{\hat{x}} D_{\hat{x}\hat{x}}(\hat{x},\hat{y},\hat{c},\hat{d}) + b_{\hat{y}} D_{\hat{y}\hat{x}}(\hat{x},\hat{y},\hat{c},\hat{d})\right) \tag{5.8a}$$

$$e_y^{dd}(\hat{x},\hat{y}) = \frac{1}{2\text{®}(\text{©}+1)}\left(b_{\hat{x}} D_{\hat{x}\hat{y}}(\hat{x},\hat{y},\hat{c},\hat{d}) + b_{\hat{y}} D_{\hat{y}\hat{y}}(\hat{x},\hat{y},\hat{c},\hat{d})\right) \tag{5.8b}$$

where $\hat{x} = \cos^{-}(x)$, $\hat{y} = \sin^{-}(x)$, $\hat{c} = \cos^{-}(c)$, and $\hat{d} = \sin^{-}(c)$, and $D_{\hat{x}\hat{x}}$, $D_{\hat{y}\hat{x}}$, $D_{\hat{x}\hat{y}}$, $D_{\hat{y}\hat{y}}$ are the transformed kernels. If we now consider the effect of a continuous distribution of infinitesimal burgers vectors along the crack line, whose densities are:

$$B_{\hat{x}}(\hat{c}) = \frac{db_{\hat{x}}(\hat{c})}{d\hat{c}};\ B_{\hat{y}}(\hat{c}) = \frac{db_{\hat{y}}(\hat{c})}{d\hat{c}} \tag{5.9}$$

The displacement at a point due to a series of dislocations becomes the integral below:

$$e_{\hat{x}}^{dd}(x,y) = \frac{1}{2\text{®}(\text{©}+1)}\left(\int_0^a \left(B_{\hat{x}}(\hat{c}) D_{\hat{x}\hat{x}}(x,y,\hat{c})\right)dc + \int_{a_{op}}^a \left(B_{\hat{y}}(\hat{c}) D_{\hat{y}\hat{x}}(x,y,\hat{c})\right)dc\right)\ \ 0 < \hat{c} < a$$

(5.10a)

$$e_{\hat{y}}^{dd}(x,y) = \frac{1}{2\text{®}(\text{©}+1)}\left(\int_0^a \left(B_{\hat{x}}(\hat{c}) D_{\hat{x}\hat{y}}(x,y,\hat{c})\right)dc + \int_{a_{op}}^a \left(B_{\hat{y}}(\hat{c}) D_{\hat{y}\hat{y}}(x,y,\hat{c})\right)dc\right)\ \ a_{op} < \hat{c} < a$$

(5.10b)

Where the dislocations are distributed along the crack line, $\hat{c}$, and the coordinates at which the displacement is being evaluated (*x,y*) are distributed along the surface of the

half-plane. The integral equations are again normalised using the discretisation scheme in Eq. 3.19, which gives the following:

$$e_{\hat{x}}^{dd}(x,y)=\frac{1}{2\pi(\kappa+1)}\left(\int_{-1}^{1}\left(B_{\hat{x}}(u)D_{\hat{x}\hat{x}}(x,y,u)\right)du+\int_{-1}^{1}\left(B_{\hat{y}}(u)D_{\hat{y}\hat{x}}(x,y,\bar{u})\right)d\bar{u}\right)\quad -1<\bar{u}<1$$

(5.11a)

$$e_{\hat{y}}^{dd}(x,y)=\frac{1}{2\pi(\kappa+1)}\left(\int_{-1}^{1}\left(B_{\hat{x}}(u)D_{\hat{x}\hat{y}}(x,y,u)\right)du+\int_{-1}^{1}\left(B_{\hat{y}}(u)D_{\hat{y}\hat{y}}(x,y,\bar{u})\right)d\bar{u}\right)\quad -1<u<1$$

(5.11b)

To evaluate the singular integrals it is again necessary to express the dislocation densities as a product of bounded functions and a weight function, see Eq 3.12. This then gives:

$$e_{\hat{x}}^{dd}(x,y)=\frac{1}{2\pi(\kappa+1)}\sum_{k=1}^{n}\left[\frac{2\pi(1+u_k)}{2n+1}\alpha_{\hat{x}}(u_k)D_{\hat{x}\hat{x}}(x,y,u_k)+\frac{2\pi(1+\bar{u}_k)}{2n+1}\alpha_{\hat{y}}(\bar{u}_k)D_{\hat{y}\hat{x}}(x,y,\bar{u}_k)\right]\quad i=1,\ldots,n$$

(5.12a)

$$e_{\hat{y}}^{dd}(x,y)=\frac{1}{2\pi(\kappa+1)}\sum_{k=1}^{n}\left[\frac{2\pi(1+u_k)}{2n+1}\alpha_{\hat{x}}(u_k)U_{\hat{x}\hat{y}}(x,y,u_k)+\frac{2\pi(1+\bar{u}_k)}{2n+1}\alpha_{\hat{y}}(\bar{u}_k)U_{\hat{y}\hat{y}}(x,y,\bar{u}_k)\right]\quad i=1,\ldots,n$$

(5.12b)

The dislocation densities are evaluated using the distributed dislocation technique as discussed in chapter three Eqs. (3.1 – 3.23), they can be substituted into Eqs. (5.8a & b) and the displacement values at any point (*x,y*), due to the presence of the crack, can then be obtained.

The rotation that is applied to the mathematical formulation inclines the dislocations at an angle that is in line with the crack. This means that the displacements that are calculated are also expressed in the rotated coordinate system, $e_{\hat{i}}^{dd}$. Therefore the displacements for the surface of the half-plane have to be rotated back into the global co-ordinate system by multiplying by the inverse of the rotation matrix. The displacement at the surface of the half-plane due to the coupled effect of the crack opening and the film pressure in the contact is evaluated by combining the deflections induced by the distributed dislocations and those due to the surface triangular pressure elements. The total deflection at the surface can therefore be expressed as:

$$e_x^{ST}(0,y) = e_x^{Sdd}(0,y) + e_x^{Str}(0,y) \tag{5.13a}$$

$$e_y^{ST}(0,y) = e_y^{Sdd}(0,y) + e_y^{Str}(0,y) \tag{5.13b}$$

where the superscript *S* denotes surface. The displacement of the crack can also be evaluated as the sum of the effect of the distributed dislocations and the Muskelishvili potential theorem along the inclined crack length, $(\hat{x},0)$:

$$e_{\hat{x}}^{CT}(\hat{x},0) = e_{\hat{x}}^{Cdd}(\hat{x},0) + e_{\hat{x}}^{Ctr}(\hat{x},0) \tag{5.14a}$$

$$e_{\hat{y}}^{CT}(\hat{x},0) = e_{\hat{y}}^{Cdd}(\hat{x},0) + e_{\hat{y}}^{Ctr}(\hat{x},0) \tag{5.14b}$$

where the superscript *C* denotes crack. However, it should be noted that if we are only interested in the relative displacements between the crack faces, the methodology described in problem (III) is not needed, because the displacement due to the dislocations along the crack length can be found directly by integrating the dislocation density, as shown in Eq 3.15.

5.2.5 Coupled EHL Algorithm

The EHL algorithm is based on the Forward Iterative Method: the scheme requires the Reynolds equation to be solved for the fluid pressure, which is then used by the solid solver to find the film thickness in the crack and the surface film; this coupling procedure is widely used and explained at length in the literature [164].

The Forward Iterative Method implemented in this model is taken directly from [164]; the novelty of the technique resides in incorporating the effects that the presence of an RCF crack has on the EHL solution. The coupling between the fluid films, the film between the contacting elements and the film within the crack is performed using the method described in Chapter 4 Eqs. (4.31 – 4.34); however, the full algorithm contains

extra iterative loops. Furthermore, the fluid formulation developed in Chapter 4 is now enriched to include the effects of pressure on the lubricant properties where the EHL coupled algorithm also accounts for the solid deformation. The numerical procedure implemented in the fully-coupled solver is outlined in Fig. 5.4 and explained in the following paragraphs.

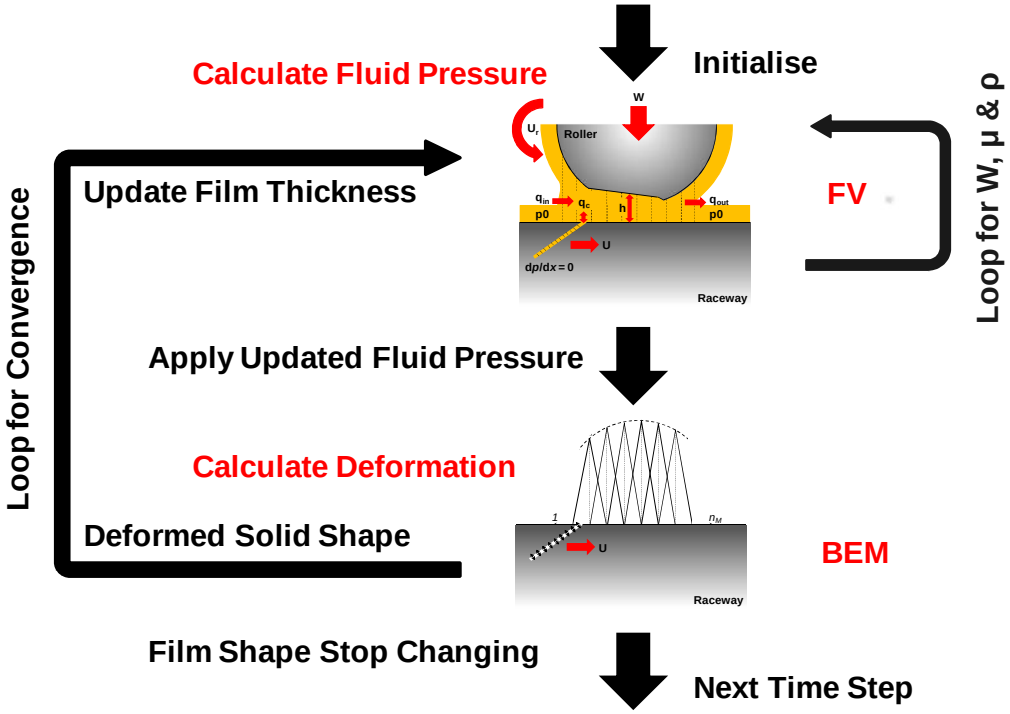


Figure 5.4 Schematic of the coupling of the segregated fluid/solid solver

For a chosen load, roller and half-plane material properties and geometry, first the dimension of the Hertzian footprint is calculated based on the theory of elastostatic contacts. This is used to initialize the solver, together with the boundary conditions,

fluid characteristics and loading conditions. The procedure adopted is now outlined in detail.

1.1.1.1. Boundary Conditions

In order to preserve computation simplicity the inlet and outlet boundary conditions for the fluid flow in the contact are based on the Swift-Steiber condition of zero pressure, these are of the Dirichlet type boundary conditions. This is deemed sufficiently accurate because the high pressures in the contact make small changes in the inlet pressure and the cavitation pressure at the outlet insignificant. The boundary conditions imposed on the crack film are the (coupling) flux at the mouth, q_c, and the Neumann condition of a zero pressure gradient at the crack tip, which are true physical boundary conditions.

1.1.1.2. Initial Conditions

At the start of the computational procedure, it is assumed that the pressure distribution is Hertzian and it is applied over the equivalent dry contact footprint; zero pressure is applied outside the predicted Hertzian contact region in the remaining domain. This is true at the first time step, after the first time-step the converged pressure from the previous time-step is used to initialize the solver. This implies that the first time-step will take longer than each subsequent time-step to solve as the initial guess provides a very crude approximation of the real pressure profile.

1.1.1.3. Computational Algorithm

The following algorithm is used to link the fluid and solid solvers. The solution method and the coupling of the different solvers are explained here. Within each time-step the following algorithm is applied.

Initialisation

1. To begin with, materials, geometry, computation zone (contact length) and mesh characteristics are defined. Then the contact load, W, the transverse speed, U, are defined and the initial un-deformed film profile, $h_{F0}(y)$, is initialised based on the shape of the roller, along with the film thickness in the crack, $h_{C0}(\hat{x})$, which is initially set to be constant and equal to the crack tip radius outlined in chapter 4.
2. Assume p_s is the Hertzian pressure distribution at the first time-step or the converged pressure from the previous time-step in subsequent time-steps.
3. Guess a value of the central EHL film thickness h_0 to be added to $h_{F0}(y)$ to generate a film shape. An initial value of h_0 = 1μm has been used for all the simulations run in this thesis based on standard EHL calculations performed under the loads and speeds tested.

Start Outer Loop

4. Calculate the film thickness distribution by:
    a. Using the pressure distribution p_s calculate the deflections on the half-plane surface and in the crack using the solid solver.

b. Find the film thickness on the surface and in the crack, $e_x^{ST}(y)$ and $e_{\hat{y}}^{CT}(\hat{x})$, from the deformation combined with the central film thickness, $h_{F0}(y)$, and the crack tip radius, $h_{C0}(\hat{x})$, respectively:

$$h_F(y) = h_{F0}(y) + e_x^{ST}(y) \tag{5,15a}$$

$$h_C(\hat{x}) = h_{C0}(\hat{x}) + e_{\hat{y}}^{CT}(\hat{x}) \tag{5,15b}$$

Start Intermediate Loop

5. Enter the EHL pressure distribution loop by initializing the pressure as p_h, which for the first iteration is taken as zero. Then the flux values, q, are calculated. The flux, q_c, is also calculated in the cell which contains the crack.
6. Using the p_h values above the density values, ρ, and the viscosity values, η, are calculated.
7. The coefficients of the finite volume form of the Reynolds equation are then calculated.

Start Innermost Loop

8. The innermost loop is started by solving the finite volume formulation of the Reynolds equation using a tri-diagonal matrix algorithm.

9. The values of q are obtained and checked for convergence with the previous values from step (5)
    a. If not converged, modified values of q are calculated by under-relaxation, producing new values of p_h. The algorithm returns to step (6).
    b. If converged, the algorithm comes out of the innermost loop and moves to the next step.

End Innermost Loop

10. New values of p_h are calculated from q.
11. p_h is then integrated to produce a load W.
12. Is W within the specified tolerance?
    a. No: Adjust the central film thickness h_0 and return to step (5).
    b. Yes: Move to next step.

End Intermediate Loop

13. The distribution of p_s and p_h are checked for convergence.
    a. If not converged, new values of p_s and p_h are calculated and the algorithm returns to step (4).
    b. If converged to the specified tolerance the solution is obtained.

End Outer Loop

14. Move to the next time step, update the crack position and return to step (3).

1.1.1.4. Convergence Criteria

Within each of the iterative loops a set of convergence criteria is imposed on the dimensionless variables, where the convergence criteria imposed to stop the outer most loop is (where all are relative tolerances):

$$\sum_{i-1}^{N} \left| p_{hi} - p_{si} \right| \leq 1e^{-3} \tag{5.16}$$

The convergence criteria for the intermediate loop is:

$$\left| W_{required} - W_{otained} \right| \leq 1e^{-3} \tag{5.17}$$

and for the innermost loop the convergence criteria is:

$$\sum_{i-1}^{N} \left| q_{inew} - q_{iold} \right| \leq 1e^{-3} \tag{5.18}$$

Once these convergence criteria are satisfied the solution is obtained.

1.1.1.5. Relaxation Factors

The solution is very sensitive to large changes in pressure or flux; therefore both have to be relaxed when solving the algorithm to avoid problems with the numerics. The relaxation method used is a standard method from the literature [164] where the under-relaxation used for the pressures in the outermost loop is;

$$p_{s_{new}} = p_{s_{old}} + \alpha_p (p_h - p_{s_{old}}) \tag{5.19}$$

and the under-relaxation for the innermost loop is;

$$q_{new} = q_{old} + \alpha_q (q - q_{old}) \tag{5.20}$$

The $^{a}_{p}$ and $^{a}_{q}$ values in both cases are chosen to avoid numerical issues while also trying to optimize the number of iterations required to obtain the correct solution.

5.3 Validation & Convergence of the EHL algorithm

The coupling between the fluid films, the applicability of the distributed dislocation technique to this type of problem and the Muskelishvili potential theorem have been validated in Chapters 3 and 4. Therefore, the EHL solver requires validation at this stage. This can be done by means of a comparison with an EHL solution from the existing literature; in this case the solution used for comparison is that of Dowson and Higginson [166] (case (c) shown in Fig 9 of the paper) . The pressure in the film and the film shape will be compared for a given contact load (1.9lb/in), Young's Modulus (7000tonnes/in^2), roller radius (78in), speed (3.22ft/s), and for given, and constant, viscosity (1.37poise) and density (500lb/yard^3). It should be noted the system of units adopted for this plot conforms to the original outputs from the Dowson and Higginson paper but SI units will be used in the rest of this chapter.

Figure 5.5 demonstrates that the results from the EHL algorithm and the solution from the literature show good agreement, both in terms of the calculated film pressure and the calculated film thickness. For the purpose of the validation the presence of the crack has been neglected for the calculation of the EHL film thickness and pressure because no theoretical solution currently exists for this coupling that can be used for comparison. But, based on the good agreement that is seen between this EHL model

and the results from the literature, this method for solving the EHL film pressure and film shape is taken to be accurate.

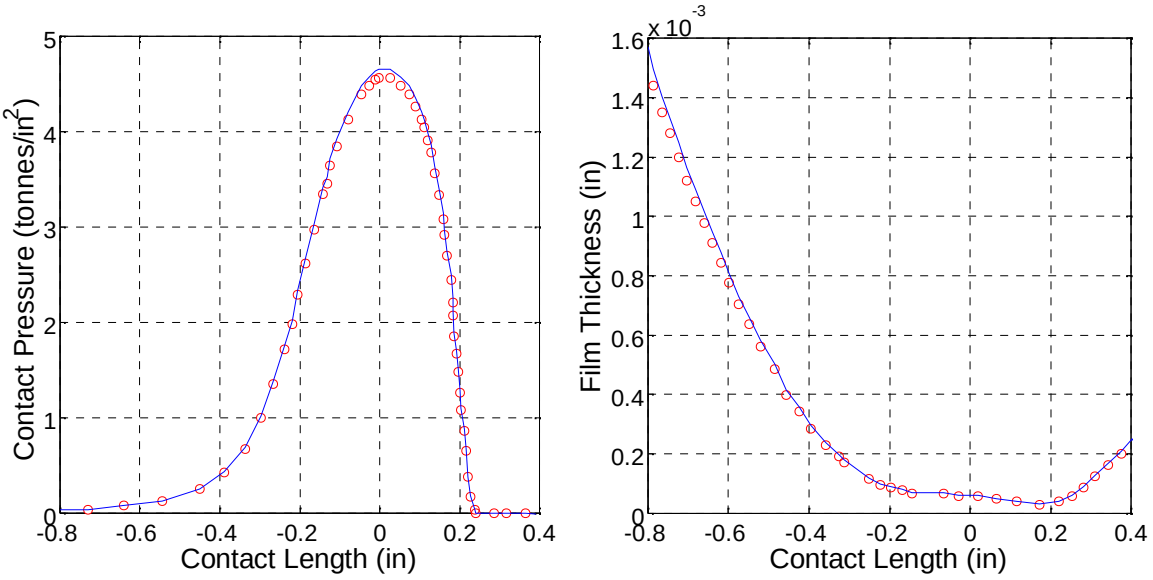


Figure 5.5 Schematic of the coupling of the segregated fluid/solid solver, where the blue line the solution form the solved used in this model and the red circles is the Dowson *et al* solution [166]

The mesh dependency of the coupled EHL algorithm has also been tested, for a cylinder on a flat surface, again solved neglecting the crack. The mesh density is incrementally increased and the film pressure and film thickness profiles are plotted and compared.

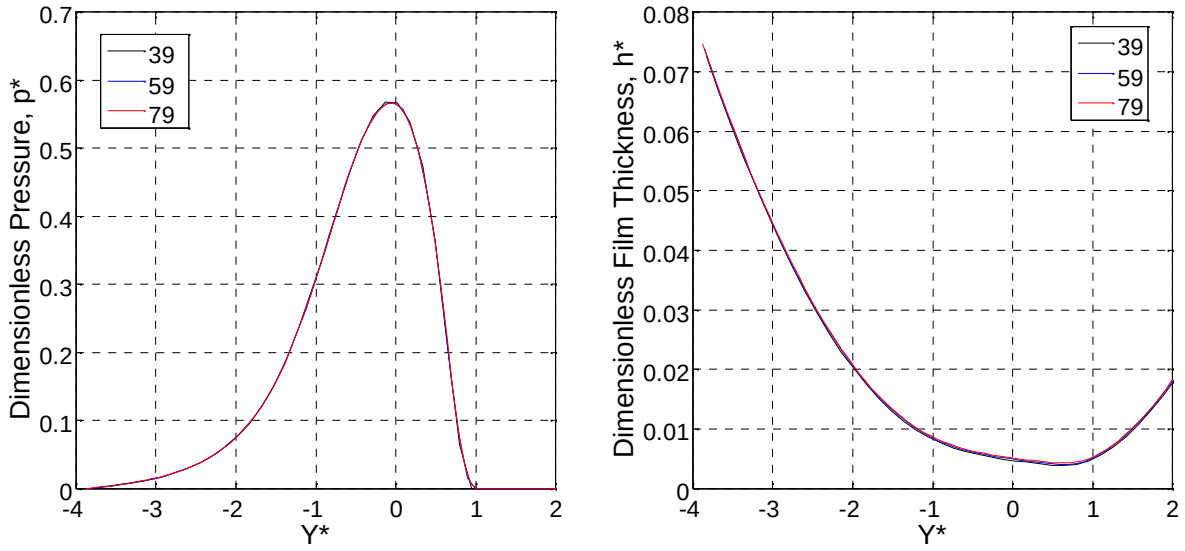


Figure 5.6 Results from different meshes for; (a) Dimensionless Pressure (b) Dimensionless Film Thickness

It can be seen, from the results shown in Fig. 5.6, that the results obtained using different meshes on the surface film rapidly approach convergence, with less than 60 nodes equally distributed along the surface providing an accurate solution for the case under consideration. This gives flexibility for the mesh to be used for evaluating the EHL film. However, the number of elements used to discretise surface film is also directly linked to the time step (d*t*): the lowest time-step that can be used in the implemented scheme corresponds to time that the crack mouth takes to move by a single mesh element. This means that more mesh elements will allow for smaller time steps. With this in mind, the resolution required in time, i.e. the minimum time step that can be taken to ensure numerical stability, will dictate the required mesh size rather than the film thickness and pressure solution. To summarise, as long as more than 39

nodes are used in the surface film the solution to the EHL model for moderate contact pressures is found to be accurate.

5.4 Results and Discussion

In this section the case of a rolling contact fatigue crack that is inclined at 25° to the surface and traversed by a loaded roller bearing is presented. This case is used to represent a typical RCF crack in a roller bearing manifold where the lubricant film separates the roller bearing from the cracked raceway. The lubricant film is pressurised due to the loading, forming an EHL film. This case reflects a real life application and is the type of lubricated contact that is found in a number of other machine components such as rail and wheel contacts. The results build on that of the idealised case studied in Chapter 4 to extend the applicability of the coupled fluid/solid methodology to the analysis of cracks in more practical scenarios, which usually involve EHL lubrication and consider the real geometry of the components under investigation.

5.4.1 HL vs EHL

The first case to be considered in this section is a comparison between the EHL model and the HL model under the same operating conditions. This will give the means to draw a direct comparison and capture the differences between the two fluid models. To facilitate this task, the deformation of the crack mouth, its effect on modifying the EHL film thickness and altering EHL film pressure is ignored. The reason for this is to

compare the results obtained with and without the surface deformation induced by the load at the contact, and to see the difference when solving the pressure based on the curvature of the roller rather and the imposed wedge shaped film, shown on Figs 4.1 & 5.1. The results for the comparison in this section will be obtained using the solid and the HL fluid solvers from Chapter 4 (see Table 5.1 - case a) and the solid and the isoviscous version of the EHL fluid solver developed in this chapter (see Table 5.1- case b). The different operating conditions to be analysed are reported in Table 5.1; note that the surface fluid film is discretised using 100 FV elements and the crack is discretised using 30 FV elements.

Case	Liquid	a	b	h_{c_0}	h_0	U_s	W^F	E	σ_Y	η	θ	k	r
a		μm	μm	nm	μm	m/s	N/m	GN/m^2	MN/m^2	Pa/s	°		mm
1	Base Oil	50	200	152	1	3	5000	210	800	0.137	25	0.325	
2	Base Oil	100	200	152	1	3	5000	210	800	0.137	25	0.325	
3	Base Oil	200	200	152	1	3	5000	210	800	0.137	25	0.325	
b													
4	Base Oil	50	200	152	1	3	5000	210	800	0.137	25		4.75
5	Base Oil	100	200	152	1	3	5000	210	800	0.137	25		4.75
6	Base Oil	200	200	152	1	3	5000	210	800	0.137	25		4.75

Table 5.1 – Operating conditions for the comparison of the HL solution and the EHL solution

The results here are once again expressed for a single load pass over the cracked half space, where for scenario (a) the load is applied in a simplified way by modelling a convergent wedge sliding over the crack and for scenario (b) the passage of a deformable roller passing over the crack is considered. The crack length, *a*, is increased from 50μm to 200μm (cases 1-3 for scenarios (a) and (b)) while all other operating conditions are maintained constant throughout, as shown in Table 5.1.

Considering first the surface film pressure for case 2, the convergent wedge model (a) and the elastohydrodynamic (EHL) solver model (b) give different pressure profiles, as shown in Fig. 5.7. This is to be expected and can be directly related to the different surface film shape that characterises the two models: the dimensionless pressure p^* is a function of the dimensionless film thickness h^*; in this case the dimensionless pressure is expressed as a function of W_F/a (the dimensional parameter used to normalise the results). In dimensional terms the maximum pressure is approximately 50 MPa and 55 MPa for the HL and EHL models respectively and the contact width is set to be 200μm for both[2].

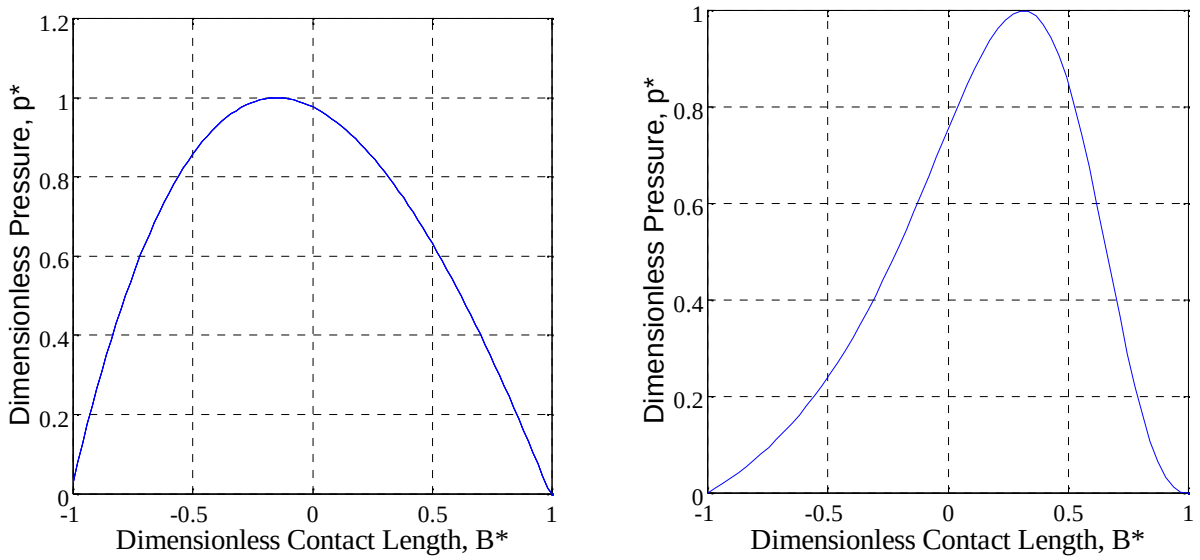


Figure 5.7 Dimensionless pressure ($\underline{p^*} = p.(W_F/a)$) plots (a) Hydrodynamic Pressure (b) EHL Pressure

[2] Note that the "contact area" for the EHL model is imposed so that it corresponds to the size of the wedge used for the HL model simply by moving inlet and outlet (and the related zero pressure boundary conditions) in accordance with the geometry used for the HL problem. This is artificial and sets the pressure to build-up in the specified area.

The film thickness obtained for scenario (a), Fig. 5.8(a), is dictated by the shape of the rigid convergent wedge; in scenario (b), Fig. 5.8(b), the film thickness is calculated using the elastic deformations imposed on the roller (4.75mm radius, *R*) by the pressurised lubricant film.

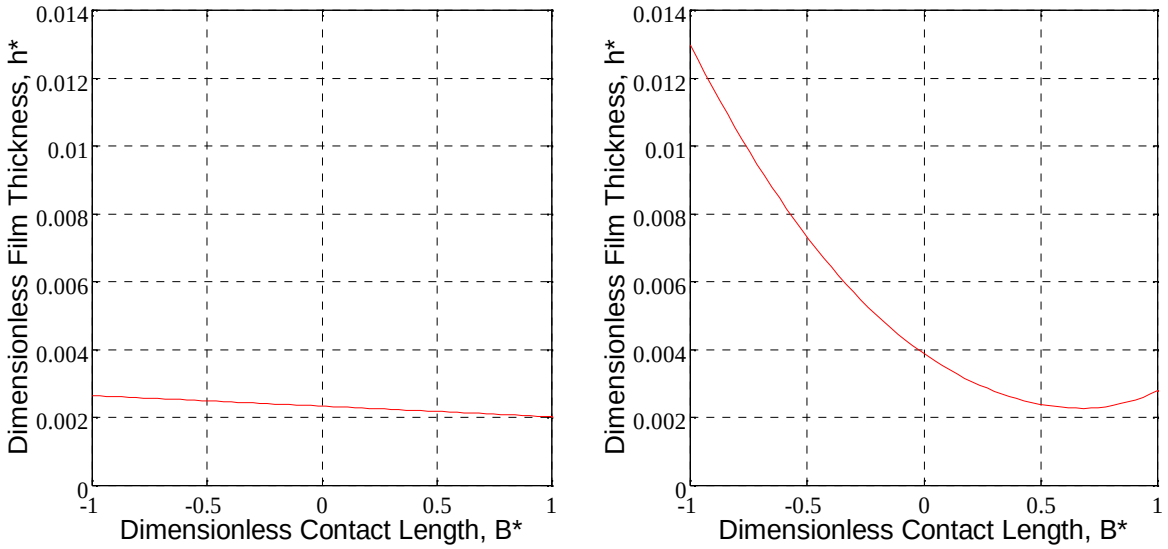


Figure 5.8 Dimensionless film thickness ($h^* = h/a$) plots (a) Hydrodynamic film thickness (b) EHL film thickness

Considering now the stress intensity factor plots *KI* and *KII* for both scenarios (a) and (b), as expected, the results are different; however, they can both be seen to be directly related to the pressure profile calculated for the surface fluid film, by comparing Figs. 5.10a & b and Figs. 5,7a & b. This is a result that is fairly compelling and clearly illustrates the strong coupling between the fluid film pressure at the surface and the evolving stress intensity factors *KI* and *KII* during a loading cycle. For *KI*, in both cases

the general trend is similar, there is an initial period where dK_I^*/dY^* > 0, then dK_I^*/dY^* = 0 followed by a period during the loading cycle where dK_I^*/dY^* < 0, shown in Figs. 5.7a & b. This is true for both scenarios (a) and (b); in both cases there exists a point, when dK_I^*/dY^* < 0, at which the stress intensity gradient changes abruptly (at around Y^* = 0.5 for the HL solution and Y^* = 1 for the EHL solution). This indicates the point at which the crack closes and therefore the crack loading mechanism changes and the fluid entrapment governs the subsequent rate of change of the SIFs, The fluid entrapment mechanism, for the EHL case is illustrated in Fig 5.9.

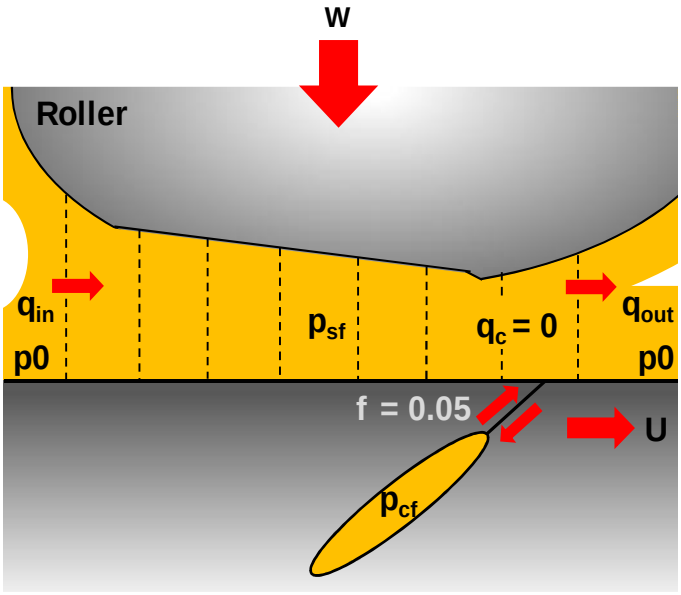


Figure 5.9 Schematic of the fluid entrapment mechanism for the EHL case

This is because, after this point, the entrapped fluid restricts further closure of the crack by maintaining a volume within the crack that must be conserved and cannot be fully compressed (this stage is governed by the compressibility of the fluid).

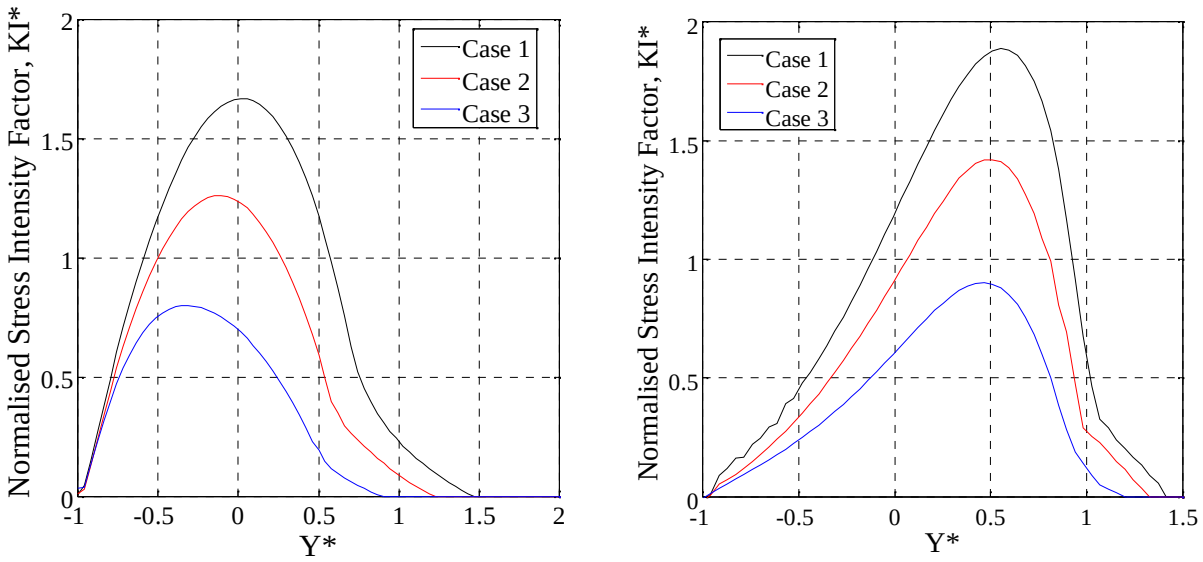


Figure 5.10 Dimensionless normal mod *KI** SIF plots (a) Hydrodynamic (b) EHL

For *KII*, in both the HL and EHL scenario the general trend is again similar; for *KII*, however, the trend is inverted where there is an initial period where d*KI**/d*Y** < 0, then d*KI**/d*Y** = 0 and d*KI**/d*Y** > 0, as shown in Figs. 5.11a & b. The K^*_{max} and the K^*_{min} values for the HL model (a) and the EHL model (b) give very similar values and therefore a similar range of mode II SIF, *ΔKII**, although in both cases the max in *KI** and the min in *KII** are larger in the EHL model.

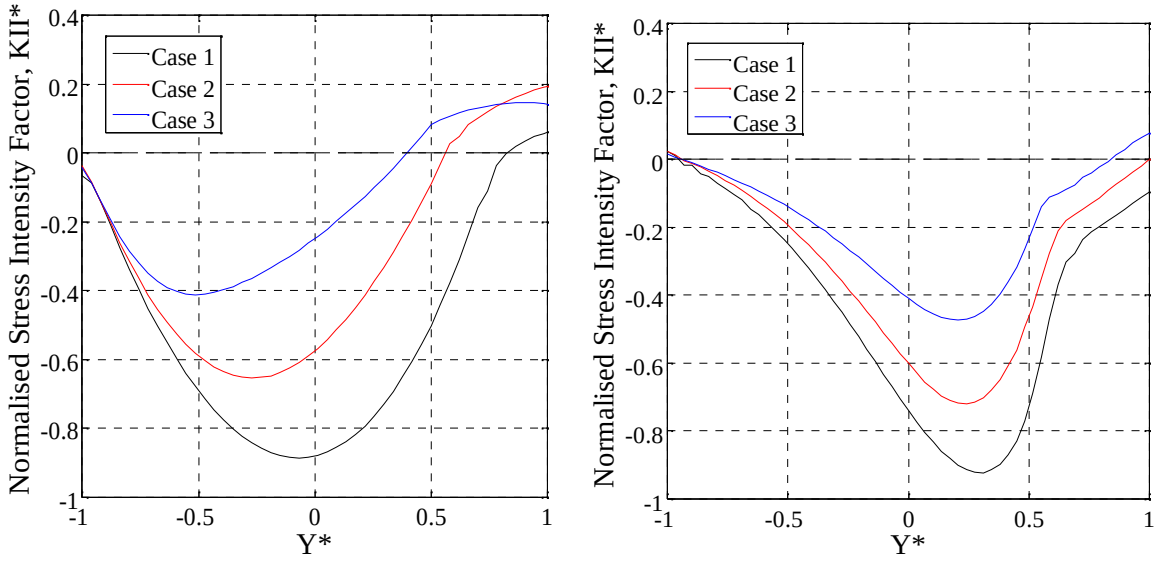
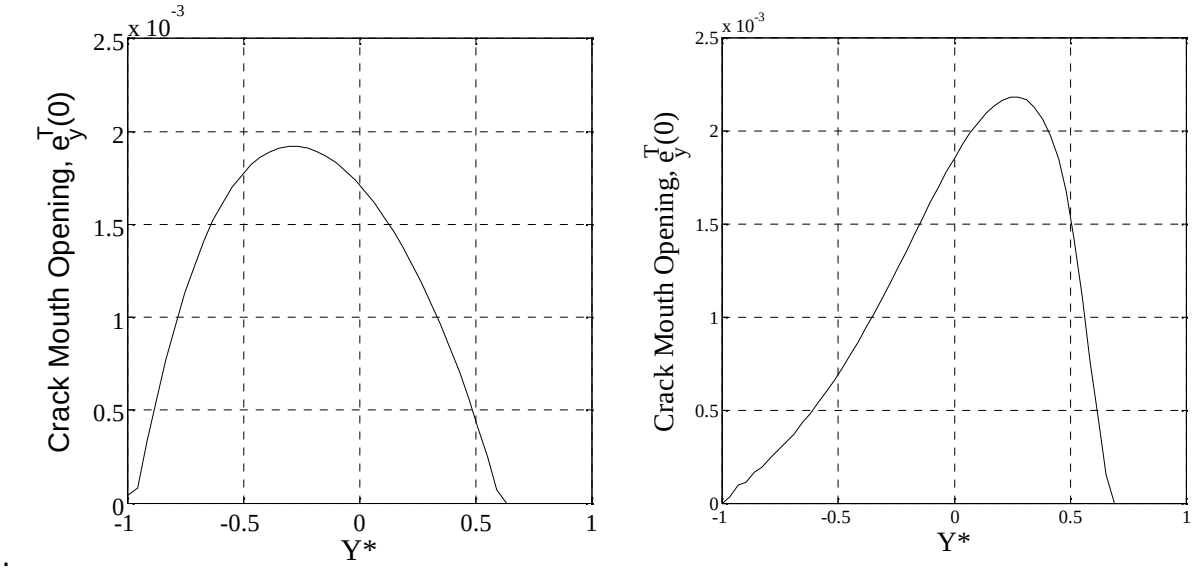


Figure 5.11 Dimensionless shear mode *KII** SIF plots (a) Hydrodynamic (b) EHL

This effect can be attributed to the fact that in the EHL scenario the pressure is distributed such that a larger amount of load is supported by the right hand side of the contact region, , where *Y** > 0; the opposite is true for the HL scenario. This means that as the pressure builds inside the crack in scenario (b), as the roller is traversing the crack, the surface pressure is lower than in the HL case and, as a result, cannot counteract the opening of the crack as effectively as in the HL scenario; hence, the crack opens further. This effect is explicitly illustrated in the Figs. 5.12a & b



.

Figure 5.12 Dimensionless crack mouth opening plots (e* = e/a) (a) Hydrodynamic (b) EHL

From these plots it can clearly be seen that in the case where the crack is coupled with the EHL fluid solver, scenario (b), the crack mouth opens about 10% more than it does in scenario (a). It is the amount that the crack opens that governs the magnitude of stress induced at the crack tip and therefore the magnitude of the stress intensity factors, in particular *KI*. What governs the amount by which the crack opens is the balance between the load acting on the surface to close the crack and the action of the pressurised fluid inside the crack, which acts to open it. Therefore, if we express the equivalent load acting on the crack faces as the difference between these two contributions

$$W_{eff}(a) = \int_0^a P_{cf}\,da - \int_0^a -\pm_{sf}\,da \qquad (5.21)$$

Where P_{cf} is the crack film pressure acting on crack faces and σ_{sf} is the stress perpendicular to the crack face induced by the surface film pressure, the sign and the magnitude of such "effective load" is responsible for the opening or closing of the crack during the transient loading cycle. If the effective load, W_{eff}, if highly positive at the beginning of the iteration for each time-step of the simulation, this will induce very large crack opening (due to the fact that by opening the crack P_{cf} decreases until the balance between the two forces is achieved) and significant changes in the *KI* and *KII* values. If W_{eff} is negative it will foster crack closure until the crack mouth closes, therefore producing negligible *KI* (for the cases analysed here) but still considerable *KII* values. The direct comparison of the stress intensity plots for scenario (a) and scenario (b) serves to further emphasise the importance of the fluid/solid coupling to the fatigue crack propagation properties, here described in terms of *KI* and *KII*; it also introduces the importance of the term denoted here as effective loading, which is based on the transient load imbalance between the fluid pressure within the crack and the external load applied by the rolling element.

5.4.2. EHL Isoviscous and Piezo-viscous

The next step is to consider the EHL model in isolation, where the applied load can be significantly increased to magnify the fluid\solid coupling effects. In this section the effect of fluid compressibility and pressure dependent viscosity, piezoviscosity, are introduced, two effects that have never been investigated in an RCF crack analysis in

the literature. The results with and without the pressure dependent fluid properties are compared to gain a better understanding of the influence they wield on the fluid/solid coupling. The effect of the piezoviscosity and compressibility is investigated by comparing the results for a load cycle with the same operating conditions, one where piezoviscosity and compressibility are included and one where these effects are neglected. This will help isolate the effects of the changing viscosity and density from all other phenomena and highlight their influence. The two cases that are compared are given in Table 5.2

Case	Liquid	a	h_{c0}	U^S	W^F	E	σ^Y	η	θ	Film Nodes	Crack Nodes
		μm	nm	m/s	N/m	GN/m^2	MN/m^2	Pa/s	°		
1	Base Oil	100	250	3	40000	210	800	0.137	25	151	30
2	Base Oil	100	250	3	40000	210	800	0.137	25	151	30

Table 5.2 – Operating conditions for the comparison of the piezoviscous and isoviscous cases

The crack tip radius h_{c0}, which is discussed in Chapter 4, used in the fluid solver is increased here to a value of 250nm, to stabilise the fluid film solver in the crack. This can be justified as crack tip blunting produced by local plasticity, which is observed in real cracks. The value of 250nm gives the crack an aspect ratio of 200:1, which when considering the comparison between a crack and slot model (see Chapter 3) means that from a structural point of view, it will still behave the same as a 1D feature; thus, a 2D structural crack model is not deemed necessary.

The results that have been discussed in the previous sections, including Chapters 3 and 4, have been expressed using dimensionless transformations; however

for the rest of this chapter, and the remainder of this thesis, the results will expressed using dimensions to give a clearer, and more tangible appreciation of the pressures, deformations, and film thicknesses that are being discussed, while also giving a means to compare with real life applications.

From the results, considering first the pressure profiles for the two different cases, shown on Fig. 5.13, where the red line is the isoviscous case and the blue line is the piezoviscous case, it is clear that the variation in the viscosity through the length of the film, inside the contact, has a considerable effect. Two key aspects show a distinct difference, namely the maximum pressures, which occur at around 0m in the contact, and the pressure distribution in the cavitated region that comes immediately after, at around 0.5E-4m. As the two solutions here are solved for the same load, the integral of the contact pressure along the contact length is the same for both cases. So, in the region where the fluid cavitates, where the contact length value is greater than 0m, in the case where the viscosity is pressure dependent the drop in the pressure is more gradual; the load is now distributed over a larger region: this implies that the maximum pressure is somewhat reduced because the load is distributed over a longer length.

The film thickness also shows a distinct difference, the case with the piezo-viscosity gives much higher film thickness, around 2μm, compared with 0.6μm for the isoviscous case. This is, of course, a physical result that is to be expected, where film thickness is directly proportional to the viscosity, higher viscosity (induced by piezoviscous effects) gives higher film thickness. This higher film thickness is also a factor in determining the surface film pressure, especially in the cavitated region;

because the film is thicker its takes longer for the surface film pressure to go to zero, where in Figs. 5.13a & b the red trace displays the isoviscous case and the red the piezoviscous case.

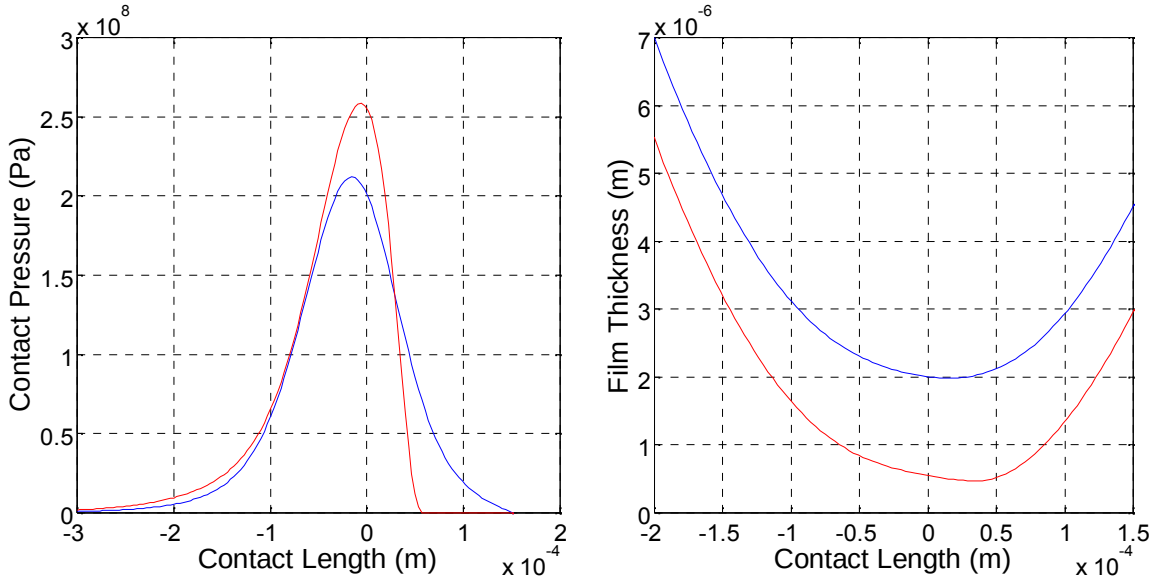


Figure 5.13 Comparison of isoviscous (red lines) and piezoviscous (blue lines) cases (a) EHL film pressure (b) EHL film thickness

To gain further insight into these effects, the viscosity and the density of the piezoviscous and compressible case are considered: the results for the variation of viscosity and density within the contact patch are show in Figs. 5.14a & b. It can be seen from the results that the viscosity of the lubricant varies noticeably through the contact, from 0.137Pa.s to around 1.6Pa.s, and the density changes, though not as dramatically, from 850Kg/m^3 to 920Kg/m^3. In terms of the viscosity the results show an increase of almost 12 times the original viscosity, whereas the density change is around

8%, therefore the main differences between the two cases is almost entirely due to viscous effects. The main effect of introducing piezoviscosity is the reduction in the pressure gradient, d*p*/d*x*, throughout the surface lubricant film; this produces a more evenly distributed load, therefore reducing the peak pressure.

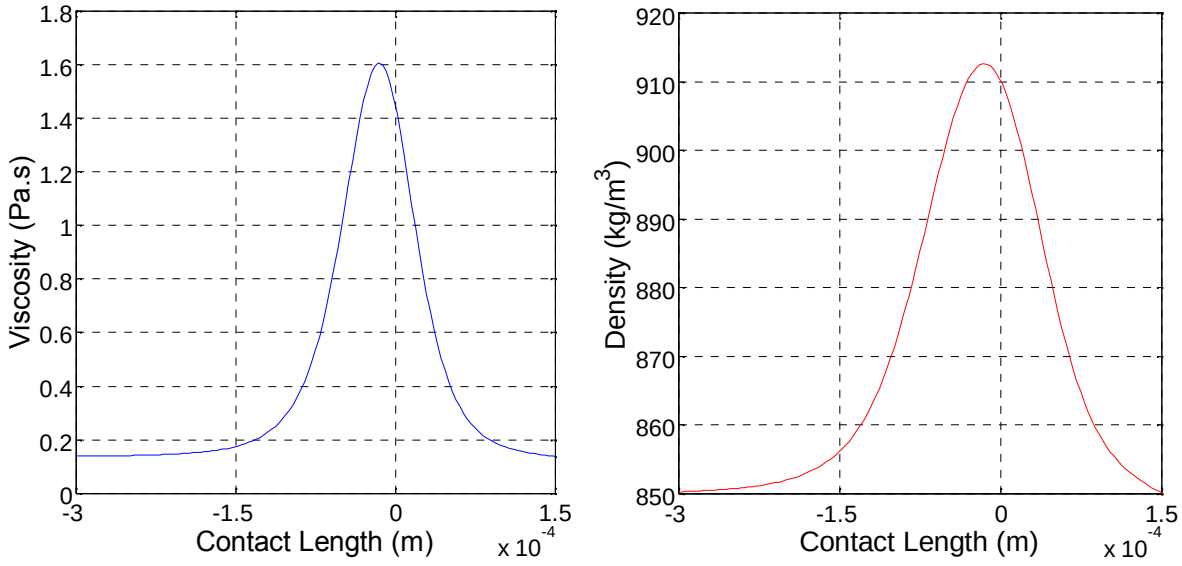


Figure 5.14 Piezoviscous results of (a) Viscosity (b) Density

The crack mouth opening for the two cases, as shown in Figs. 5.15a, reflects the result seen for the pressure. In the piezoviscous case, the crack does not open as much as for the isoviscous case, an effect that can, almost entirely, be attributed to the reduced peak in the surface film pressure. The differential pressure Δp, Eq. (4.43), that is seen inside the crack, which gives an indication of the pressure gradient also gives a stark contrast between the two cases. Where the lubricant is assumed to be isoviscous, the pressure gradient inside the crack is not as steep as when the lubricant is solved as

piezoviscous. The reason for this is that when the lubricant is more viscous the pressure takes longer to become constant inside the crack film; this induces a more pronounced pressure gradient in the fluid. Although the velocity of the crack displacement dh_c/dt is in fact lower, viscous effects in the fluid restrict the build-up of pressure from the crack mouth to the crack tip; thus, the process of pressurizing the crack takes longer, giving larger pressure gradients. This also ties in with the changes in the pressure profile observed in the cavitation region of the surface film.

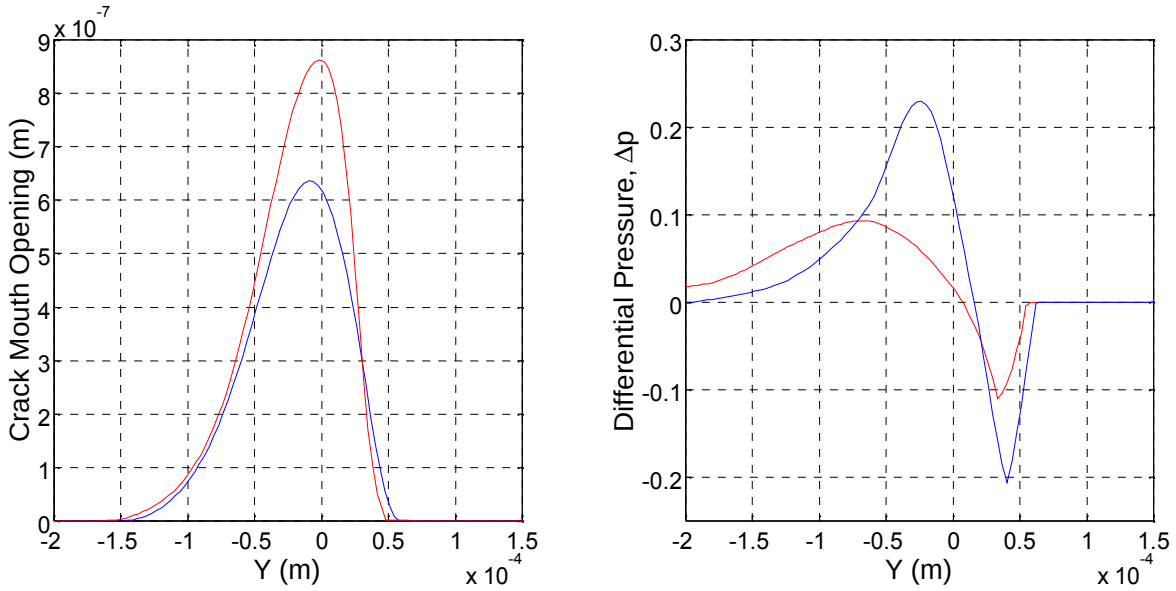


Figure 5.15 Comparison of isoviscous case (red) and piezoviscous case (blue) (a) Crack Mouth Opening (b) Differential Pressure

The stress intensity factors, *KI* and *KII*, are once again, largely affected by the fluid pressure inside the crack. However, the differences that can be seen between the two cases are characterized by the coupled effects that have been described in the surface

film and in the crack film, namely the reduced maximum surface film pressure and the increased pressure gradient due to the piezoviscosity. The maximum values, and the SIFs ranges are reduced for both *KI* and *KII* due to the piezoviscous effect of reducing the peak pressure in the surface film. Another feature of the solutions is that the two models produce similar results, when the crack is at *Y* = 0.4E-4m, this is because the surface film pressure is higher in the piezoviscous case at this location, but also the pressure gradient inside the crack is positive and larger for the piezoviscous case with respect to the isoviscous.

This means that the higher the viscosity, the more the load is distributed through the contact length, which in turn reduces the peak pressure; as a consequence, the stress intensity factors and the crack growth induced by a loading cycle are also reduced. If the load is increased, and the viscosity increases further, the changing viscosity will act to somewhat reduce the peak pressure and help to distribute the load more evenly in the contact, therefore reducing the damaging effect induced by the passage of the roller over the RCF crack.

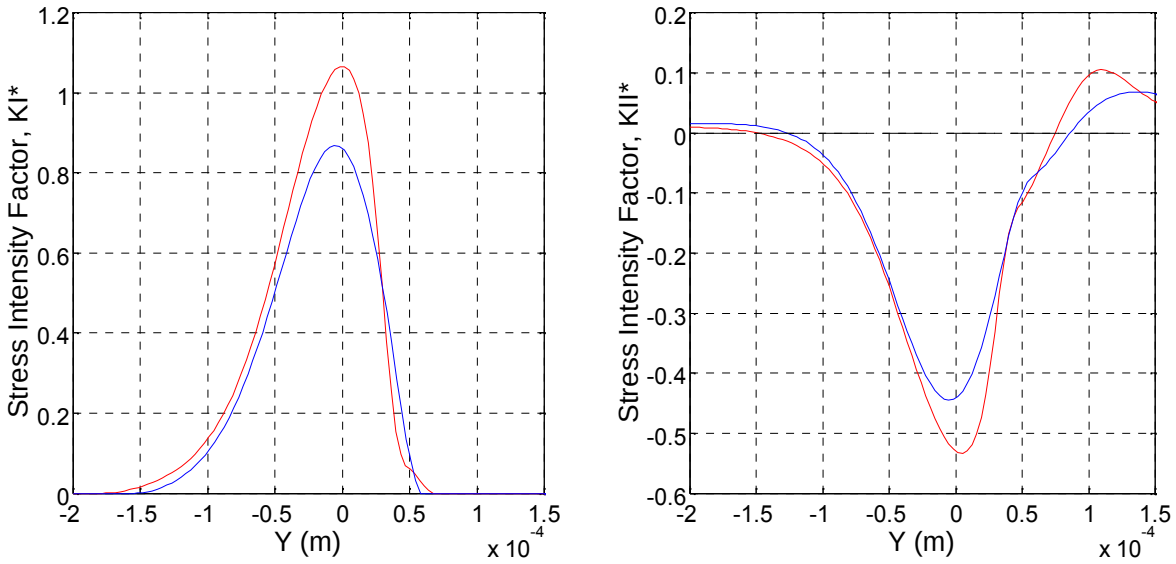


Figure 5.16 Comparison of isoviscous case (red) and piezoviscous case (blue) (a) *KI** (b) *KII**

By considering the effect of piezoviscosity, and to a lesser extent compressibility, and comparing the results with an isoviscous and incompressible case, the effects of these two phenomena have been investigated. The main effects are a reduction in the peak pressure of the surface film, an increase in the film thickness of the surface film and an increase in the pressure gradient inside the crack. The consequence of these effects is a marked reduction in the stress intensity factor ranges, for both Δ*KI* and Δ*KII*, obtained for the same operating conditions, i.e. load, crack length and geometry.

5.4.3 Higher Pressure Isoviscous EHL models

The load that is applied for the analysis is now increased even further, and the effect of the crack mouth on the surface fluid film is now also introduced. When the crack mouth

opening becomes large its influence on the surface film shape will begin to dominate over surface asperities and it is assumed that this effect only becomes significant when the pressures in both the surface film and the crack become large; hence it has been neglected to this point. This will be confirmed in the following sub-sections. The operating conditions for the analyses that are described in this section are contained in Table 5.3.

Case	Liquid	a	h_c^0	U^S	W^F	E	σ^Y	η	θ	Film Nodes	Crack Nodes
		µm	nm	m/s	N/m	GN/m^2	MN/m^2	Pa/s	°		
1	Base Oil	100	250	3	50000	210	800	0.137	25	151	30
2	Base Oil	100	250	3	60000	210	800	0.137	25	151	30
3	Base Oil	100	250	3	70000	210	800	0.137	25	151	30
4	Base Oil	50	250	3	70000	210	800	0.137	25	151	30
5	Base Oil	150	250	3	70000	210	800	0.137	25	151	30

Table 5.3 – Operating conditions for the higher pressure isoviscous cases

The fluid solver used for this section is the one developed for the isoviscous case. This is due to the fact that the piezoviscous solver could not converge at high loads; as explained below, this is due to (i) the large variations in the surface pressure gradients in the neighbourhood of the crack mouth, and (ii) the film thickness reduction at the crack mouth is such that, in certain circumstances, the fluid film breaks and the solver would need to be able to explicitly capture film formation and re-formation during cavitation in order to cope with such situations. This will be the focus of further developments to the formulations presented in this thesis. However, a case will be discussed for an isoviscous fluid characterised by high viscosity to help deduce what

would be the effect of the higher viscosities that would be obtained at high loads. The tests can be divided into two sub-sections: cases 1 - 3, consider the effects of incrementally increasing the load and case 3 - 5 are aimed at uncovering the effect of changing the crack length. These cases have been run including the crack deflection in the surface film but also neglecting it, in order to gain a better understanding of the influence of this effect. This has never been included in an RCF crack analysis nor captured during other numerical studies reported in the literature. It should be noted, that with the increased load and the introduction of the crack mouth, the numerical code is much less stable than for the cases discussed up to this point. Therefore, the results in this section do display some oscillatory characteristics. This could be resolved by using tighter convergence criteria and more time steps; however, this would make the solution much more computationally expensive.

Considering first, cases 1 – 3, and referring to Appendix B, Figs. B1 – 15, for the sequential results obtained from the simulation performed by the author, the results obtained during a loading cycle are illustrated displaying the film thickness, the contact pressure and the crack shape for each separate loading condition. The solid red line gives the results from the analysis including the crack mouth deflection and the blue, broken line, gives the results from the analysis neglecting the crack mouth deflection. On the x-axis of the plots, of the contact pressure and the fluid film shape, there is a red dot that is used to illustrate the position of the crack mouth in the contact, where the crack is orientated in the direction displayed in Fig. 5.1.

The pressures that are induced by the given contact loads from Table 5.3 give peak values of the order of 300MPa, 345MPa, 375MPa, from the loads 50kN/m, 60kN/m and 70kN/m respectively, where the contact length (measured as the region where the fluid pressure is positive) is approximately 0.5mm for each case. This means that because of the pressures, and the isoviscous nature of the fluid solver used here, the results could be directly applied to describe in-service operating conditions encountered in rail/wheel contacts and of roller bearings under 'light' loading, which is defined in the SKF catalogue as around 5% of the maximum load [170], where the maximum load gives pressures of around 4GPa. These levels of pressure are, unfortunately, beyond the stable running conditions of the fluid solver that has been implemented here. To be able to consider pressure of this scale a more sophisticated fluid solver is required, one that can incorporate fluid cavitations [171] and also glass transition [172]. The velocity that has been chosen, 3m/s, means that each loading cycle lasts, in real time, 0.002s.

The first of the three dependent variables to consider is the fluid pressure; using the plots given in Appendix B a good overall representation of the evolution of the contact pressure during the loading cycle is provided. Each of the six plots represents a point in time during the loading cycle. It should be noted that each sequence of images depicting the pressure profiles and the other characteristics for each loading condition does not represent the same six time frames during the loading cycles for the three cases studied here. The reason for this is that the features of the solution that have

been deemed of interest to discuss occur at different instants for each of the three cases analysed.

From the results shown in Figs. B1.1 – 9.1 in Appendix B, it can be seen that with the crack length of 100μm used in cases 1 – 3, neglecting the crack mouth in the solution of the surface film, shown with the blue broken line, gives an almost constant pressure profile for each time step, where in case 3, see Figs. B6.1 – 9.1, some slight effects can be seen as the crack approaches the peak contact pressure. The effect seen here can be attributed to fluid suction and squeeze inside the crack: the fluid is first drawn into the crack from the surface film and then pushed out of the crack into the surface film. When fluid is sucked from the surface film into the crack the fluid pressure at the crack mouth drops and when fluid is squeezed into the surface film the fluid pressure at the mouth has a spike; this can clearly be seen with the blue broken line Figs. B7.1(f) & B13.1(f) where the pressure drop at the crack mouth corresponds to the fluid is being sucked into the crack.

With the introduction of the crack mouth deflection to the analysis the effects are, as expected more pronounced, shown in Figs. B1.1 – 9.1 using the red solid line. As the crack opens, it creates a step in the surface film thickness, as shown in Figs. B2.1, B5.1, B8.1 B11.1, B14.1. The magnitude of the step corresponds to the vertical component of the crack opening located at the mouth, where the crack opening is shown in Figs. B3.1, B6.1, B8.1, B12.1.1 and B15.1. To describe this effect it is important to consider the interdependence and the coupling of the three variables plotted in this series of figures, namely the film thickness, the crack opening and the

contact pressure. As the crack opens, it creates a step across the mouth which also means there is a step in the film thickness; the step then induces a cusp in the contact pressure in the vicinity of the crack mouth. This is due to the fact that immediately before the crack mouth the film thickness is lower, and this corresponds to a pressure spike; immediately after the crack mouth, where the film thickness is larger, there is a dip in the contact pressure when compared to the case where the crack mouth deformation and its effect on the film shape is neglected.

Let us now turn to the time evolution of the crack opening, displayed in Fig. 5.17. Only the results for case 3 are considered here as representative of the three cases analysed (1 – 3) , as the crack opening histories are very similar and do not need to be discussed individually. It can be seen that the mouth deflection has a considerable effect on the evolution of the crack shape during a load cycle. On the graph shown in Fig. 5.17, the blue line displays the crack mouth opening computed neglecting the crack mouth deflection and the red line displays the crack mouth opening calculated including the crack mouth deflection. The difference is considerable; but what is responsible for this large difference. As the crack mouth opens, the step in the surface film creates the pressure spike immediately before the crack mouth and a dip after the mouth. The effects of this are twofold: first of all, the pressure at the crack mouth and the fluid pressurisation inside the crack are lower due to the combined effect of the crack mouth deflection and the “sucking in” effect. The second effect is that the surface fluid film pressure directly above the inclined RCF is larger (due to the pressure spike forming in the proximity of the crack mouth), which in turn means that the load acting to close the

crack is higher. Therefore, the crack tends to close much earlier and not to open as much as when the crack mouth deflection is neglected in the calculations; this has strong implications for the evolution of the stress intensity factors, as shown in Fig. 5.20.

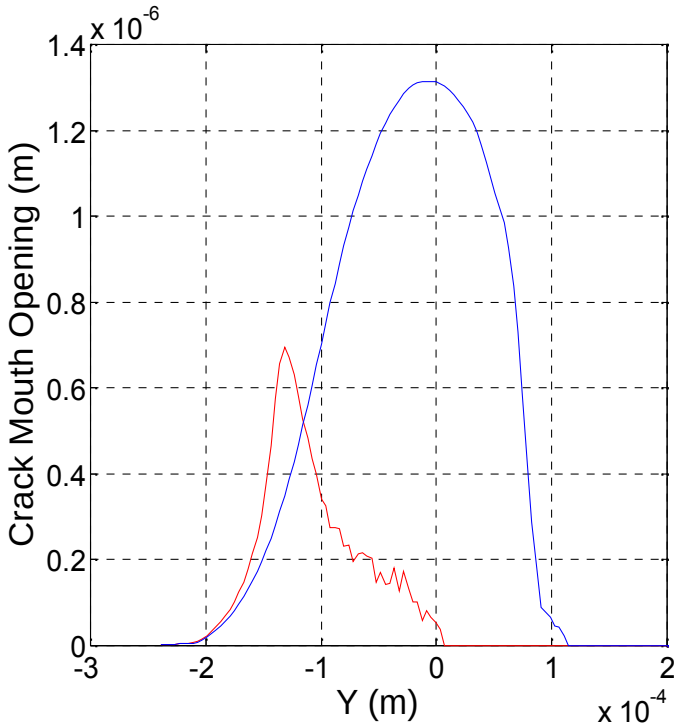


Figure 5.17 Isoviscous crack mouth opening including problem (III) (red) and neglecting problem (III) (blue)

The pressure gradient that is calculated inside the crack during the loading cycle, shown in Fig. 5.18, is in perfect agreement with the results of the crack displacement. Here Δp represents the pressure gradient based on Eq. (4.14).

While the crack is opening the pressure gradient is positive and when the crack is closing the pressure gradient is negative; the magnitude of the pressure gradient is

directly proportional to the velocity of the crack displacement, dh_c/dt; the influence of the crack opening on the pressure gradient stems from the formulation of the Reynolds equation (Eq. (4.9)) [166]. This confirms the results showing the strong effect of the fluid/solid interaction discussed in Chapter 4 and strengthens the argument that to accurately model fluid pressurization in RCF cracks the pressure gradient of the crack film should be calculated rather than imposed using a constant gradient in the crack film for the whole loading cycle. This is one of the fundamental findings reported in this thesis.

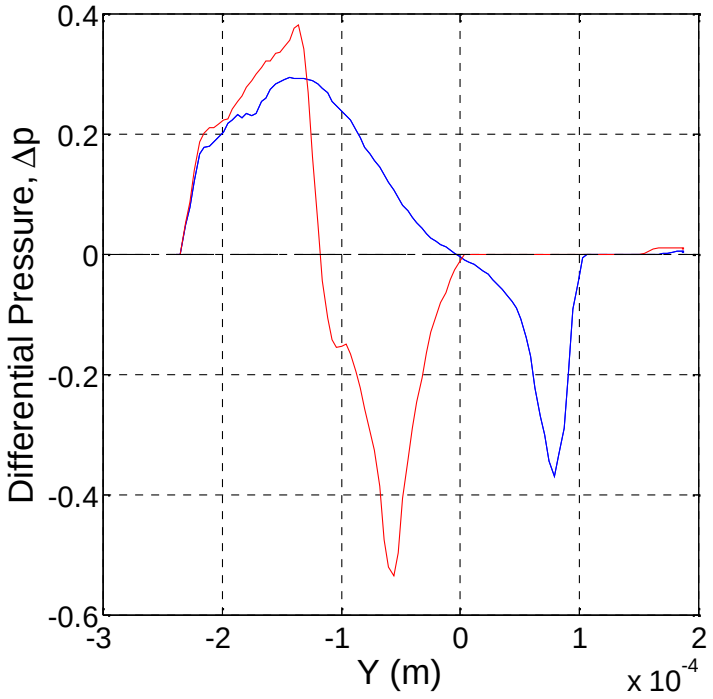


Figure 5.18 Isoviscous differential pressure, *Δp*, including problem (III) (red) and neglecting problem (III) (blue)

The evolution of the volumetric flux shown in Fig. 5.19, is also directly linked to the pressure gradient effect seen in the crack film: where the flux is positive, i.e. the flux is such that fluid is drained into the crack, the pressure gradient is positive and the crack is opening; the flux is negative, i.e. fluid is expelled from the crack, when the pressure gradient is negative and the crack is closing. This relationship demonstrates the full coupling of the system, where the crack opening, the flux and the crack film pressure are all interrelated and display the characteristics and dependencies that are expected in a fully-coupled solution.

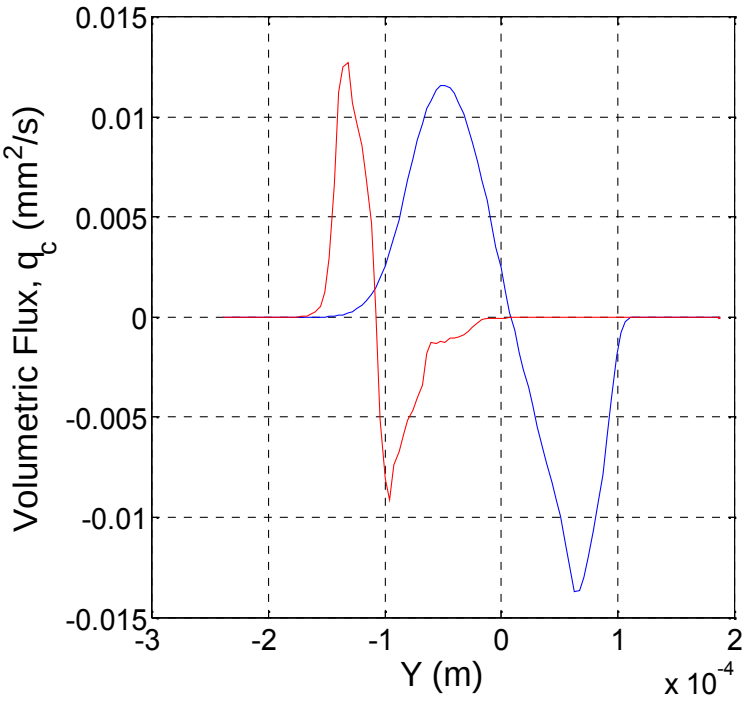


Figure 5.19 Isoviscous volumetric flux, q_c, including problem (III) (red) and neglecting problem (III) (blue)

Let us now consider the stress intensity factors, *KI* and *KII*, as shown in Figs. 5.20a & b, where case 3 is again considered in isolation; the blue line represents the results obtained neglecting the crack mouth in the surface film and the red line represents the results including the effect of the deflection of the crack mouth on the surface film. The normal stress intensity factor, *KI*, is driven by the crack opening and, as expected, the trend that is shown in Fig. 5.20a reflects the trend shown in the crack opening plot in Fig. 5.17: when the crack mouth effect is neglected, the evolution of K_I is almost identical to the profile of the surface film pressure, which is the driving force of the opening mechanism and regulated the fluid pressurisation of the crack film during the loading cycle. As already discussed before, this demonstrates the strong effect that the surface film pressure has on *KI*, and also corroborates the main initial hypothesis of this work, i.e. that surface film pressure influences and drives crack opening, directly affecting the evolution of the normal stress intensity factor that leads to crack propagation. The results obtained when the deflection of the crack mouth is included, show a very much reduced *KI* range (Δ*KI*), where the maximum normalised value is around 0.5, about half of the value obtained when neglecting this effect. The reason for this has already been identified in the discussion about the complex relationship between the cracks opening, the surface film thickness and the surface film pressure; this shows that the fluid/solid interactions affect the performance of components affected by RCF in a non-trivial way and that every single element needs to be considered in the model to obtain a full picture.

The implications of the mode I SIF evolution discussed above are far-reaching: the main consequence of the results displayed in Fig. 5.20a & b is that, since *KI* is hypothesised to be the main mode responsible for propagation, the model that is solved with the inclusion of the crack mouth deflections predicts much lower crack growth rates than the model that neglects the crack mouth deformations. This is an interesting result, and it may go some way to addressing the observation made by Kaneta, Keer and co-workers [3] [97] that existing fluid pressure models for analyzing RCF cracks predict unrealistically high crack propagation rates. However, it is shown here that by correctly solving for the process of the lubricant filling the crack, and the interaction between the crack and the surface film this key flaw that has been identified in existing fluid pressure models could potentially be addressed.

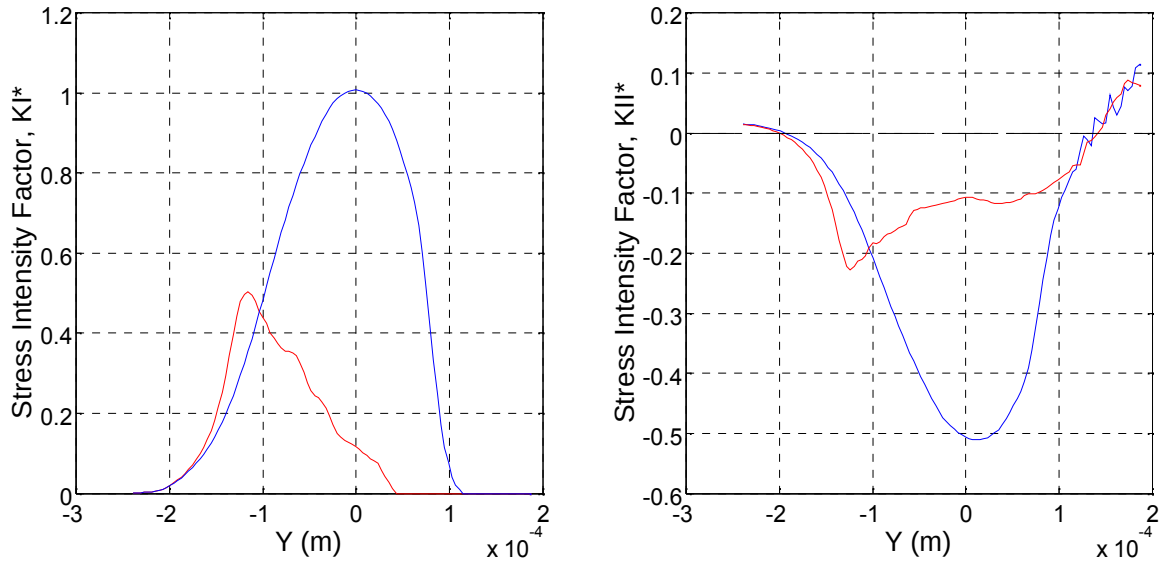


Figure 5.20 Isoviscous case including problem (III) (red) and neglecting problem (III) (blue) (a) *KI** (b) *KII**

The shearing stress intensity, *KII*, like the normal stress intensity factor, *KI*, is also drastically reduced when the crack mouth deflection is introduced; the peak in the evolution of *KII* is now around -0.23, much lower than the value, -0.51, obtained in the absence of the inclusion of the effect of the crack mouth deflection on the surface film shape. Although the intensity factors have both been modified, the relative difference between *KI* and *KII* remains similar, with the maximum value for *KI* being roughly twice as large as the maximum value obtained for *KII*. This implies that, based on this model, the crack would propagate in mixed mode, with *KI* playing a dominant role. This is a reasonable and sensible result that confirms the observation from in experimental studies, that it is very difficult to propagate a crack only in mode II [129].

Turning now to the effect of the crack length on the evolution of the system under investigation, cases 3 – 5 are compared and discussed in detail. These three cases simulate the effect of increasing the crack length, and the effect this has on the coupled solution during a loading cycle. Results obtained at different time-steps during the loading cycles, for the film pressure, the film thickness and the crack opening are shown in Appendix B.

5.4.3.1 Changing the crack length

The interrelationship between these three variables again plays an important part in the response of the system: for a 50μm crack, the opening is less than the one observed for 100μm crack, and this is in turn lower than the opening experienced by the crack characterised by a 150μm length. This means that because the largest crack mouth

opening is obtained for the 150μm case, the difference between the solution that includes the effect of crack mouth opening on the surface film and the one that neglects this effect is more pronounced. At this longer crack length, looking first at the results that neglect the effect of the crack mouth deflection (see Fig. 5.21a), it becomes apparent that the fluid flow in and out of the crack has a larger effect, becoming more influential. This is explicitly shown in Fig.B13.1(f), where the blue broken line displays a more pronounced influence on the contact pressure than the results obtained for the other two crack length cases, see Fig. B7.1(f) and B10.1(f). The cusp in the contact pressure profile is caused entirely by fluid suction induced by rapid opening. This is directly related to the history of the crack opening shown in Figs. 5.21(a) The plots in Fig. 5.21a & b show both sets of displacements, where the effect of the crack mouth deflection on the surface film calculation is neglected (Fig 5.21a), and where the crack opening displacements account for the effect of crack mouth deformation on the fluid flow (Fig 5.21b). From the plots it is clear that by increasing the crack length, where the blue line is for a 50μm crack length, the red line is for a 100μm crack and the black line represents a 150μm crack, the crack opening increases; this is somewhat to be expected as the shorter crack is more difficult to open due to the reduced effect of the fluid pressure (if fluid pressures are similar then increasing the crack length results in an increased opening load acting on the crack face) and its stiffer nature. One of the limitations of these simulations is that it has been assumed that the crack must be short enough to be fully filled with fluid during the entire duration of the loading cycle. However, the lengths of crack used for this study justify this assumption, also confirmed

by other studies reported in the literature (see Bogdanski *et al* [1]). Interestingly, as the crack length is increased, the crack opens more which is expected, but somewhat unexpected is the fact that the process of opening and closing is quicker, and by comparing the results for a 50μm crack, shown in blue, with those for a crack length of 150μm, shown in black, the latter closes considerably quicker.

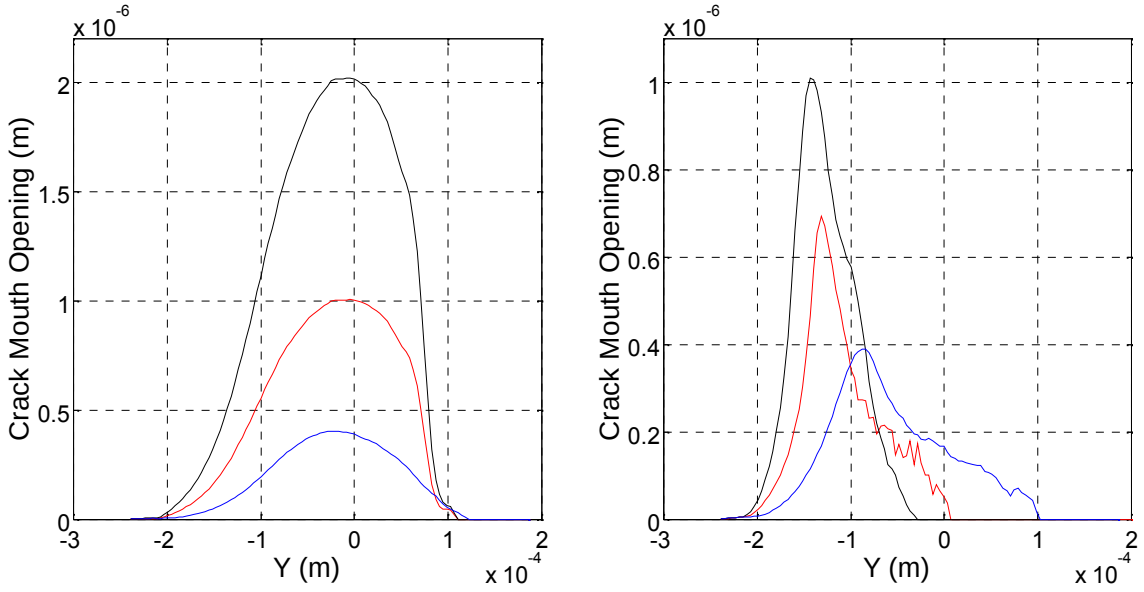


Figure 5.21 Crack mouth opening for 3 crack lengths; 150µm (black), 100µm (blue), 50 µm (red) (a) including problem (III) (b) and neglecting problem (III)

This phenomenon can be almost entirely attributed to the inclusion of the deflection of the crack mouth and its effect on the surface film shape and thickness. As the crack mouth opening increases, the step in the surface film increases, this causes a larger spike in the contact pressure, as shown in Fig. B13.1(e) in Appendix B, which in turn forces the crack to close.

Looking at this in terms of the stress intensity factors, and in particular at *KI*, it is clear that, although the longer crack does not stay open for the majority of the loading cycle, and certainly not as long as the opening is observed for shorter cracks, the rapid crack opening experienced during the first phase of the loading cycle h induces a large maximum value in the stress intensity factor history plot, see Fig. 5.21. In contrast, for the case where the crack length is 50μm, the mode I stress intensity increases and decreases with a much shallower gradient. So, although the longer crack open and closes quicker, the large amount of opening could lead to a considerable increase in crack growth and crack growth rate in comparison to shorter cracks (this will be discussed in more detail in Chapter 6).

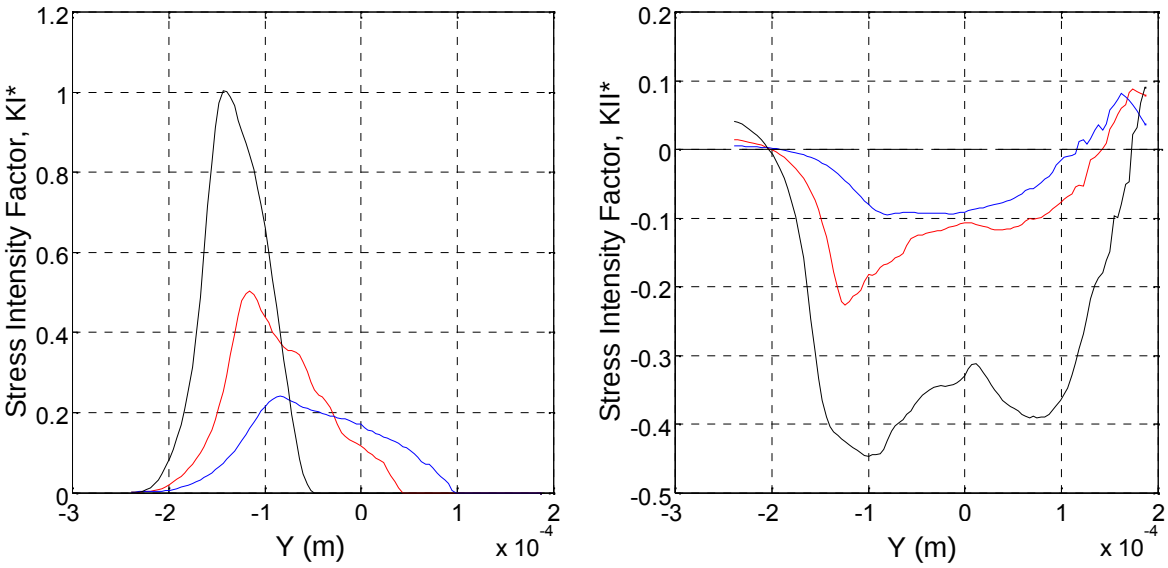


Figure 5.21 SIF's for 3 crack lengths; 150μm (black), 100μm (blue), 50 μm (red) (a) *KI** (b) *KII**

The shearing mode stress intensity factor, *KII*, also influences the crack propagation, especially in determining the direction in which the crack grows. In the strain energy density function method used to determine crack growth (see Chapter 6 for more details), the function that dictates the crack growth direction is more heavily influenced by *KII*. In general, high Δ*KII* values in the presence of limited reversibility of the shearing action, i.e. for values of *KII* mostly positive or negative throughout the loading cycle, tend to cause the crack to kink and grow in a curvilinear direction. In typical RCF problems, and in the absence of remote bending or of tension acting on the cracked body in addition to the contact load, the crack tip tends to follow an arc shaped path toward the surface, eventually leading to part of the surface material breaking away in the form of a pit. The magnitude of the stress intensity ranges, Δ*KII*, computed by the author for the different cracks analysed in this study compare well with some of the values from the literature [2] that have been deemed to be most accurate in predicting crack propagation since they predict crack propagation paths in line with those seen experimentally and when studying failures in real components. To summarize, for the loading conditions and geometries studied here, *KI* is larger than *KII* and has greater influence on the crack growth rate, while *KII* affects the crack growth direction. Explicit crack growth simulation for some of the example problem studied in this chapter will be performed and discussed in Chapter 6.

5.4.3.2 Viscosity effect including the crack mouth (problem (III))

The effect of the viscosity is now considered. As mentioned above, the piezoviscous model could not be run at higher loads due to numerical instabilities; hence, isoviscous simulations performed using a value of viscosity representative of the higher viscosity levels which would be encountered if a piezoviscous analyses was carried out. This provides a qualitative indication of what the effects of the pressure-induced viscosity changes would be. The value of viscosity adopted here is taken from the Doolittle model assuming a pressure peak of about 300MPa; therefore, a value of 3Pa.s is used in the following analysis. The crack mouth deflection and its effect on the surface film are incorporated into the model so that the effect of the viscosity on the phenomena that have been discussed in the previous paragraphs can be investigated. The operating conditions for the analyses discussed in this section are summarised in Table 5.4.

Case	Liquid	a	h_{c0}	U^S	W^F	E	σ^Y	η	θ	Film Nodes	Crack Nodes
		µm	nm	m/s	N/m	GN/m^2	MN/m^2	Pa/s	°		
1	Base Oil	100	250	3	50000	210	800	0.137	25	151	30
2	Base Oil	100	250	3	50000	210	800	3	25	151	30

Table 5.4 – Operating conditions for the low and high viscosity isocviscous cases

The pressure for both the high viscosity case and the lower viscosity case are shown in Figs. 5.22, where the blue line characterizes the low viscosity case and the red line the high viscosity case. As already discussed when comparing the piezoviscous and the iscoviscous cases in the previous section, higher viscosity leads to a lower maximum surface film pressure; when the effect of the crack mouth deflection is also considered,

it becomes apparent that the higher viscosity reduces the fluctuations of the surface film pressure induced by the coupling between the fluid flow inside and outside the crack.

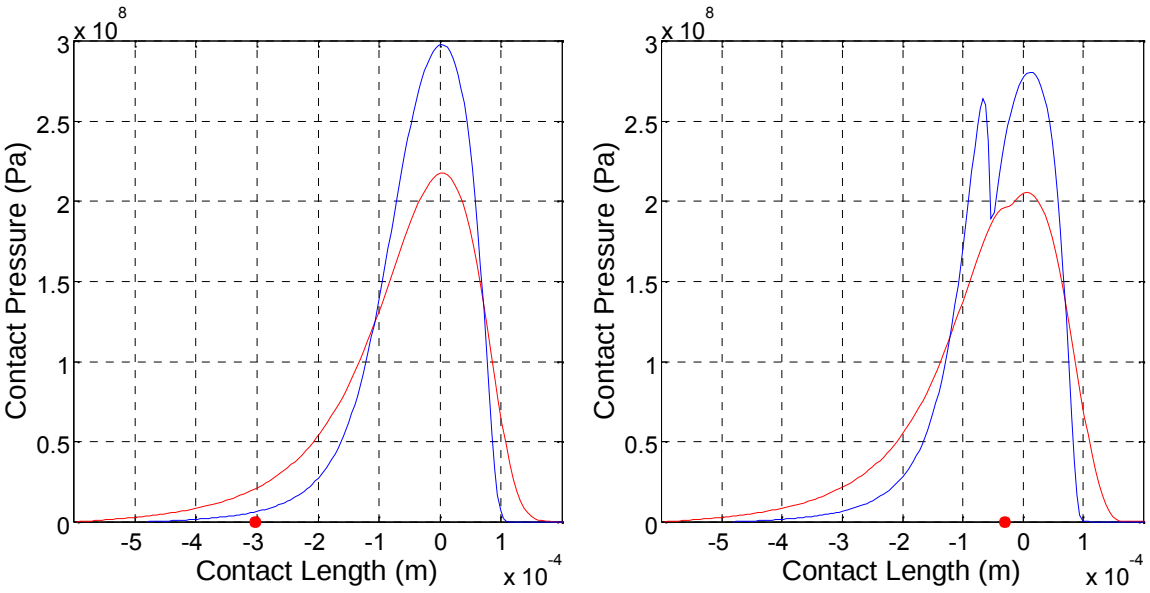


Figure 5.22 EHL contact Pressure for low viscosity (blue) and high viscosity case (red) (a) Y = -3E-4 (b) Y = -0.3E-4

This can be explained by looking at the film thickness plots in Figs. 5.23; as expected, the film thickness for the higher viscosity case is much larger, and because of this, the step that is induced in the surface film by the crack mouth deformation has a reduced effect on the surface pressure - the percentage reduction of the overall film thickness is much reduced and the inclusion of the crack mouth deflections in the calculations has a milder effect. This also effects the evolution of the stress intensity factors, as shown in Figs. 5.24.

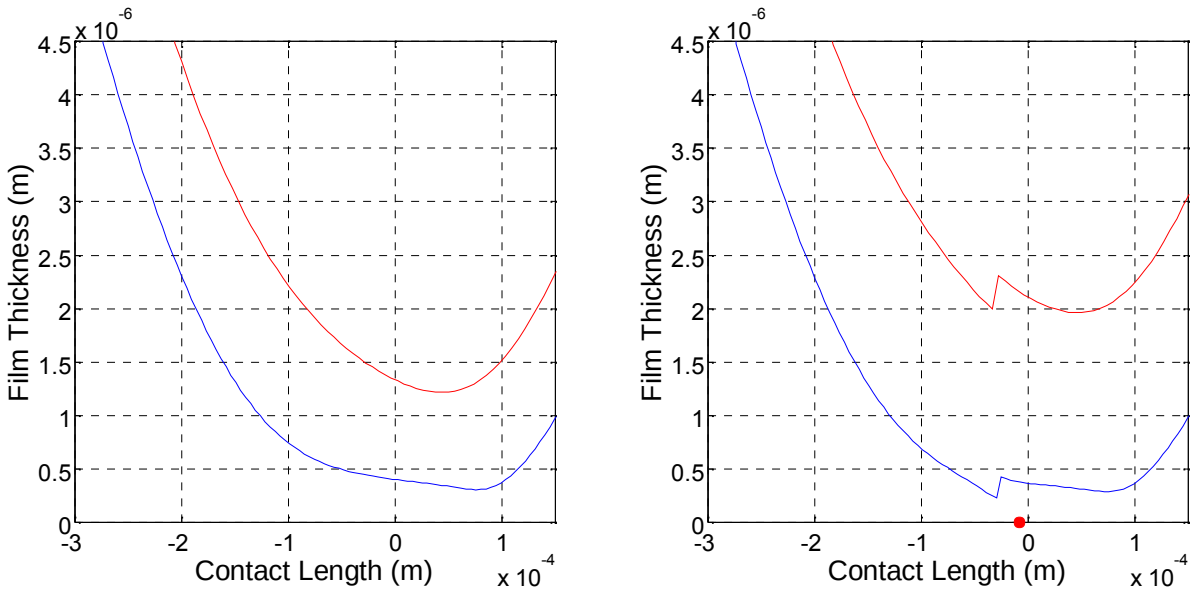


Figure 5.23 EHL film shape for low viscosity (blue) and high viscosity case (red) (a) *Y* = -3*E*-4 (b) *Y* = -0.3*E*-4

While in the lower viscosity isoviscous case the stress intensity factors are heavily influenced by the crack mouth deflection, in the high viscosity case the effect is less pronounced. The *KI* and *KII* results for the two cases considered here, which are characterised by the same geometry, load and crack length, show noticeable differences. The low viscosity case, shown in red, reaches a maximum very rapidly and then slowly decrease as already discussed in the previous sub-section. In the higher viscosity case, however, the *KI* value follow more the profile of the surface film pressure because no real pressure fluctuation occurs in the surface film, as shown in Fig. 5.22b. Interestingly however, the higher viscosity produced a larger *KI* stress intensity factor

maximum, even though it has a lower peak surface pressure; this is because in the lower viscosity case, the pressure spike in the surface film induced by the crack mouth deflection fosters the closure of the crack. A very similar trend is also observed for the mode II stress intensity factor (see Fig. 5.24b).

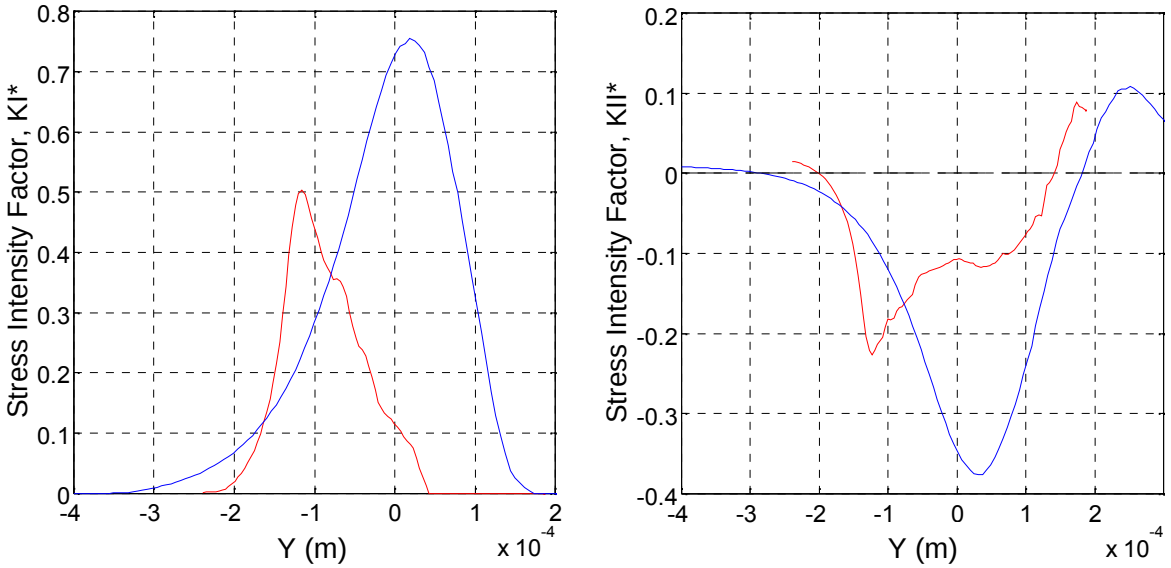


Figure 5.24 SIF's for low viscosity (blue) and high viscosity (red) cases (a) *KI** (b) *KII**

5.4.3.3 Directional Effect

Another important aspect of the problem that has not yet been addressed in the literature using existing fluid/solid RCF crack models is the influence of the directionality on RCF crack growth with respect to the loading trajectory (the rolling direction). Fujita et al. [124] have experimentally shown that once an RCF crack nucleates and grows to a certain length, reversing the direction of rotation of the roller causes a drastic

reduction in the rate of propagation of the crack. With this in mind, a simulation is performed using the current coupled model and inverting the direction of motion of the two components. The example problem studied is case 3 from Table 5.3, for which the evolution of the stress intensity factors are computed and shown in Fig. 5.25. The results suggest that, first of all, the normal stress intensity factor *KI*, is zero for the whole loading cycle; this is because when the crack is initially loaded as the contact load approaches the crack, the load act to close the crack faces before pressurisation of the fluid within the crack can take place; as a result there is no fluid entrapped or pressurised within the crack and it remains closed during the whole loading cycle. The shearing effect is still non-zero however, the main difference with respect to the case run using the opposite rolling direction being that the shearing direction changes and both the magnitude of the shearing stress intensity factor, KII^*, and the range, ΔKII^*, are reduced by about 50%.

Based on these analyses, the model appears to produce results which are in agreement with the experimental evidence that the crack propagation rate of an existing and fully formed RCF crack is very much influenced by the loading direction. When the crack is loaded from tip to mouth no crack opening, and therefore no mode I stress intensity factor is induced, and the rate of propagation of the crack decreases almost to zero.

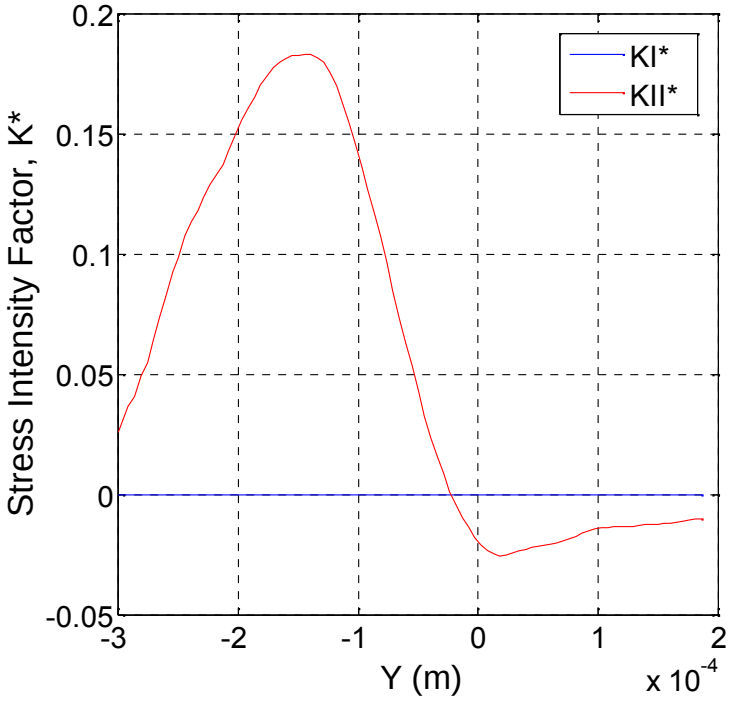


Figure 5.25 SIF's from analysis run in the inverse direction

5.5 Summary

To summarise, chapter 5, starting from the methodology developed in Chapter 4, develops both the fluid and solid formulations further so that the algorithms implemented by the author can tackle EHL contact problems in the presence of RCF cracks. The aim of this is to apply the methodology tested and validated on the contrived HL example problem to cases of much more practical relevance and representative of typical applications. The effect of the viscosity on the results obtained during a full loading cycle, and the effect of solving the surface film with the inclusion of the crack mouth deflection are discussed; this has been tackled here for the first time

and the novel results presented by the author seem to be able to clarify some of the experimental observations that have remained unexplained for decades. Two particular effects, piezo-viscosity and crack mouth deformation, are shown to have a unique influence on the response of the system, and this has a marked effect on the main variables of interest in terms of being able to predict crack propagation in RCF, i.e. the stress intensity factors. The range and the maximum value obtained for the evolution of the stress intensity factors during a loading cycle is strongly affected by the transient evolution of the fluid flow, with the solid/fluid coupling playing a vital role in determining how strong the effect of different loading conditions, material properties or geometries, is on the predicted crack propagation rates; this has significant implications for the propagation rates calculated using existing fluid pressurization models, which do not consider the mutual interaction of fluid and solid when studying RCF cracks.

Chapter 6

RCF Crack Propagation in EHL

6.1 Introduction

The way an RCF crack propagates is the final step performed by the author to gain a better understanding of the physical mechanisms responsible for RCF crack growth. The analysis of the propagation illustrates the effect of lubricant pressurisation on RCF cracks and the role that the lubricant plays in the process of pitting formation. This chapter builds on the work from the previous chapters to add the evolution of the crack shape and its propagation to the coupled fluid/solid EHL model. The determination of the direction of growth is based on evaluating the stress intensity factors for a loading cycle combined with an empirical crack growth model taken from the literature [75]. This is the final stage of the development of the solver and the analyses performed in

this chapter provide the full history of the fluid/solid interactions and predict both the crack growth and the evolving crack trajectory.

Crack growth in RCF is caused by the repeated contact loading applied to the cracked surface. The severity of the crack growth is dictated by the magnitude of the relative perpendicular and tangential displacement between the crack faces induced by the loading; this, and the severity of the stresses in the neighbourhood of the crack tip are quantified by the stress intensity factors. The relative magnitude of mode I and mode II stress intensity factors, *KI* and *KII*, not only dictate the crack growth rate, but also the direction of growth. Therefore the modelling technique developed, as thoroughly discussed in Chapters 3 – 5, for solving the stress intensity factors while capturing the fluid/solid coupling at the contact interface, can be directly applied in this chapter. This is complemented by the additional features introduced here for the crack length to be incrementally increased at an angle that is different from the initial angle of inclination and is evaluated based on the evolution of the stress intensity factors during the loading cycle.

A schematic of the physical problem to be considered in this chapter is shown in Fig. 6.1(a). The problem to be solved is the same as the one described in Chapter 5, a roller loaded against a cracked half-plane, where the bodies are separated by a pressurised fluid film.

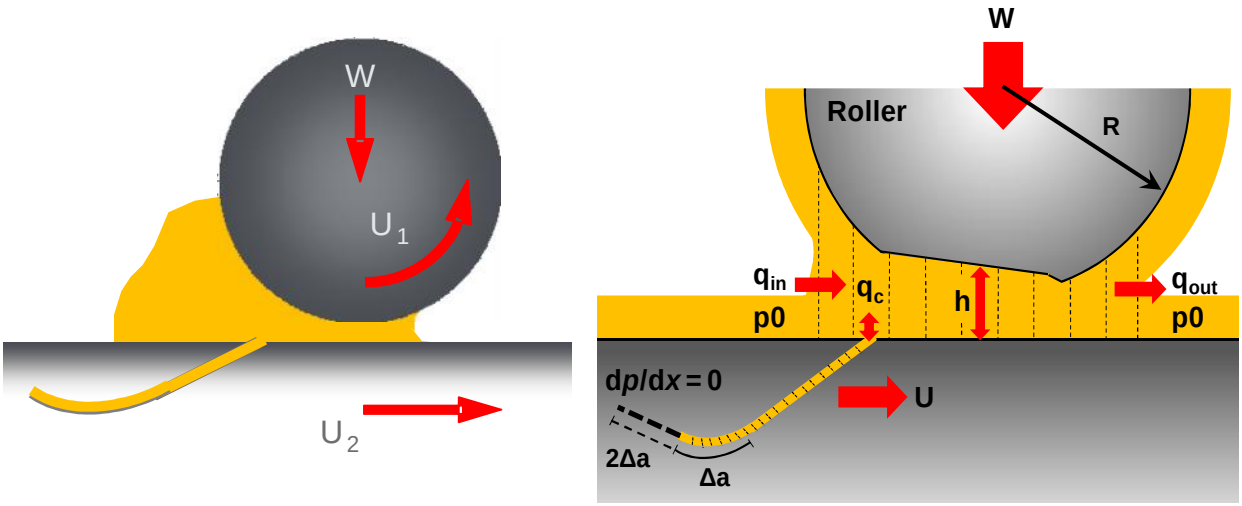


Figure 6.1 Diagram (a) and schematic (b) of the coupled EHL and RCF crack propagation problem, where the crack length is increased by an incremental step *Δa*

The fully coupled EHL model is once again used to solve for the fluid film. For the simulations performed in this chapter, however, multiple load passes are considered and the crack length is increased at every load cycle and follows the computed trajectory. The computational cost is reduced by assuming that the crack propagation direction does not change for a finite number of cycles. This allows fast simulations of crack propagation to failure without introducing large inaccuracies.

Some simplifying assumptions are made when formulating the problem; the assumption applied to the example problems solved here are the same as the assumptions applied to Chapter 5, with the addition of the crack propagation trajectory assumption discussed above:

1. The solid model obeys linear elasticity;
2. The crack surface and outer surfaces are perfectly smooth;

3. The problem can be modelled in 2D;
4. The radius of curvature of the roller is much larger than the contact region;
5. The fluid domain is always fully flooded;
6. The conditions are isothermal;
7. The lubricant is Newtonian;
8. The Doolittle pressure viscosity [165] and Dowson pressure density model [166] are taken to be accurate and correct.
9. The crack follows a certain propagation trajectory for a given length.

Assumptions (1-8) have been addressed and justified in the previous chapters. As mentioned above, assumption (9) imposes that the crack will propagate along a certain path for a given length: this assumption is applied to allow the crack propagation path to be computed using the results in terms of SIFs obtained from a limited number of loading cycles instead of having to solve the problem for *every* loading cycle, therefore having to run the simulations for the number of cycles required for a crack to evolve into a pit (which is computationally very expensive).

6.2 Modelling Strategy and Formulation

The modelling strategy for each of the individual loading cycles is the same as that used in Chapter 5; the novelty introduced here is the capability to capture the evolving crack

shape and to determine the crack growth rate. With this in mind, only the extension of the methodology described in Chapter 5 to include the propagation will be explained.

The methodology is based on analysing the stress intensity factors for a series of repeated, identical loading cycles. The range of the stress intensity factors, *KI* and *KII*, are computed, along with the strain energy density formula used to define the angle of crack growth [173]: this is achieved by minimising the differential of the strain energy density function by means of an iterative method to find the crack growth angle that gives the lowest strain energy density value. This angle can also be thought of as the angle that provides the least resistance to growth. Once this angle has been evaluated, the crack is then assumed to propagate along this path for an imposed length (obviously, the smaller the length the larger is the number of cycles to be solved to predicted the final shape of the pit). The angle of growth is then re-evaluated based on the new SIFs and the crack propagation path is updated. The method is based on calculating the new crack growth angle with respect to the current angle; therefore at each re-evaluation of the crack angle, the calculated angle is added to the existing angle. This method has been applied to uncoupled models in the literature [132, 173], and the strain energy density method is widely applied in the literature and considered as one of the most accurate ways to calculate the trajectory of crack growth.

At each increment when the crack length is extended, the mesh nodes are re-distributed along the entire length of the modified crack so that the nodal distribution and the number of nodes remain constant throughout the solution. The points are distributed based on the set of points from the first crack shape and the position of the

crack tip from the current crack shape; the nodes are re-distributed after curve-fitting between the nodes has been performed. This provides a much smoother transition of the crack shape from a linear to a curvilinear (rather than piece-wise linear) crack; such smoothening is applied to avoid having sharp edges along the crack length (due to discrete kinks) such sharp transitions may lead to unrealistic stress concentrations, stemming from numerical error.

6.2.1 Solid Solver

The solid solver used in this chapter is the same as that of Chapter 5, however for crack propagation; the formulation is no longer based on an inclined slant crack (of constant angle of incline). The formulation is re-derived for a crack that can be defined with nodes distributed along a curvilinear trajectory, and is therefore based on the formulation for a curved crack similar to that described in [150].

The same boundary conditions are used for the formulation of the solid solver in this chapter that have been used previously in Chapters 4 and 5.

$$N(\hat{x}) = p_f \qquad a_{op} < \hat{x} < a$$

$$S(\hat{x}) + fH(\hat{x} - a_{op})N(\hat{x}) = 0 \quad 0 < \hat{x} < a \tag{6.1}$$

where p_f is the fluid pressure at the crack face. There is no shearing effect on the crack face from the fluid pressure because the fluid pressure acts perpendicular to the surface

therefore inducing no shearing component at the surface (as the viscous shear losses in the fluid are neglected in first approximation).

Again, as described in Chapter 3, to simplify the mathematical formulation of the problem, it is formulated with respect to a local coordinate system that is rotated to the angle of incline of the crack, θ. However, in this case, each dislocation that is located at a point (c,d) along the curved crack length can have a unique angle of rotation, and every stress that is evaluated at a point (x,y) along the crack path can also have a unique angle of rotation.

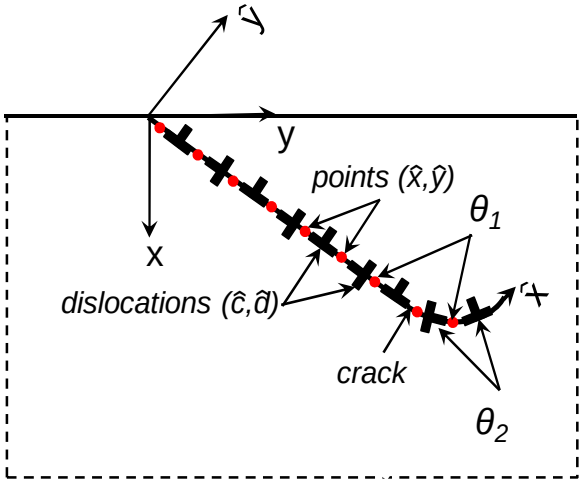


Figure 6.2 Method of rotating the formulation so the axes are in line with the crack

Therefore, to rotate the formulation so that it follows the path of the crack, two sets of angles are used, where the stress influence functions at the points are rotated using one set of angles (θ_1) and the Burgers vector components at the dislocations are rotated using the other (θ_2). This has the effect of rotating the formulation so that the new

transformed co-ordinate system, $(\hat{x},\hat{y})$, follows the curvilinear path of crack. This means that at any point along the crack path $\hat{y}=0$. To do this, the stress influence functions at the points (*K*) have to be rotated first of all, using Mohr's circle and the first set of angles (θ_1), then the Burgers components (*b*) have to be rotated using the rotation matrix and the second set of angles (θ_2). This is done using the following matrix operations, where *M* is Mohr's circle and *R* is the rotation matrix:

$$[M(\theta_1)].[b(c,d)*K(x,y,c,d)].[R(\theta_2)] \tag{6.2}$$

where the influence functions ,K, that are used are the same in the previous chapters.

6.2.2 Crack Growth

The instantaneous angle of propagation of the crack cannot be pre-determined as it is a strong function of the stress field experienced by the crack; this means that the crack can grow at any arbitrary angle depending on the driving forces. With this in mind, the effect of the mixed mode on crack growth needs to be resolved as all the example problems treated so far are characterised by both a positive *KI* and a non-zero *KII*. Evidence suggests that in a situation where both stress intensity factors are present, the crack may extend in a plane normal to the current crack edge, where both the direction of crack growth and the fracture toughness are governed by the strain energy density function [173]. Where the angle of crack growth, with respect to the angle of the

existing crack tip, can be defined using the strain energy density function *s*. The hypothesis is that the direction that gives the lowest strain energy density is the direction in which the crack will grow. Therefore the aim is to find the stationary minimum value, in θ, where:

$$\frac{ds}{d\theta} = 0 \qquad \frac{d^2 s}{d\theta^2} > 0 \tag{6.3}$$

where θ varies between $-\pi$ and π (although this range can probably be reduced due to the fact that a crack cannot usually propagate kinking back to more than $\pi/2$). The strain-energy density function, *s*, is defined as an expression of both stress intensity factors, combined with a set of influence functions (E_{ij}):

$$s = E_{11}K_I^{\,2} + 2E_{12}K_I K_{II} + E_{22}K_I^{\,2}, \tag{6,4}$$

where the influence functions are given in [173], and they are defined as a function of the material properties of the cracked body and the potential crack growth angle, θ.

The function *s* is first computed using the stress intensity factor range ΔK ($K_{max} - K_{min}$) calculated for a loading cycle for the current crack configuration; then, using incremental values of θ, the angle at which the crack propagates is found based on the minimisation strategy defined in Eqs. (6.3 & 6.4) using a simple linear programming algorithm, such as the bisection method.

6.2.3 Crack Propagation Rate

Once the angle at which the crack propagates has been determined, the crack growth is imposed using the pre-defined incremental length, i.e. the crack is assumed to propagate along a given angle for a given length before it changes direction. The angle at which the crack grows is updated again by assessing the SIFs in the modified crack configuration. For each incremental step a back calculation will be performed based on the stress intensity factor range to give the propagation rate; this will be calculated from the Paris law proposed by Paris and Erdogan [75], using Eq. (6.5);

$$\frac{da}{dN} = C(\Delta K)^m \tag{6.5}$$

where the values of C and m are experimentally derived values. These values will be taken from the literature for the purpose of this analysis, which is simply to show the capabilities of the developed code to predict crack propagation rather than performing an extensive comparison with experimental data, and are set to be 5.07E-4 (N/nm$^{-3/2}$) and 2.9 [174] respectively. As a consequence of the fact that for the cases under investigation mixed mode crack growth takes place, an effective ΔK value will be used, that incorporates a weighted influence of ΔKI and ΔKII to generate the input required to evaluate the crack propagation rate from Eq. 6.5. The expression used to calculate the crack propagation rate is based on that of Tanaka et al. [74]:

$$\Delta K_{eff} = (K_I^4 + 8K_{II}^4)^{0.25} \tag{6.6}$$

6.3 Validation

The new crack model that is used in this chapter is validated against a solution for curved cracks reported in the literature. [175]. A schematic of the problem used for validation is shown in Fig. 6.3 a straight ($c_1 - c_2$) and curved section (c_2) of a crack are modelled in a uniform tensile stress field (σ_y).

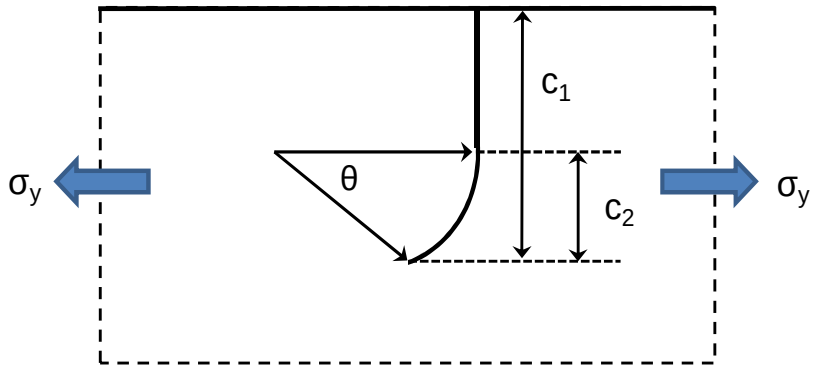


Figure 6.3 Schematic of the problem used to validate the curvilinear crack model

The stress intensity factors obtained using the proposed distributed dislocation technique methodology and the results obtained using the methodology outlined in [175] are compared for a series of curved cracks, where both the angle that the crack tip forms with respect to the half-plane surface and the ratio between the straight length and the curved length of the cracks, c2/c1, are varied.

The results of this comparison are reported in Table 6.1. The results are in good agreement, although this has to be expected because both sets of results are derived

from semi-analytical integral methods, although in the case of the formulation proposed by Noda and Oda [175] a body force method is applied.

Noda & Oda								
	15		30		45		60	
c2/c1	KI	KII	KI	KII	KI	KII	KI	KII
0.2	1.0689	0.1649	0.9212	0.295	0.7065	0.3629	0.4639	0.3539
0.6	1.0684	0.1706	0.9196	0.3037	0.704	0.3704	0.4618	0.3562
1	1.0684	0.172	0.9197	0.3051	0.7044	0.3699	0.4627	0.3525
Balcombe								
	15		30		45		60	
c2/c1	KI	KII	KI	KII	KI	KII	KI	KII
0.2	1.0731	0.1624	0.9266	0.2903	0.7122	0.3602	0.4721	0.3488
0.6	1.0717	0.1647	0.9234	0.2931	0.7131	0.3644	0.4703	0.3503
1	1.0706	0.1662	0.9209	0.2946	0.7154	0.3667	0.4683	0.3499

Table 6.1 – Comparison between the method used in this chapter and Node et al [175]

6.4 Results and Discussion

In order to study propagation in an RCF scenario, one of the cases investigated in Chapter 5, case b(1) in Table 5.3, is considered to simulate the evolution of the crack shape based on the stress intensity factors history and variation within each individual loading cycle. The operating conditions, to which the increment for the crack propagation, Δa, is added, are again reported in Table 6.2. For the purpose of analysing the crack propagation the isoviscous fluid model is used and combined with the solid model that includes the effect of the crack mouth deflection on the half-plane surface flow; thus, the algorithm used is the one that is discussed in section 5.4.3 of Chapter 5.

Case	Liquid	a	h_{c0}	U_S	W_F	E	σ_Y	η	θ	Δa
		μm	nm	m/s	N/m	GN/m^2	MN/m^2	Pa/s	°	μm
1	Base Oil	100	250	3	50000	210	800	0.137	25	10

Table 6.2 Operating conditions of the case used to study propagation

The solution procedure can be simply described as follows: first of all, a loading cycle on the initial (straight) crack is solved to obtain the initial stress intensity factors and to calculate the path of the first step of propagation. This process is then repeated after making the crack evolve by changing the crack length and adding the incremental length chosen for the simulation of the crack; the stress intensity factors are then re-evaluated to find the path along which the crack will continue to grow. The crack is assumed to propagate along the same path for a length of $\Delta a = 10\mu$m, which is defined arbitrarily as a fraction of the initial crack length, i.e. $a = 100\mu$m. Other simulations were carried out with reduced values of the crack increment and showed that the crack path is already well captured with such an increment and that this incremental length gives the best compromise in terms of computational speed and accuracy of the results.

Considering the shape of the crack obtained after performing the crack propagation simulations using the fluid/solid coupled algorithm, it is predicted that the crack curves toward the surface, resulting in a pit breaking away from the surface (see Fig. 6.4(A-H)). The process of the crack evolving from a straight crack to a fully formed micro-pit takes 8 propagation steps of increasing a crack of an initial length 100μm by 10μm at each step. It should be noted here that when increasing the crack length the algorithm that is used to plot the nodal points of the crack causes some deviations from

the crack path determined in the previous propagation steps, and hence the depth of the micropit is less than the initial depth of the crack, as shown in Fig. 6.4(a-h). This stems from the method of curve fitting a spline to the end point of the crack and the initial point of the curve that is created by the propagation and then re-distributing the collocation points along the full length of the crack. This issue can easily be overcome by reducing Δa and/or increasing the number of collocation points used for each propagation step, so that a more uniform distribution is obtained during the full propagation process. Such refinements will be the object of future investigations. However, it has been shown in the literature [175] that the angle formed by the crack tip with respect to the half-plane surface is the key factor influencing the stress intensity factor instead of the full crack path; this result suggests that this slight discrepancy should not significantly alter the calculated stress intensity factors, and, although the final crack path is somewhat approximated, the final shape of the fully propagated crack should not be affected by the procedure adopted here.

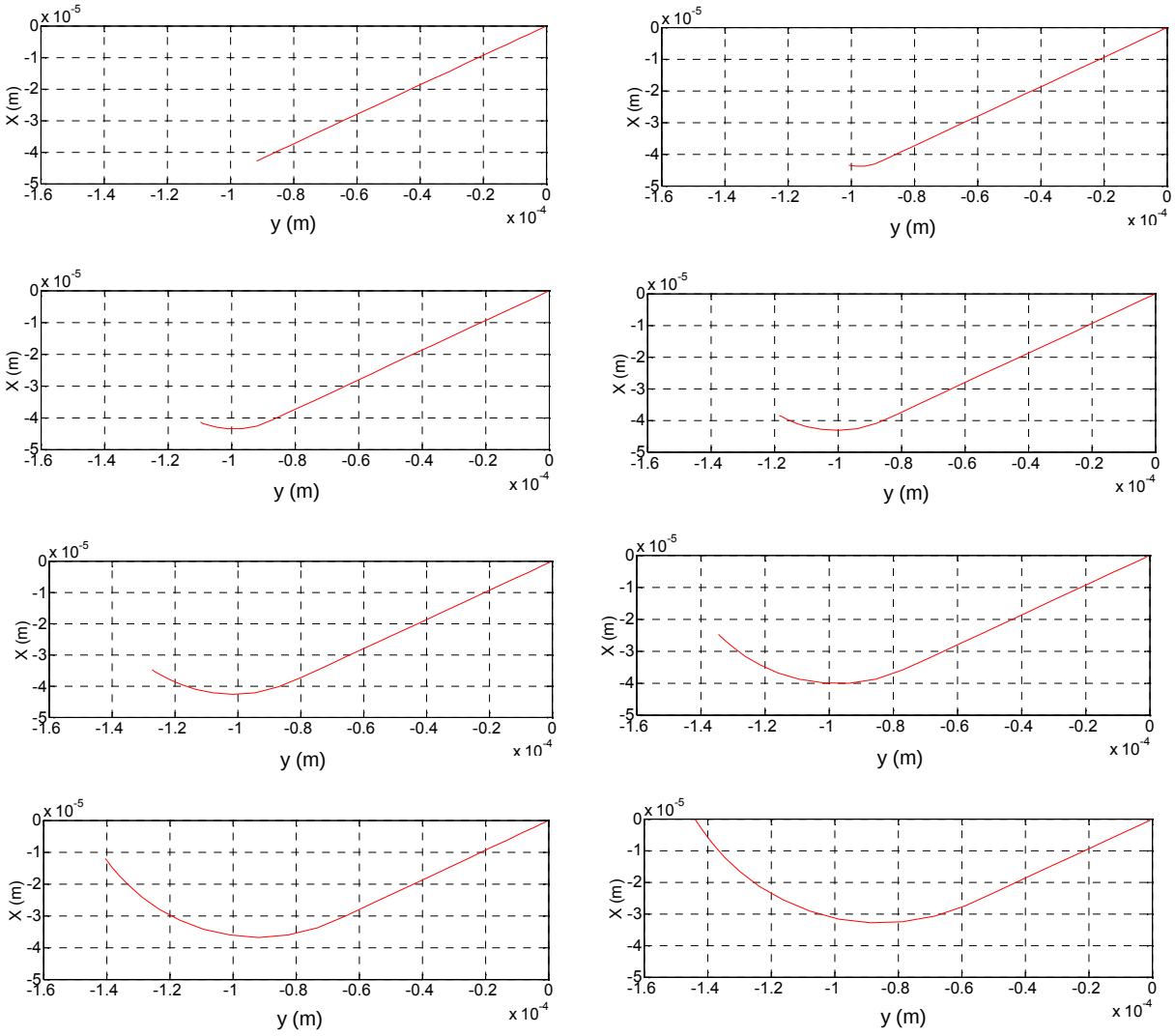


Figure 6.4 (a – f) Evolution of the crack path due to the propagation steps, *Δa*

The shape of the crack that the propagation study predicts, shown in Fig. 6.4(f), appears to compare well with the shape of micro-pits observed and reported in the literature [176]. The pit generated by an initial crack of 100*μ*m is around 145*μ*m long and 40*μ*m deep. The propagation path predicted by the model, in particular, compares well with an experimentally observed pit observed by Glodež et al., shown in Fig. 6.5.

Although the crack dimension and loading used by the author produce a smaller pit, the qualitative match with the experimentally observed pit geometry suggests that the model predicts the propagation of the crack with a good degree of accuracy.

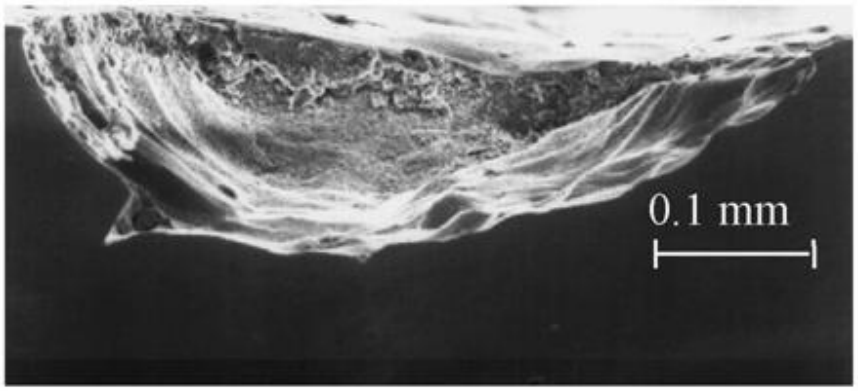


Fig. 6.5 Micropit as experimentally observed by Glodež *et al.* [176]

We turn now to the determination of the number of cycles required to propagate the crack for each step of the total crack propagation to failure. Paris law is used along with the ΔK values calculated and used to determine the evolution of the crack path. From the solution of the stress intensity factors, shown in Fig. 6.6a & b, it is clear that as the crack grows the stress intensity factors increase. This behaviour has already been seen in Chapter 5 for straight cracks of different length; considering crack propagating along a curvilinear path rather than along the linear trajectories that have been considered thus far. The qualitative behaviour observed does not change but the fact that crack advances along a curvilinear path, therefore being subjected to a different stress field, does have an influence on the quantitative values obtained for the propagation life. Even though the angle of orientation of the crack tip is changing as it propagates the

stress intensity factors still increases. From the propagation study the ratio of the stress intensity factors, *KI/KII*, also appears to give the similar trend, with their maximum magnitudes being related by *KII* ≈ 0.5 *KI*. This ratio stays, approximately, constant throughout the propagation phase.

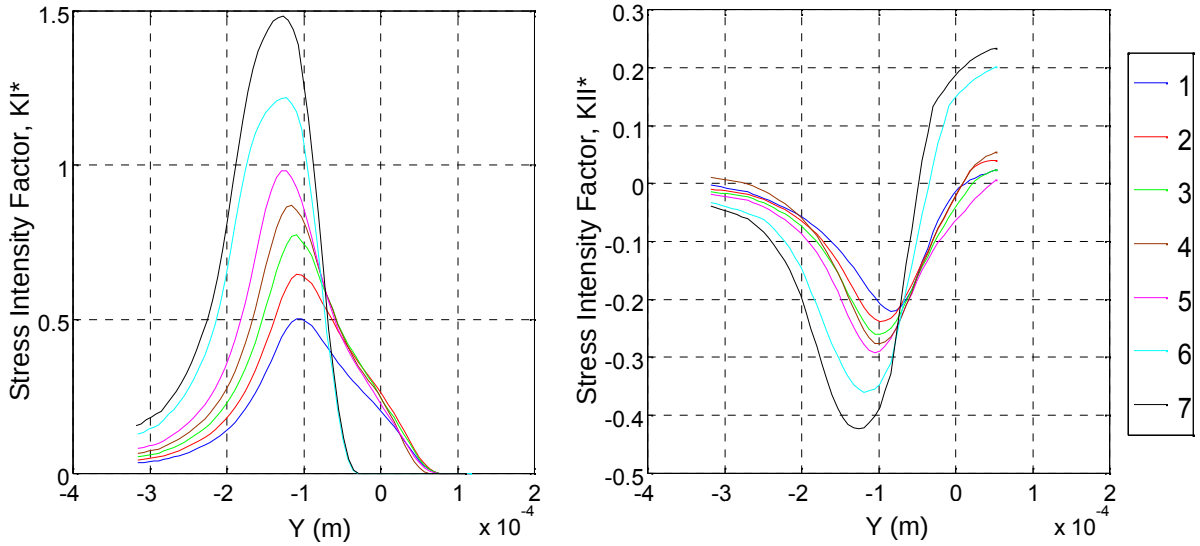


Figure 6.6 Evolution of SIF histories for each load cycle during propagation (a) *KI* (b) *KII*

The results presented in the validation section of chapter 3 (Fig. 3.9) suggested that as the crack orientation changes the stress intensity factors are largely affected by such change, both in terms of magnitude of *KI* and *KII* and their ratio, *KI/KII*; in that case however the presence of the fluid was neglected and the driving forces were the stresses induced locally by the external load. Therefore, as the crack orientation changed, the stress field around the crack tip also changed significantly. In the case analysed here, there are two diving forces which contribute to the evolution of the SIFs, the surface film pressure and the fluid pressure within the crack; although the stress

field induced by the surface film pressure is influenced by the cracks orientation and its path in the half-plane, the crack pressure always acts perpendicular to the crack face and is therefore, not significantly influenced by the orientation of the crack. This is why the trend that is seen from the results of the stress intensity factors solved from the curvilinear crack in this propagation study is the same as the trend seen by increasing the crack length in the straight crack study. It should be noted, however, that the calculation performed here are carried out assuming that the crack is always fully filled, assumption that might not remain valid throughout the crack propagation life as the crack grows in length.

Using the computed stress intensity factors, the propagation of the crack is analysed using Paris law [161] combined with Tanaka's [74] method for combining Δ*KI* and Δ*KII* for mixed mode crack growth to give an effective stress intensity factor ΔK_{eff}. The evolution of these values during the propagation of the crack are reported in Table 6.3, where the stress intensity factors are expressed dimensionally using the following transformation:

$$K = K^{*}.p_{f\max}\sqrt{®a} \qquad (6.7)$$

where p_{fmax} is the maximum EHL contact pressure

Each propagation step of 10μm is analysed separately to find the number of cycles required to propagate the crack for that length along the given path; the coefficient for Paris law C (N/nm$^{-3/2}$) is expressed in Table 6.3 in, which corresponds to da/dN

calculated nm/cycle, and therefore Δa is also expressed in nm. The first step of the propagation cycle gives a growth rate of d*a*/d*N* of 0.0107 nm/cycle, and this means that to grow the crack by the 10*μ*m takes 932522 cycles. However, as the crack length increases, and so too does the stress intensity factor range, the crack growth rate increases exponentially; thus, by the last propagation increment, the number of cycles required to grow the crack by 10*μ*m is only 20519 cycles (a reduction by a factor of 45).

Step No.	Δa	a	C	m	ΔKI	ΔKII	ΔK_{eff}	da/dN	No. Cycles	Total Cycles
	μm	μm	$N/nm^{3/2}$		$MPa.m^{1/2}$	$MPa.m^{1/2}$	$MPa.m^{1/2}$	nm		
1	10	100	5.07E-04	2.90	2.606	1.276	2.864	1.07E-02	932522	932522
2	10	110	5.07E-04	2.90	3.586	1.506	3.791	2.42E-02	413720	1346241
3	10	120	5.07E-04	2.90	4.485	1.689	4.656	4.39E-02	227953	1574194
4	10	130	5.07E-04	2.90	5.244	2.001	5.454	6.94E-02	144085	1718278
5	10	140	5.07E-04	2.90	6.186	1.887	6.290	1.05E-01	95239	1813518
6	10	150	5.07E-04	2.90	7.939	3.582	8.528	2.54E-01	39407	1852925
7	10	160	5.07E-04	2.90	10.022	4.372	10.680	4.87E-01	20519	1873443

Table 6.3 Paris law calculation of the crack propagation rate

The growth rate of the crack, d*a*/d*N*, is plotted against the crack length in Fig. 6.7(a), where an almost exponential relationship between these two variables is shown, demonstrating the considerable acceleration of crack growth rate with the increasing crack length; this would suggest that for very long cracks propagating in a stress field similar to the one used here, crack growth would be very rapid. However, as mentioned above, this study is based on a fundamental assumption that the crack is fully filled with fluid and that this fluid film becomes pressurised; in practice this assumption may not be valid when cracks become very long as they are likely to be only partially filled with fluid and, therefore, the contribution of the hydraulic pressure may vanish. Hence, the cracks

are more likely to close when they enter the contact and their behaviour resembles more the one observed using an entrapment model [177]. Therefore, although this result is valid in the case of shorter cracks, the exponential relationship between crack length and growth rate cannot be extrapolated for larger cracks without further investigation.

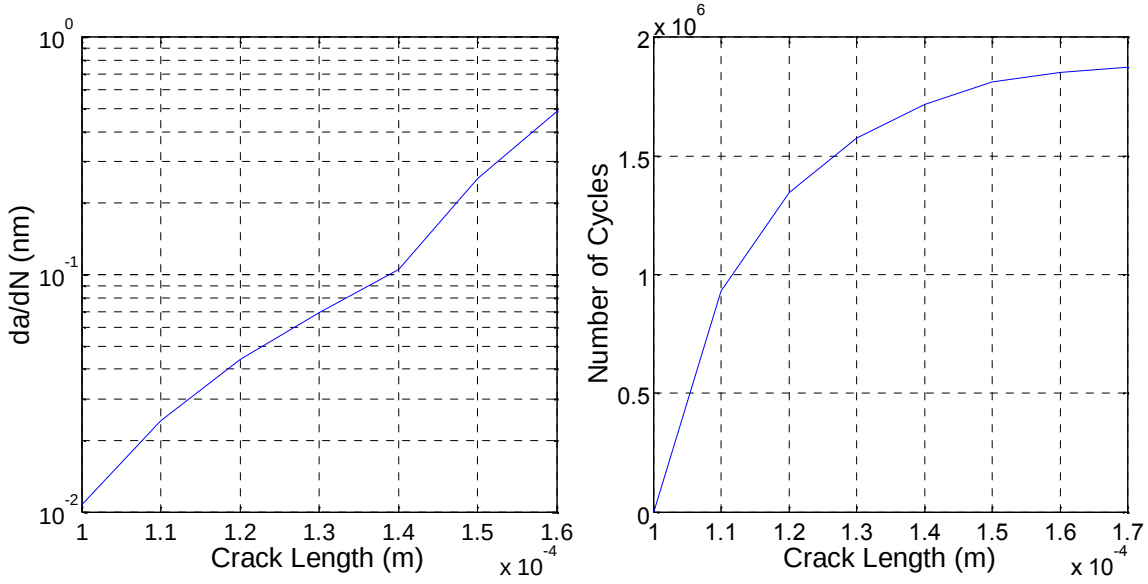


Figure 6.7 (a) Crack propagation rate (b) Number of loading cycle required grow the crack by *Δa*

The number of loading cycles plotted against the crack length, shown on Fig. 6.7(b), reveals that the first step in the propagation cycle takes as long as the rest of the propagation process; this underlines the rapid acceleration of the crack growth as the crack length increases.

The influence of the two stress intensity factors on the rate of crack propagation is now considered. The results given in Table 6.4 show the influence on the propagation

process of *KII*. The propagation based on Paris law is calculated here using only one of the two stress intensity factors to study the relative influence they have on the crack propagation process. It has been assumed that the crack path is not altered and that the ratio between the two SIFs still determines the crack path.

ΔKI	da/dN	No. Cycles	Total Cycles	ΔKII	da/dN	No. Cycles	Total Cycles
$MPa.m^{1/2}$	nm			$MPa.m^{1/2}$	nm		
2.606	8.15E-03	1227169	1227169	1.276	1.03E-03	9724348	9724348
3.586	2.06E-02	486006	1713175	1.506	1.66E-03	6018646	15742994
4.485	3.94E-02	254002	1967178	1.689	2.32E-03	4312271	20055265
5.244	6.20E-02	161402	2128579	2.001	3.79E-03	2639762	22695027
6.186	1.00E-01	99983	2228562	1.887	3.20E-03	3125617	25820644
7.939	2.06E-01	48499	2277061	3.582	2.05E-02	487628	26308273
10.022	4.05E-01	24675	2301736	4.372	3.66E-02	273559	26581831

Table 6.4 Comparison of Paris law calculated only with (a) KI and only with (b) KII

From the results reported in Table 6.4 it can be seen that there is very little difference in the number of cycles required to form a micro-pit from an initial surface breaking crack when combining both SIFs and when only considering *KI*. If both *KI* and *KII* are used, the simulation predicts 1873443 cycles to failure, while in the case where only *KI* is considered; the prediction gives 2301736 cycles to failure, a difference of around 20%.

Now repeating this exercise, but this time solving the propagation calculations using solely *KII* to determine ΔK_{eff}, provides a very different picture. While the mixed mode calculations predict 2233544 cycles to form a micro-pit from the surface breaking RCF crack, using only *KII* and neglecting *KI* predicts 26581831 cycles, an increase by a factor greater than 12.

By plotting the difference between the calculations based on both SIFs and the calculations based solely on *KI* or *KII*, the very large difference between the two sets of calculations is immediately apparent. Fig. 6.8(a) shows the difference in the propagation rate d*a*/d*N*, while Fig. 6.8(b) shows the difference in the number of cycles required to propagate the crack, where the blue line is the solution based on *KI* and *KII* and the red line is the solution based solely on KI (though the red and blue lines are almost overlaid) and the black line is the solution based solely on *KII*.

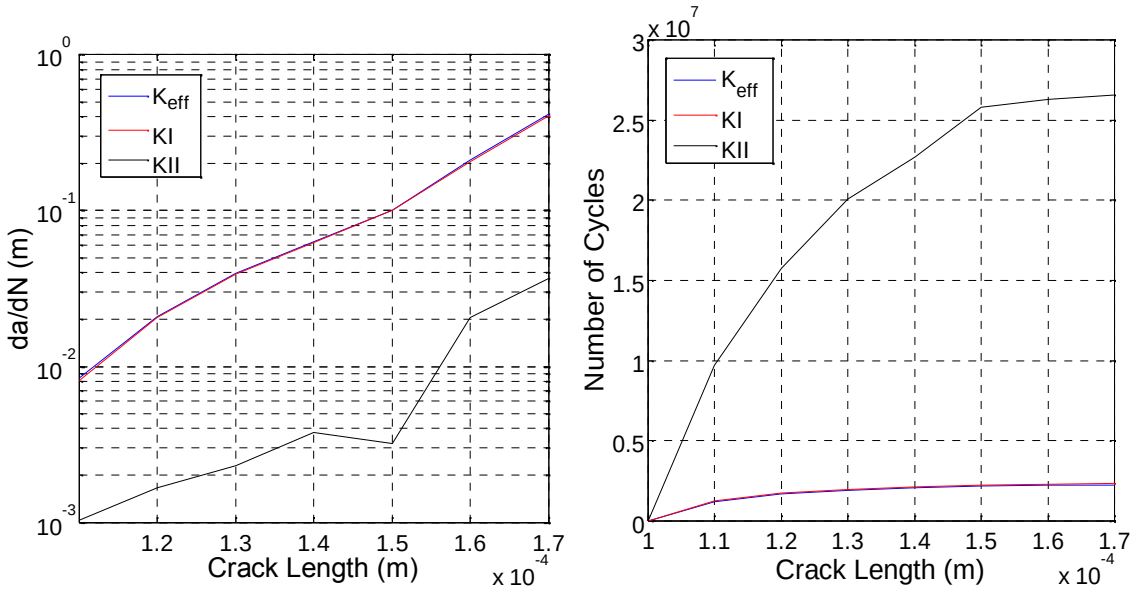


Figure 6.8 The effect of chaging *the SIF mode used to calculate:* (a) Crack propagation rate (b) Number of loading cycle required to grow the crack by *Δa*

The reason that it is important to consider this difference is because *KI* is almost entirely induced by the fluid pressure inside the crack, and is heavily influenced by the behaviour of the fluid pressure in the surface film inside the contact. Therefore, any model that is used to analyse the growth of RCF cracks in EHL contacts needs to

accurately account for this behaviour or else large discrepancies will be introduced into the prediction of the crack growth rate.

If we consider now, as an example, the problem solved in Chapter 3, where the crack is solved without considering any hydraulic effects induced by the fluid pressure, it is solved simply using a Hertzian contact pressure acting in the interface between the rolling element and the cracked half-plane. The model predicts crack growth rates that are based almost solely on *KII*, where a non-zero mode I SIF (*KI*) needs to be allied with a high surface friction coefficient so that crack opening is induced by shearing. However, by not considering the hydraulic fluid pressure acting inside the crack the predicted number of cycles taken to propagate a surface crack to a micro-pit (and indeed the shape of the pit), would be very different. This means that if fluid pressure does build up in an RCF crack (and the modelling work done during this study suggests that it does for the operating conditions that have been solved here), then this mechanism needs to be taken into account when analysing crack propagation. If this contribution to loading of an RCF crack is neglected then highly inaccurate estimates of the number of cycles needed to form a micro-pit from a surface breaking crack will be calculated.

The reason that, based on the results used in this chapter for the propagation calculations, *KI* exerts so much influence over the calculated propagation rate is because the values of *KI* are around 2 → 2.5 times larger than the values of *KII*. This means that including *KI* greatly increases the value of the solved ΔK_{eff} used to evaluate the propagation rate in Paris' law. Where the value of ΔK_{eff} is raised by the exponent

2.9, so an increase in ΔK_{eff} of, for example, 2.25 will give an increase in the growth rate of $2.25^{2.9}$, which gives a factor of 10.5.

The propagation study that is done here uses case b1 that is discussed in Chapter 5. The operating conditions applied to this case give a maximum contact pressure in the surface film of around 300MPa. If we now assume that the dimensionless stress intensity factors that are evaluated in case b1 were to remain constant as the load is increased and the values of *KI* and *KII* can be used to re-compute what effect increasing load would have on the propagation rate. So by changing the value of p_{max} in Eq. (6.7) from 300MPa to 1GPa and re-computing the propagation rates it can be seen that this would influence the propagation rate a significant amount.

Step No.	Δa	a	C	m	ΔKI	ΔKII	ΔK_{eff}	da/dN	No. Cycles	Total Cycles
	µm	µm	$N/nm^{3/2}$		$MPa.m^{1/2}$	$MPa.m^{1/2}$	$MPa.m^{1/2}$	nm		
1	10	100	5.07E-04	2.90	8.685	4.254	9.548	3.52E-01	28399	28399
2	10	110	5.07E-04	2.90	11.953	5.019	12.636	7.94E-01	12600	40999
3	10	120	5.07E-04	2.90	14.951	5.631	15.519	1.44E+00	6942	47941
4	10	130	5.07E-04	2.90	17.481	6.669	18.179	2.28E+00	4388	52329
5	10	140	5.07E-04	2.90	20.620	6.292	20.968	3.45E+00	2900	55230
6	10	150	5.07E-04	2.90	26.462	11.939	28.426	8.33E+00	1200	56430
7	10	160	5.07E-04	2.90	33.406	14.573	35.600	1.60E+01	625	57055

Table 6.5 Re-evaluation of Paris law assuming a 1GPa EHL pressure

With a peak pressure of 1 GPa and assuming that similar values of dimensionless *KI** and *KII** obtained for a lower contact pressure still apply to this case, the results predict that a pit could be formed from an initial surface breaking RCF crack in less than 60000 cycles. This suggests that at higher contact pressures the crack growth rate increases

considerably. However, since the above assumption needs to be verified and is not likely to hold true due to the large non-linearity's present in the system under investigation, this calculation only provides an indication of what the effect of high contact pressure would be, and the potential implications for the rate of crack growth and the time taken for pits to form when working with high contact pressures. A more detailed quantitative study of such effect will be the subject of a future investigation.

6.5 Summary

To summarise, in this chapter the fully-coupled EHL solver developed and validated in the previous chapters has been used to analyse crack propagation for an example RCF problem. A single case has been used to demonstrate the capabilities of model to predict both the crack shape evolution and the crack propagation rate. The results have been qualitatively compared with an experimentally observed micro-pit reported by Glodež *et al* [176]. The implications of neglecting fluid pressurisation when calculating crack propagation rates have also been outlined: it is shown that models that do not consider the effect of hydraulic action inside the crack due to fluid pressurisation will lead to inaccurate estimates of the number of cycles required to propagate a surface breaking crack to form a pit or a micro-pit.

Chapter 7

Experimental Development

7.1. Introduction

This chapter will give an overview of the experimental technique that has been identified as suitable for studying lubricated cracks; its development will be described and the preliminary results will be presented. The experimental work presented in this chapter was conducted by the author in collaboration with Dr Mark Fowell of the Tribology Group at Imperial College, as part of a larger EPSRC funded research project (grant EP/E034179/1). Therefore, although this work constitutes part of author's PhD studies, the credit for the development and application of the experimental technique described here needs to be shared equally between the two researchers.

The objectives of the experimental work were twofold: (i) to develop a viable technique for analyzing RCF cracks as they pass through an EHL contact in real time. This is sought to give a means for comparison with the modelling work to validate the model. (ii) The secondary objective of the experimental work is aimed at justifying the assumption that the crack fills with fluid, and remains fully filled, as it passes through the EHL contact, one of the fundamental assumptions of the model.

7.2. Simulating a Surface-Breaking Crack

The challenge when developing any experimental set up is to replicate the “real life” situation as closely as possible with chosen test conditions. For rolling contact fatigue this presents a particular challenge. Firstly, the length scale of RCF cracks is measured in microns and secondly, steel is an opaque material and, therefore, it is difficult to observe any cracks in-situ in steel-on-steel contact. Furthermore, the loading frequency in a typical RCF situation is very high, generally greater than 100Hz [170], which means that the loading cycle of an RCF crack is very short in real time.

With this in mind, the first simplification made in the development of the experimental method was to scale-up the crack by two orders of magnitude, from 50 - 150 microns in the model to around 10mm in the experimental set up. The second simplification dealt with the problem of the opaque steel material which obviously makes monitoring and recording what happens inside the crack in an EHL contact, very difficult. Established techniques of studying EHL contacts overcome this problem by

using sapphire as one of the counter faces [5, 178]. Sapphire is transparent and has relatively similar material properties to steel; in particular, it has comparable rigidity and is more suitable than glass in replicating steel-on-steel contacts. Given this background, a replica RCF crack in sapphire was developed so that the fluid could be monitored using a high speed camera as the cracked sample passes through an EHL contact. From the modelling work done in this study and elsewhere in the literature, it is clear that the angle of incline of the crack to the surface is very influential on the crack's behaviour when in the EHL contact. Therefore, in the experiments presented here, care was taken to ensure that the crack is inclined at the correct angle, i.e. ~25° from the horizontal.

To create the EHL line contact, a roller on disc set-up found in a standard PCS Instruments EHL rig is used. The sapphire specimen used in the experiments is very expensive and difficult to machine to the tolerance required, hence difficult to replace, while, unfortunately, being easily chipped. In order to prevent damage to the sapphire, a special polymer roller counter-face was used in the study, leading to an increased contact area and decreased contact pressures. The increased contact area is also necessary so that the contact patch is scaled up appropriately in relation to the larger crack used here to simulate much smaller RCF cracks.

To incorporate the model crack into the overall experimental set-up, a metal disk was made with a cut out suitable to hold a sapphire window containing the model crack. The crack is formed between the two accurately machined pieces of sapphire, which are then inserted into the metal disk as shown in Fig. 7.1. The two pieces of sapphire

are machined with an identical incline on both, machined to a very high tolerance of < 1μm.

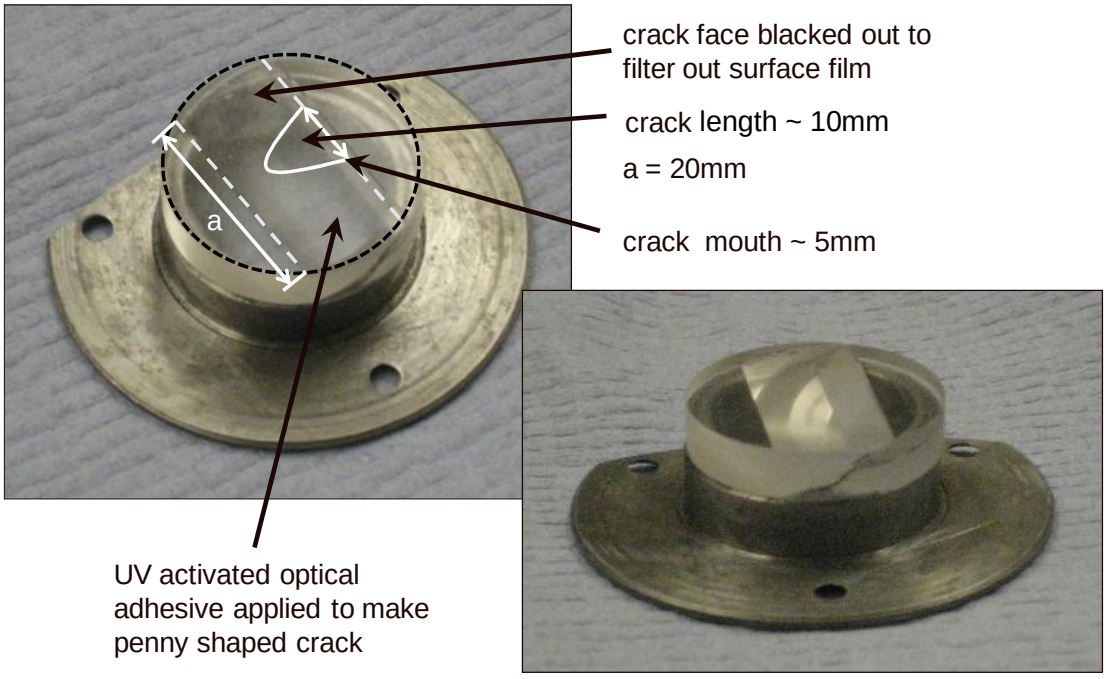


Figure 7.1. Idealised crack created using sapphire inserts.

The matching of the two sapphire inserts is achieved by cutting a single piece of sapphire to obtain both pieces. A strong UV activated adhesive is applied to the edges of the inclined faces of the sapphire inserts so that a penny shaped region is left un-adhered. This penny shaped, un-adhered region, forms the model crack. The experimental set up is shown in Fig. 7.2.

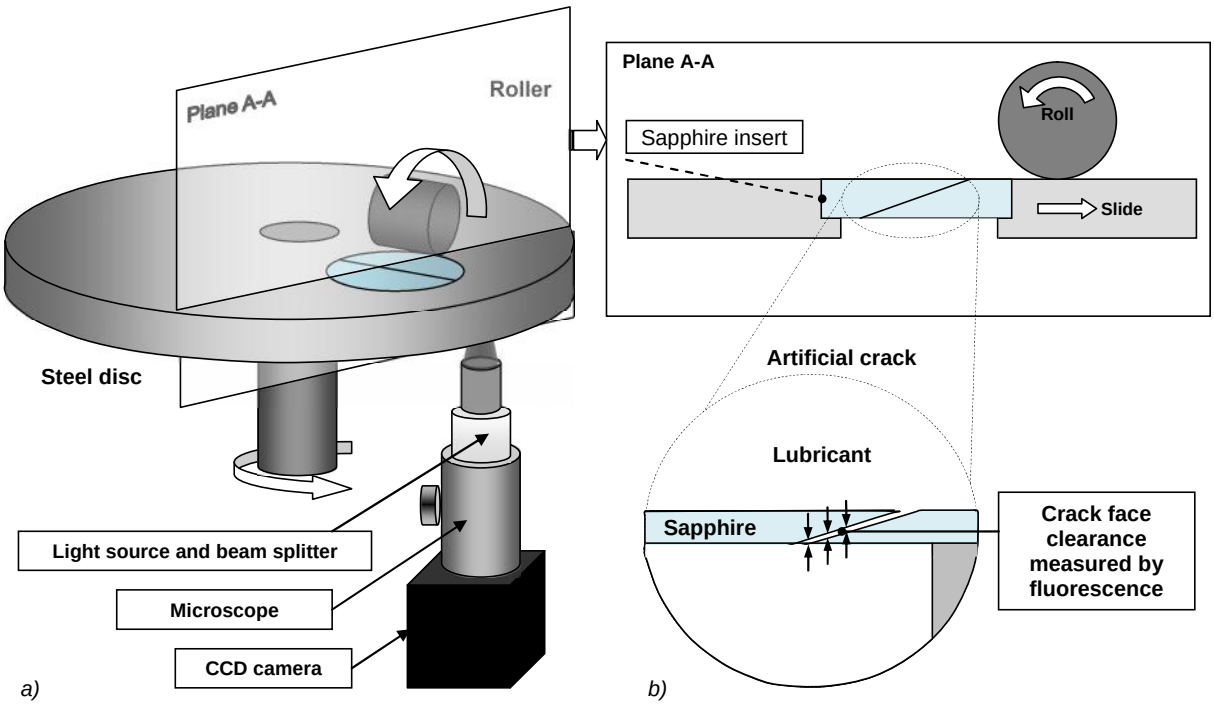


Figure 7.2. Experimental setup with sapphire windows used to simulate a RCF crack.

7.3. Experimental Method for Monitoring the Crack

To monitor the crack as it passes through the EHL line contact, the possibility of using different techniques was explored, including optical interferometry [178], ultrasound [179] (this is also applicable to an opaque crack) and laser induced fluorescence (LIF) [180]. As both optical interferometry and LIF had already been successfully applied to EHL line contact studies in the tribology group at Imperial College, using the PCS Instruments EHL rig, it was deemed sensible to utilize the existing expertise and focus on the viability of these two techniques. Application of optical interferometry to the

proposed contact set-up was considered to be problematic given the number of reflective surfaces present when the crack opens (the contact surface and the two crack faces) as well as the fact that these reflective surfaces have complex orientation. These complications would make it extremely difficult to accurately analyse the interference images from this technique. Therefore, given these considerations, the LIF technique was chosen as the most suitable for the proposed experiment.

7.3.1 Principles of Laser Induced Fluorescence[3]

Laser induced fluorescence (LIF), is a technique based on the photo-excitation of a fluorophore or fluorescent dye. It has become a commonly used visualization technique for numerous 1D, 2D and 3D applications [181]. In order to understand the principles of this technique and the advantages it presents, it is necessary to understand the fundamental characteristics of dye photo-fluorescence and how it can be used to determine a scalar of interest [181], in this case the internal crack film thickness. Fluorescence is the result of a three-stage process that occurs in certain molecules called *fluorophores* or fluorescent dyes. These three stages are outlined in Fig. 7.3 and described by Haugland [182] and Hidrovo [181] as:

[3] Much of the description of the LIF method is taken from [178] and is used with the permission of the author.

A. Excitation: A photon of energy $h\nu_{EX}$ is supplied by an external source, such as an incandescent lamp or a laser, and is absorbed by the fluorophore, creating an excited electronic singlet state (S'_1).

B. Excited-State Lifetime: The excited state exists for a finite time (typically 1 ns to 10 ns). During this time, the fluorophore undergoes conformational changes and is subject to a multitude of possible interactions with its molecular environment. These processes have two important consequences. First, the energy of S'_1 is partially dissipated, yielding a relaxed singlet excited state (S_1), from which fluorescent emission originates (see point C below). Second, not all the molecules initially excited by absorption (Stage 1) return to the ground state (S_0) by fluorescent emission. Other processes such as coalitional quenching, fluorescence energy transfer and intersystem crossing may also depopulate S_1. The fluorescence quantum yield, which is the ratio of the number of fluorescence photons emitted (Stage 3) to the number of photons absorbed (Stage 1), is a measure of the relative extent to which these processes occur.

C. Fluorescence Emission: A photon of energy $h\nu_{EM}$ is emitted, returning the fluorophore to its ground state S_0. Due to energy dissipation during the excited-state lifetime, the energy of this photon is lower, and therefore of longer wavelength, than the excitation photon $h\nu_{EX}$. The difference in energy, or wavelength represented by ($h\nu_{EX} - h\nu_{EM}$), is called the Stokes shift. The Stokes

shift is fundamental to the sensitivity of fluorescence techniques because it allows emission photons to be detected against a low background, isolated from excitation photons.

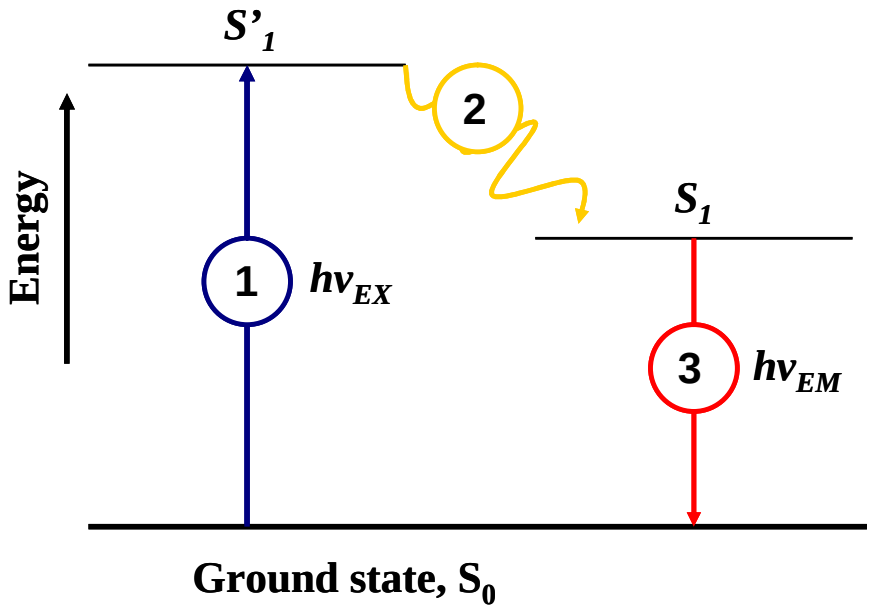


Figure 7.3. Fluorescence principle: a schematic.

Hidrovo *et al.* [181], state that photo fluorescence can be used to characterize any scalar that affects the fluorescence of the dye. Fluorescence is a function of the dye characteristics, the dye concentration, the exciting light intensity, and the scalar value being measured. Once a particular dye and concentration are selected, the fluorescence dependence on these factors is constant.

The intensity of the measured fluorescence from the LIF technique, in relation to this experimental study is therefore dependent on [181]:

- Excitation intensity
- Dye concentration, which is a measure of the number of molecules present.
- The thickness of the fluid element analysed; individual pixels from an optical image in this case.

If the excitation and the dye concentration are kept constant, the thickness of the fluid element is the only variable, so that the thicker the film, the greater the measured fluorescent intensity. Problems can lie in the irregularity of the illumination light intensity. Most illumination sources are far from uniform, they vary in intensity, in space and in time [181], however for this study these effects are neglected and only the direct correlation between the fluorescent intensity and the film thickness is drawn.

7.4 Experimental Apparatus

The experimental setup in this the study uses an adapted EHL optical interferometry rig (PCS-Instruments, UK), shown in Fig. 7.4. Excitation of the fluorescent dye and illumination of the contact is provided by a solid-state, diode-pumped, pulsed laser, which produces green light with wavelength of 532nm. A low power laser (Laser2000 Ltd, Northants, UK) with a maximum power output of 40mW at 3kHz is used.

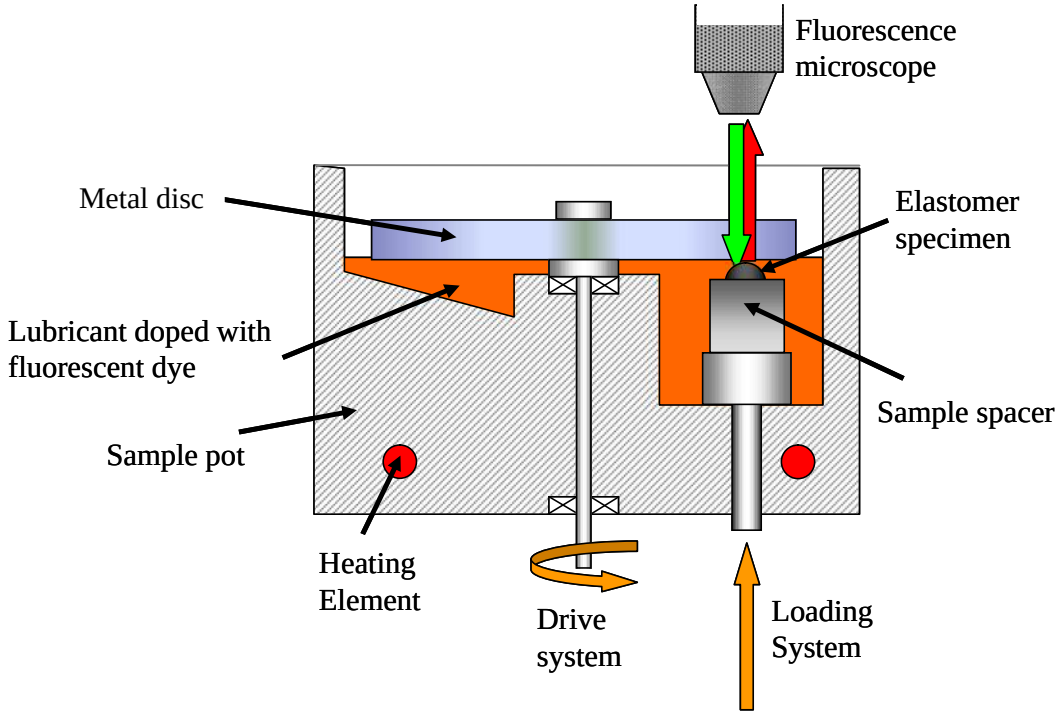


Figure 7.4 Contact and sample pot

7.4.1 Drive and Load System

The standard EHL optical interferometry rig employs a steel ball supported on a bearing carriage, to allow free rotation of the ball. For the current study, the ball and carriage are replaced by a polymer roller. The bottom surface of the roller is immersed in a lubricant bath so that lubricant is entrained into the contact by the rotation of the polymer roller against the steel disk. The set-up is shown in Fig. 7.5.

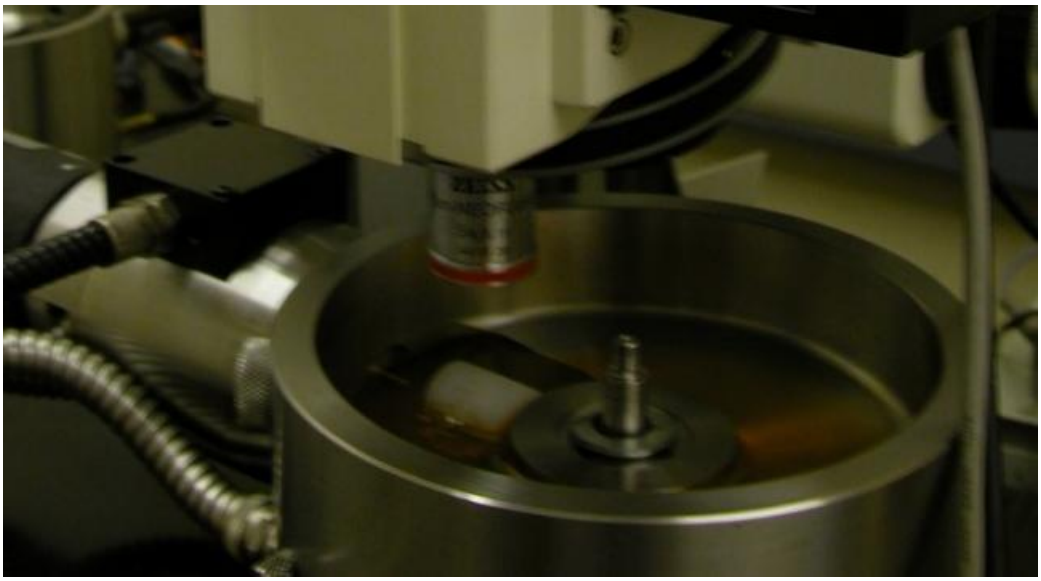


Figure 7.5. Polymer roller and lubricant pot.

The drive system is the standard one supplied with the PCS Instrument rig, where the disk is driven by a DC electrical motor with an optional 25:1 reduction gear box. This allows for accurate control of entrainment speed in the range of $3ms^{-1}$ to $0.1mm\ s^{-1}$.The entrainment speed, *U*, is defined as the mean speed of the two surfaces. In the present experiment, both surfaces are travelling at the same speed so that the system is in pure rolling, and the entrainment speed is equal to the rolling speed:

$$U = \frac{u_b + u_d}{2} \qquad (7.1)$$

Where u_d is the disk speed and u_b is the speed of the ball or, in this case, the polymer roller, which, in this case, is $u_b \equiv u_d$.

The loading is achieved through the existing displacement controlled loading system, designed for hard/metallic contacts. The sapphire inserts are placed in the metal disk and the polymer roller is loaded against the disk, with the sapphire inserts, from below.

7.4.2 Optical Equipment

The fluorescence intensity images were observed with an Axiotech Vario microscope (Zeiss, Germany), whose position is adjustable along the vertical axis. The mechanical rig was placed on an X-Y platform, allowing image capture of the tribological contact to take place along both axes. A magnification of 3X was found to be convenient for observing the contact region. No eyepiece was needed for the experimental setup as a live image display is provided on the camera's operating PC. Excitation was provided using a solid-state, diode-pumped pulsed laser which generates a wavelength of 532 nm.

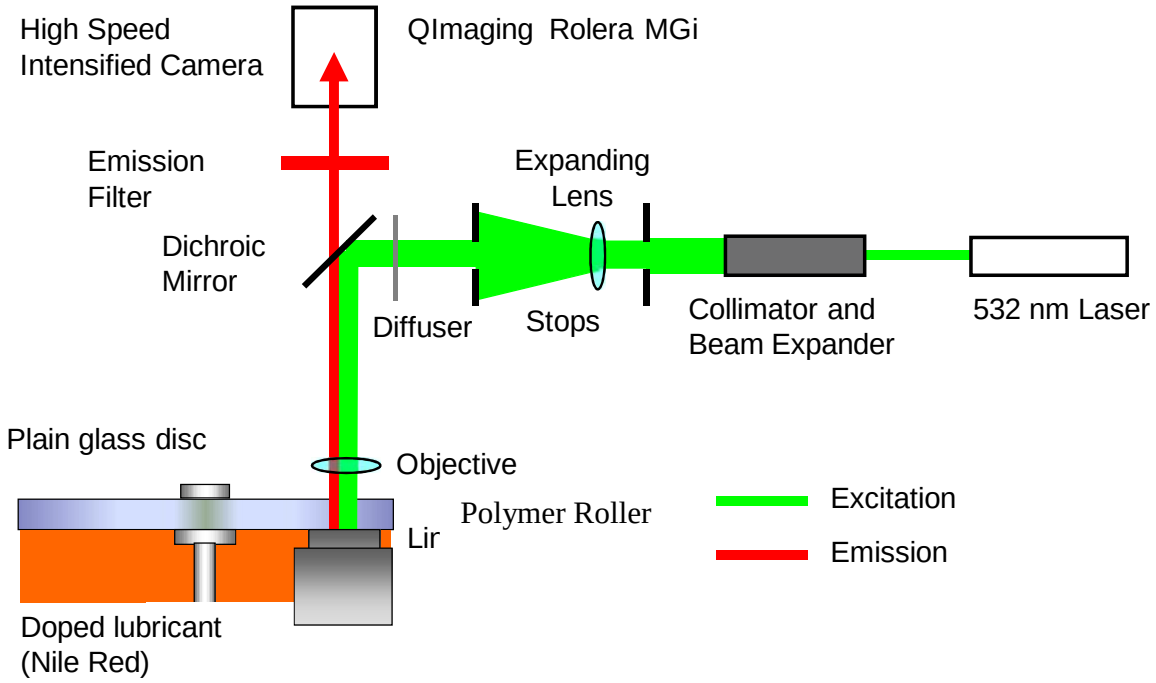


Figure 7.6. Schematic of the optical set up and the tribological contact.

As described above, the fluorescent light emitted from the contact is of a longer wavelength than the excitation wavelength of the laser. This allows for the separation of the two light beams by a dichroic mirror, 532nm (Chroma, USA), located between the objective and the camera as shown in Fig. 7.6. An emission filter (Chroma, USA) located above the dichroic mirror is used to filter any light which is not produced by the excited fluorescent dye. The optical setup is selected so that emissions within the range of 580 - 640 nm can be observed by the camera, with the related range of suitable dyes. A diffuser is placed before the dichroic mirror to reduce irregularity in the illuminating light. To flatten the intensity distribution the beam was expanded *ca* 30X

using lenses and the beam expander. The titling mirrors 1 and 2 were employed for laser beam alignment. These components are mounted on a common rail and were fully adjustable in the *xyz* axis. The light source was mounted on its own Z stage at the end of the optical setup.

Images are captured using the high speed Rolera MGi B/W EMCCD camera (QImaging, UK). A computer-processing technique was then used to analyse the captured images, pixel by pixel, to create film thickness results based on the grey scale intensity. Images were captured as 16 bit tif files, in a 512x512 array. The camera was able to accept an external trigger. The triggering circuit supplied a 5 V TTL signal to the camera using an optical sensor, mounted next to the disk drive shaft, as the triggering switch.

7.5 Testing and Results

The tests involved dissolving a chosen fluorescently excited dye, ‘nile red’ in this case, into the lubricant, a process known as doping, followed by applying a given load to the polymer roller to create a line contact between the roller and the disk and then applying a chosen range of entrainment speeds to the contact set-up. A triggering system using an opto-switch is used to trigger the high speed camera to take images of the intensity of the emitted fluorescence from inside the crack, when the crack is inside the contact, using the LIF technique discussed. The location where the images are captured is shown in Fig 7.7, where the red dot indicates the intended location of the images taken using the high speed camera. To ensure that images were indeed taken at this position,

the triggering system was calibrated using the crack mouth so that the crack mouth was always in the image.

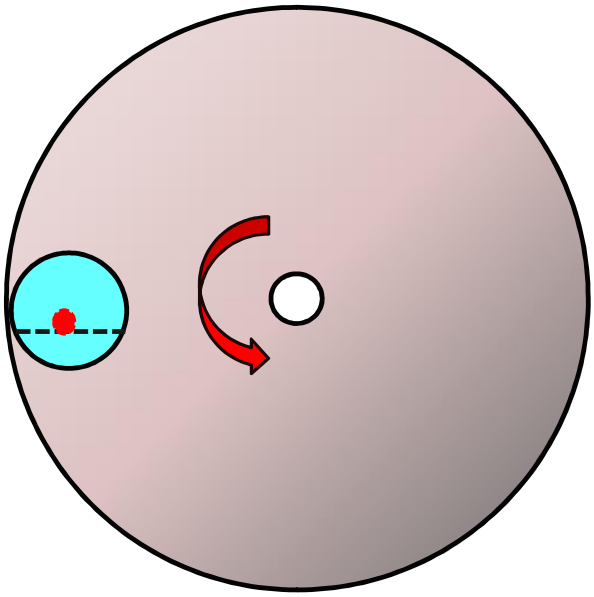


Figure 7.7. Red dot illustrates the intended location of the image capture.

The images are captured from above the disk, and the contact is loaded from below, as evident in Fig. 7.2. To ensure only the emitted fluorescence from inside the crack is captured, the bottom crack face is blacked out, masking any emitted fluorescence from the doped oil in the EHL contact. The crack film thickness results are then extracted from the images using a Matlab program that analyses the grey scale intensity of each pixel, where higher intensity indicates more fluorescence emissions and therefore the presence of more of the fluorescent dye. The more dye that is present in a given pixel, the thicker the film thickness in that location.

The aim of this study is to investigate only the qualitative trend of the film thickness inside the crack during a loading cycle, and not the quantitative values of the film thickness and therefore, a full calibration of the experimental setup in relation to film thickness is not deemed necessary and was not carried out.

The test conditions used in the experimental analyses are given below:

- Lubricant temperature : 20° Celsius
- Speed: 5mm/s Pure Rolling
- Load : 5 to 25N (~60 to 150 MPa)
- Crack incline angle: ~25°
- Oil : Castrol 262A (Group 1)
- Oil Viscosity: 248 mPa.s
- Dye : Nile Red

Fig 7.8(a) shows an example of a grey image taken with the high speed camera. Since one of the crack faces is blacked out, the mouth of the crack can clearly be seen, as indicated at point 1, in Fig 7.8(b). This image was taken on the first load cycle, and it can been that the meniscus of the lubricant has not yet filled the crack, indicated by point 2 in Fig 7.8(b), but has, nevertheless, partially penetrated down the length of the crack. This result is only seen during the start up, as after 4 cycles the crack becomes fully filled when in the contact.

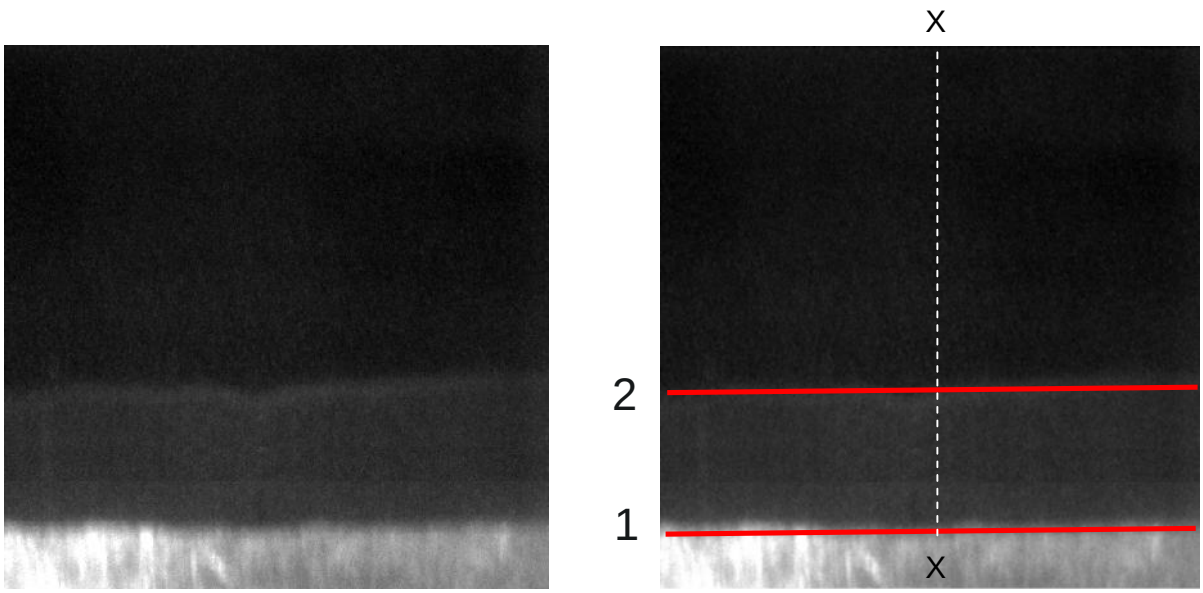


Figure 7.8. Grey scale image captured by the CCD camera of the fluorescence intensity in the crack (a) with no markings (b) with crack mouth and the meniscus marked on the figure

A plot of fluorescent intensity from the crack mouth to the crack tip is shown in Fig 7.9, In this image, which was taken on the first loading cycle, it can be clearly seen that there is a step in the intensity of the fluorescence somewhere around pixel 75 on the x-axis. In the vicinity of the crack mouth the intensity is high, then at a location of approximately 70 pixels, point 1 from Fig. 7.8(b), the intensity drops sharply this identifies the crack mouth. Then at the around 175 pixels there is a second drop in the intensity which indicates the head of the meniscus penetrating the crack because the step decrease in fluorescent intensity indicates a sudden drop in the crack film thickness.

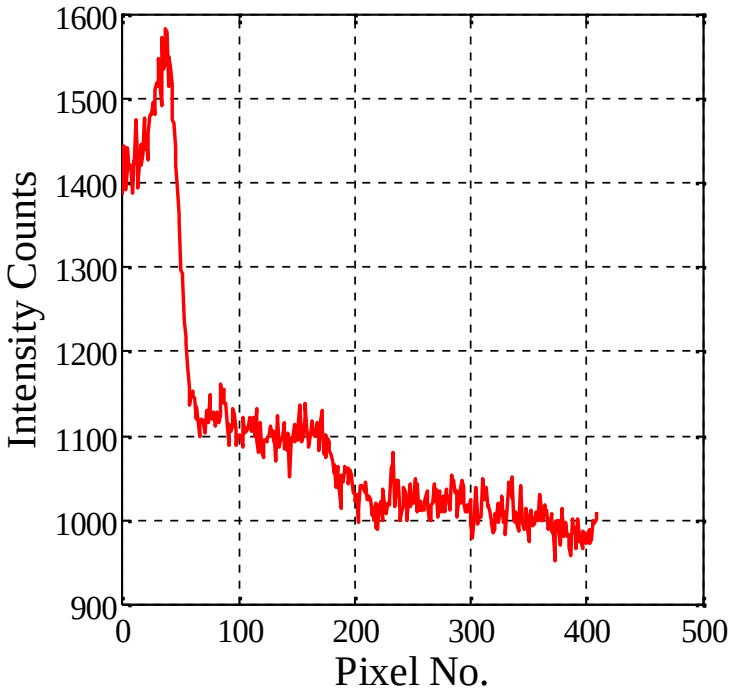


Fig.7.9 Flourescence intensity along line X-X marked on Fig 7.7(b)

This observation, although not showing the effect of the lubricant pressure, indicates two important things: the first is that the fluid enters the model RCF crack that has been created using the sapphire inserts; the second is that the LIF method can potentially be used to measure the film thickness inside the crack. Multiple images cannot be taken during a single load cycle because of the short duration of each cycle.

The effect of different loading conditions has also been considered. The graph in Fig 7.10 gives the intensity for the different loading conditions. The results from the tests with the different loading conditions appear to suggest that as the load is increased, the intensity of the fluorescence goes down.

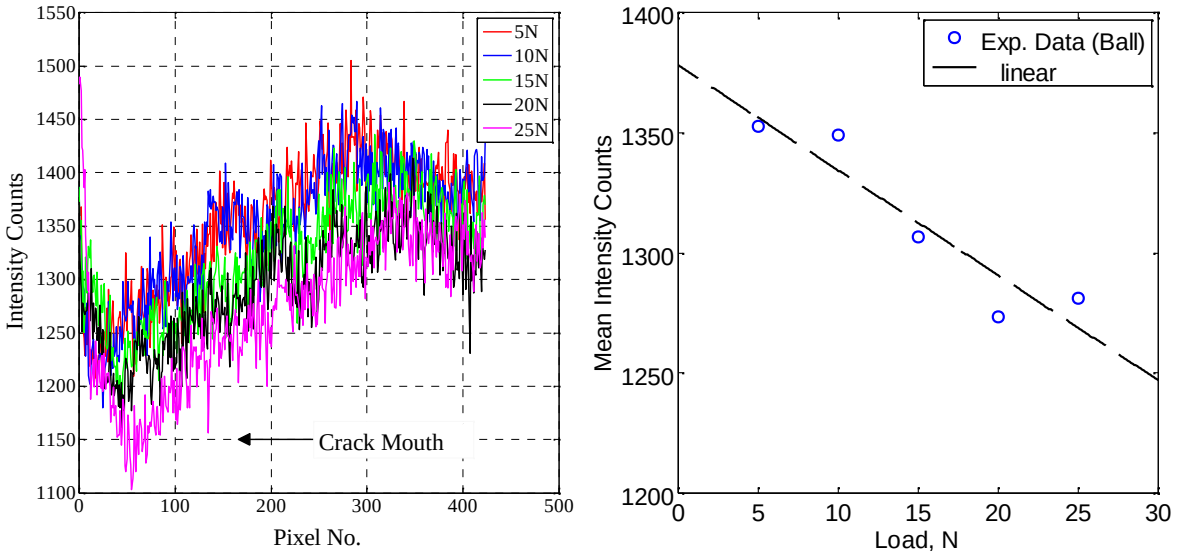


Figure 7.10. (a) Fluorescence intensity along line X-X for different loading conditions (b) Average intensity count for different loading conditions

The first interesting observation is that the results show different values of recorded intensity for the different loading conditions. This would suggest that the film thickness inside the crack is changing with the load; however it suggests that the crack film thickness seems to decrease with the increasing load. This trend appears to be in contrast with the modelling results if the images are taken during the approaching phase of the load therefore further studies are needed to explore this in more detail. In particular, it should be noted that the location of the captured images, in relation to the contact loading cycle, is not certain, given the difficulties in accurate camera triggering. It is possible that the images correspond to the situation where the crack itself may not be contained fully within the contact patch, in such a case the fluid would be squeezed out of the crack as the crack is loaded, with the consequence that less fluid is present in

the crack as the load is increased. Such a scenario would seem as the most likely explanation for the observed, and unexpected, trend of decreasing crack film thickness with increasing contact load.

7.6. Summary

The LIF based experimental technique described here has been shown to provide means of measuring fluorescent intensity inside a model crack, which, through a suitable calibration, can in turn be related to film thickness and the lubricant present inside the crack. Some encouraging preliminary results have been obtained using the developed LIF technique that have shed some light on the important mechanisms that affect the behaviour of lubricated cracks, not least confirming that that lubricant does indeed flow into an existing crack.

However, significant further development is required to obtain quantitative results that could eventually be compared to the results of the numerical modelling work and therefore, validate such models. The process of the fluid/solid interaction in an RCF crack is very difficult to monitor in-situ experimentally. Although the time evolving fluid film shape within the crack has not been tracked during the load cycle due to a number of difficulties, the LIF based experimental method described here, does have the potential to provide further answers to some of the questions that still remain with respect to RCF cracks and in particular the fluid/solid interaction in RCF cracks.

Chapter 8

Conclusions and Future Work

A novel method for coupling fluid pressure and crack deformation for the purpose of analysing RCF cracks in lubricated hydrodynamic and elastohydrodynamic contacts has been developed and presented. The model has been used to simulate the effect of lubricant/crack interaction inside an RCF crack as it passes through a rolling contact; which has direct application to bearings and rail/wheel contacts. Where in particular, in the case of bearings, rolling contact fatigue cracks, and the resulting pits are the major cause of component failure and have huge influence of bearing life. Therefore, the importance of understanding the phenomena of lubricant pressurisation and its influence on rolling contact fatigue cannot be over emphasised.

The model presented addresses some of the simplifying assumptions applied to existing models available in the current literature as reviewed in this thesis. These include:

- imposed fluid pressure gradient inside the RCF crack,
- imposed fluid pressure at the crack mouth,
- imposed contact pressure on the surface of the cracked half-plane, Hertzian or EHL.

In the present model, these assumed and imposed quantities have been explicitly and fully solved for, by using realistic and physical boundary conditions, namely atmospheric pressure in the fluid film, remote from the contact patch and a zero pressure gradient in the fluid film at the crack tip. Existing models deal with one or more of these assumptions [1, 99], but the present model is the first attempt to remove all of these assumptions and to solve for:

- fluid pressure inside the crack,
- fluid pressure inside the lubricated contact,
- flow of lubricant between the surface film and the crack film,
- the effect of the elastic deformations, in the contact interface and in the crack on fluid film thickness and the fluid pressure,
- the evolution of the crack shape and the SIFs as the hydraulically pressurised crack grows under repeated contact loading.

Although the assumptions outlined above have been addressed, some assumptions still remain, namely that the crack is fully filled as it enters the contact and the contact surfaces are perfectly smooth. These assumptions should be addressed in future work.

The results of the simulations suggest that the cracked component/lubricant interaction has a significant effect in stimulating and accelerating the growth of the crack. It has been shown through the simulation that the lubricant acts inside the crack to convert the compressive contact load into a tensile fatigue mechanism, through the effect of fluid pressurisation inside the crack. The results from the simulation suggest that this tensile fatigue mechanism induced is the principal factor that influences the rate of crack growth, which eventually leads to fragments of material breaking away from the surface of the component to leave surface voids or pits, a pre-cursor to component failure. The results from the modelling work suggest that neglecting fluid pressure effects when analysing RCF cracks could lead to significant overestimates of the number of cycles required to generate a pit from an existing RCF crack, the case considered in chapter 6 of this thesis suggests that this could lead to a value that is overestimated by a factor of around 11.

The influence of the lubricant pressure on RCF crack growth has been explicitly modelled using the novel approach presented in this thesis. The obtained results show that the lubricant pressure exerts considerable influence on the rate of crack growth. The results from the crack growth simulations have been compared with a micro-pit

experimentally observed and reported by S.Glodež *et al* [176] and the results of the analysis give a good comparison.

The coupling between the lubricant and the crack has been considered in terms of the effect on crack growth, but also the interaction that occurs as a direct result of the coupling has been simulated, not only in terms of the calculated propagation rates but also in terms of the localised effects in the crack and in the surface film. The influence that the presence of the crack and the deformation of the crack faces have on the EHL surface film has been captured; it is shown that, when the crack opens, the EHL film pressure and film shape is modified: the opening of the crack creates a step on the contact surface of the cracked component. The effect of this is to create a discontinuity in the EHL film thickness, which in turn induces a pressure fluctuation at the crack mouth. This illustrates the strong fluid/solid coupling: not only is the effect of the fluid pressure on the crack considered but, because the model is fully coupled the effects of the crack deformation on the fluid pressure are also resolved. Such features are responsible for some interesting behaviour and the importance of the coupling has been clearly highlighted in the results presented and discussed in Chapters 4-6. One of the important phenomena that has been elucidated, is the behaviour of the fluid inside the crack. The crack displacement is used to compute the pressure gradient inside the crack, where crack opening yields positive pressure gradients and crack closing yields negative pressure gradients. This implies that the pressure gradient in the crack cannot be assumed to be constant, like the models presented by Keer *et al* [4] and Murakami *et al* [3].

In addition to the modelling work, an experimental method of analysing RCF cracks in real time has been developed based on an existing technique that is referred to in the literature as the laser induced fluorescence technique or LIF. Although the LIF experimental set-up outlined in this thesis requires further development if it is to provide accurate quantitative results that could be used for a direct comparison with the presented model, some encouraging preliminary results have been successfully attained. The technique has been shown to be suitable for observing the build-up of fluid film in the crack, in real time. The experimental works has also been successful in demonstrating the fluid does penetrate an RCF crack.

The model presented in this thesis was developed with the application of roller bearings in mind. However, due to instability in the fluid element of the fluid/solid algorithm the maximum contact pressure that is induced by the operating conditions that are used in this thesis is only really suitable for considering relatively 'light' loading of roller bearings, but is more applicable to rail/wheel contacts. This instability is the primary limitation of the model. To be able to consider the lubricant/crack interaction in bearings under heavier loading conditions, the maximum contact pressure that is solved for in the fluid solver needs to be higher. A more sophisticated fluid solver would be able to model fluid/solid interaction at pressures at and above 1GPa. One of the inherent limitations of the existing solver is that there is no built-in functionality to deal with cavitation and film breakdown at the crack mouth, though this is something that the group at Imperial College are working on [183]. This means that in the current solver, when the fluid pressure becomes negative, due to either rapid expansion of the crack

film due to rapid crack opening, or due to greater fluctuation in the surface film resulting from the step created by the crack mouth deflection, then the fluid solver fails (oscillates and/or diverges), mainly due to the impossibility to conserve mass and stabilise the algorithm. Instabilities, oscillations and divergence are also partly due to the forward iterative method that is used to solve the EHL problem; this is something that has been documented in the literature, where it is noted that this method is not stable at high pressure [164]. Other authors have succeeded in solving EHL at much higher pressures using for example the Newton Rhapson method [164]. However, the author believes that even without changing the iterative scheme, if a method for resolving cavitation were introduced, then the solver would be more stable and could be used to solve for the fluid/solid interaction at higher contact pressures.

Furthermore, the method introduced to include piezoviscosity, and compressibility when modelling the lubricant in the current fluid solver is explicit, i.e. viscosity and density are updated using the pressure solution from the previous iteration in the algorithm. This introduces instabilities because varying the viscosity has implications for the pressure solution and the integral of the pressure must coincide with the external load in order for the algorithm to converge. An implicit way of solving for the evolution of viscosity and density within the lubricant films (i.e. where the solver computes the new pressure, viscosity and density in a single step) would greatly contribute to stabilise the solver and remove one of the iterative loops from the algorithm.

To conclude, the work that is reported in this thesis has added a level of sophistication to the RCF crack models reported in the literature that attempted to tackle the issue of fluid/solid interactions. This is the first study to provide solutions for the evolution of the film shape and the fluid pressures within the lubricant both in the crack and in the EHL contact, while also explicitly considering the deformation of the crack faces and the contact surface. The results presented by the author demonstrate that the crack deformation and lubricant film thickness and pressure are strongly coupled and as such, only a fully-coupled solver can satisfactorily capture the behaviour of RCF cracks in lubricated contacts without important and unphysical assumptions having to be made. Experimental corroboration of the effects that have been simulated during this study was also sought; however, time constraints have not allowed this to be achieved in the present study and this is one of the main areas that would benefit from future work. After all: “In theory, there is no difference between theory and practice. But, in practice, there is.” - Jan L. A. van de Snepscheut, *An Introduction to the Art of Programming* (1986).

References

1. Bogdanski, S., *A rolling contact fatigue crack driven by squeeze fluid film.* Fatigue and Fracture of Engineering Materials and Structures, 2002. **25**(11): p. 1061-1071.

2. Bower, A.F., *The influence of crack face friction and trapped fluid on surface initiated rolling contact fatigue cracks.* Journal of tribology, 1988. **110**(4): p. 704-11.

3. Kaneta, M. and Y. Murakami, *Effects of oil hydraulic pressure on surface crack growth in rolling/sliding contact.* Tribology international, 1987. **20**(4): p. 210-217.

4. Keer, L.M. and M.D. Bryant, *A pitting model for rolling-contact fatigue.* Transactions of the ASME - Journal of Lubrication Technology, 1983. **105**(2): p. 198-205.

5. Olver, A.V. *et al.*, *Direct observations of a micropit in an elastohydrodynamic contact.* Wear, 2004. **256**(1-2): p. 168.

6. Way, S., *Pitting due to rolling contact.* American Society of Mechanical Engineers -- Transactions -- Journal of the Applied Mechanics, 1935. **2**(3): p. -110--114.

7. Keer, L.M., M.D. Bryant, and G.K. Haritos, *Subsurface and surface cracking due to hertzian contact.* Transactions of the ASME - Journal of Lubrication Technology, 1982. **104**(3): p. 347-351.

8. Bower, A.F., *Some Aspects of Plastic Flow, Residual Stress and Fatigue Cracks Due To Rolling and Sliding Contact*, in *School of Engineering*1987, University of Cambridge: Cambridge. p. 98.

9. Olver, A.V., *The mechanism of rolling contact fatigue: an update.* Proceedings of the Institution of Mechanical Engineers Part J-Journal of Engineering Tribology, 2005. **219**(J5): p. 313-330.

10. Barlow, K.W. and R. Chandra, *Fatigue crack propagation simulation in an aircraft engine fan blade attachment.* International Journal of Fatigue, 2005. **27**(10-12): p. 1661-1668.

11. Beynon, J.H., A. Kapoor, and W.R. Tyfour, *Deterioration of rolling contact fatigue life of pearlitic rail steel due to dry-wet rolling-sliding line contact.* Wear, 1996. **197**(1-2): p. 255-265.

12. Bogdanski, S., *A rolling contact fatigue crack driven by squeeze fluid film.* Fatigue & Fracture of Engineering Materials & Structures, 2002. **25**(11): p. 1061-1071.

13. Bower, A.F., *The Influence of Crack Face Friction and Trapped Fluid on Surface Initiated Rolling-Contact Fatigue Cracks.* Journal of Tribology-Transactions of the Asme, 1988. **110**(4): p. 704-711.

14. Bower, A.F. and N.A. Fleck, *Brittle-Fracture under a Sliding Line Contact.* Journal of the Mechanics and Physics of Solids, 1994. **42**(9): p. 1375-1396.

15. Bunger, A.P., E. Detournay, and R.G. Jeffrey, *Crack tip behavior in near-surface fluid-driven fracture experiments.* Comptes Rendus Mecanique, 2005. **333**(4): p. 299-304.

16. Cheng, W., H.S. Cheng, and L.M. Keer, *Experimental Investigation on Rolling Sliding Contact Fatigue-Crack Initiation with Artificial Defects.* Tribology Transactions, 1994. **37**(1): p. 1-12.

17. Cheng, W., H.S. Cheng, and L.M. Keer, *Longitudinal Crack Initiation under Pure Rolling-Contact Fatigue.* Tribology Transactions, 1994. **37**(1): p. 51-58.

18. Clayton, P. and X. Su, *Surface initiated fatigue of pearlitic and bainitic steels under water lubricated rolling/sliding contact.* Wear, 1996. **200**(1–2): p. 63-73.

19. Datsyshyn, O.P. and V.M. Kadyra, *A fracture mechanics approach to prediction of pitting under fretting fatigue conditions.* International Journal of Fatigue, 2006. **28**(4): p. 375-385.

20. Datsyshyn, O.P. and V.V. Panasyuk, *Pitting of the rolling bodies contact surface.* Wear, 2001. **251**(1-12): p. 1347-1355.

21. Dini, D., D. Nowell, and I.N. Dyson, *The use of notch and short crack approaches to fretting fatigue threshold prediction: Theory and experimental validation.* Tribology International. **In Press, Corrected Proof**.

22. Dubourg, M.C., A. Chateauminois, and B. Villechaise, *In situ analysis and modeling of crack initiation and propagation within model fretting contacts using polymer materials.* Tribology International, 2003. **36**(2): p. 109-119.

23. Fajdiga, G., J. Flasker, and S. Glodez, *The influence of different parameters on surface pitting of contacting mechanical elements.* Engineering Fracture Mechanics, 2004. **71**(4-6): p. 747-758.

24. Glodez, S., et al., *Evaluation of the service life of gears in regard to surface pitting.* Engineering Fracture Mechanics, 2004. **71**(4-6): p. 429-438.

25. Hanson, M.T. and L.M. Keer, *An Analytical Life Prediction Model for the Crack-Propagation Occurring in Contact Fatigue Failure.* Tribology Transactions, 1992. **35**(3): p. 451-461.

26. Kaneta, M. and Y. Murakami, *Effects of oil hydraulic pressure on surface crack growth in rolling/sliding contact.* Tribology International, 1987. **20**(4): p. 210-217.

27. Keer, L.M. and M.D. Bryant, *A Pitting Model for Rolling-Contact Fatigue.* Journal of Lubrication Technology-Transactions of the Asme, 1983. **105**(2): p. 198-205.

28. Liu, Y., B. Stratman, and S. Mahadevan, *Fatigue crack initiation life prediction of railroad wheels.* International Journal of Fatigue. **In Press, Corrected Proof**.

29. Lu, B.T., et al., *Pitting and stress corrosion cracking behavior in welded austenitic stainless steel.* Electrochimica Acta, 2005. **50**(6): p. 1391-1403.

30. Murakami, Y., et al., *Experimental and fracture mechanics study of the pit formation mechanism under repeated lubricated rolling-sliding contact: Effects of reversal of rotation and change of the driving roller.* Journal of Tribology-Transactions of the Asme, 1997. **119**(4): p. 788-796.

31. Navarro, C., S. Munoz, and J. Dominguez, *Propagation in fretting fatigue from a surface defect.* Tribology International. **In Press, Corrected Proof**.

32. Nowell, D., D. Dini, and D.A. Hills, *Recent developments in the understanding of fretting fatigue.* Engineering Fracture Mechanics, 2006. **73**(2): p. 207-222.

33. Ren, Z. and S. Glodez, *Computational service life estimation of contacting mechanical elements in regard to pitting.* Computers & Structures, 2002. **80**(27-30): p. 2209-2216.

34. Ren, Z., et al., *Surface initiated crack growth simulation in moving lubricated contact.* Theoretical and Applied Fracture Mechanics, 2002. **38**(2): p. 141-149.

35. Ringsberg, J.W., et al., *Prediction of fatigue crack initiation for rolling contact fatigue.* International Journal of Fatigue, 2000. **22**(3): p. 205-215.

36. Rokhlin, S.I., et al., *Effect of pitting corrosion on fatigue crack initiation and fatigue life.* Engineering Fracture Mechanics, 1999. **62**(4-5): p. 425-444.

37. Turnbull, A. and S. Zhou, *Pit to crack transition in stress corrosion cracking of a steam turbine disc steel.* Corrosion Science, 2004. **46**(5): p. 1239-1264.

38. Tyfour, W.R., J.H. Beynon, and A. Kapoor, *Deterioration of rolling contact fatigue life of pearlitic rail steel due to dry-wet rolling-sliding line contact.* Wear, 1996. **197**(1-2): p. 255-265.

39. Wang, Y. and M. Hadfield, *A study of line defect fatigue failure of ceramic rolling elements in rolling contact.* Wear, 2002. **253**(9-10): p. 975-985.

40. Wang, Y. and M. Hadfield, *Failure modes of ceramic rolling elements with surface crack defects.* Wear, 2004. **256**(1-2): p. 208-219.

41. Way, S., *Pitting due to rolling contact* Journal of Applied Mechanics-Transactions of the Asme, 1935. **2**: p. A49-A58.

42. Xie, Y.J. and D.A. Hills, *Crack initiation at contact surface.* Theoretical and Applied Fracture Mechanics, 2003. **40**(3): p. 279-283.

43. Zhao, P., et al., *Subsurface propagation of partial ring cracks under rolling contact: Part II. Fracture mechanics analysis.* Wear. **In Press, Corrected Proof**.

44. Zhao, P., et al., *Subsurface propagation of partial ring cracks under rolling contact: Part I. Experimental studies.* Wear. **In Press, Corrected Proof**.

45. Dini, D., *Studies in fretting fatigue with particular application to almost complete contacts*. D.Phil. thesis2004: University of Oxford.

46. Murakami, Y., C. Sakae, and K. Ichimaru, *3-Dimensional Fracture-Mechanics Analysis of Pit Formation Mechanism under Lubricated Rolling-Sliding Contact Loading.* Tribology Transactions, 1994. **37**(3): p. 445-454.

47. Bogdanski, S., *Liquid-solid interaction at opening in rolling contact fatigue cracks.* Wear, 2005. **258**(7-8): p. 1273-1279.

48. Bogdanski, S. and M.W. Brown, *Modelling the three-dimensional behaviour of shallow rolling contact fatigue cracks in rails.* Wear, 2002. **253**(1-2): p. 17-25.

49. Hsia, K.J. and Z.Q. Xu, *The mathematical framework and an approximate solution of surface crack propagation under hydraulic pressure loading.* International Journal of Fracture, 1996. **78**(3-4): p. 363-378.

50. Xu, Z.Q. and K.J. Hsia, *A numerical solution of a surface crack under cyclic hydraulic pressure loading.* Journal of Tribology-Transactions of the Asme, 1997. **119**(4): p. 637-645.

51. Bogdanski, S., P. Lewicki, and M. Szymaniak, *Experimental and theoretical investigation of the phenomenon of filling the RCF crack with liquid.* Wear, 2005. **258**(7-8): p. 1280-1287.

52. Suresh, S., *Fatigue of Materials*. Second Edition 1998: Cambridge University Press.

53. Benham, P., R.J. Crawford, and C.G. Armstraong, *Mechanic of Engineering Materials*. 2nd ed1996: Longman.

54. Torrance, A., J.E. Morgan, and G.T.Y. Wan, *An additive's influence on the pitting and wear of ball bearing steel.* Wear, 1996. **192**(1–2): p. 66-73.

55. Hills, D.A., et al., *Solutions of Cracks Problems - The Distributed Dislocation Technique*. Vol. 1. 1996: Kluwer Academic Publishers.

56. Knott, J.F., *Fundamentals of fracture mechanics*1973: Butterworth.

57. Lundberg G., A. Palmgren, *A Dynamic Capacity for Roller Bearings.* Ing. Vetanskaps Akad. -Handl., 1952. **No. 210**(1952).

58. Coy J., E.V. Zaretsky, *The Life Analysis of Helical Gears Using Lundgren and Palmgren Theory*, 1975, Nasa Technical Note: U.S. Army Air Mobility R&D Laboratory.

59. Scott, D., *Rolling Contact Fatigue.* Wear, 1979. **1979**: p. pp. 321-361.

60. Carter, T.L., E.V. Zaretsky, and W.J. Anderson, *EFFECT OF HARDNESS AND OTHER MECHANICAL PROPERTIES ON ROLLING-CONTACT FATIGUE LIFE OF FOUR HIGH-TEMPERATURE BEARING STEELS*, in *Other Information: Orig. Receipt Date: 31-DEC-60*1960. p. Medium: X; Size: Pages: 52.

61. Ciruna, J.A. and H.J. Szieleit, *The effect of hydrogen on the rolling contact fatigue life of AISI 52100 and 440C steel balls.* Wear, 1973. **24**(1): p. 107-118.

62. Scott, D., *The effect of material properties, lubricant and environment on rolling contact fatigue.* I. Mech. E, 1963. **1963**.

63. Tallian, T., *Weibull Distribution of Rolling Contact Fatigue Life and Deviations Therefrom.* A S L E Transactions, 1962. **5**(1): p. 183-196.

64. Comninou M., J. Dundurs, *Some consequences of the inequality conditions in contact and crack problems* Journal of Elasticity, 1979. **Volume 9**: p. 71 - 82.

65. Hills, D.A. and D.W. Ashelby, *On the application of fracture mechanics to wear.* Wear, 1979. **54**(2): p. 321-330.

66. Dundurs, J., M. Comninou, *The angular dislocation in a half space.* Journal of Elasticity, 1975. **Volume 5**: p. 203 - 215.

67. Bridgman, P.W., *The stress distribution at the neck of a tension specimen.* Trans Am. Soc Metals, 1944(1944).

68. Rice, J.R., *A Path Independent Integral and the Approximate Analysis of Strain Concentrations by Notches and Cracks*, 1967: Brown University Providence Ri Division of Engineering.

69. Hutchinson, J.W., *Singular behaviour at the end of a tensile crack in a hardening material.* Journal of the Mechanics and Physics of Solids, 1968. **16**(1): p. 13-31.

70. Lin, K.Y. and P. Tong, *Singular finite elements for the fracture analysis of V-notched plate.* International Journal for Numerical Methods in Engineering, 1980. **15**(9): p. 1343-1354.

71. Irwin, G.R., *Linear fracture mechanics, fracture transition, and fracture control.* Engineering Fracture Mechanics, 1968. **1**(2): p. 241-257.

72. Irwin, G.R., *Analysis of Stresses and Strains Near the End of a Crack Traversing a Plate.* J. Appl. Mech., 1957.

73. Irwin, G.R., *Fracture Mode Transition for a Crack Traversing a Plate.* J. Basic Engineering 1960. **82**(2): p. 417 - 423.

74. Tanaka, K. and T. Mura, *A Dislocation Model for Fatigue Crack Initiation.* Journal of Applied Mechanics, 1981. **48**(1): p. 97-103.

75. Paris P.C., F.Erdogan, *A critical analysis of crack propagation laws.* Journal Of Basic Engineering 1963. **85**(4): p. 528 - 534.

76. McEvily Jr, A.J. and R.G. Boettner, *On fatigue crack propagation in F.C.C. metals.* Acta Metallurgica, 1963. **11**(7): p. 725-743.

77. Garwood, S.J., J.N. Robinson, and C.E. Turner, *The measurement of crack growth resistance curves (R-curves) using the J integral.* International Journal of Fracture, 1975. **11**(3): p. 528-530.

78. Shih, C.F., *Relationships between the J-integral and the crack opening displacement for stationary and extending cracks.* Journal of the Mechanics and Physics of Solids, 1981. **29**(4): p. 305-326.

79. Robinson, J.N., *An experimental investigation of the effect of specimen type on the crack tip opening displacement and J-integral fracture criteria.* International Journal of Fracture, 1976. **12**(5): p. 723-737.

80. Rice, J.R. and G.F. Rosengren, *Plane strain deformation near a crack tip in a power-law hardening material.* Journal of the Mechanics and Physics of Solids, 1968. **16**(1): p. 1-12.

81. Ida, Y., *Cohesive Force across the Tip of a Longitudinal-Shear Crack and Griffith's Specific Surface Energy.* J. Geophys. Res., 1972. **77**(20): p. 3796-3805.

82. Hua, G.A.O., M.W. Brown, and K.J. Miller, *MIXED-MODE FATIGUE THRESHOLDS.* Fatigue & Fracture of Engineering Materials & Structures, 1982. **5**(1): p. 1-17.

83. Qian, J. and A. Fatemi, *Mixed mode fatigue crack growth: A literature survey.* Engineering Fracture Mechanics, 1996. **55**(6): p. 969-990.

84. Wong S., *et al*., *Fatigue crack growth rates under sequential mixed-mode I and II loading cycles.* Fatigue & fracture of engineering materials & structures, 2000. **23**(8): p. 667-74.

85. Erdogan F., Sih G.C., *On the crack extension in plates under plane loading and transverse shear (Crack extension in a large plate under plane loading and transverse shear, studied in terms of local stress and strain concentrations)* ASME, Transactions, Seris D - Journal of Basic Engineering, 1963.

86. Sih, G.C., *On westergaard method of crack analysis.* International journal of fracture mechanics, 1966. **2**(4): p. 628-631.

87. Mahajan, R.V. and K. Ravi-Chandar, *An experimental investigation of mixed-mode fracture.* International Journal of Fracture, 1989. **41**(4): p. 235-252.

88. Pook, L.P., *On fatigue crack paths.* International Journal of Fatigue, 1995. **17**(1): p. 5-13.

89. Chambers, A.C., T.H. Hyde, and J. Webster, *Mixed mode fatigue crack growth at 550°c under plane stress conditions in Jethete M152.* Engineering Fracture Mechanics, 1991. **39**(3): p. 603-619.

90. Keisuke, T., *Fatigue crack propagation from a crack inclined to the cyclic tensile axis.* Engineering Fracture Mechanics, 1974. **6**(3): p. 493-507.

91. Yan, A.M. and H. Nguyen-Dang, *Multiple-cracked fatigue crack growth by BEM.* Computational Mechanics, 1995. **16**(5): p. 273-280.

92. Fleming, J.R. and N.P. Suh, *Mechanics of crack propagation in delamination wear.* Wear, 1977. **44**(1): p. 39-56.

93. Rosenfield, A.R., *A dislocation theory approach to wear.* Wear, 1981. **72**(1): p. 97-103.

94. O'Regan, S.D., G.T. Hahn, and C.A. Rubin, *The driving force for mode II crack growth under rolling contact.* Wear, 1985. **101**(4): p. 333-346.

95. Hearle, A.D. and K.L. Johnson, *Mode II stress intensity factors for a crack parallel to the surface of an elastic half-space subjected to a moving point load.* Journal of the Mechanics and Physics of Solids, 1985. **33**(1): p. 61-81.

96. Comninou, M., D. Schmueser, and J. Dundurs, *FRICTIONAL SLIP BETWEEN A LAYER AND A SUBSTRATE CAUSED BY A NORMAL LOAD.* International Journal of Engineering Science, 1980. **18**(1): p. 131-137.

97. Keer L., et al, *A pitting model for rolling contact fatigue.* American Society of Mechanical Engineers and American Society of Lubrication Engineers, Lubrication Conference, 1983. **Washington, DC; United States; 5-7 Oct. 1982**: p. 8 - 20.

98. Nowell, D. and D.A. Hills, *Open cracks at or near free edges.* The Journal of strain analysis for engineering design, 1987. **22**(3): p. 177-85.

99. Kudish, I. and K.W. Burris, *Modeling of surface and subsurface crack behavior under contact load in the presence of lubricant.* International Journal of Fracture, 2004. **125**(1): p. 125-147.

100. Krenk, S., *On the use of the interpolation polynomial for solutions of singular integral equations.* Quarterly of Applied Mathematics, 1975 **Vol. 32**(Jan. 1975): p. 479-484.

101. Meshii, T. and K. Watanabe, *Maximum stress intensity factor for a circumferential crack in a finite-length thin-walled cylinder under transient radial temperature distribution.* Engineering Fracture Mechanics, 1999. **63**(1): p. 23-38.

102. Vainshtok, V.A., *Engineering methods of computing fracture mechanics based on the application of weight functions.* Strength of Materials, 1988. **20**(3): p. 309-316.

103. Beghini, M., L.Bertini, and V Fontanari, *A weight function technique for partially closed inclined edge cracks analysis.* International Journal of Fracture, 2001. **112**(1): p. 57-68.

104. Beghini, M, L. Bertini, and V. Fontanari, *A weight function for 2D subsurface cracks under general loading conditions.* Engineering fracture mechanics, 2008. **75**(3-4): p. 427.

105. Rybicki, E.F. and M.F. Kanninen, *A finite element calculation of stress intensity factors by a modified crack closure integral.* Engineering Fracture Mechanics, 1977. **9**(4): p. 931-938.

106. Henshell, R.D. and K.G. Shaw, *Crack tip finite elements are unnecessary.* International Journal for Numerical Methods in Engineering, 1975. **9**(3): p. 495-507.

107. Hillerborg, A., M. Modéer, and P.E. Petersson, *Analysis of crack formation and crack growth in concrete by means of fracture mechanics and finite elements.* Cement and Concrete Research, 1976. **6**(6): p. 773-781.

108. Nishioka, T. and S.N. Atluri, *Analytical solution for embedded elliptical cracks, and finite element alternating method for elliptical surface cracks,*

subjected to arbitrary loadings. Engineering Fracture Mechanics, 1983. **17**(3): p. 247-268.

109. Sin, H.C. and N.P. Suh, *Subsurface Crack Propagation Due to Surface Traction in Sliding Wear.* Journal of Applied Mechanics, 1984. **51**(2): p. 317-323.

110. Xiao, Q.Z. and B.L. Karihaloo, *Improving the accuracy of XFEM crack tip fields using higher order quadrature and statically admissible stress recovery.* International Journal for Numerical Methods in Engineering, 2006. **66**(9): p. 1378-1410.

111. Chahine, E., P. Laborde, and Y. Renard, *Crack tip enrichment in the XFEM using a cutoff function.* International Journal for Numerical Methods in Engineering, 2008. **75**(6): p. 629-646.

112. Liu, X.Y., Q.Z. Xiao, and B.L. Karihaloo, *XFEM for direct evaluation of mixed mode SIFs in homogeneous and bi-materials.* International Journal for Numerical Methods in Engineering, 2004. **59**(8): p. 1103-1118.

113. Tarancón, J.E., et al., *Enhanced blending elements for XFEM applied to linear elastic fracture mechanics.* International Journal for Numerical Methods in Engineering, 2009. **77**(1): p. 126-148.

114. Gohar, R., *Elastohydrodynamics*, Second Edition 2001, Imperial College Press

115. Zi, G. and T. Belytschko, *New crack-tip elements for XFEM and applications to cohesive cracks.* International Journal for Numerical Methods in Engineering, 2003. **57**(15): p. 2221-2240.

116. Wyart, E., *et al.*, *A substructured FE-shell/XFE-3D method for crack analysis in thin-walled structures.* International Journal for Numerical Methods in Engineering, 2007. **72**(7): p. 757-779.

117. Dubourg, M. and V. Lamacq, *A predictive rolling contact fatigue crack growth model: Onset of branching, direction, and growth - Role of dry and lubricated conditions on crack patterns.* Journal of tribology, 2002. **124**(4): p. 680-688.

118. Bogdanski, S., P. Lewicki, and M.M. Szymaniak, *Experimental and theoretical investigation of the phenomenon of filling the RCF crack with liquid.* Wear, 2005. **258**(7-8): p. 1280-7.

119. Michau, B., D. Berthe, and M. Godet, *Observations of oil pressure effects in surface crack development.* Tribology, 1974. **7**(3): p. 119-122.

120. S, J., *Examination of wear mechanisms in automotive camshafts.* Wear, 1986. **108**(3): p. 235-254.

121. Fletcher, D.I., P. Hyde, and A. Kapoor, *Modelling and Full Scale Trials to Investigate Fluid Pressurisation of Rolling Contact Fatigue Cracks.* Wear, 2008(265): p. 1317-1324.

122. Fletcher, D.I., P. Hyde, and A. Kapoor, *Modelling and full-scale trials to investigate fluid pressurisation of rolling contact fatigue cracks.* Wear, 2008. **265**(9–10): p. 1317-1324.

123. Johnson, K.L., *Contact Mechanics*. 1st ed1985: Cambridge University Press.

124. Fujita, K. and A. Yoshida, *The effect of changing the rolling direction on the rolling contact fatigue lives of annealed and case-hardened steel rollers.* Wear, 1977. **43**(3): p. 315-327.

125. Bogdanski, S. and M. Trajer, *A dimensionless multi-size finite element model of a rolling contact fatigue crack.* Wear, 2005. **258**(7-8): p. 1265-1272.

126. Miller, G.R., L.M. Keer, and H.S. Cheng, *On the Mechanics of Fatigue Crack Growth Due to Contact Loading.* Proceedings of the Royal Society of London. A. Mathematical and Physical Sciences, 1985. **397**(1813): p. 197-209.

127. Kaneta, M., Y. Murakami, and T. Okazaki, *Growth Mechanism of Subsurface Crack Due to Hertzian Contact.* Journal of Tribology, 1986. **108**(1): p. 134-139.

128. Laird, C. and G.C. Smith, *Crack propagation in high stress fatigue.* Philosophical Magazine, 1962. **7**(77): p. 847-857.

129. Otsuka, A., K. Mori, and T. Miyata, *The condition of fatigue crack growth in mixed mode condition.* Engineering Fracture Mechanics, 1975. **7**(3): p. 429-439.

130. Akama, M. and T. Mori, *Boundary element analysis of effects of crack face friction and trapped fluid on rolling contact fatigue cracks.* Quarterly Report of RTRI (Railway Technical Research Institute) (Japan), 2005. **46**(4): p. 231-237.

131. Ringsberg, J.W., *Life prediction of rolling contact fatigue crack initiation.* International journal of fatigue, 2001. **23**(7): p. 575-586.

132. Flasker, J., *et al.*, *Numerical simulation of surface pitting due to contact loading.* International journal of fatigue, 2001. **23**(7): p. 599.

133. Zafošnik, B., *et al.*, *Modelling of Surface Crack Growth under Lubricated Rolling–Sliding Contact Loading.* International Journal of Fracture, 2005. **134**(2): p. 127-149.

134. Foord C.A., Cameron A., *Pitting of steel under varying speeds and combined stresses.* Trans. ASME, J. Lubr. Technol, 1969. **91**: p. 282–293.

135. Fletcher, D.I., L. Smith, and A. Kapoor, *Rail rolling contact fatigue dependence on friction, predicted using fracture mechanics with a three-dimensional boundary element model.* Engineering fracture mechanics, 2009. **76**(17): p. 2612-2625.

136. Kaneta, M. and Y. Murakami, *Propagation of Semi-Elliptical Surface Cracks in Lubricated Rolling/Sliding Elliptical Contacts.* Journal of Tribology, 1991. **113**(2): p. 270-275.

137. Bogdanski, S. and M.W. Brown, *Modelling the three-dimensional behaviour of shallow rolling contact fatigue cracks in rails.* Wear, 2002. **253**(1-2): p. 17-25.

138. Bogdanski, S. and P. Lewicki, *3-D Model of Liquid Entrapment Mechanism for Rolling Contact Fatigue Cracks in Rails.* Wear, 2008. **2008**(265): p. 1356-1362.

139. Bogdański, S., P. Lewicki, and M. Szymaniak, *Experimental and theoretical investigation of the phenomenon of filling the RCF crack with liquid.* Wear, 2005. **258**(7–8): p. 1280-1287.

140. Hertz H. R., *Ueber die Beruehrung elastischer Koerper (On Contact Between Elastic Bodies).* Gesammelte Werke (Collected Works), 1882. **Vol. 1**.

141. Rice, J.R., *Limitations to the small scale yielding approximation for crack tip plasticity.* Journal of the Mechanics and Physics of Solids, 1974. **22**(1): p. 17-26.

142. Coulomb, C.A., *Essai sur une application des regles des maximis et minimis a quelquels problemesde statique relatifs, a la architecture.* Mem. Acad. Roy. Div. Sav, 1776. **7**: p. p343 - 387.

143. Hills, D..A. and M.Comninou, *An analysis of fretting fatigue cracks during loading phase.* International journal of solids and structures, 1985. **21**(7): p. 721-30.

144. Hills, D.A., D. Nowell, and A. Sackfield, *Mechanic of Elastic Contacts*. First ed1993: Butterworth-Heinemann Ltd.

145. Bentall, R.H. and K.L. Johnson, *An elastic strip in plane rolling contact.* International Journal of Mechanical Science, 1968. **Vol.10**(1968): p. 637-668.

146. Tong, S., *Interval number and fuzzy number linear programmings.* Fuzzy Sets and Systems, 1994. **66**(3): p. 301-306.

147. Erdogan F., *et al*, *Numerical solution of singular integral equations.* Methods in Analysis and Solutions of Crack Problems, 1973. **1973**: p. 368-425.

148. Krenk S., *On the use of interpolation polynomial for solutions of singular integral equations.* International Journal of Solids and Structures, 1975. **32**: p. 479-484.

149. Jalalahmadi, B. and F. Sadeghi, *A Voronoi Finite Element Study of Fatigue Life Scatter in Rolling Contacts.* Journal of tribology, 2009. **131**(2): p. 022203.

150. Nowell, D., D. Dini, and P. Duo, *Stress analysis of V-notches with and without cracks, with application to foreign object damage.* Journal of Strain Analysis for Engineering Design, 2003. **38**(5): p. 429-442.

151. Balcombe, R., *et al.*, *A coupled approach for rolling contact fatigue cracks in the hydrodynamic lubrication regime: The importance of fluid/solid interactions.* Wear, 2011. **271**(5–6): p. 720-733.

152. Sommerfeld, A., *Zur hydrodynamischen Theorie der Schmiermittelreibung.* Zeitschrift fur Mathematik und Physik, 1904. **40**: p. 97-155.

153. Fletcher, D.I., P. Hyde, and A. Kapoor, *Investigating fluid penetration of rolling contact fatigue cracks in rails using a newly developed full-scale test facility.* Proceedings of the Institution of Mechanical Engineers, Part F: Journal of Rail and Rapid Transit, 2007. **221**(1): p. 35-44.

154. Arghir, M., A. Alsayed, and D. Nicolas, *The finite volume solution of the Reynolds equation of lubrication with film discontinuities.* International Journal of Mechanical Sciences, 2002. **44**(10): p. 2119-2132.

155. Hsia, K.J. and X. Zhiqiao, *The mathematical framework and an approximate solution of surface crack propagation under hydraulic pressure loading.* International Journal of Fracture, 1996. **78**(3-4): p. 363-78.

156. Fowell, M.T. *et al.*, *Two Mechanisms of Hydrodynamic Lubrication in Textured Bearings.* ASME Conference Proceedings, 2006. **2006**(42592a): p. 511-512.

157. Wu, S.X., Y.W. Mai, and B.B. Cotterell, *A model of fatigue crack growth based on Dugdale model and damage accumulation.* International Journal of Fracture, 1992. **57**(3): p. 253-67.

158. Cameron, A., *Basic Lubrication Theory* 1971, London: Longman.

159. Bower, A.F., *The influence of crack face friction and trapped fluid on surface initiated rolling contact fatigue cracks.* Transaction of the ASME - Journal of Tribology, 1988. **110**(4): p. 704-11.

160. Kaneta, M., M. Suetsugu, and Y. Murakami, *Mechanism of surface crack-growth in lubricated rolling-sliding spherical contact.* Transactions of the ASME - Journal of Applied Mechanics, 1986. **53**(2): p. 354-360.

161. Paris, P.C., M.P. Gomez, and W.P. Anderson, *A rational analtyic theory of fatigue* The Trend in Engineering, 1961. **13**: p. 9-14.

162. Glodez, S., *et al.*, *Numerical modelling of crack path in the lubricated rolling-sliding contact problems.* Engineering fracture mechanics, 2008. **75**(3-4): p. 880-891.

163. Zhao, P., *et al*., *Subsurface propagation of partial ring cracks under rolling contact: Part II. Fracture mechanics analysis.* Wear, 2006. **261**(3-4): p. 390-397.

164. Gohar, R., *Elastohydrodynamics*. 2nd Edition ed, ed. I.C. Press2001.

165. Doolittle A.K., *Studies in Newtonian Flow II: The Dependence of the Viscosity of Liquids on Free-Space.* J. Appl. Phys., 1951. **22(12)**: p. 1471.

166. Dowson, D., *A generalised Reynolds equation for fluid lubrication.* International Journal of Mechanical Science, 1961. **4**: p. 159-170.

167. Liu, Y., *et al.*, *EHL simulation using the free-volume viscosity model* Tribology letters 2006. **23**.

168. Eyring, W.K., *The Viscous Flow of Large Molecules.* J. Am. Chem. SOC., 1940. **62**.

169. Dundurs, J., M. Cominou, *Interaction between an edge dislocation and a circular inclusion.* J. Mesh. Phys. Solid, 1963. **Vol. 12**: p. pp177 - 189.

170. SKF, *General Catalogue*2008.

171. Elrod, H.G., *A cavitation algorithm.* Trans. ASME, J. Lubr. Technology, 1981. **103**: p. pp350 - 354.

172. Alsaad, M.A., *et al.*, *Glass transitions in lubricants; it's relation to elastohydrodynamic lubrication (EHD).* Trans ASME,, 1978. **Vol. 100**: p. pp404 - 417.

173. Sih G.C., *Strain-energy-density factor applied to mixed mode crack problems.* International Journal of Fracture 1973. **10**(3): p. pp305 - 321.

174. Benson, J.P. and D.V. Edmonds, *Relationship between the parameters C and m of Paris' law for fatigue crack growth in a low-alloy steel.* Journal Name: Scr. Metall.; (United States); Journal Volume: 12:7, 1978: p. Medium: X; Size: Pages: 645-647.

175. Noda N.A., K. Oda, *Effect of curvature at the crack tip on the stress intensity factor.* International Journal of Fracture, 1993. **64**.

176. Glodež, S. and Z. Ren, *Modelling of crack growth under cyclic contact loading.* Theoretical and Applied Fracture Mechanics, 1998. **30**(2): p. 159-173.

177. Bower, A.F., *The Influence of Crack Face Friction and Trapped Fluid on Surface Initiated Rolling Contact Fatigue Cracks.* Journal of tribology, 1988. **110**(4): p. 704-711.

178. Myant, C., H.A. Spikes, and J.R. Stokes, *Influence of load and elastic properties on the rolling and sliding friction of lubricated compliant contacts.* Tribology International, 2010. **43**(1–2): p. 55-63.

179. Dwyer-Joyce, R.S., T. Reddyhoff, and B.W. Drinkwater, *Operating Limits for Acoustic Measurement of Rolling Bearing Oil Film Thickness.* Tribology Transactions, 2004. **47**(3): p. 366-375.

180. Myant, C., T. Reddyhoff, and H.A. Spikes, *Laser-induced fluorescence for film thickness mapping in pure sliding lubricated, compliant, contacts.* Tribology International, 2010. **43**(11): p. 1960-1969.

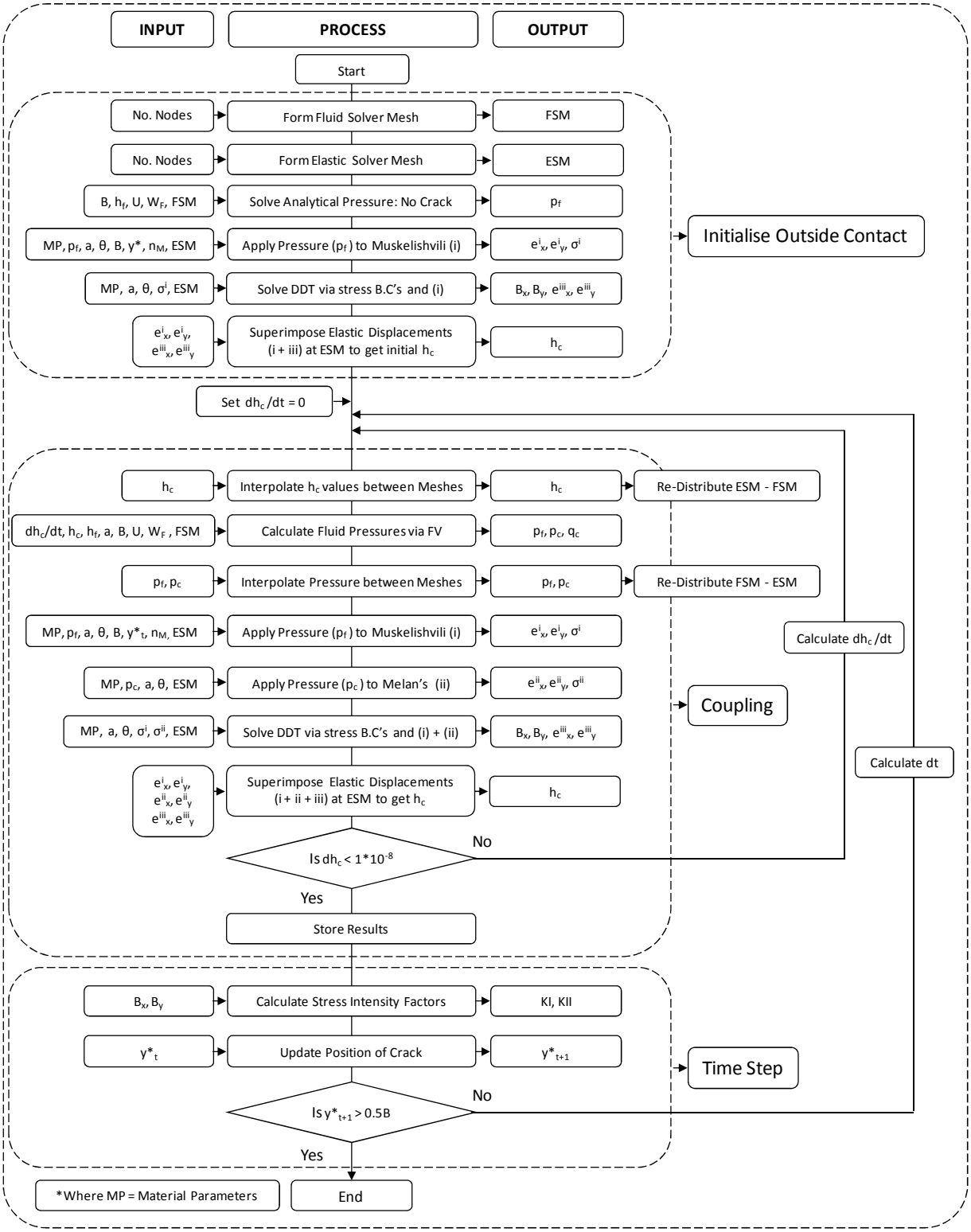
181. Hidrovo, C.H., *2D Thickness and temperature mapping of fluids by means of a two-dye laser induced fluorescence ratiometric scheme.* 2002. **9**(2&3): p. 21.

182. Haugland R.P., Johnson I.D., *Handbook of fluorescent probes and research chemicals*. Vol. 6th Edition. 1996: Molecular Probes

183. Giacopini, M., et al., *A Mass-Conserving Complementarity Formulation to Study Lubricant Films in the Presence of Cavitation.* Journal of Tribology, 2010. **132**(4): p. 041702.

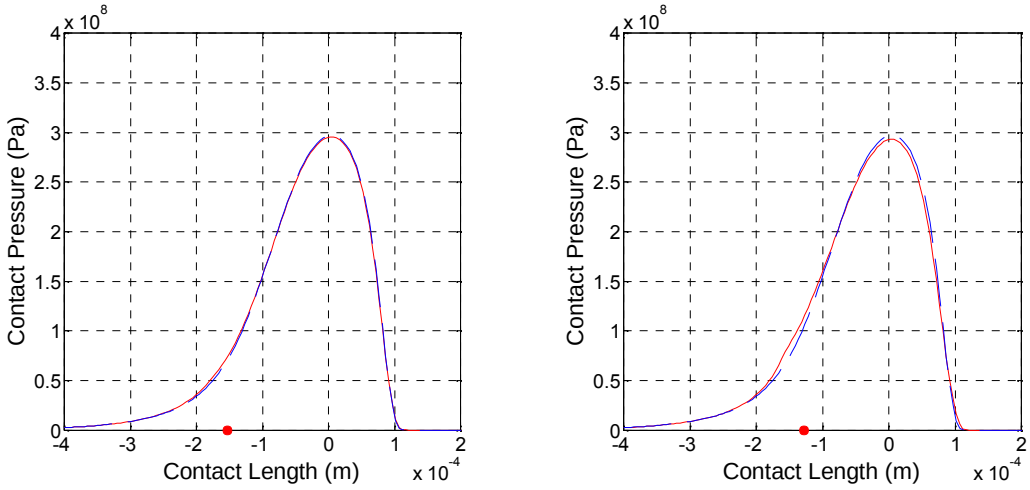
Appendices

Appendix A

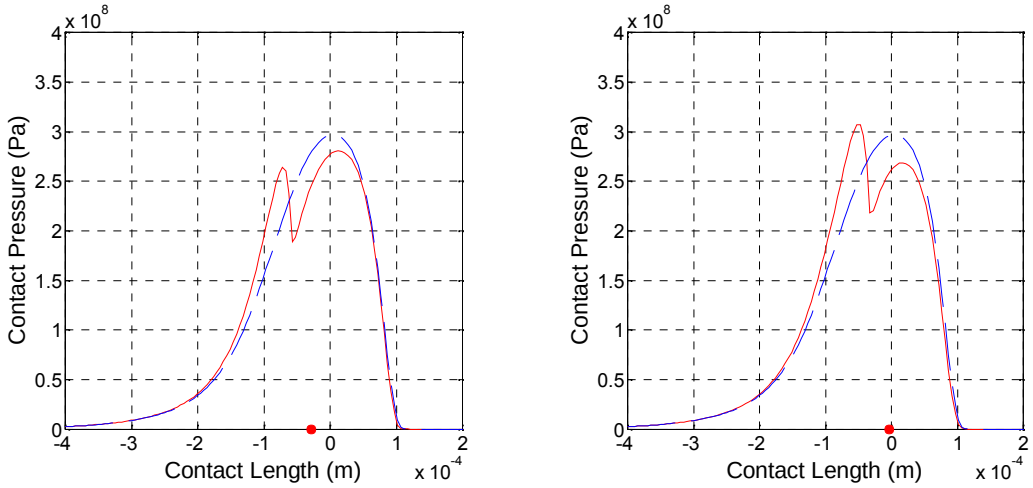

INPUT
PROCESS
OUTPUT
Start
No. Nodes
Form Fluid Solver Mesh
FSM
No. Nodes
Form Elastic Solver Mesh
ESM
B, h_f, U, W_F, FSM
Solve Analytical Pressure: No Crack
p_f
MP, p_f, a, θ, B, y*, n_M, ESM
Apply Pressure (p_f) to Muskelishvili (i)
e^i_x, e^i_y, σ^i
Initialise Outside Contact
MP, a, θ, σ^i, ESM
Solve DDT via stress B.C's and (i)
B_x, B_y, e^{iii}_x, e^{iii}_y
e^i_x, e^i_y, e^{iii}_x, e^{iii}_y
Superimpose Elastic Displacements (i + iii) at ESM to get initial h_c
h_c
Set $dh_c/dt = 0$
h_c
Interpolate h_c values between Meshes
h_c
Re-Distribute ESM - FSM
dh_c/dt, h_c, h_f, a, B, U, W_F , FSM
Calculate Fluid Pressures via FV
p_f, p_c, q_c
p_f, p_c
Interpolate Pressure between Meshes
p_f, p_c
Re-Distribute FSM - ESM
MP, p_f, a, θ, B, y*t, n_M, ESM
Apply Pressure (p_f) to Muskelishvili (i)
e^i_x, e^i_y, σ^i
Calculate dh_c/dt
MP, p_c, a, θ, ESM
Apply Pressure (p_c) to Melan's (ii)
e^{ii}_x, e^{ii}_y, σ^{ii}
Coupling
MP, a, θ, σ^i, σ^{ii}, ESM
Solve DDT via stress B.C's and (i) + (ii)
B_x, B_y, e^{iii}_x, e^{iii}_y
Calculate dt
e^i_x, e^i_y, e^{ii}_x, e^{ii}_y e^{iii}_x, e^{iii}_y
Superimpose Elastic Displacements (i + ii + iii) at ESM to get h_c
h_c
Is $dh_c < 1*10^{-8}$
No
Yes
Store Results
B_x, B_y
Calculate Stress Intensity Factors
KI, KII
y^*_t
Update Position of Crack
y^*_{t+1}
Time Step
Is $y^*_{t+1} > 0.5B$
No
Yes
*Where MP = Material Parameters
End

Appendix B

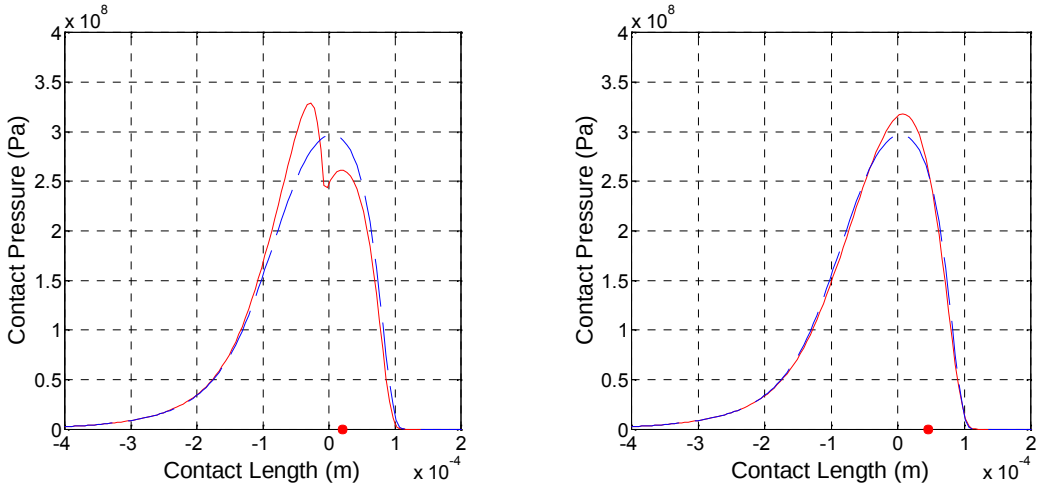
B1 - Load: 50000N/m Crack Length: 100um, Contact Pressure Plots



Fig, B1.1 EHL contact pressure (a) *Y* = -1.5E-4m (b) *Y* = -1.2E-4m

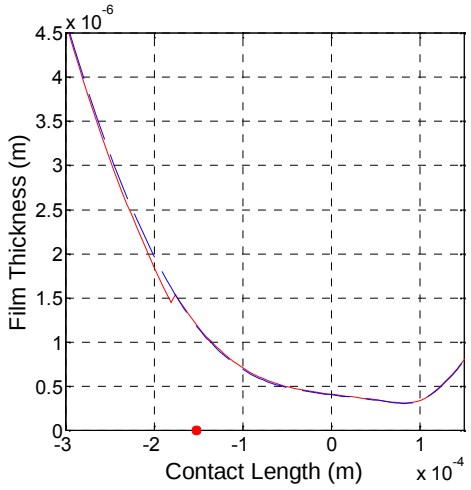


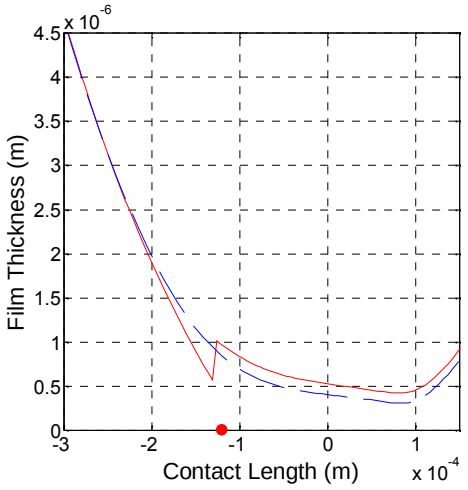
Fig, B1.1 EHL contact pressure (c) *Y* = -0.1E-4m (d) *Y* = -0.01E-4m



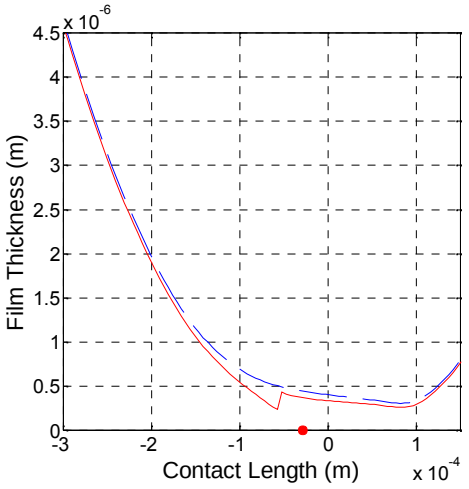
Fig, B1.1 EHL contact pressure (e) *Y* = 0.1E-4m (f) *Y* = 0.4E-4m

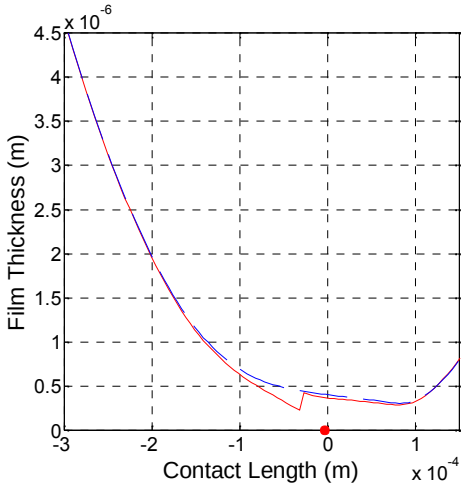
B2 - Load: 50000N/m Crack Length: 100um, Film Thickness Plots



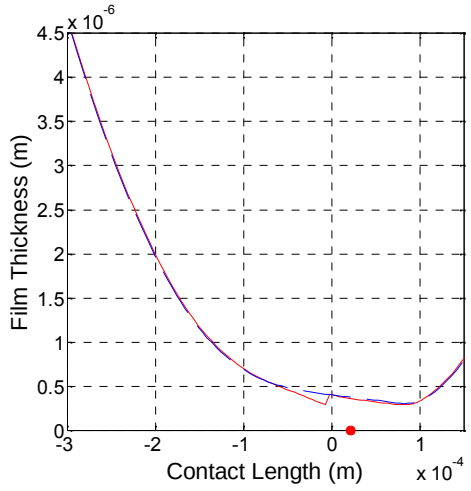


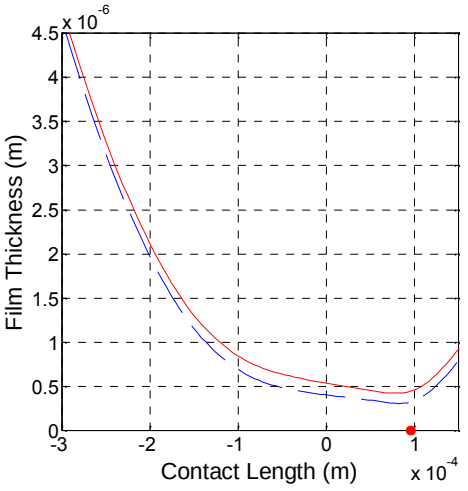
Fig, B2.1 EHL film shape (a) *Y* = -1.5E-4m (b) *Y* = -1.2E-4m





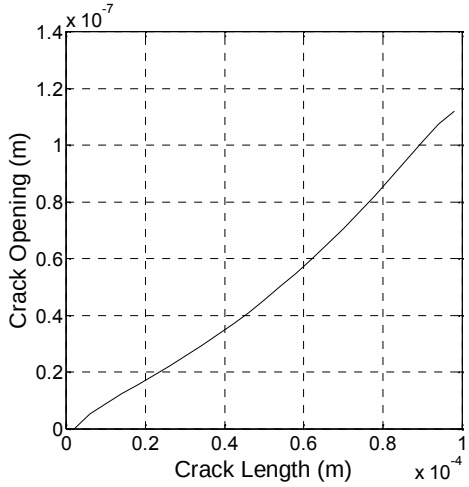
Fig, B2.1 EHL film shape (c) *Y* = -0.1E-4m (d) *Y* = -0.01E-4m

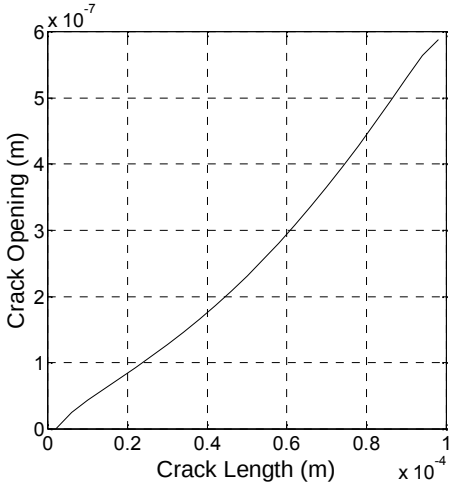




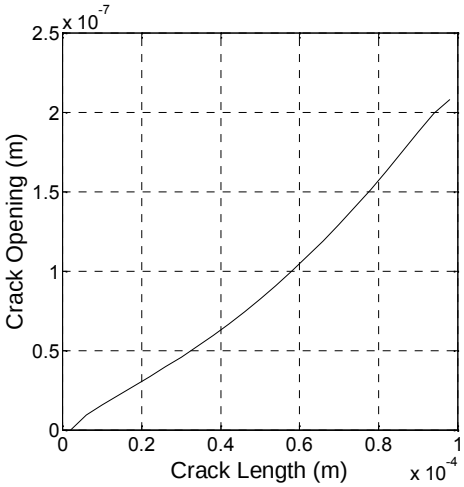
Fig, B2.1 EHL film shape (e) *Y* = 0.1E-4m (f) *Y* = 0.4E-4m

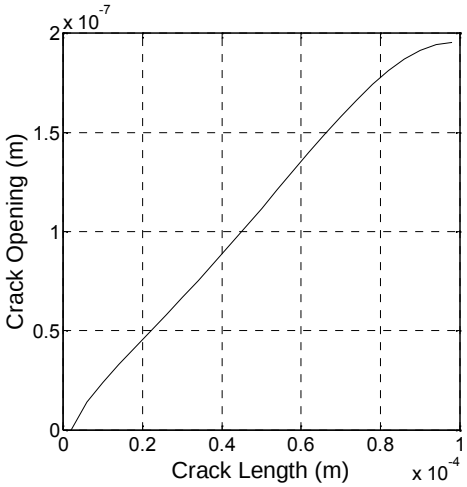
B3 - Load: 50000N/m Crack Length: 100um, Crack Shape Plots



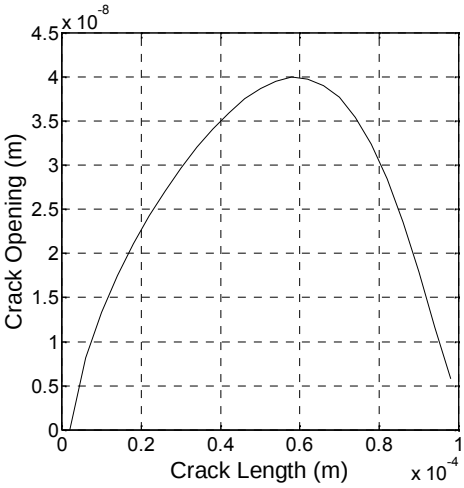


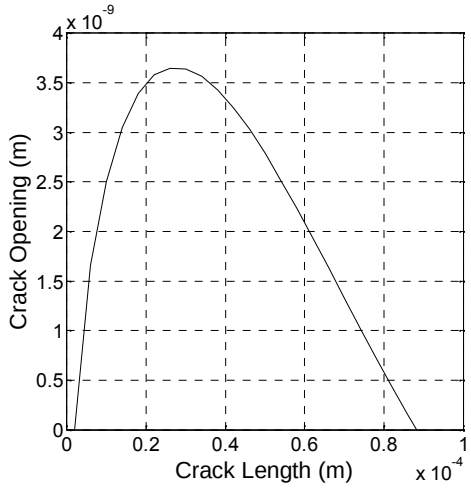
Fig, B3.1 Crack shape (a) *Y* = -1.5E-4m (b) *Y* = -1.2E-4m





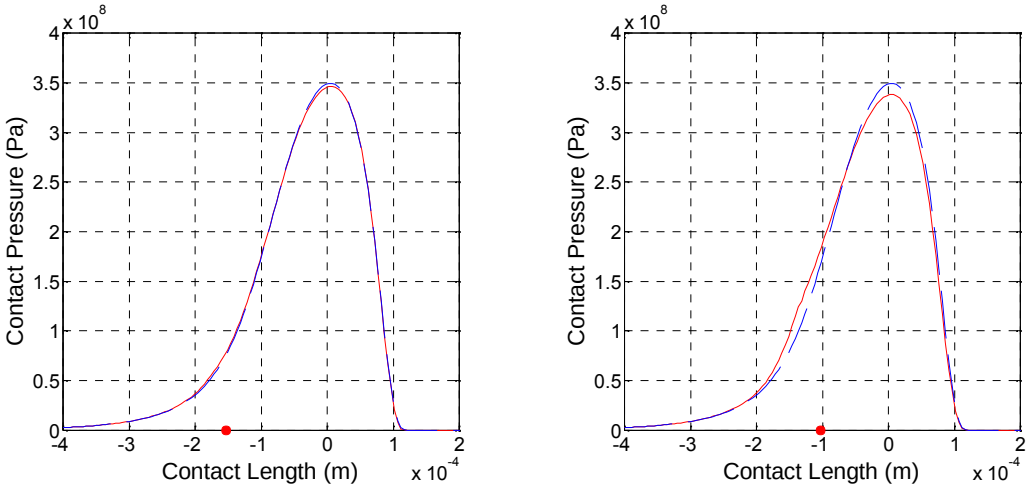
Fig, B2.1 Crack shape (c) *Y* = -0.1E-4m (d) *Y* = -0.01E-4m



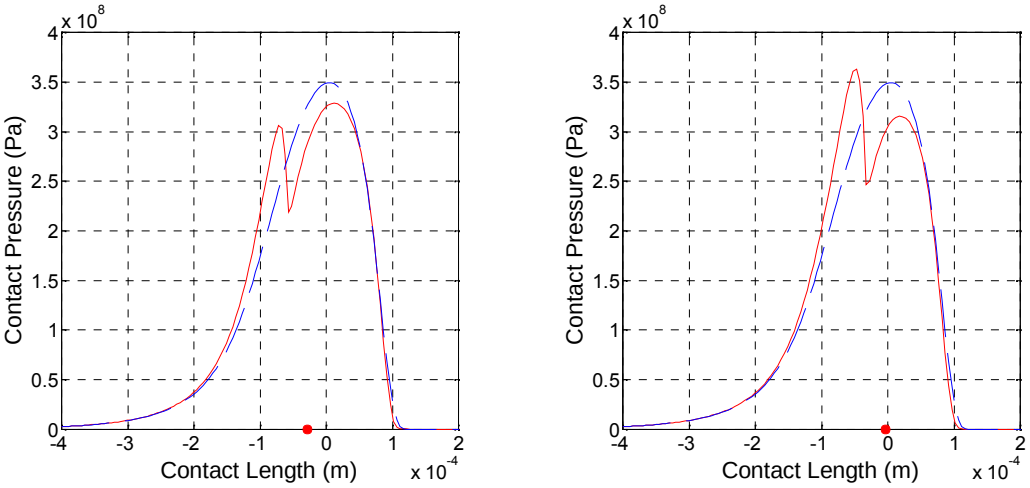


Fig, B2.1 Crack shape (e) *Y* = 0.1E-4m (f) *Y* = 0.4E-4m

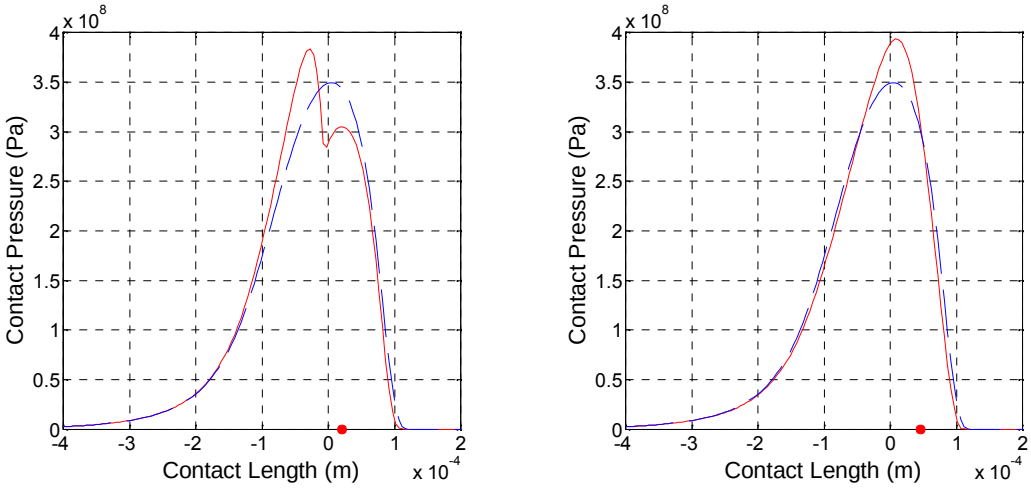
B4 - Load: 60000N/m Crack Length: 100um, Contact Pressure Plots



Fig, B4.1 EHL contact pressure (a) *Y* = -1.5E-4m (b) *Y* = -1E-4m

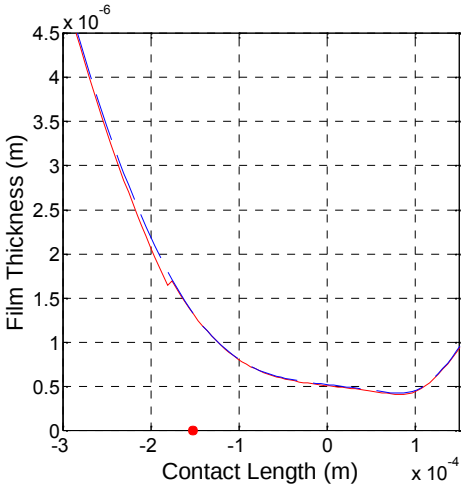


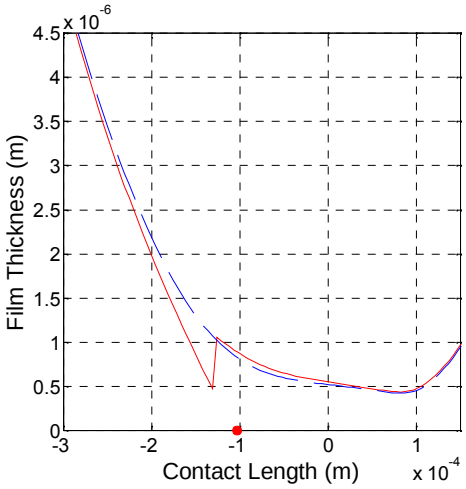
Fig, B4.1 EHL contact pressure (c) *Y* = -0.2E-4m (d) *Y* = -0.01E-4m



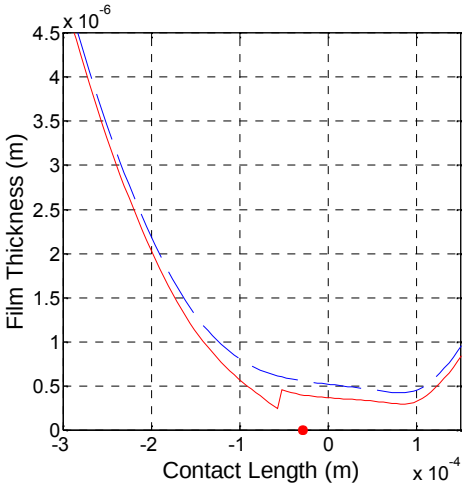
Fig, B4.1 EHL contact pressure (e) *Y* = 0.2E-4m (f) *Y* = 0.45E-4m

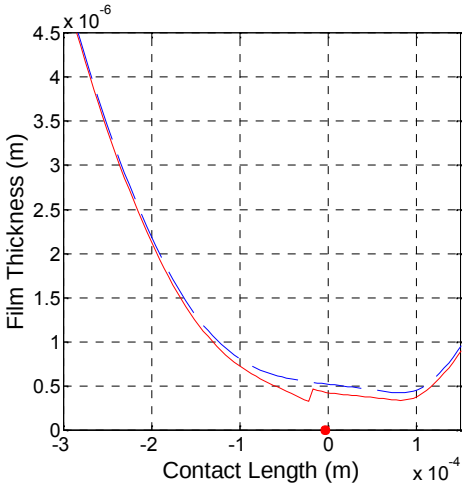
B5 - Load: 60000N/m Crack Length: 100um, Film Thickness Plots



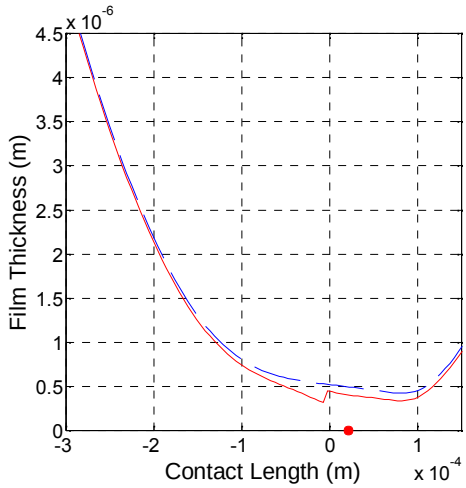


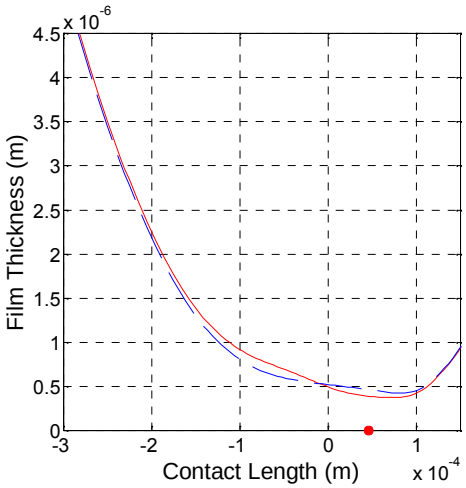
Fig, B5.1 EHL film shape (a) *Y* = -1.5E-4m (b) *Y* = -1E-4m





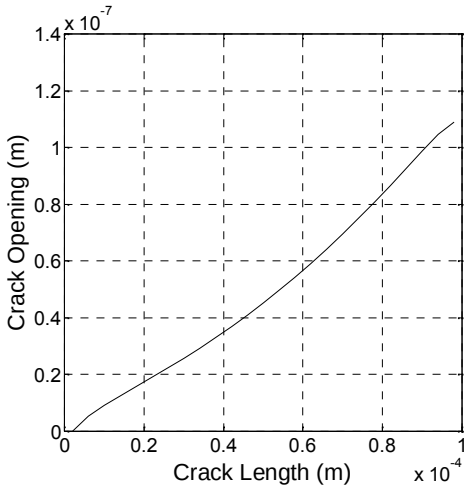
Fig, B5.1 EHL film shape (c) *Y* = -0.2E-4m (d) *Y* = -0.01E-4m

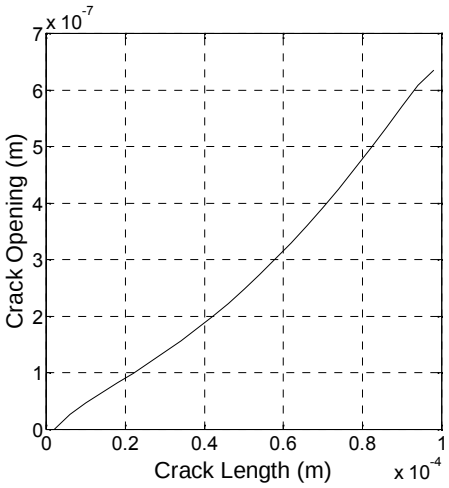




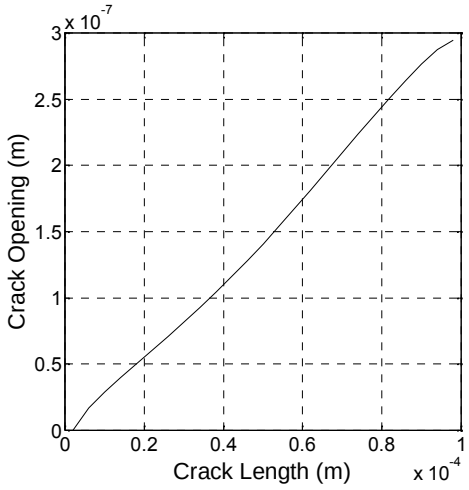
Fig, B5.1 EHL film shape (e) *Y* = 0.2E-4m (f) *Y* = 0.45E-4m

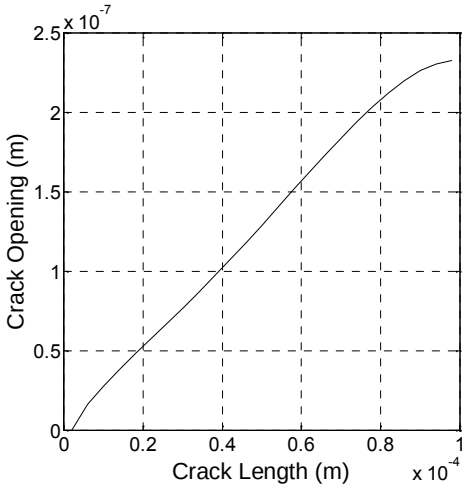
B6 - Load: 60000N/m Crack Length: 100um, Crack Shape Plots



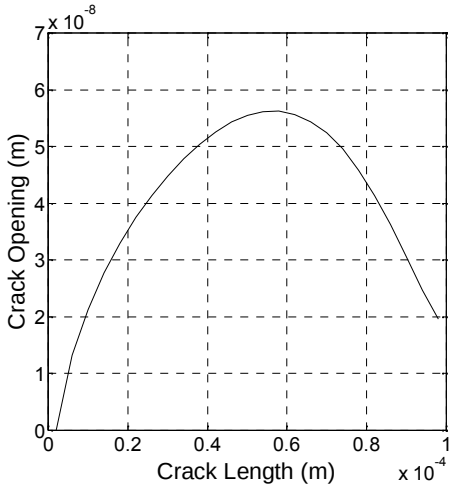


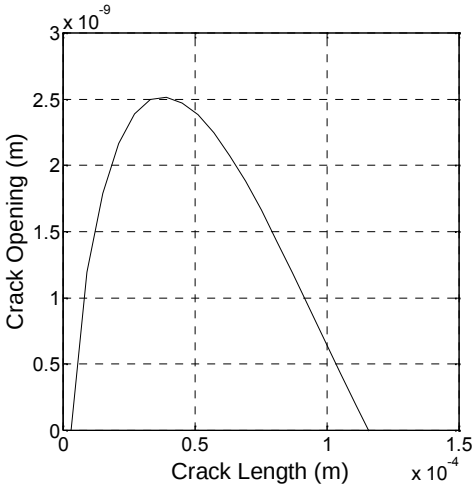
Fig, B6.1 Crack shape (a) *Y* = -1.5E-4m (b) *Y* = -1E-4m





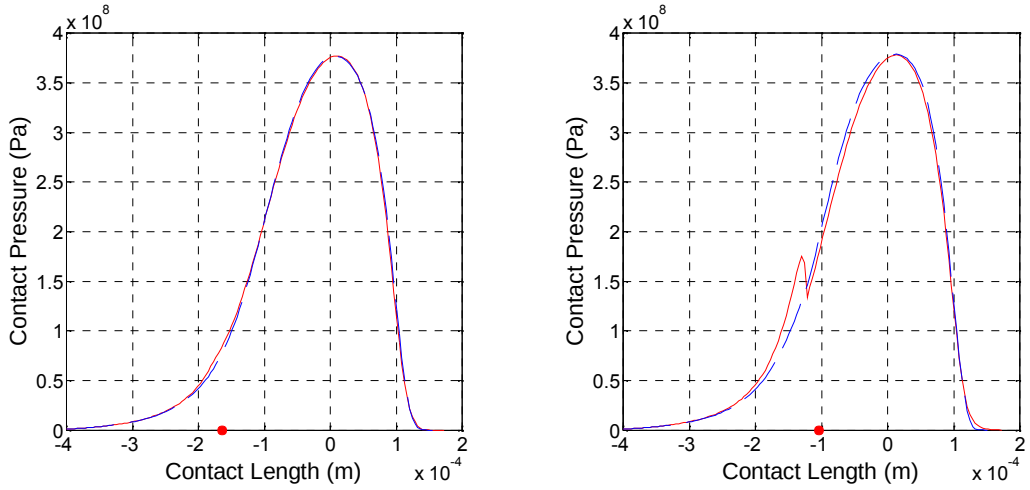
Fig, B6.1 Crack (c) *Y* = -0.2E-4m (d) *Y* = -0.01E-4m



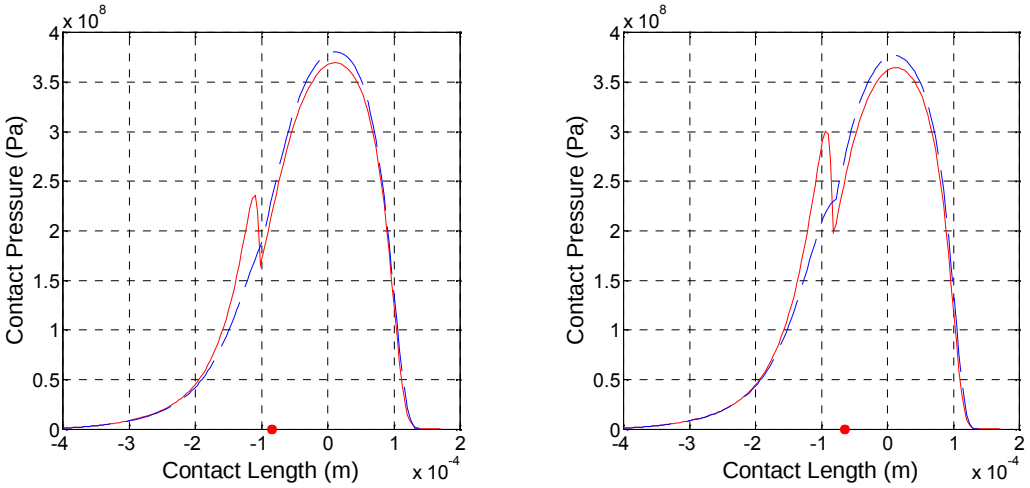


Fig, B6.1 Crack shape (e) *Y* = 0.2E-4m (f) *Y* = 0.45E-4m

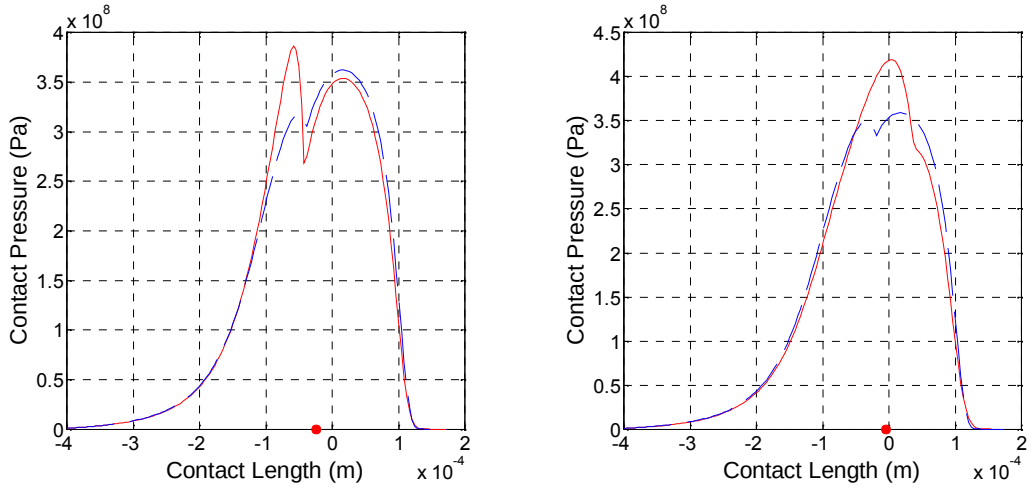
B7 - Load: 70000N/m Crack Length: 100um, Contact Pressure Plots



Fig, B7.1 EHL contact pressure (a) *Y* = -1.7E-4m (b) *Y* = -1.05E-4m

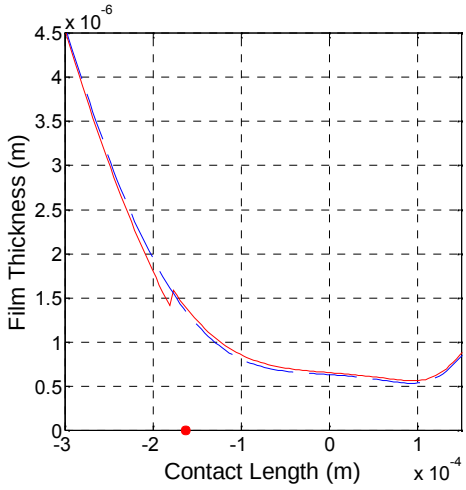


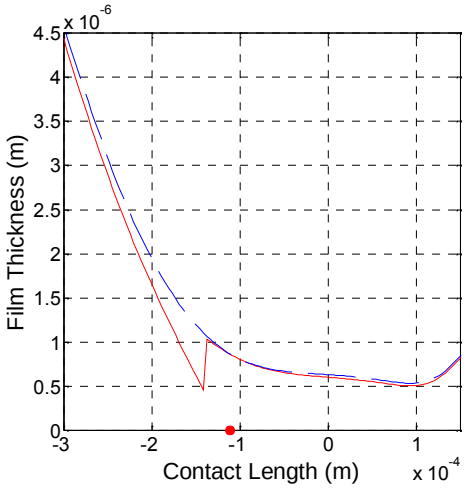
B7.1 EHL contact pressure (c) *Y* = -0.9E-4m (d) *Y* = -0.7E-4m



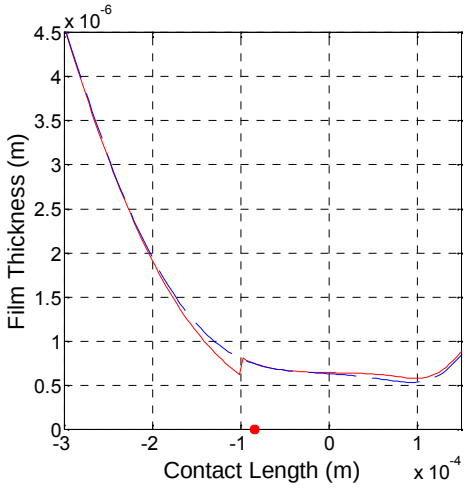
Fig, B7.1 EHL contact pressure (e) *Y* = -0.15E-4m (f) *Y* = 0E-4m

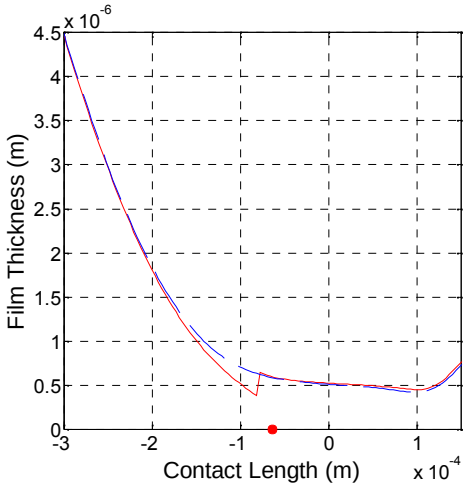
B8 - Load: 70000N/m Crack Length: 100um, Film Thickness Plots



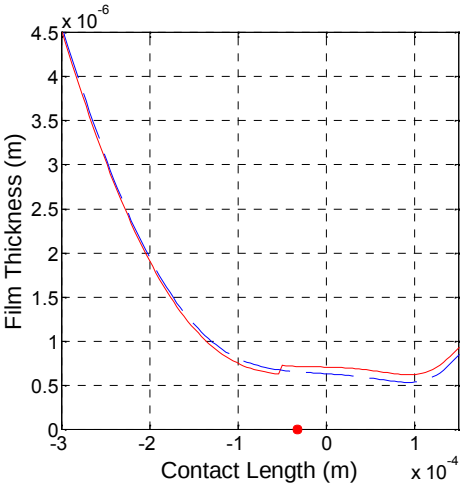


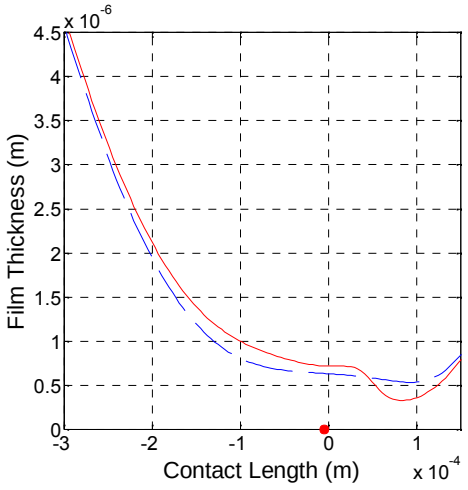
Fig, B8.1 EHL film shape (a) *Y* = -1.7E-4m (b) *Y* = -1.05E-4m





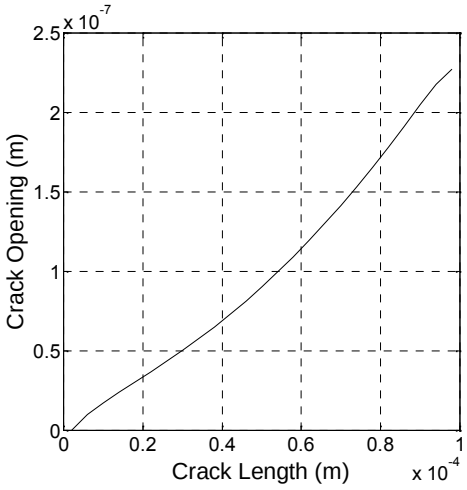
B8.1 EHL film shape (c) *Y* = -0.9E-4m (d) *Y* = -0.7E-4m

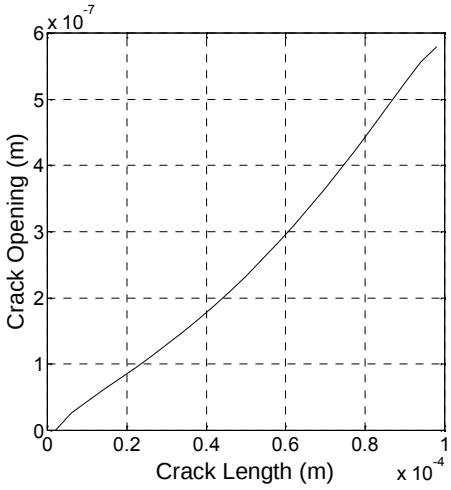




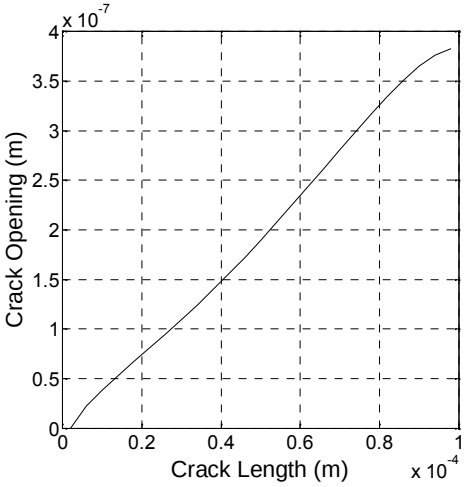
Fig, B8.1 EHL film shape (e) *Y* = -0.15E-4m (f) *Y* = 0E-4m

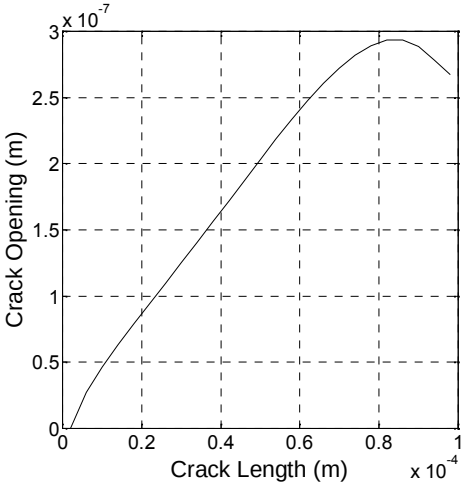
B9 - Load: 70000N/m Crack Length: 100um, Crack Shape Plots



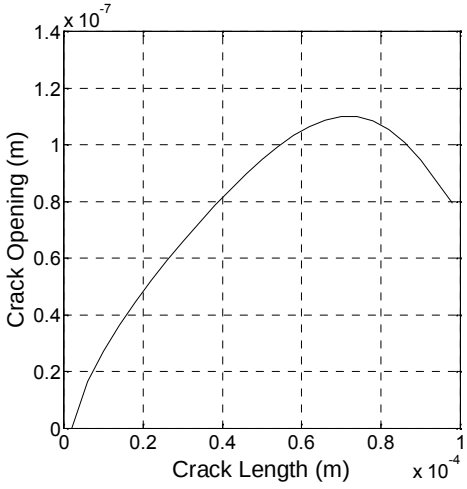


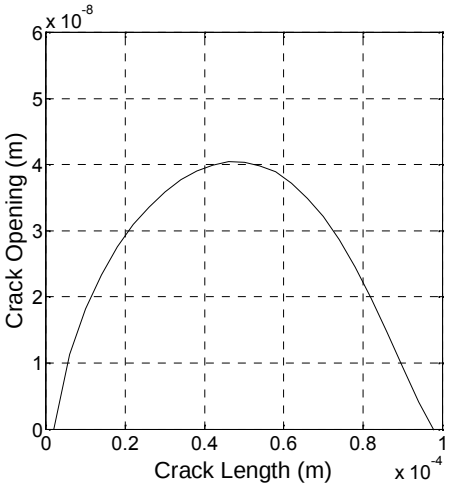
Fig, B9.1 Crack shape (a) *Y* = -1.7E-4m (b) *Y* = -1.05E-4m





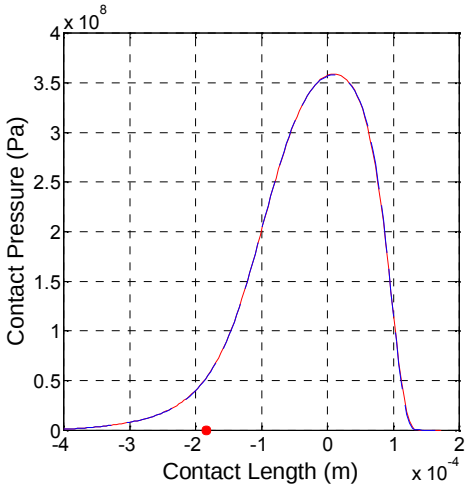
B9.1 Crack shape (c) *Y* = -0.9E-4m (d) *Y* = -0.7E-4m

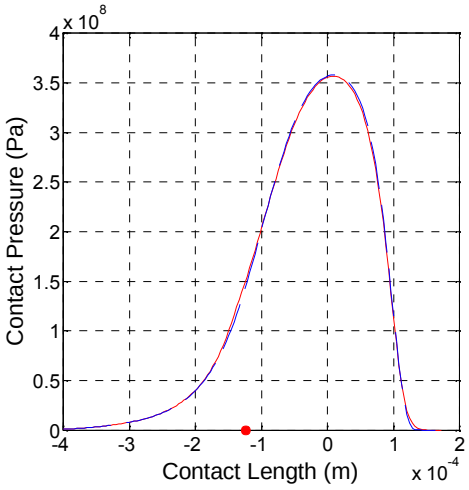




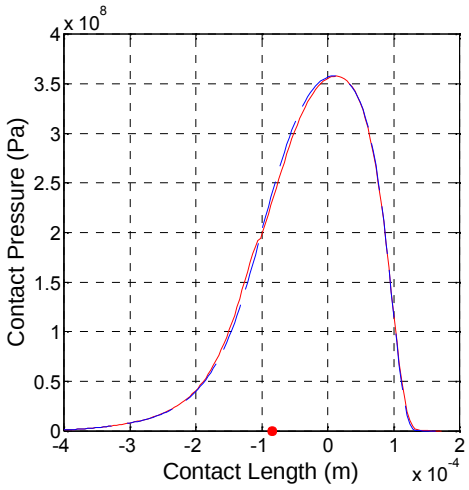
Fig, B9.1 Crack shape (e) *Y* = -0.15E-4m (f) *Y* = 0E-4m

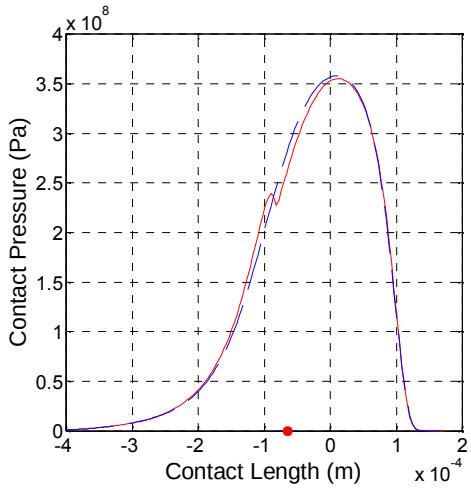
B -10 Load: 70000N/m Crack Length: 50um, Contact Pressure Plots



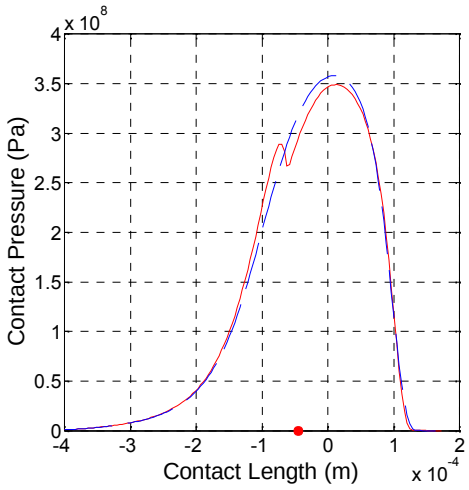


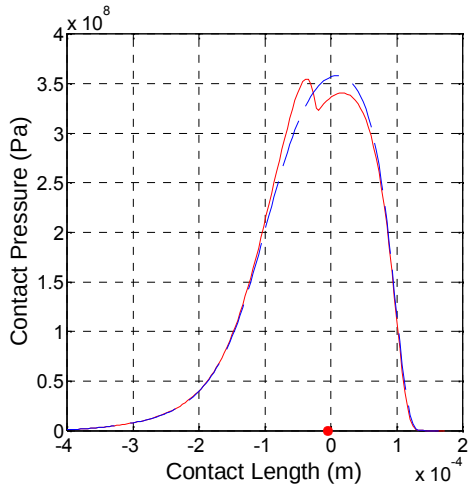
Fig, B10.1 EHL contact pressure (a) *Y* = -1.9E-4m (b) *Y* = -1.2E-4m





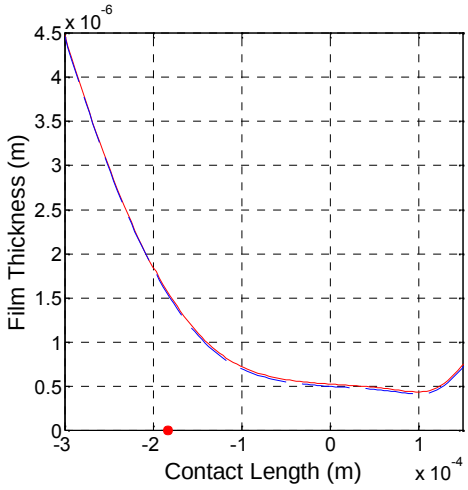
Fig, B10.1 EHL contact pressure (c) *Y* = -0.9E-4m (d) *Y* = -0.7E-4m

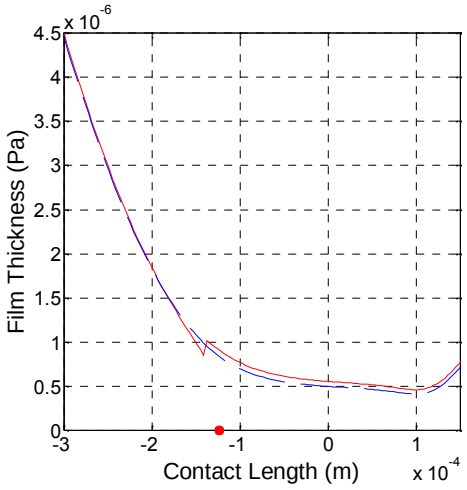




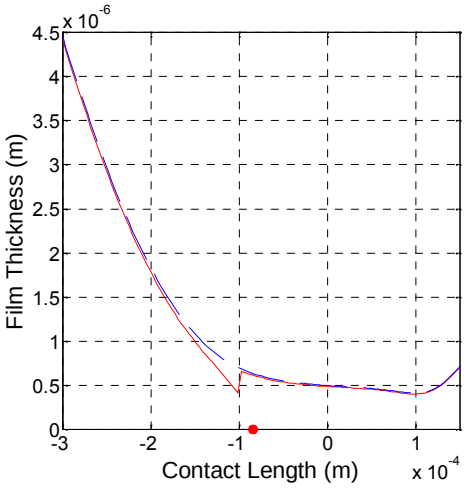
Fig, B10.1 EHL contact pressure (e) *Y* = -0.45E-4m (f) *Y* = -0.01E-4m

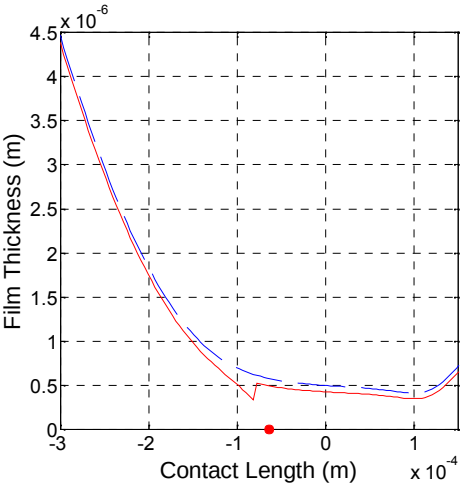
B11 - Load: 70000N/m Crack Length: 50um, Film Thickness Plots



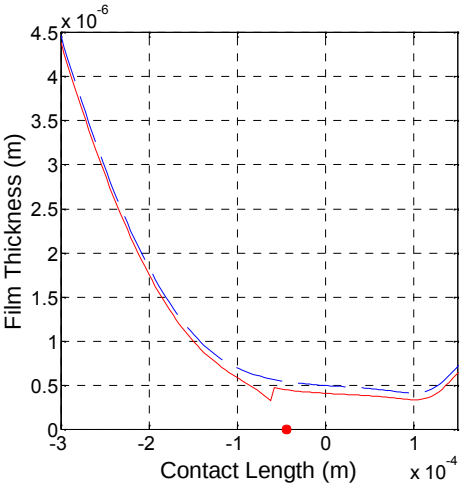


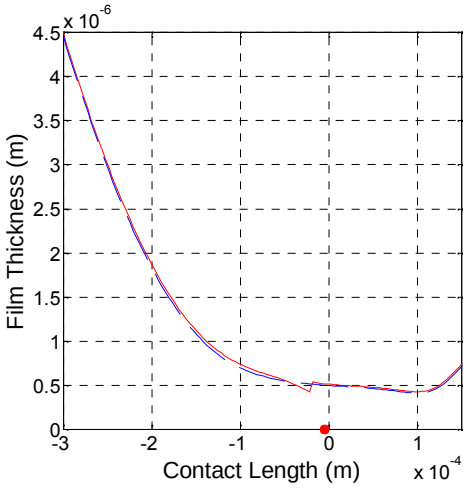
Fig, B11.1 EHL film shape (a) *Y* = -1.9E-4m (b) *Y* = -1.2E-4m





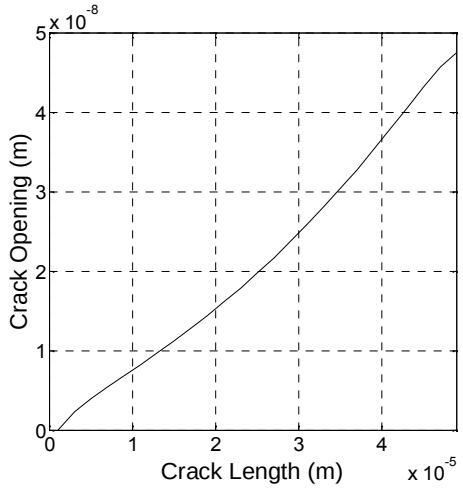
Fig, B11.1 EHL film shape (c) *Y* = -0.9E-4m (d) *Y* = -0.7E-4m

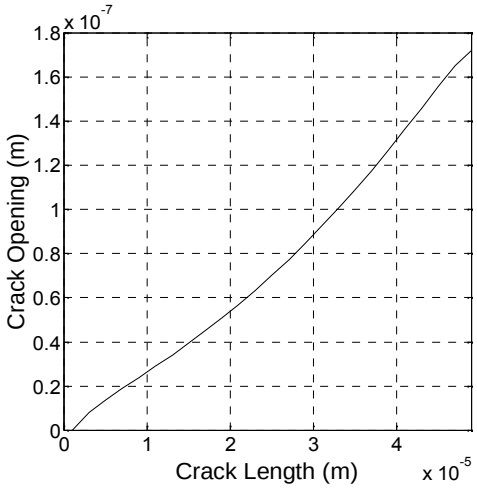




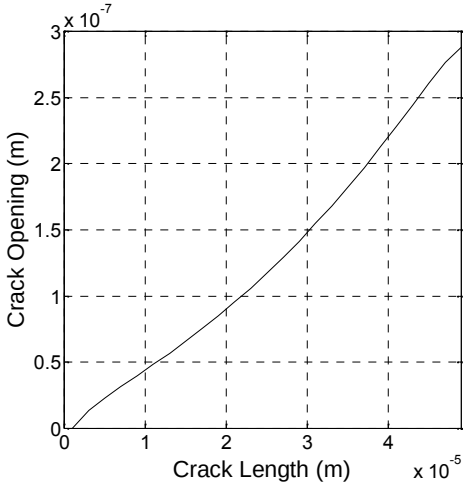
Fig, B11.1 EHL film shape (e) *Y* = -0.45E-4m (f) *Y* = -0.01E-4m

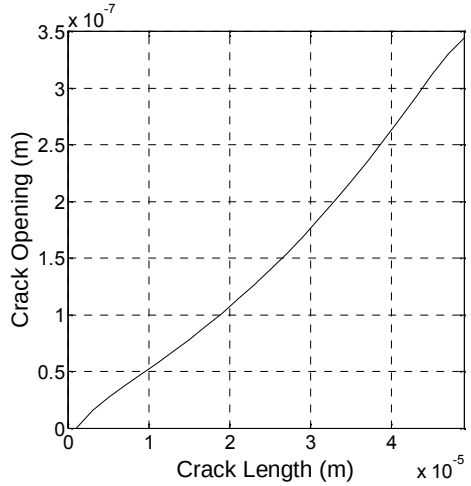
B12 - Load: 70000N/m Crack Length: 50um, Crack Shape Plots



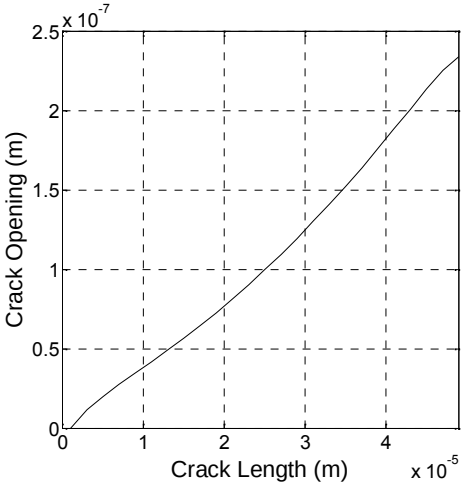


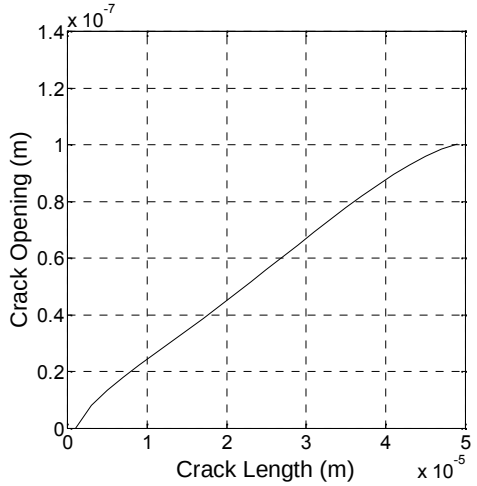
Fig, B12.1 Crack shape (a) *Y* = -1.9E-4m (b) *Y* = -1.2E-4m





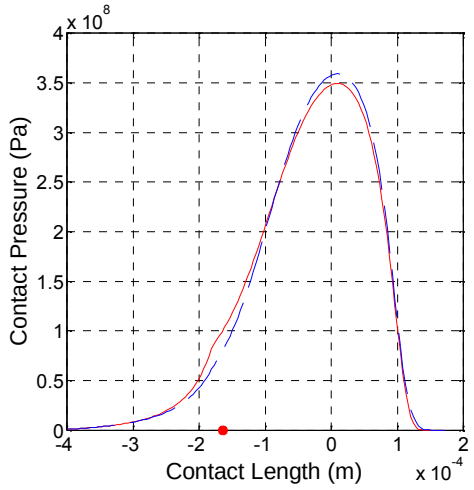
Fig, B12.1 Crack shape (c) *Y* = -0.9E-4m (d) *Y* = -0.7E-4m

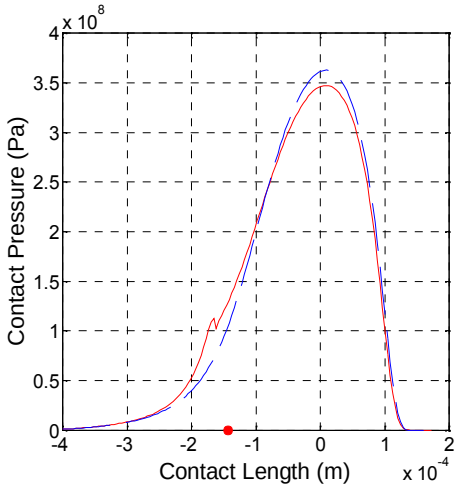




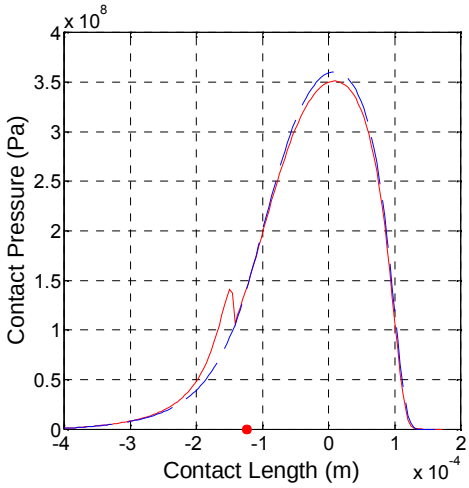
Fig, B12.1 Crack shape (e) *Y* = -0.45E-4m (f) *Y* = -0.01E-4m

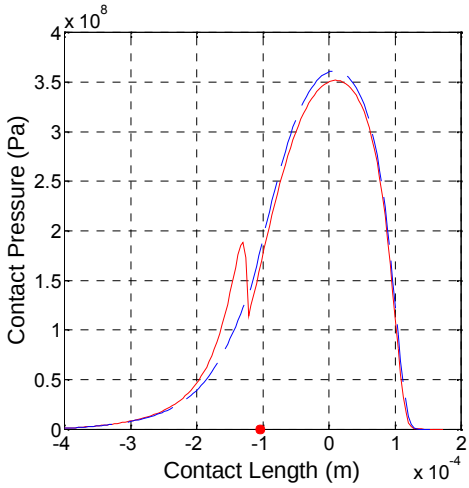
B13 - Load: 70000N/m Crack Length: 150um, Contact Pressure Plots



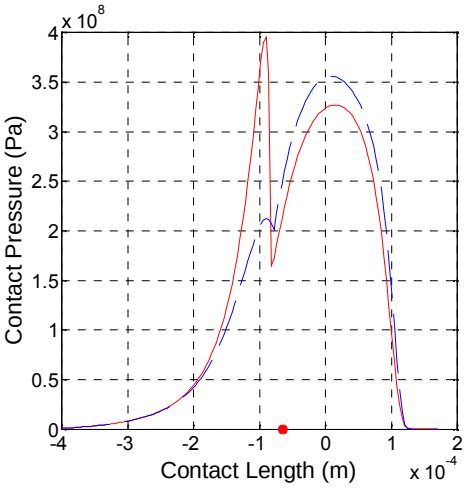


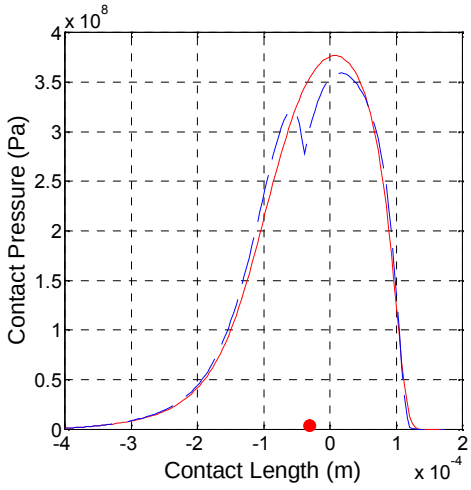
Fig, B13.1 EHL contact pressure (a) *Y* = -1.7E-4m (b) *Y* = -1.4E-4m





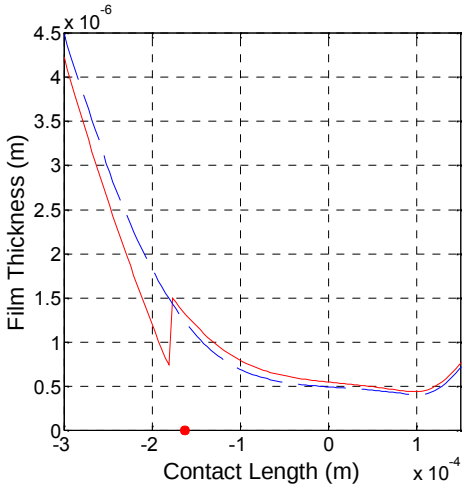
Fig, B13.1 EHL contact pressure (c) *Y* = -1.2E-4m (d) *Y* = -1.05E-4m

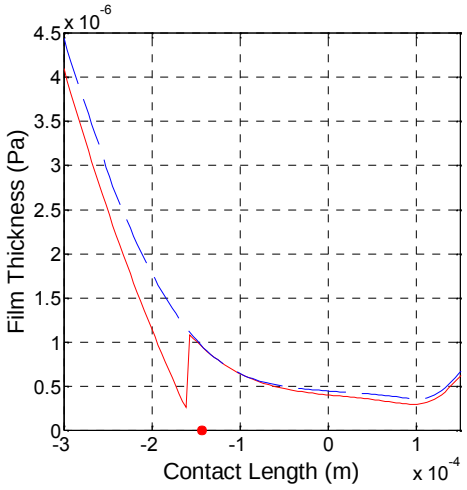




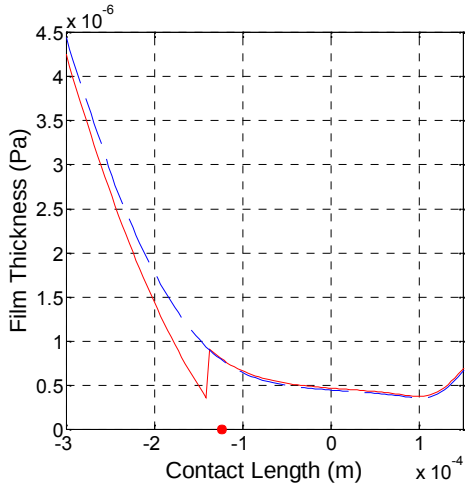
Fig, B13.1 EHL contact pressure (e) *Y* = -0.7E-4m (f) *Y* = -0.2E-4m

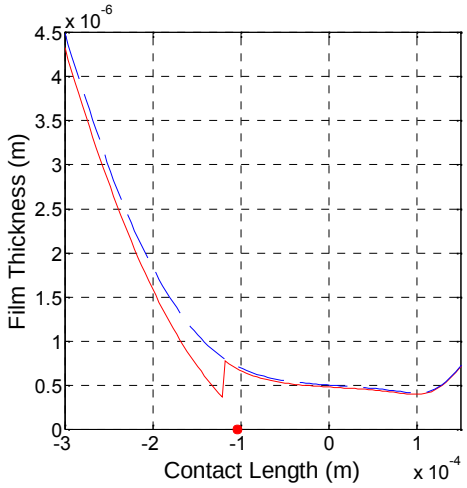
B14 - Load: 70000N/m Crack Length: 150um, Film Thickness Plots



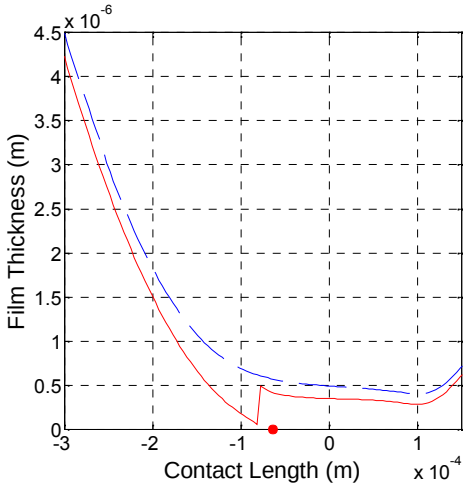


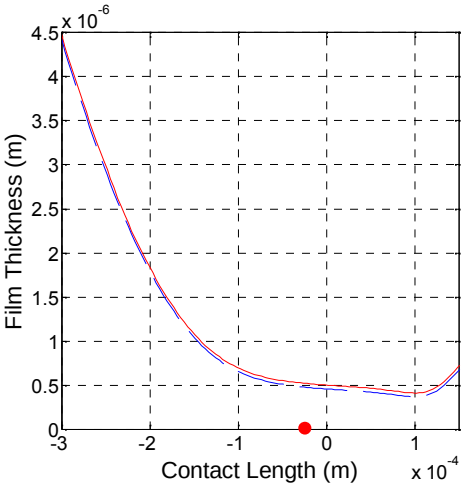
Fig, B14.1 EHL film shape (a) *Y* = -1.7E-4m (b) *Y* = -1.4E-4m





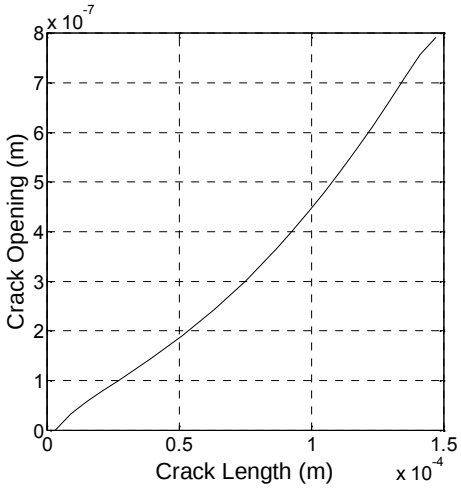
Fig, B14.1 EHL film shape (c) *Y* = -1.2E-4m (d) *Y* = -1.05E-4m

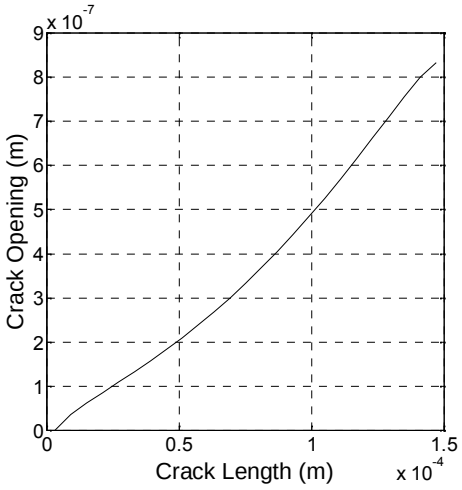




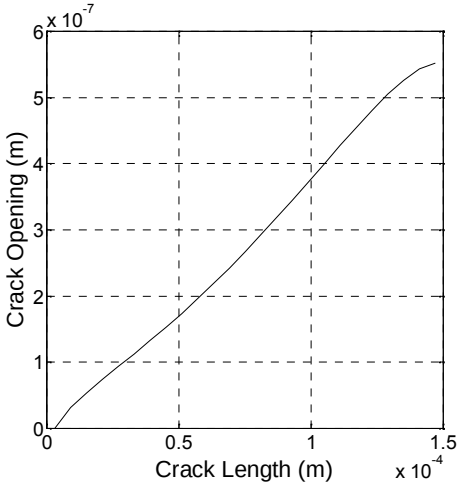
Fig, B14.1 EHL film shape (e) *Y* = -0.7E-4m (f) *Y* = -0.2E-4m

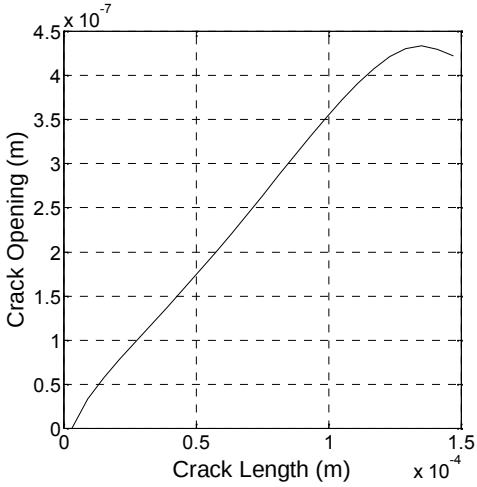
B15 - Load: 70000N/m Crack Length: 150um, Crack Shape Plots



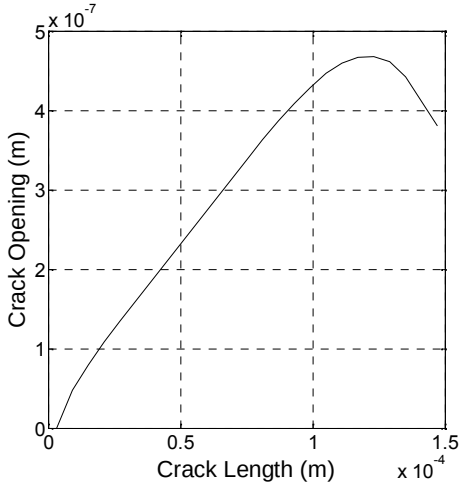


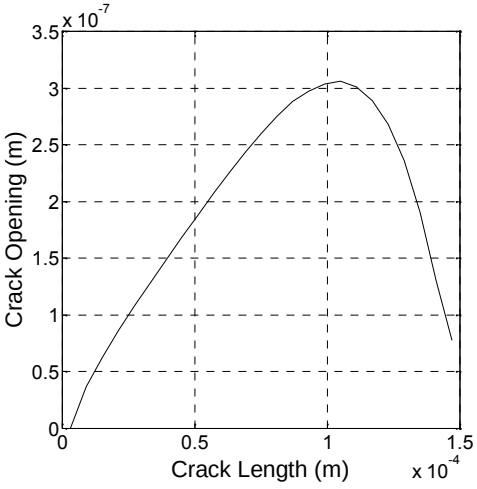
Fig, B15.1 Crack shape (a) *Y* = -1.7E-4m (b) *Y* = -1.4E-4m





Fig, B14.1 Crack shape (c) *Y* = -1.2E-4m (d) *Y* = -1.05E-4m





Fig, B14.1 Crack shape (e) *Y* = -0.7E-4m (f) *Y* = -0.2E-4